University of Trento – Italy

Department of Cellular, Computational and Integrative Biology - CIBIO
International PhD Program in Biomolecular Sciences
XXXII Cycle

Truncated BRPF1 cooperates with Smoothened to promote adult Shh medulloblastoma

Ph.D. Thesis of:
Giuseppe Aiello
Mat. 190369

Tutor:
Prof. Alberto Inga, PhD
Laboratory of Transcriptional Networks - CIBIO

Advisor:
Prof. Luca Tiberi, PhD
Armenise-Harvard Laboratory of Brain Disorders and Cancer - CIBIO

Declaration

I, the undersigned Giuseppe Aiello, hereby declare that this is my own work and the use of all materials from other sources has been properly and fully acknowledged.

No amount of experimentation can ever prove me right; a single experiment can prove me wrong.

Albert Einstein

Acknowledgement

should change the saying "who finds a friend finds a treasure" to "who finds FRENCY, finds a treasure". Thank you!

I would like to thank **Riccardo Ruggeri**, also known as "the little Riccardino Fuffolo". He has been my Lab soulmate for almost 2 years, with him I have shared everything. In him I found a confidant, a friend and a brother. I don't know where we will be in the future, but I hope that when we will be old men, we will continue to support each other. Thanks for all you've done for me!

But my biggest thanks go to **Ilaria Morassut**. She is the person who knows me more than anyone else. She was present at any time, even if distant, helping me at all times. She is capable of infusing me with passion and the strength to always push me beyond my limits. But most importantly, she is capable of transmitting me happiness. "HAPPINESS ONLY REAL WHEN SHARED - cit. Into The Wild".
I don't know where I will be in the future, but I will certainly be with you. Thank You!

Finally, all this would not have been possible without the help of my family, my parents **Gaetano Aiello** and **Antonella Gueli** and my sister **Rita Aiello**. Obviously it is not possible to choose your family, but if it were possible, I will always choose them. They represent everything for me, past, present and future and if today I am what I am, it is largely thanks to them. I love you, thank you very much!

Table of contents

Abbreviations

ATOH1	=	Atonal BHLH transcription factor 1
BARHL1	=	BarH like Homeobox 1
BR140	=	Bromodomain-Containing Protein, 140kD
BRPF1	=	Bromodomain And PHD Finger Containing 1
CGNP	=	Cerebellar granule neuron progenitors
CK1	=	Casein kinase 1α
CMV	=	Cytomegalovirus
CNA	=	Copy number aberrations
CNS	=	Central nervous system
DCN	=	Deep Cerebellar Nuclei
DCX	=	Doublecortin
DHH	=	Desert hedgehog
Dpn	=	Deadpan
EAF6	=	Esa1 Associated Factor 6
EGL	=	External granule layer
EN1	=	Engrailed 1
EPC	=	Enhancer of polycomb
Etv1	=	ETS Variant transcription factor 1
FGF8	=	Fibroblast growth factor 8
FZZ	=	Frizzled
GAB1	=	GRB2 associated binding protein 1
GABRA6	=	Gamma-aminobutyric acid type A receptor alpha6 subunit
GBM	=	Glioblastoma
GBX2	=	Gastrulation brain homeobox 2
GLI	=	GLI family zinc finger
GMC	=	Ganglion mother cell
GSK3β	=	Glycogen synthase kinase 3β
H3	=	Histone 3
H3K36me3	=	Trimethylated residue 36 of histone H3
HAT	=	Histone acetyltransferase
HBO1	=	Histone acetyltransferase bound to ORC1
HDAC	=	Histone deacetylase
HDM	=	Histone demethylase
HOX	=	Homeobox
hSynI	=	Human Synapsin I
ICP	=	Increased intracranial pressure
IECs	=	Intestinal epithelial cells
iEGL	=	inner external granule layer
IFT	=	Intra-flagellar transport
IGL	=	internal granule layer
IHH	=	Indian hedgehog
ING5	=	Inhibitor of Growth Family Member 5
IsO	=	Isthmic organizer

KO	= Knock-out
LCA	= Large cell anaplastic
LGR5	= Leucine rich repeat containing G protein-coupled receptor 5
LHX2	= LIM homeobox 2
Lola-N	= Longitudinal lacking-N
LTR	= Long terminal repeat
MATH1	= Atonal BHLH transcription factor 1
MB	= Medulloblastoma
MBEN	= Medulloblastoma with extensive nodularity
MHB	= Midbrain-hindbrain boundary
MORF	= MOZ-related factor
MOZ	= Monocytic leukemia zinc finger protein
MYCN	= MYCN Proto-Oncogene, BHLH Transcription Factor
N	= Necrosis
NeuroD1	= Neuronal Differentiation 1
NGS	= Next-generation Sequencing
NSCL1	= Nescient Helix-Loop-Helix 1
oEGL	= outer external granule layer
OTX2	= Orthodenticle homologue 2
pAKT	= Phosphorylated AKT Serine/Threonine Kinase
PC	= Purkinje cells
PHD	= Plant homeo domain linked
PKA	= Protein kinase A
pS6	= Phoshorylated Ribosomal Protein S6 Kinase
PTCH1	= Patched1
PTEN	= Phosphatase And Tensin Homolog
PWM	= Prospective white matter
PZP	= PHD finger-zinc knuckle-PHD finger
R	= Repressor
RBFOX3	= RNA binding fox-1 homolog 3
RGC	= Retinal ganglion cells
RL	= Rhombic lip
SCID	= Severe combined immunodeficiency
SCNAs	= Somatic copy number aberrations
SHH	= Sonic Hedgehog
shRNA	= Short hairpin RNA
SMO	= Smoothened
SUFU	= Suppressor of Fused
TERT	= Telomerase reverse transcriptase
TP53	= Tumor Protein P53
TUJ1	= tubulin-associated tubulin beta 3 class III
VZ	= Ventricular zone
WNT1	= Wingless-related MMTV integration site 1
YAP1	= Yes associated protein 1
ZIC	= Zinc family member

Abstract

Tumors are composed of proliferating cells that invade healthy tissue and grow over time. Even though it is still unclear, it is a common opinion that the cells of origin should possess a proliferative capacity (Blanpain, 2013; Visvader, 2011). Particularly for brain cancers, the transition of neural progenitors to differentiated postmitotic neurons is considered irreversible in physiological and pathological conditions. Therefore, postmitotic neurons have not been considered as suitable cell of origin for brain cancer. Here, we show that neurons reprograming may occur upon Shh activation leading to medulloblastoma (MB) formation *in vivo*. Human SHH medulloblastoma (MB) is a brain tumor affecting adults and infants that is thought to originate from cerebellar granule neuron progenitors. Notably, several groups have shown that Shh pathway activation (SmoM2 overexpression) in mouse granule neuron progenitors is able to induce Shh MB (Schuller et al., 2008; Z.-J. Yang et al., 2008). These progenitors are present in infants and newborn mice, but they seem to be absent in adult humans and mice (Biran, Verney, & Ferriero, 2012; Marzban et al., 2014; Z.-J. Yang et al., 2008). Furthermore, it was recently discovered that the two different forms of SHH MB are distinguished by different transcriptome/methylome levels suggesting that the adult SHH MB may originate from a different cell of origin (Cavalli et al., 2017; Kool et al., 2014). Relying on these data, we take advantage of a conditional Cre-Lox recombination system to recapitulate the human adult medulloblastoma pathogenesis in mice, demonstrating that cerebellar post-migratory mature granule neurons upon SmoM2 overexpression can dedifferentiate and give rise to SHH MB *in vivo*. Moreover, human adult patients present inactivating mutations of the chromatin reader BRPF1 that are associated with SMO mutations and absent in pediatric and adolescent patients. Here we found that truncated BRPF1 protein, as found in human adult patients, is able to induce medulloblastoma in adult mice upon SmoM2 activation. Notably, gene expression profiling on our samples allowed to associate "cerebellar granule progenitors-derived MB" with the human infant form while "truncated BRPF1-induced tumors" clustered with human adult SHH MB. Furthermore, as previously described by Kool et al., 2014, human adult SHH MB is characterised by the co-presence of p-AKT and p-S6, compared to the human infant SHH MB that are positive for either p-AKT or p-S6 and always in a mutually exclusive way. Truncated BRPF1-induced tumors are double positive for p-AKT and p-S6, similarly to adult patients, while cerebellar granule progenitors derived MB present only p-S6. Furthermore, to define the contribution of chromatin changes in granule neurons dedifferentiation in response to Shh activation, we profiled changes in chromatin accessibility by ATAC-seq analysis on mice cerebella. SmoM2 overexpression changed the epigenetic landscape of granule neurons, enriching the number of open chromatin regions

associated with stem/progenitor-like genes. Moreover, the cooperation between truncated BRPF1 and SmoM2 in reshaping the chromatin arrangement of granule neurons was explored applying ATAC-seq on differentiated human cerebellar neurons derived from neuroepithelial cells. ATAC-seq analysis pointed out a synergistic mechanism between SmoM2 and truncated BRPF1 in modifying the epigenetic landscape of postmitotic neurons, increasing the chromatin accessibility of super-enhancers, associated with stemness and chromatin organization/modification genes. Our novel model of cancer development could explain the human SHH medulloblastoma onset in adult individuals where granule neuron progenitors are no more present. For these reasons, we strongly believe that our model configures as an important starting point for a new field in cancer and stem cell biology focusing on the study of mechanisms driving tumorigenesis in postmitotic cells.

1. Introduction

1.1 The dedifferentiation role in cancer development

1.1.1 Dedifferentiation: a break point in Waddington's landscape

In 1957, Conrad Waddington described mammalian cell development as a unidirectional path towards differentiation. In its metaphor, he depicted a cell as a ball rolling from the top of the Waddington's mountain, where the highest degree of freedom for cell fate is, down to the bottom of the valley, where the final differentiated state is reached thanks to unique combinations of genetic and environmental factors. (Waddington, 1956) (Figure 1A). This landscape illustrates a progressive physiological restriction of the differentiation process during normal development.

However, Waddington's dogma was definitely destroyed by the discovery of Yamanaka et al. that has shown how terminally differentiated cells can be reprogrammed up to their original pluripotent state (Takahashi & Yamanaka, 2006). Nevertheless, the acceptance of the same concept is still under discussion when applied to cancer development. It is a common idea that tumor initiating cells should possess a proliferative capacity (Blanpain, 2013; Visvader, 2011). Genetic perturbation might affect multipotent or unipotent progenitors leading to an uncontrolled proliferation burst. However, several recent discoveries have revised this idea, leading to the distinction of two possible cancer development models, the "genetic mutation model" and the "cell-of-origin model" (Figure 1B and Figure 1C) (Visvader, 2011). The two models have been conceptualized to explain intertumoral heterogeneity, but at the same time imply the concept that mutations in different cells and at different timing could promote different tumor subtypes. This outstanding theory can also be useful to explain the great heterogeneity found among molecular subtypes of the same cancer and goes against the Waddington's dogma. Indeed, different cells of origin, including post-mitotic cells, could lead to the development of similar but not identical tumours from the same tissue. The dedifferentiation process occurring in the mature cells during cancer development could be caused by mutational hits in genes involved in cells epigenetic organization. Indeed, it is already known that the cell maturation process requires a great reorganization of chromatin structure, which usually assumes a more closedconformation compared to pluripotent stem cells. Consequently, mutations in DNA-methylation-associated genes and chromatin regulators genes could have more relevance in dedifferentiation-induced cancer compared to other kind of tumours (Blanpain, 2013; Visvader, 2011; Visvader & Lindeman, 2012).
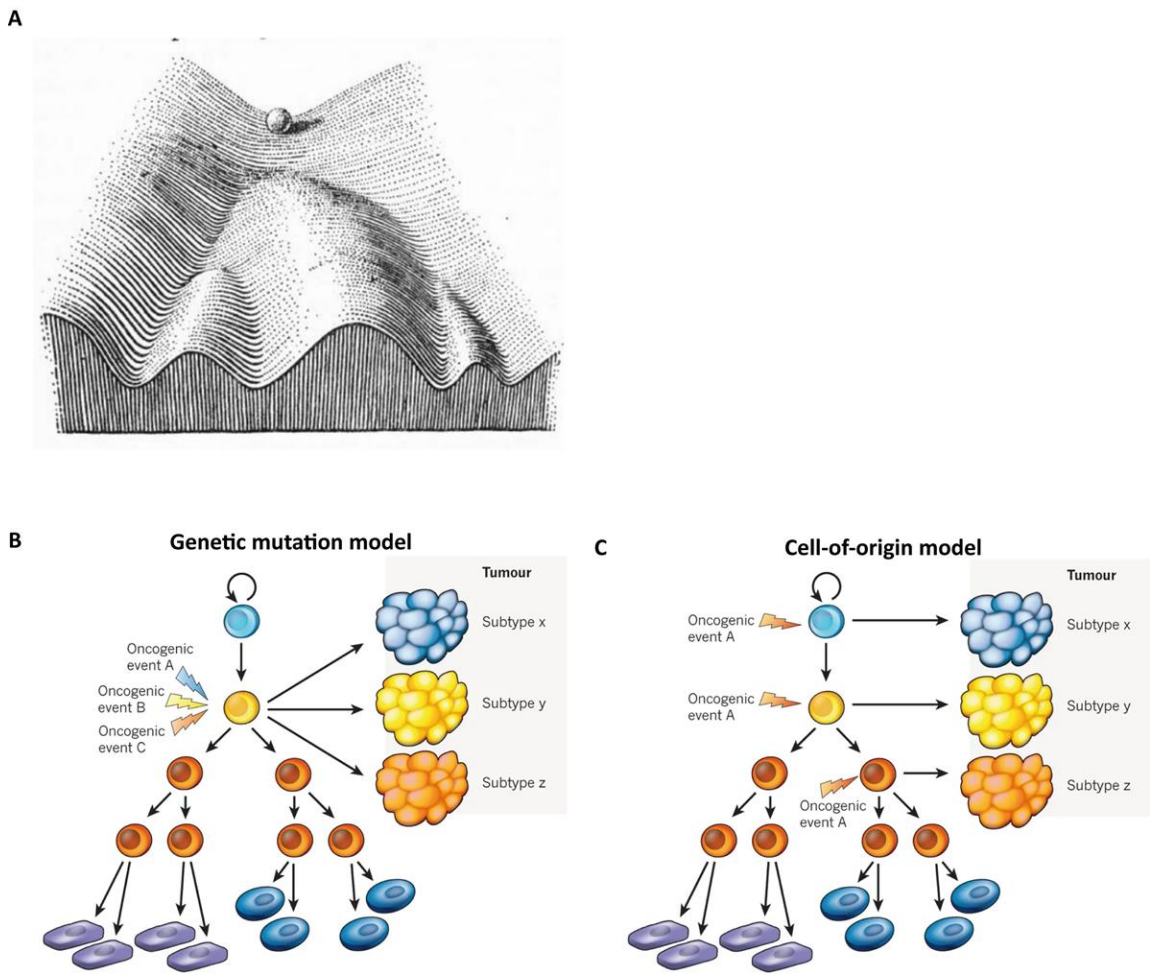
Figure 1: Difference between genetic mutation and cell-of-origin model explains intertumoral heterogeneity. **(A)** Waddington's landscape describing the differentiation path followed by an embryonic stem cell. As a ball, it rolls down towards more differentiated states. There are alternative paths, which, however, can only be reached over a certain threshold (Waddington, 1956). **(B)** The genetic mutation model explains how different mutations in the same cell of origin could generate different tumour subtypes. **(C)** The cell-of-origin model shows that the same mutation can hit different cell populations in the lineage hierarchy, triggering the development of different cancer subtypes, arising within the same organ or tissue (Visvader, 2011).

1.1.2 Dedifferentiation-induced cancers in blood, liver and intestine

For several kind of tumors, the dedifferentiation process has been already proposed as a triggering factor. Solid evidence of a bidirectional path between stemness and differentiation have been suggested for other tissues such as blood, liver and intestine. Mature and differentiated cells have been considered as cancer cell-of-origin, thus denying a strict unidirectional model of the stem-differentiation hierarchy. In the context of blood cancers, Cobaleda et al. in 2007 demonstrated how mature B cells from peripheral lymphoid organs depleted of the transcription factor PAX5 dedifferentiate *in vivo,* back to early uncommitted

progenitors status in the bone marrow. Those dedifferentiated cells are able to repopulate T-cell population in thymus-deficient mice and also to contribute to the development of aggressive lymphomas (Cobaleda, Jochum, & Busslinger, 2007). The dedifferentiation process has been observed also in solid tumors. Remarkable are the works of Tschaharganeh et al, 2014 and Schwitalla et al., 2013 that indicated mature differentiated cells as tumor cell-of-origin in liver and intestine cancers respectively. Indeed, mature hepatocytes depleted of p53 can abrogate the Sp1/3 transcription factors-mediated repression of Nestin, leading to a conversion in progenitors-like cells that are able to expand and generate hepatocellular carcinomas or cholangiocarcinomas (Tschaharganeh et al., 2014). Moreover, intestinal epithelial cells (IECs) characterized by the simultaneous presence of KRAS oncogenic hit and microenvironment-induced activation of NF-kB resulted in the overactivation of Wnt pathway, that pushed them towards a stem-like state. IECs are characterised by the expression of leucine rich repeat containing G protein-coupled receptor 5 (*Lgr5*), a stemness marker that defines the cell population at the bottom of intestinal crypts, and can dedifferentiate to LGR5+ cells that are already known to be involved in intestinal colon cancer development (Schwitalla et al., 2013). Those studies on hepatocytes, intestinal cells and B lymphocytes indicate the dedifferentiation as a possible mechanism for cancer development. However, those cells still retain the ability to proliferate and the physiological high rate of cell plasticity in these tissues may justify and facilitate the dedifferentiation compared to other organs characterized by more committed and differentiated cells such as the central nervous system (CNS).

1.1.3 Dedifferentiation-induced cancers in the central nervous system

The CNS is characterized by neurons that are generally considered as "permanently post-mitotic cells" (Herrup & Yang, 2007). The different timing of differentiation, from neural stem cells to mature neurons, determine well-defined morphologies and functions among different nervous system regions. Indeed, the cerebral cortex is subdivided into several specialized areas (Nguyen, Besson, Roberts, & Guillemot, 2006). The transition of neural progenitors to differentiated postmitotic neurons is considered irreversible in physiological and pathological conditions. However, recently, several research groups have attempted to understand how neuronal identity is regulated and maintained through life. Up to now, it is known that neuronal differentiation is based on early gene regulatory programs which are maintained throughout all neurons life. Indeed, several transcription factors involved in the specification of neurotransmitters machinery seem to be required for the maintenance of neuronal identity, therefore a deep understanding of this mechanism could clarify if the disruption of this genetic program can evolve in pathological

conditions or be exploited for regenerative therapies (Deneris & Hobert, 2014; Nguyen et al., 2006). Furthermore, several groups attempted to demonstrate that post-mitotic neurons retain a cell plasticity rate and can undergo a dedifferentiation process, candidating as putative tumor-initiating cell for certain kinds of cancers. Southall et al. in 2014 studied this phenomenon in *Drosophila melanogaster*. They demonstrated that the knock-down of *longitudinal lacking-N* (*lola-N*), a robust repressor of neural stem cell genes, forced post-mitotic neurons to dedifferentiate and re-enter in the cell cycle (Figure 2A). *Lola-N* is an orthologous of the vertebrate BTB-ZF family gene, it could act in the same way, recruiting histone deacetylases (HDACs) and inducing sequence-specific silencing of gene expression. Lola-N-depleted neurons start to re-express neuroblast-associated markers such as Deadpan (Dpn) and produce proliferating masses in the optic lobes of adult fly brain, showing that Lola-N can act as a differentiation lock (Figure 2B) (Southall, Davidson, Miller, Carr, & Brand, 2014). The strong limitation in the reliability of this work relies on the conditional driver Elav-Gal4 that they used to induce the *lola-N* knock-down. Indeed, Elav-Gal4 can be expressed also in neuroblasts (Berger, Renner, Luer, & Technau, 2007; Yao & White, 1994) thus not avoiding a possible contribution of uncommitted cells in tumor formation.
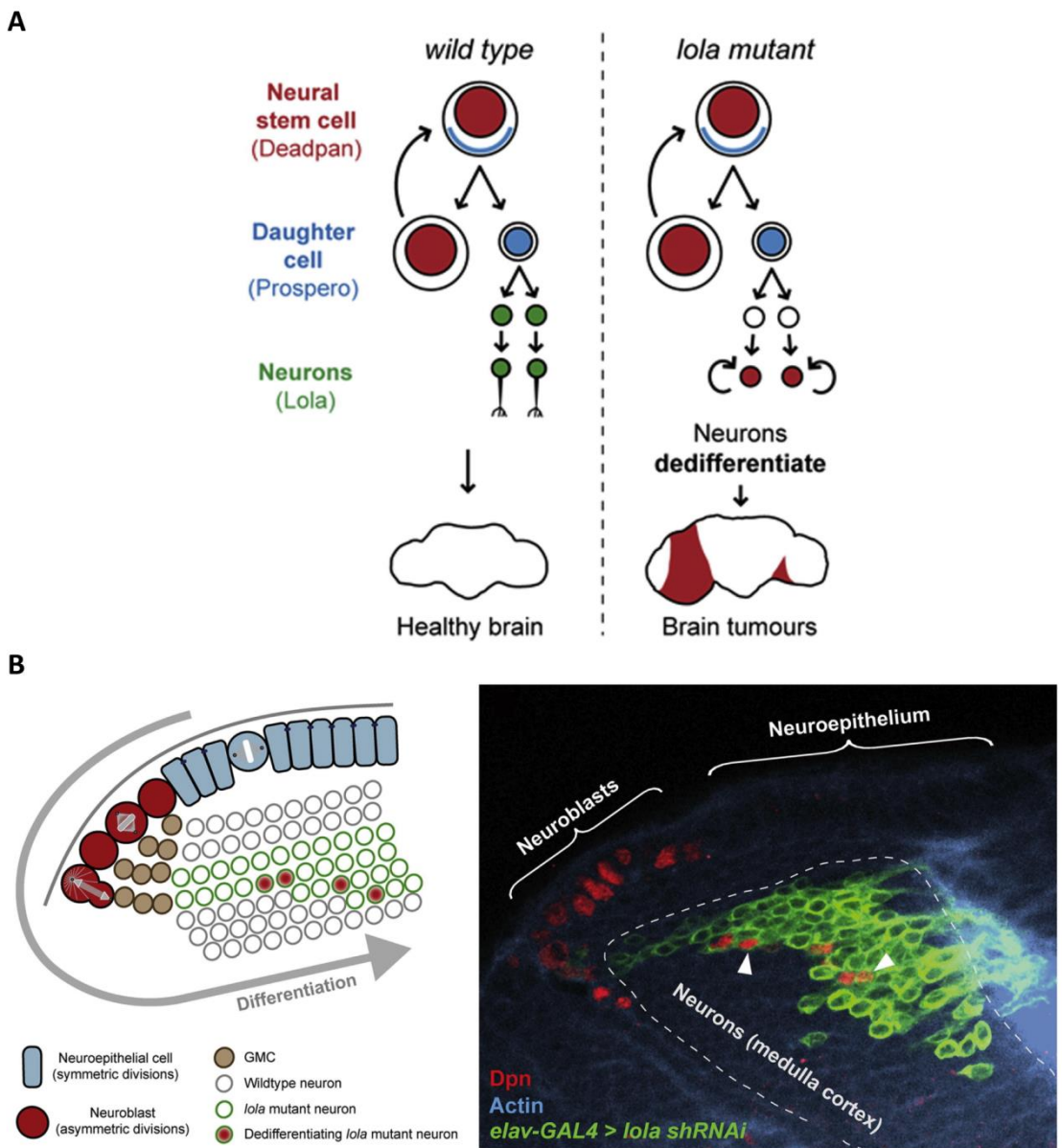
Figure 2: Lola mutant neurons dedifferentiate to a neural stem cell fate. (A) Graphical representation of neurons dedifferentiation model in lola mutant background. **(B)** Representation of differentiation hierarchy in larval optic lobe and immunofluorescence that shows dedifferentiating elav-GAL4 neurons (green) expressing deadpan. Abbreviations: ganglion mother cell (GMC), Deadpan (Dpn), Longitudinal lacking (Lola) (Southall et al., 2014).

Furthermore, two remarkable works on *Mus musculus* try to show the involvement of neuronal dedifferentiation in cancer development. Ajioka et al. in 2007 demonstrated that differentiated horizontal interneurons located in the inner nuclear layer of the retina can clonally expand to form metastatic retinoblastomas in mice upon genetic perturbations. This work showed that differentiated (Rb)(-/-);p107(+/-);p130(-/-) horizontal interneurons re-entered the cell cycle, clonally expanded and formed metastatic retinoblastoma. Nevertheless, the limitation of this paper consists in the application of genetic deletion without any spatial restriction; indeed, authors used a full knock-out (KO) of p130 and p107, which cannot avoid the involvement of retinal progenitors during cancer development. Moreover, they exploit Chx10 promoter to induce

the recombination in Rb lox/lox locus and this approach, again, cannot exclude with certainty that the genetic perturbation is also present in retinal progenitors, since in these cells, during development, Chx10-Cre transgene is expressed with a mosaic pattern (Ajioka et al., 2007). Lastly, Friedmann-Morvinski et al. in 2012 showed glioblastoma (GBM) formation knocking down simultaneously p53 and NF1 in post-mitotic neurons. To achieve this purpose, they injected hSynI-cre mice with oncogenic lentiviral vectors carrying shRNAs for p53 and NF1 under the control of constitutive promoters and a reporter cassette composed of RFP, flanked by two loxP sites, and IRES-GFP (Figure 3A). Hippocampal injection lead to formation of GBM (Figure 3B) characterized by GFP$^+$/RFP$^-$, cells in which recombination occurred and that theoretically represent neurons beginning to dedifferentiate, and by GFP$^+$/RFP$^+$ cells, in which no recombination occurred/took place (S. R. Alcantara Llaguno & Parada, 2016; Friedmann-Morvinski et al., 2012). The limitation in the reliability of this work is based on the fact that neuron dedifferentiation is led by a vector carrying a short hairpin RNA (shRNA) targeting p53 that is not under the control of a cre system. As reported in the work of Wang et al, the lack of p53 itself can lead to the tumor formation and this can happen within progenitor cells (Y. Wang et al., 2009).

Although these works are promising, due to intrinsic limitations, a valid and precise model able to clarify the dedifferentiation process has not yet been realized. Consequently, the confirmation of neuronal dedifferentiation is an outstanding and necessary information to acquire in order to understand cancer outcomes and develop new potential therapeutic strategies.
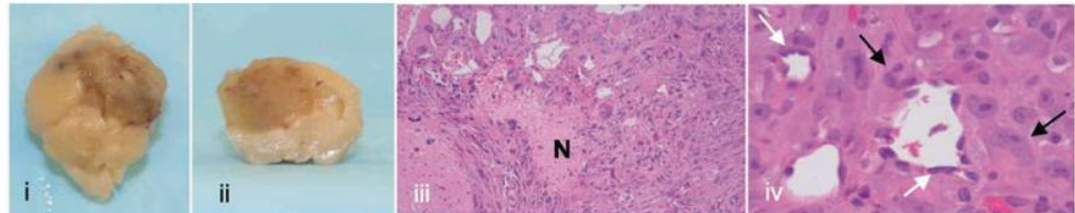
Figure 3: GBM tumor induced by lentiviral vector transduction in hSynI-cre mice. (A) Schematic representation of the lentiviral vector. In the shNF1-shp53 vector, the hairpin targeting NF1 is cloned under the H1 promoter at the 3' untranslated region, and the hairpin targeting p53 is cloned under the U6 promoter and 5' to the reporter cassette composed of cytomegalovirus promoter, RFP flanked by loxP sites and IRES- GFP. **(B)** Images of GBM tumor (i) and (ii). (iii) H&E staining of shNF1-shp53–induced tumors in the CTX of SynI-Cre mice, white arrows show perivascular infiltration instead black arrows indicated a multinucleated giant cell. Abbreviations: long terminal repeat (LTR), cytomegalovirus (CMV), necrosis (N) (Friedmann-Morvinski et al., 2012).

1.2 Overview on SHH medulloblastoma features and cerebellum development

1.2.1 Molecular subgroups classification of medulloblastoma

Medulloblastoma (MB) is a tumor that specifically arises and localises in the cerebellum. MB is mostly considered as a pediatric tumor, since the highest peak of incidence is during the first decades of life, even though this disease can occurs through adulthood. It is ranked as the second most frequent cancer in children, after leukemia, and as the most common malignant paediatric brain tumour (Millard & De Braganca, 2016; Northcott et al., 2012). Nowadays, an effective cure has not yet been found and 40% of affected children experience tumour recurrence, while 30% die because of MB (Jones et al., 2012). Increased intracranial pressure (ICP) and cerebellar dysfunction are the main clinical manifestations used to diagnose MB since they can lead to neurological symptoms and motor manifestations such as truncal or appendicular ataxia (Millard & De Braganca, 2016). Recently, new next-generation techniques have been applied to analyze MB molecular features/profiles. Genome-sequencing (Jones et al., 2012; Pugh et al., 2012) and/or array-based transcriptional profiling (Northcott, Korshunov, et al., 2011) allowed to divide MB in four molecular subgroups (Wnt, SHH, Group 3 and Group 4) depending on a broad variety of macro and micro-genetic aberrations which define specific cytogenetics, mutational patterns and gene expression signatures in association with different demographic characteristics, cell of origin, histopathological hallmarks and patient outcomes (Figure 4) (Northcott et al., 2012). However, several features are common among molecular subtypes such as the alteration of chromatin-modifiers genes and the presence of tetraploidy in early phases of disease. Indeed histone demethylases (HDMs), histone acetyltransferases (HATs) and histone deacetylases (HDACs) are frequently mutated in several subtypes (Jones et al., 2012) and the genome duplication is observed in 54% of group 3, 40% of group 4, 29 % of children with SHH MB and for the 14 % WNT MB patients. Moreover, in group 3 and SHH MBs, tetraploidy is often accompanied by genomic instability derived from an erroneous DNA repair (Northcott et al., 2012; Schroeder & Gururangan, 2014). Furthermore, continuous efforts to improve diagnostic methods are developed day after day; indeed, Capper et al. in 2018 developed a diagnostic approach based on DNA methylation showing a change of diagnosis in up to 12% of prospective cases compared to standard methods (Capper et al., 2018; Hovestadt et al., 2014).
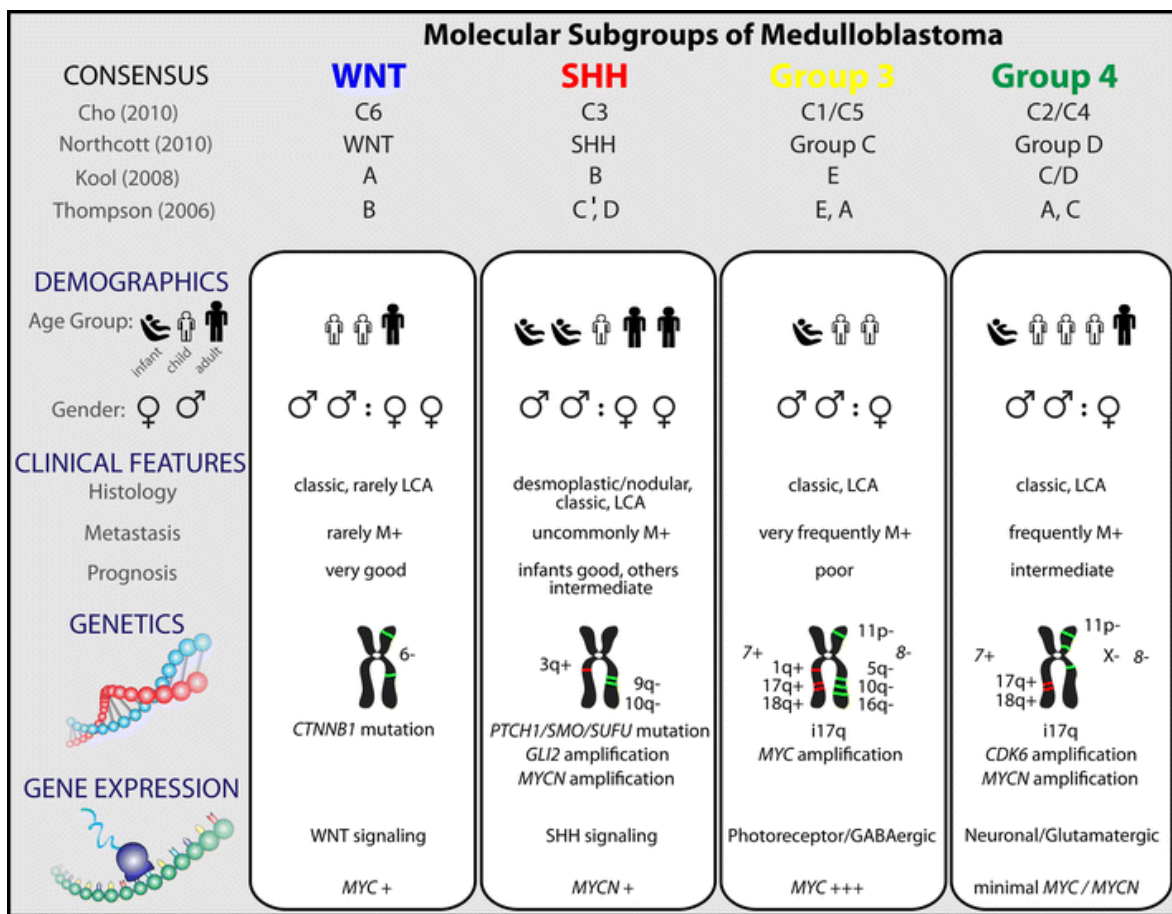
Figure 4: Differences between WNT, SHH, Group 3 and Group 4 MB based on demographics incidence, clinical features, genetic aberration and gene expression profile. (Taylor et al., 2012)

1.2.2 Sonic hedgehog (SHH) medulloblastoma

The sonic hedgehog medulloblastoma (SHH MB) is characterized by genetic alteration on the SHH pathway. This pathway is considered as the key driver in the development of this pathology. Considering all the MB subgroups, the SHH MB comprises the 25% of MB patients, with a small prevalence for males. Fortunately, there is an high level of survival, since 60-80 % of patients survive to the disease. The human incidence of SHH MB is curious and particular, as there is a divergent temporal incidence. Indeed, SHH MB is very frequent in both infants (0-3 years) and adult (> 16 years), but much more rare in children (3–16 years) (Northcott et al., 2012; Schroeder & Gururangan, 2014; Taylor et al., 2012). Germline/somatic mutations or somatic copy number aberrations (SCNAs) in genes involved in SHH pathway, such as patched1 (*PTCH1*) or suppressor of fused (*SUFU*), negative regulators of SHH pathway, trigger SHH MB development. *PTCH1* gene is located in the 9q22 and the deletion of chromosome 9q is a specific cytogenetic signature of SHH MB. Furthermore, mutations in *PTCH1* gene, often associated with Gorlin syndrome predisposes patient to the formation of SHH MB. Moreover, other recurrent SCNAs associated with SHH MB prognosis, occur in effectors and target genes of SHH pathway, such as GLI family zinc finger 2

(*GLI2*) and MYCN Proto-Oncogene, BHLH Transcription Factor (*MYCN*) amplification (Northcott et al., 2012; Schroeder & Gururangan, 2014; Taylor et al., 2012). From an histopathological point of view, the SHH MB is exclusively characterized by desmoplastic (or nodular) histology with the presence of several nodules inside the tumour composed of partially differentiated cells surrounded by fibrous and connective tissue. If this kind of phenotypic observation is largely diffused in the tumour, it is classified as medulloblastoma with extensive nodularity (MBEN). Furthermore, the expression of GRB2 associated binding protein 1 (*GAB1*), secreted frizzled related protein 1 (*SFRP1*) and *GLI1* are reliable histological hallmarks to distinguish SHH MB for the others molecular subtypes (Northcott et al., 2012; Taylor et al., 2012). Nowadays, scientific community has proposed an alternative treatment for SHH MB. Indeed, since SHH pathway plays a key role in the tumor onset, new drugs that specifically inhibit this transduction signal have been proposed to limit the activation of the pathway. A promising drug, called NVP-LDE225 has already been applied in phase III clinical trials to eradicate relapses of childhood SHH MBs and adult SHH MBs(Pan et al., 2010). However, those kind of drugs show short-term beneficial effects probably due to inherent amplification in key SHH pathway target genes (*GLI1*, *GLI2* or *MYCN*); or by *de novo* resistance of the tumor, due to new mutations in the components of SHH pathway or other tumour suppressor genes, such as PTEN (Schroeder & Gururangan, 2014).

1.2.3 The Sonic Hedgehog pathway

Hedgehog signalling pathway has multiple roles, among which the regulation of embryonic development. Hedgehog signalling was initially discovered studying the segment polarity genes in *Drosophila melanogaster*, since it is required in the spatial specification of each anatomical region during fly embryogenesis. Further studies on mammals revealed the presence of three homologues sonic hedgehog (SHH), indian hedgehog (IHH) and desert hedgehog (DHH), that are devoted to different functions. Focusing on SHH, it is considered has a key regulator of CNS, both in flies and mammals. It acts as a mitogen favouring the self-renewal of different stem cell populations and as a morphogen, determining the cell fate of neurons and glia. Furthermore, recent studies showed its role also in axon pathfinding, regulating the neuronal projection of commissural neurons, retinal ganglion cells (RGCs) and midbrain dopaminergic neurons (Fuccillo, Joyner, & Fishell, 2006; Petrova & Joyner, 2014; Yam & Charron, 2013). Recently, it was discovered that SHH can be implicated also during the adult life, showing its ability in triggering stem cells proliferation during tissue repairing period and in promoting survival, plasticity and transdifferentiation of cells (Fuccillo et al., 2006; Petrova & Joyner, 2014; Yam & Charron, 2013). SHH is synthetized as a precursor of 45 kDa, subsequently auto-proteolytically cleaved into 19kDa

amino terminus (SHH-N), containing a signalling domain, and a 26kDa carboxy terminus (SHH-C). This process is necessary to add a cholesterol moiety to SHH-N enabling its multimerization and the release of soluble SHH-N molecules. Once released, SHH can bind PTCH1, a 12-pass transmembrane protein belonging to the Frizzled (FZZ) family. SHH binding to PTCH1 causes its exit from the cilium, leading to the activation of Smoothened (SMO) a 7-pass transmembrane receptor-like protein. SHH-PTCH1 binding triggers the intracellular signalling cascade, thus leading to the GLI proteins accumulation in the ciliary tip and their successively exit from the cilium as full-length transcriptional activators, GLI2A and GLI3A. They translocate to the nucleus to induce the expression of Hh responsive genes, including the transcriptional activator *GLI1*. GLI proteins activates the transcription of pro-proliferative target genes such as *MYCN*, *CCND*, *CCNE*, *FOXM1*. Intra-flagellar transport (IFT) machinery is responsible for moving GLI proteins in and out of the cilium. In the absence of SHH ligand, PTCH1 is sequestered into the primary cilium where it prevents SMO activation. GLI proteins (GLI2 and GLI3) can be phosphorylated by protein kinase A (PKA), casein kinase 1α (CK1) and glycogen synthase kinase 3β (GSK3β), resulting in proteolytic cleavage that eliminates the C-terminal activator domain. GLI2R and GLI3R (R=repressor) suppress transcription of HH target genes in the nucleus (Figure 5) (Choudhry et al., 2014; Petrova & Joyner, 2014; Zhang, Williams, Guo, Lum, & Beachy, 2004).
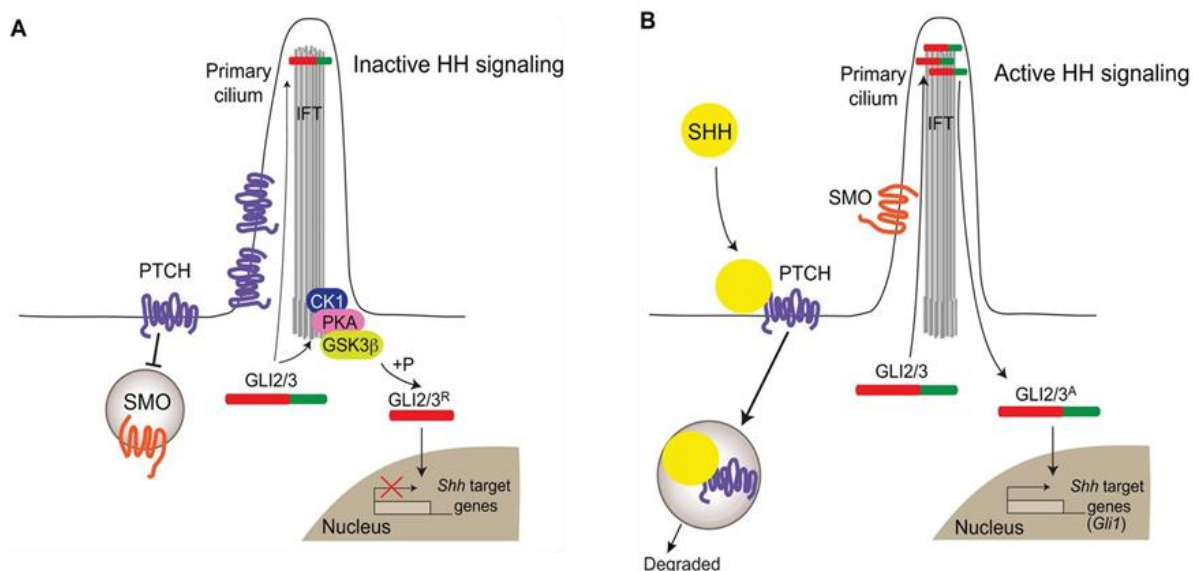
Figure 5: Graphical representation of Sonic hedgehog signalling pathway. (A) Graphical representation of Sonic hedgehog signalling pathway in the absence of SHH. **(B)** Graphical representation of Sonic hedgehog signalling pathway in the presence of SHH (Petrova & Joyner, 2014).

1.2.4 Mouse and human cerebellum comparison

The mammalian cerebellum is localized in the posterior cranial fossa and it is responsible for the motor coordination through the integration of motor programs, coming from cerebral motor cortex, and sensory information derived by pre-cerebellar system of brainstem. In addition, several non-motor functions have become evident in last years, such as language, emotions and sleep and all of them have facilitated the comprehension between cerebellar circuits and several pathologies, such as neurodevelopmental or autism spectrum disorders (Marzban et al., 2014). Cerebellar anatomy was described, for the first time, at the end of 19th century by Ramon y Cajal. Cerebellum represents only the 10 % of the entire brain volume, but it contains more than half of the total neurons number. Both mouse and human cerebellum are composed of two lateral hemispheres separated by a midline vermis and are divided into 3 lobes (anterior, central and posterior) and 10 lobules (I-X) by folds and fissures, which all together take the name of cerebellar foliation (Marzban et al., 2014). In the cerebellar cortex, there are three distinct layers: molecular layer, Purkinje cell layer and granule cell layer. Neuronal classification and connections are conserved among mouse and human cerebellum. The molecular layer contains GABAergic inhibitory interneurons (stellate and basket cells) and excitatory parallel and climbing fibres, which come from the underlying granule neurons and from cells of inferior olivary nucleus, respectively. In the middle layer, there are GABAergic Purkinje neurons, which are aligned in a monolayer called the Purkinje cell layer. The most internal layer, is the granular layer, which takes its name from the high amount of glutamatergic granule neurons present in this region. The granule layer is also characterized by three other cell populations: Golgi cells, unipolar brush cells and Lugaro cells (Figure 6A and 6B) (Marzban et al., 2014; Miterko, Lackey, Heck, & Sillitoe, 2018). External sensory information reach the granule cell layer through the pre-cerebellar system or the inferior olivary nucleus. The pre-cerebellar system projects to granule neurons through mossy fibres and later to Purkinje cell using the parallel fibres, instead olivary nucleus cells synapse directly with Purkinje cells thanks to climbing fibres. Those information are modulated by GABAergic interneurons (Golgi cells and Lugaro cells) or excitatory interneurons (unipolar bush cells) located in the granule cell layer, which together provide the feedback inhibition and refine the acquired signals. When Purkinje cells are excited, they become the first output nucleus for the cerebellum, sending inhibitory stimuli to deep cerebellar nuclei (DCN), which are groups of glutamatergic neurons localized in the cerebellar white matter. Obviously, like the input information, also the output signal is modulated before reaching DCN, through the activity of GABAergic inhibitory interneurons of molecular layer (stellate and basket cells). Finally, DCN work

as the secondary output station of cerebellum and project to the cerebral cortex, mediating the fine control of motor movements and balance (Leto et al., 2016; Marzban et al., 2014; Miterko et al., 2018)
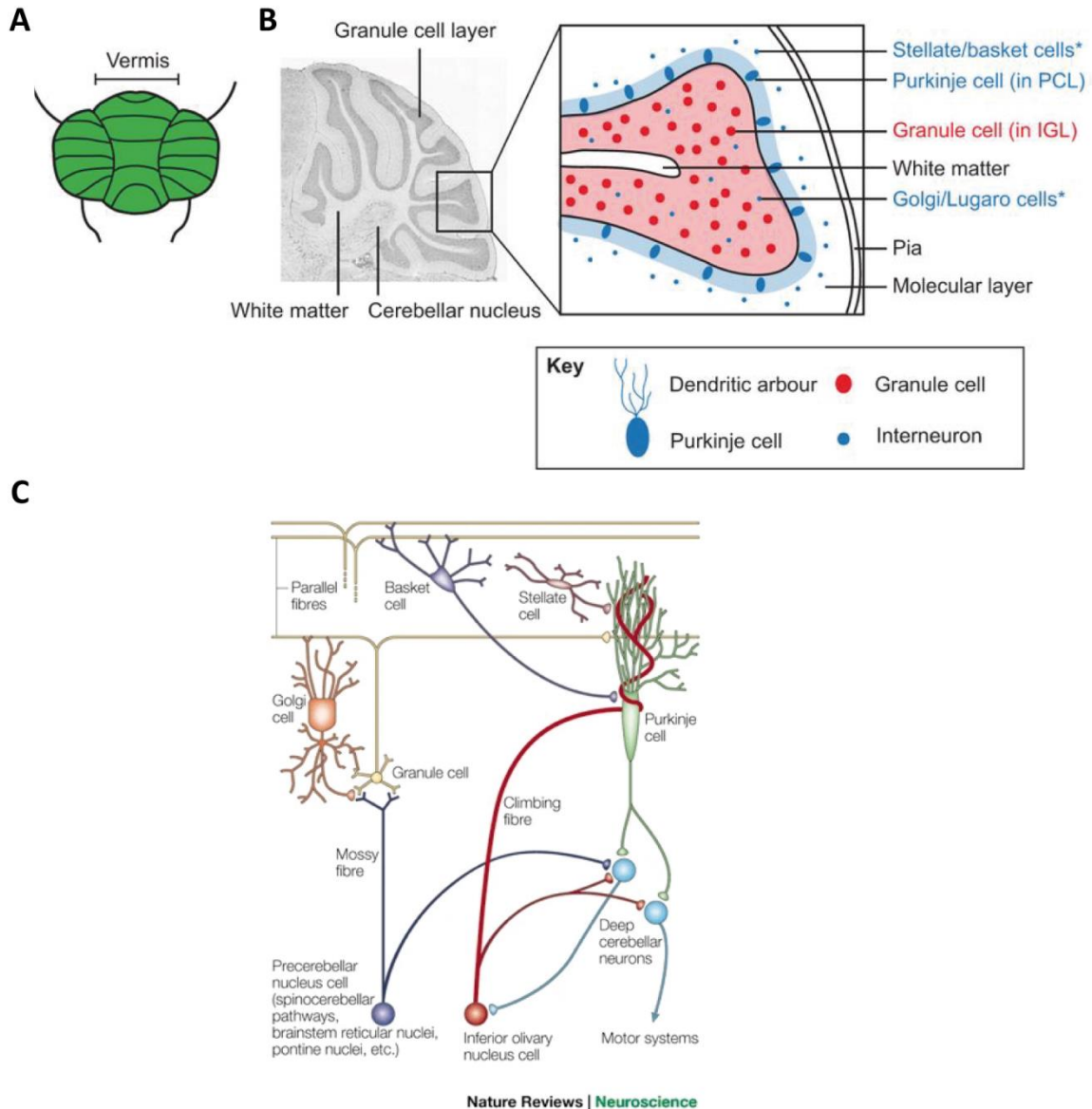
Figure 6: Cerebellum structure. (A) The cerebellum is divided into transverse folia. The mammalian cerebellum is composed of two hemispheres separated by a vermis. **(B)** Sagittal section highlights three distinct cellular layers made of different cell types: Purkinje cell layer (blue), granule cell layer (red) and molecular layer (not colored). White matter contains deep cerebellar nuclei (DCN). Each layer has characteristic GABAergic interneuron subtypes(*). Of these, only the stellate neurons appear to be present in all vertebrates, whereas others have a variable distribution: Lugaro (mammals only), basket (birds and mammals), Golgi (birds, reptiles and mammals) (Llinás and Hillman, 1969). Glutamatergic interneurons (unipolar brush cells) have also been found in the IGL in both birds and mammals (Butts, Green, & Wingate, 2014; Takacs, Markova, Borostyankoi, Gorcs, & Hamori, 1999). **(C)** Schematic picture of cerebellar neural circuit involved in motor coordination and balance (V. Y. Wang & Zoghbi, 2001).

Human and mouse cerebellum development shares a lot of similarities and occurs in comparable temporal windows. Cerebellum begins its development during embryogenesis in the region of posterior neural tube, which establishes the border between mesencephalon and metencephalon. In humans, this anatomical region forms two symmetric bulges in the dorsal region, which expand and reorganize themselves in order to generate, at the end of the process, two cerebellar hemispheres. Moreover, the fusion of the bulges at the rhomboencephalic midline creates the cerebellum vermis. In mice, the expression of two mutually exclusive transcription factors, *Otx2* in the rostral domain and *Gbx2* in the caudal domain, determines the position of a region called Isthmic organizer (IsO) which represents the midbrain-hindbrain boundary (MHB). This region is essential to define the anterior limit of cerebellum and generate a gradient of FGF8, a morphogen driving the IsO patterning activity and activating other factors such as *En1*, *Pax2* and *Wnt1* to guide the following specification of cerebellar progenitors and the differential maturation of cerebellar regions (Figure 7A and 7B) (Leto et al., 2016; V. Y. Wang & Zoghbi, 2001).
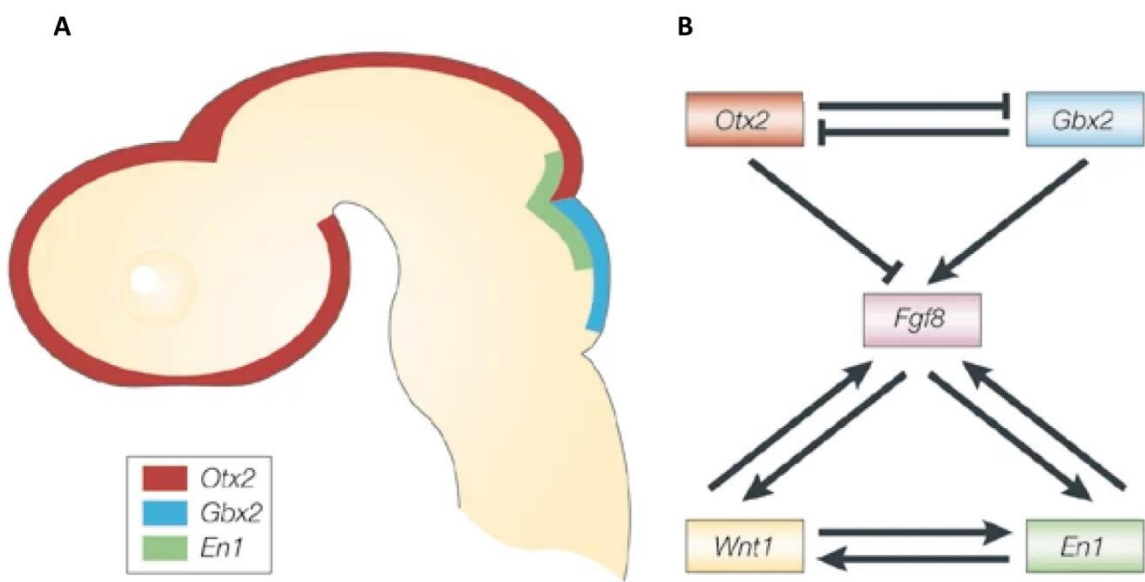
Nature Reviews | Neuroscience

Figure 7: Patterning of the midbrain/hindbrain region. (A) Formation of the mid-/hindbrain region is dependent on proper functioning of the isthmus organizer, which is formed by the interaction, or reciprocal repression, of *Otx2* and *Gbx2*. En1 is expressed in both the mid- and hindbrain regions. **(B)** The genetic interactions among *Otx2*, *Gbx2*, *Fgf8*, *Wnt1* and *En1*. Abbreviations: engrailed 1 (En1), fibroblast growth factor 8 (Fgf8), gastrulation brain homeobox 2 (Gbx2), orthodenticle homologue 2 (Otx2), wingless-related MMTV integration site 1 (Wnt1) (V. Y. Wang & Zoghbi, 2001).

Mouse begins the specification of cerebellar progenitors at E9; indeed, at this age the neuroepithelium of rhombomere 1 can be divided in the dorsal part, from which originate the roof plate, and the ventral and intermediate regions that give rise to ventricular zone (VZ) and rhombic lip (RL). Then, mouse VZ at E13 gives rise to immature Purkinje cells (PC), which diffuse laterally overcoming DCN until reelin signal determines the stop of this cell migration establishing PCs layer. The same process occurs in humans, starting form gestational week 24. As expected, also in humans, cerebellar specification starts with the generation of two different germinal matrices, the ventricular germinal matrix and the rhombic lip. DCN is the first neuronal population created, both in humans and mice, from the VZ and ventricular germinal matrix. When the migration is completed, these immature neurons need to create connections with other cell populations (granule neurons, DCN and inferior olivary neurons) and this process takes a lot of time both in humans and mice, indeed, it ends during the first post-natal weeks. Moreover, Purkinje cells development is paralleled by the production and the migration in the proper cerebellar cortex layer of all cerebellar GABAergic interneurons and glial cells, coming from ventricular zone (mice) or ventricular germinal matrix (humans). Then, there is the specification pattern of the rhombic lip. RL gives rise only to cerebellar granule neuron progenitors (CGNPs), which in mice appear at E9.5 and are characterised by atonal BHLH transcription factor 1 (*Atoh1* or *Math1*) expression; while in humans this event occurs at gestational week 11. Almost immediately, in E13 mice CGNPs begin to migrate out of the RL, populate the roof plate and express new markers such as zinc family member 1 (*Zic1*) and 3 (*Zic3*) to establish a new zone of proliferation called external granule layer (EGL). The same migrating process has been observed in human embryogenesis by gestational week 27. After that, GNPs maintenance and proliferation require Purkinje cells contribution through the release of diffusible factor Sonic Hedgehog (SHH). The process continues when the EGL reorganizes itself in the outer EGL (oEGL), which contains still proliferating CGNPs and inner EGL (iEGL) that consists of immature post-mitotic cells in a pre-migratory state. Notably, cells contained in iEGL can be identified by the loss of *Math1* expression and gain of two other transcription factor called Neuronal Differentiation 1 (NeuroD1) and Nescient Helix-Loop-Helix 1 (NSCL1). The final stage of granule neuron's development is the inward migration guided by anchoring signals of Bergmann glia. After the migration, new-born granule neurons establish the internal granule layer (IGL) and express mature neuronal markers such as tubulin-associated tubulin beta 3 class III (TUJ1) and RNA binding fox-1 homolog 3 (RBFOX3 or NeuN). This final migration continues after birth and EGL disappears within P21 in mice and first year of life in humans (Figure 8A and 8B) (Leto et al., 2016; V. Y. Wang & Zoghbi, 2001). Finally, SHH has a key central role in the cerebellum during physiological and pathological conditions, both in mice and humans. For example, as anticipated before, SHH exerts an essential role in many phases of cerebellar development, starting as a mitogen for common cerebellar

progenitors in rhombic lip and ventricular zone. Then, SHH is also released as diffusible protein from Purkinje cells, in order to sustain both neurogenic niches found in EGL and prospective white matter (PWM), respectively. In addition, SHH signalling contributes to gliogenesis and cerebellar foliation. On the contrary, when the fine control of Shh mitogenic role fails, the uncontrolled expansion of progenitors can degenerate up to the formation of cancers, such as SHH medulloblastoma (De Luca et al., 2016; Lewis, Gritli-Linde, Smeyne, Kottmann, & McMahon, 2004)
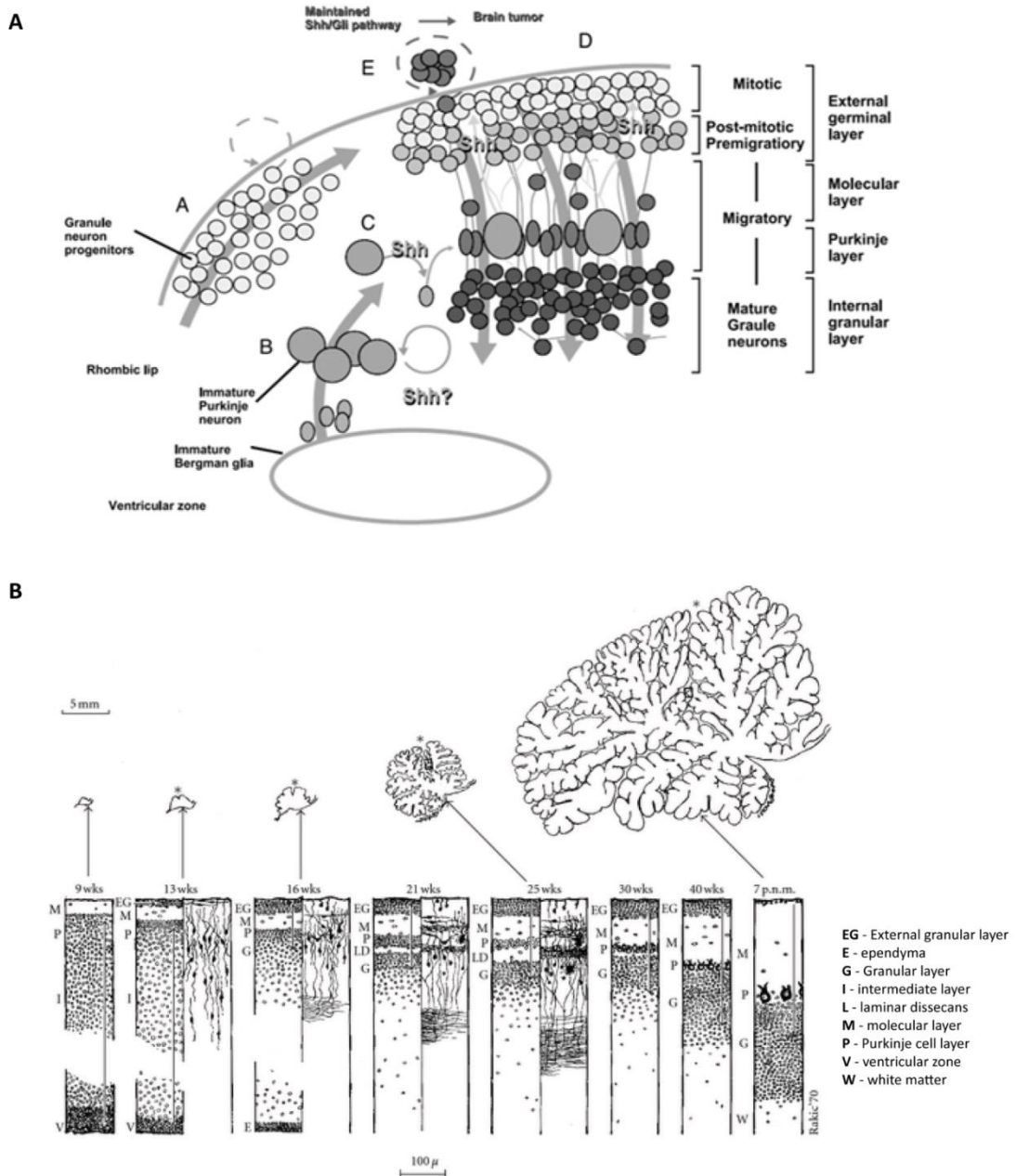
Figure 8: Role of Shh in cerebellar development and human cerebellum development. (A) Graphical summary of Shh functions during development. Timing progression from A to E. A) CGNPs migrate tangentially from the RL thanks to autocrine Shh-signaling pathway. B) Purkinje neurons and Bergmann glia from the VZ migrate toward the EGL. C) Purkinje neurons releases SHH that induces Bergmann glia maturation and CGNPs proliferation in the outer zone of EGL. D) Mature glia send extensions toward the inner region of EGL and these or other cortical cells may provide factors that

promote granule neurons differentiation, opposing to Shh effect. Granule cells migrate on glial fibres across molecular and Purkinje layers to form the IGL. E) Prolonged autocrine Shh signaling in the EGL may result in cerebellar tumors formation (Raffel, 2004) . **(B)** Development of the human cerebellum from the ninth gestational week (wks) to the seventh postnatal month (p.n.m.) shown in sagittal plane at the level of the primary fissure. E: ependyma, EG: external granular layer, G: Granular layer, I: intermediate layer, L: laminar dissecans, M: molecular layer, P: Purkinje cell layer, V: ventricular zone. W: white matter (Biran et al., 2012).

1.2.5 Granule lineage identity is required for SHH medulloblastoma development

The work of Schüller et Al. in 2008 represents a milestone for the SHH MB understanding. Indeed, for the first time they proposed that granule lineage identity is critical for SHH medulloblastoma onset and in order to investigate whether medulloblastoma originates from stem cells or progenitors, they induced the activation of the Hh pathway into multipotent progenitors (hGFAP$^+$ or Olig2$^+$) and unipotent (Math1$^+$) progenitors. Indeed, taking advantage of CRE-Lox system, they crossed transgenic mice with different cre associated promoters (hGFAP-cre, Olig2-tva-cre or Math1-cre) with LSL-SmoM2 animals. SmoM2 encodes a mutant form of *Smo*. In this allele, an activating mutation in the seventh transmembrane domain results in ligand-independent constitutive activation of Hh signalling in target tissues. Interestingly, hGFAP$^+$ or Olig2$^+$ progenitors are able to give rise to almost all cerebellar cell types, such as CGNPs, interneurons, astrocytes and oligodendrocytes. Despite this, the constitutive activation of Hh pathway in those cells gives rise only to cerebellar tumors with classic features of medulloblastomas. Moreover, they transplanted tumors in forebrain and cerebellum of severe combined immunodeficiency (SCID) mice and observed the formation in both cases of similar tumors. Therefore, some cell-intrinsic factors, rather than the environment, induced the tumor formation. When transgene expression was driven in unipotent CGNPs (Math1-cre;LSL-SmoM2 mice) of RL and in the entire EGL at P7-10, all mice developed tumors suggesting that CGNP identity is essential for the acquisition of the competence to form Hh-induced MB (Schuller et al., 2008). Further evidences were provided by Yang et al. in 2008. Again, they showed the granule lineage identity to be required for oncogenic effects of SHH signalling hyperactivation. In particular, using conditional Patched knockout mice, they showed that SHH pathway activation in granule neuron precursors and stem cells gives rise in both cases to medulloblastomas and no other tumor types. Indeed, they observed MB formation both in hGFAP-cre;Ptch1$^{flox/flox}$ (multipotent progenitors) and Math1-cre;Ptch1$^{flox/flox}$ (unipotent progenitor) suggesting that it can be initiated in progenitors or stem cells, but that multipotent progenitors need to undertake neuronal lineage to be susceptible of Shh-induced tumorigenesis (Figure 9). Indeed, the deletion of *Ptch1* in stem cells does not lead to the formation of astrocytomas or oligodendrogliomas but only medulloblastoma, characterized by the expression of post-mitotic granule neurons markers, such as NeuN or gamma-aminobutyric

acid type A receptor alpha6 subunit (GABRA6). Finally, Math1-cre;Ptch1^{flox/flox} mice develop tumors with some weeks of latency compared to hGFAP-cre;Ptch1^{flox/flox} mice, probably due to the rapid expansion of multipotent progenitors induced by *Ptch1* deletion, which consequently generate an increased pool of *Ptch1*-deleted GNPs as a source for following tumorigenesis (Z.-J. Yang et al., 2008).
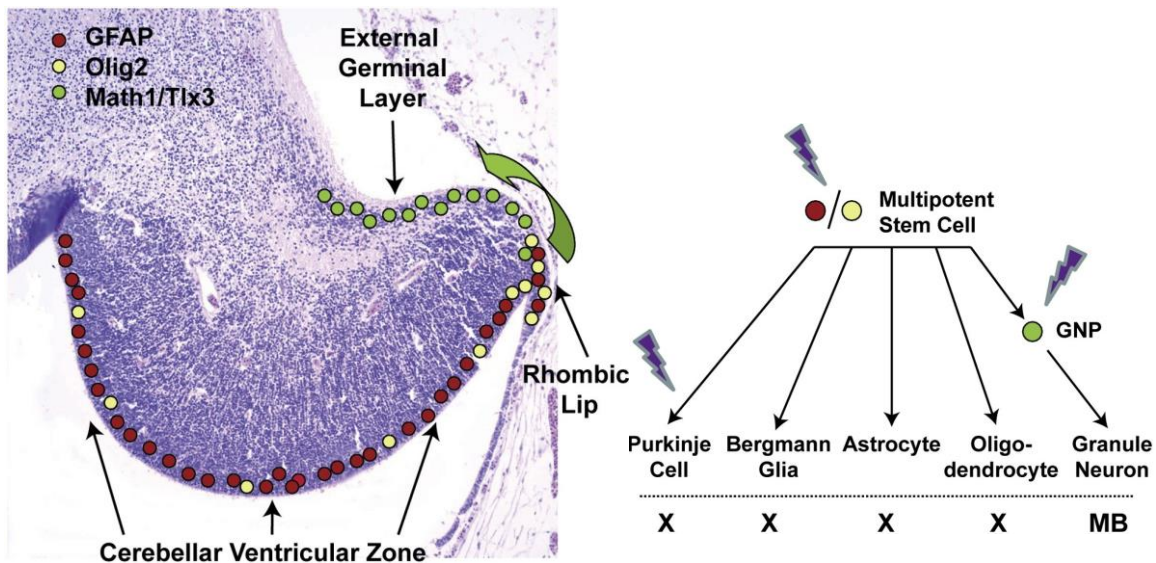
Figure 9: Hedgehog-Induced Medulloblastoma in Multipotent and Lineage-Restricted unipotent progenitors. Multipotent cells expressing GFAP or Olig2 populate the foetal cerebellar ventricular zone and give rise to Purkinje cells, Bergmann glia, astrocytes and oligodendrocytes. They also generate cerebellar granule neuron precursors (CGNP) in the rhombic lip that migrate over the cerebellar surface to form the EGL, committed to differentiate into granule neurons. Activating Hedgehog signalling, in either multipotent stem cells or CGNPs results in the formation of MBs that express markers of granule neuron differentiation, but not tumors resembling other glial or neuronal cell types. Activation of Hedgehog in Purkinje cells fails to generate tumors (Eberhart, 2008).

1.3 Adult SHH MB as a model to study dedifferentiation-induced cancer

1.3.1 SHH MB heterogeneity supports the hypothesis that infant, children and adult subgroups may have a different cell-of-origin

SHH MB presents an intriguing bimodal human incidence, representing the most common molecular subgroup in both infants (<3 years of age) and adults (>17 years of age), with fewer cases during childhood and adolescence (Figure 10A). The classification in infant, children and adult subgroups is supported, not only by the incidence, but also, by several other observations. Indeed, genomic and transcriptomic data analysis underline a substantial heterogeneity between

paediatric and adult SHH patients (Hovestadt et al., 2019; Northcott, Hielscher, et al., 2011). Moreover, the subclassification of SHH MB was robustly confirmed by a Next-generation Sequencing (NGS) study performed by Kool et Al. in 2014 on a large cohort of SHH MB patients. The analysis revealed different mutational signatures in infant (<3 years), children (3-16 years) and adult (>16 years) patients. In particular, all the three groups exhibit equal mutational frequency in *PTCH1*, but mutations in *SUFU*, *TP53* and *SMO* are significantly enriched in infant, children and adult respectively (Figure 10B). Afterwards, children patients showed an increased level of *GLI2* and *MYCN* amplification. The different signatures clarified the higher responsiveness to SMO inhibitors of adult subgroups compared to the infant and children subgroups, since 82% of them have mutations in either *PTCH1* or *SMO*, while infant and children patients appeared to be more intrinsically resistant to this therapy, due to mutations in downstream components of the SHH pathway (Kool et al., 2014).
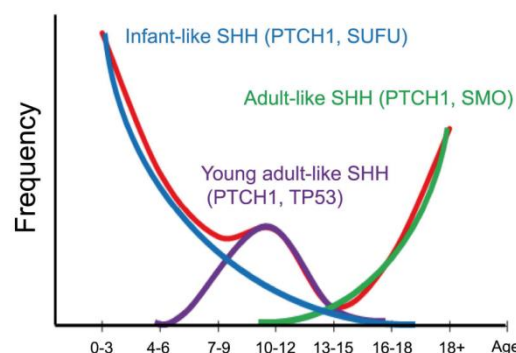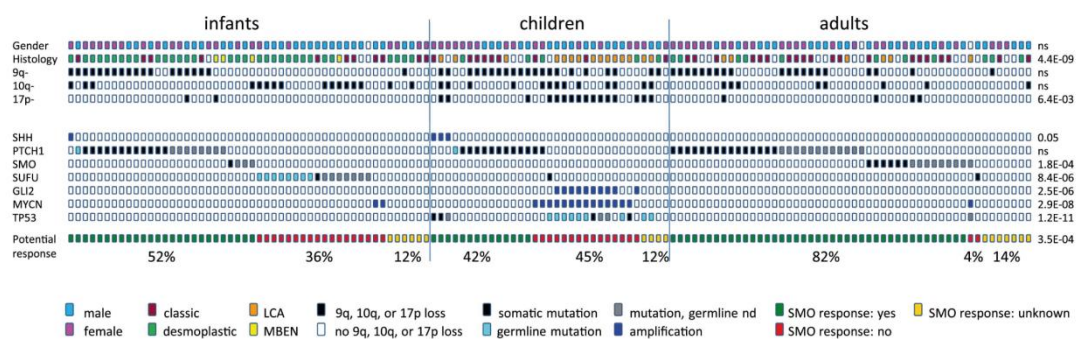
Figure 10: SHH-MB mutational analysis. **(A)** Age distribution of patients with SHH-MB. Red line indicates age distribution of all patients with SHH-MB. **(B)** SHH pathway mutations, gender, histology and chromosomal aberrations (133 sequenced SHH-MBs). Analysis of response to SMO inhibition: the response is positive with *SHH* amplifications, *PTCH1* or *SMO* mutations while it is negative with *SUFU* mutations or *MYCN/GLI2* amplifications. When mutations on SHH pathway are not detected, the response is unknown (Kool et al., 2014).

Recently, Cavalli et al. proposed an integrative analysis between genome-wide DNA methylation and gene expression data among 763 primary MBs, in order to characterize the heterogeneity within each molecular subgroup. Surprisingly, they observed that SHH MBs can be classified in four cytogenetically and clinically different groups (SHHα, SHHβ, SHHγ, SHHδ), rather than with the tripartite classification of Kool et al. In detail, SHHβ and SHHγ correspond to the infant subtypes, while SHHα and SHHδ correspond to childhood/adolescent and adult subtypes, respectively. SHHβ and SHHγ display different genetic signatures. Indeed, the first exhibits focal deletion of the tumor suppressor *PTEN* and high rate of metastasis at diagnosis, which overall lead to a worse prognosis; the second shows no evident gene expression signatures or CNAs, so it is characterised by a better prognosis. SHHα revealed also a specific amplification of Yes associated protein 1 (*YAP1*) and specific copy number aberrations (CNAs) such as 9q, 10q and 17p losses. Lastly, they renamed the adult SHH MB as SHHδ and associated to this group a favourable prognosis and a strong enrichment for telomerase reverse transcriptase (*TERT*) promoter mutations. In addition, Cavalli et al. focused their attention on differential gene expression analysis of each identified subtype, revealing that developmental pathways and electrical activity-associated genes appear more enriched in SHHβ and SHHγ; otherwise, SHHα and SHHδ are characterised by the enrichment of DNA repair, cell cycle and telomerase maintenance associated pathways (Figure 11). This new classification, obviously, could be important for planning specific clinical trials of infant SHH MB and developing targeted mouse models (Cavalli et al., 2017). SHH MB heterogeneity strengthens the hypothesis that infant, children and adult SHH-MBs may have a different cellular origin or that the same progenitor cell could be hit at different stages of differentiation, leading to different tumor subtypes. For these reasons, in the last years, special efforts have been made to define specific signatures of the different SHH MB subgroups, showing their clinical, transcriptional, genetic and prognostic differences. In particular, two alternative point mutations in the TERT promoter (C228T and C205T) occur with high frequency in adult SHH MBs (83% of cases n=66) (Remke et al., 2013), compared to rare cases in infant SHH MBs. Moreover, these mutations appear to be mutually exclusive with the 10q deletion, so the absence of this cytogenetic can be considered another adult SHH MB specific feature (Northcott, Hielscher, et al., 2011; Remke et al., 2013). At the transcriptional level, adult and infant SHH MBs can be also distinguished checking the over-expression in adult patients of homeobox (*HOX*) family and subfamily genes, such as BarH like Homeobox 1 (*BARHL1*) and LIM homeobox 2 (*LHX2*), that could be used as histological markers to characterise new mouse models (Northcott, Hielscher, et al., 2011). Furthermore, it was discovered that several mutations targeting the PI3K/AKT/mTOR pathway can lead to the hyperactivation of SHH pathway overcoming SMO, PTCH1 and SUFU mutations. Upregulation of the PI3K/AKT/mTOR pathway can be observed by checking the levels

of phosphorylated AKT Serine/Threonine Kinase (pAKT) and phosphorylated Ribosomal Protein S6 Kinase (pS6). Almost all patients of adult SHH medulloblastoma were positive for both markers, while none of considered infant SHH MB patients exhibit this specific double immunohistochemical-reactivity. Consequently, adult patients with SHH-MB could be the best group to obtain benefits from therapy with only PI3K/ AKT/mTOR inhibition or in combination with Smo inhibitors (Figure 12) (Kool et al., 2014).
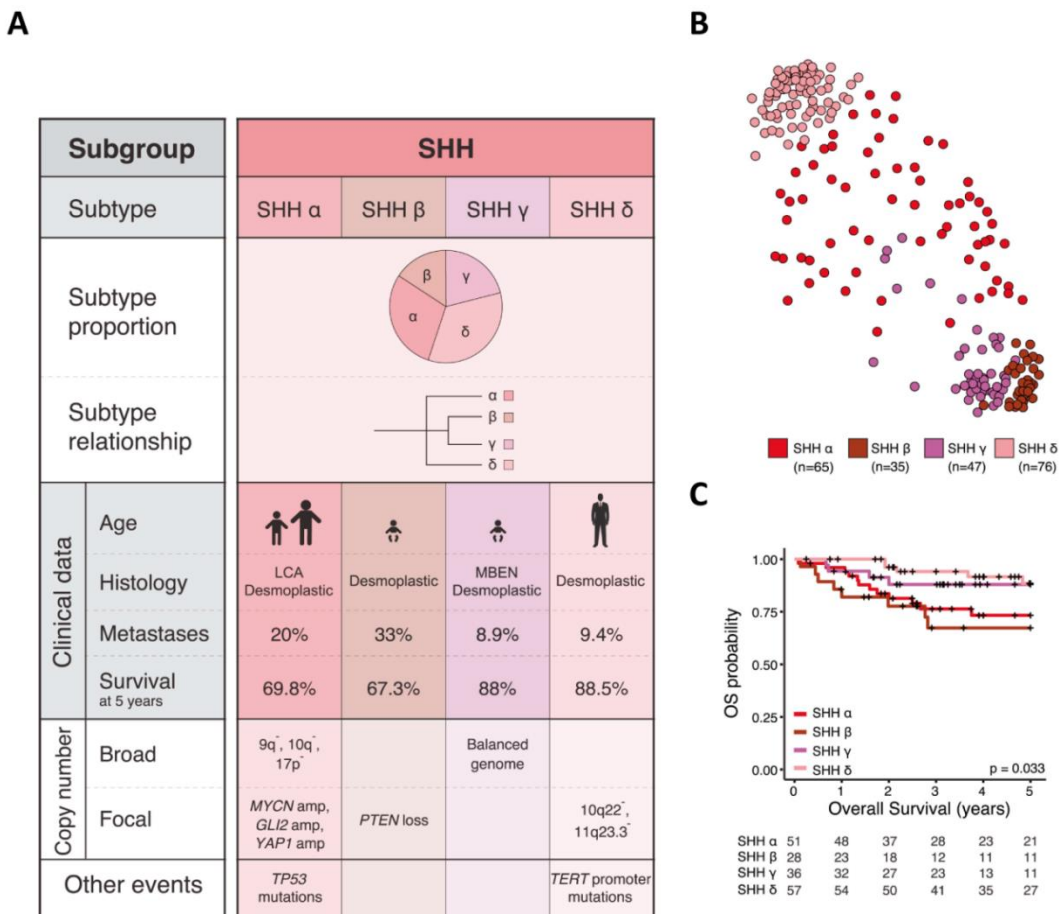
Figure 11: Cavalli classification of SHH-MBs subgroups. (A) Schematic representation of key clinical data, copy-number events and relationship between the subtypes inside each of the four SHH medulloblastoma subgroups. The percentages of patients with metastases and the 5-year survival percentages are presented. The age groups are: infant 0–3 years, child >3–10 years, adolescent >10–17 years, and adult >17 years. **(B)** Network representation map of four SHH-MB subtypes based on integrative analyses (n=223 primary tumors). **(C)** Overall survival of SHH subtypes (log rank test), + indicates censored cases. Abbreviations: large cell anaplastic (LCA), medulloblastoma with extensive nodularity (MBEN), MYCN Proto-Oncogene, BHLH Transcription Factor (MYCN), GLI Family Zinc Finger 2 (GLI2), Yes Associated Protein 1 (YAP1), Tumor Protein P53 (TP53), Phosphatase And Tensin Homolog (PTEN), Telomerase Reverse Transcriptase (TERT), overall survival (OS). Adapted by (Cavalli et al., 2017).
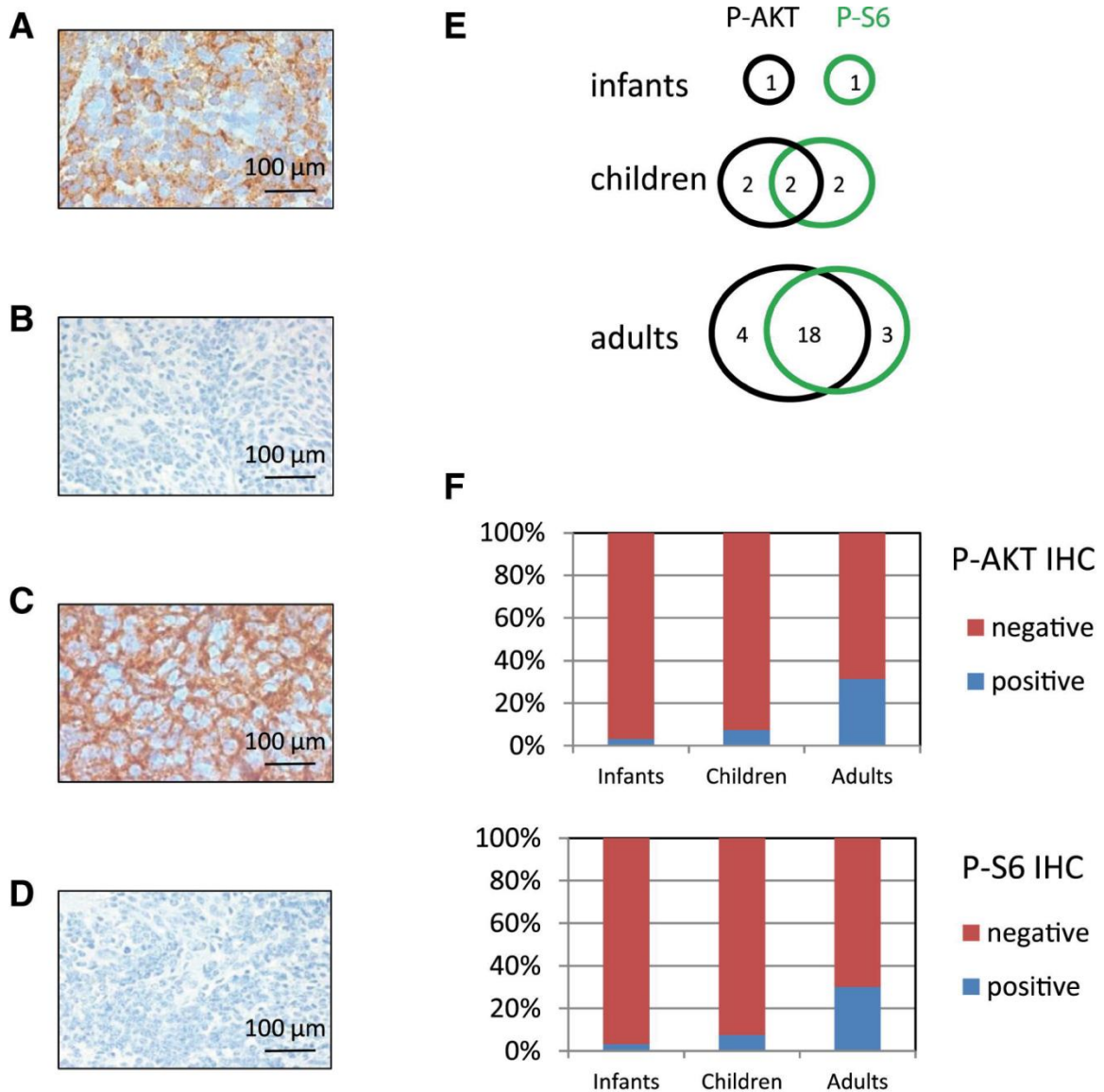
Figure 12: Involvement of PI3K/AKT/mTOR pathway in SHH MB. (A) Example of positive p-AKT MB. **(B)** Example of negative p-AKT MB. **(C)** Example of positive p-S6 MB. **(D)** Example of negative p-S6 MB. **(E)** Overlap in staining results between p-AKT and p-S6 in infant, children and adult SHH MBs. **(F)** Frequencies of p-AKT and p-S6 staining in infants, children, and adults (Kool et al., 2014).

Lastly, adult SHH MB differs from the infant subgroup based on the enrichment of genetic mutations in chromatin modifiers and/or transcription regulators. In particular BRPF1, KIAA0182, TCF4, CREBBP, NEB, LRP1B, PIK3CA, FBXW7, KDM3B, XPO1, PRKAR1A, and PDE4D appeared to be most frequently mutated in adult compared to infant SHH MBs. Of all these mutations, the Bromodomain and PHD Finger Containing 1 (BRPF1) appears to be altered only in the adult form and, in particular, often co-mutated with *SMO* gain of function mutations (Figure 13) (Hovestadt

et al., 2019; Kool et al., 2014). *BRPF1* appeared to be an interesting gene to investigate as a possible target for the already theorised epigenetic therapy in medulloblastoma and a key gene to model adult SHH MB.
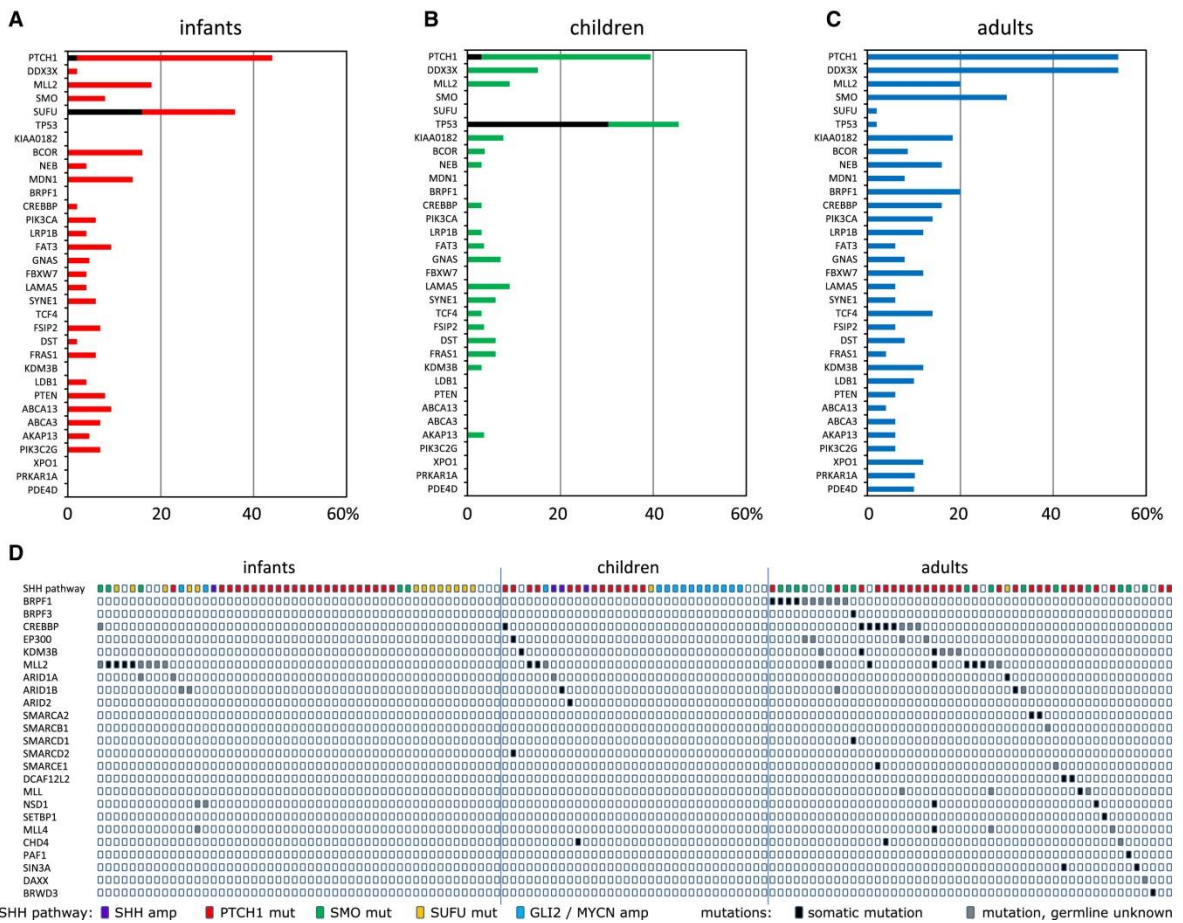
Figure 13: BRPF1 is mutated only in the adult SHH MB.

(A–C) Mutation frequencies of 33 genes that are mutated either in ≥5% of all SHH-MB cases or in ≥10% of SHH-MB cases in one of the age categories. Mutation frequencies for these 33 genes are shown in infants **(A)**, children **(B)**, and adults **(C)**. Black indicates the fraction of mutations found in the germline. **(D)** Mutations in chromatin modifiers in infants, children, and adults with SHH-MB. The top line shows the mutations in the SHH pathway for each case.

1.3.2 Bromodomain and PHD finger-containing protein 1 (BRPF1)

Bromodomain and PHD finger-containing protein 1 (BRPF1) is the ortholog of Bromodomain-Containing Protein, 140kD (Br140) in *Drosophila melanogaster*. Brpf1 encodes for a chromatin reader and regulator that is associated to several physiological processes, such as foetal haematopoiesis, adult neurogenesis and development (Laue et al., 2008; You et al., 2016; You, Yan, et al., 2015), but also to pathological conditions such as intellectual disability, leukaemia and

adult SHH medulloblastoma (Kool et al., 2014; Yan et al., 2017; You, Zou, et al., 2015). The structure of BRPF1 defines it as a chromatin reader endowed with the capability to recognize specific histone code combination. Indeed, BRPF1 is characterized of multiple nucleosome-binding modules, including double plant homeodomain linked (PHD) fingers domain, PWWP domain and a bromodomain. The double PHD fingers are linked with a C2HC zinc knuckle and form a bivalent nucleosome-binding unit, known as the PZP (PHD finger-zinc knuckle-PHD finger) domain, devoted to the recognition of histone 3 (H3). The bromodomain, located C-terminally to PZP module is able to read specific acetyl-lysine moieties, while PWWP domain possesses specific affinity for trimethylated residue 36 of histone H3 (H3K36me3). Furthermore, BRPF1 is composed by two enhancer of Polycomb (EPC)-like motifs flanking the PZP domain (Figure 14).

A
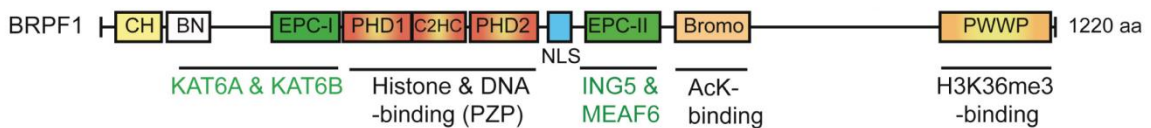
B
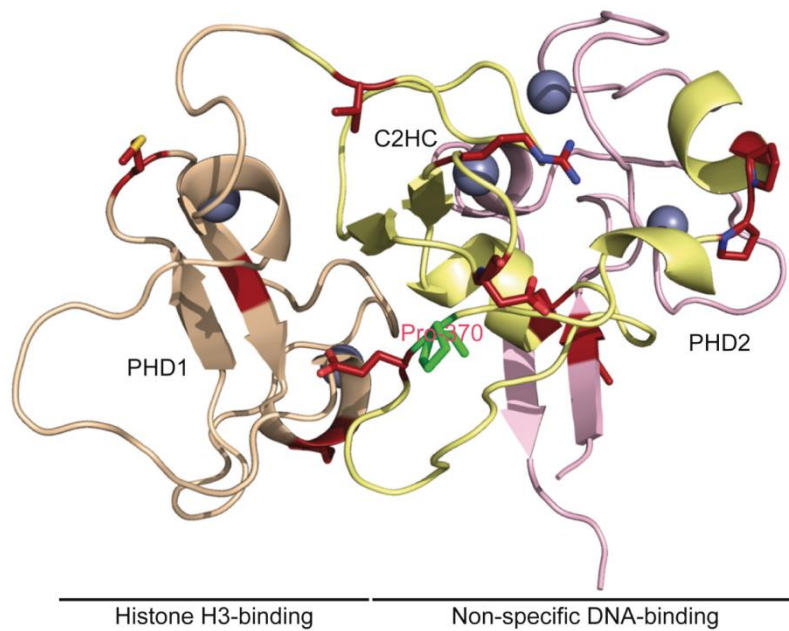
Figure 14: BRPF1 structure. (A-B) Schematic representation of BRPF1. BRPF1 possesses multiple modules, including the PZP domain, bromodomain and PWWP domain, for chromatin association. The PZP domain comprises two PHD fingers linked with a C2HC zinc finger. The first PHD finger recognizes the N terminus of histone H3. The C2HC zinc knuckle and the second PHD finger form a non-specific DNA binding domain. The bromodomain has acetyl-lysine-binding ability and the PWWP domain targets trimethylated histone H3. The EPC-like motif C-terminal to the PZP domain is essential for the formation of a stable trimeric complex with ING5 and MEAF6. Through the EPC-like motif, N-terminal to the PZP domain, and a conserved region further N-terminal to this motif, BRPF1 interacts with and activates MOZ, MORF and HBO1. Abbreviations are as follows: CH, C2H2 zinc finger; BN, conserved BRPF N-terminal domain; EPC, enhancer of polycomb-like motif; NLS, nuclear localization signal (Yan et al., 2017).

The N-terminal EPC motif contributes to the interaction with MOZ (monocytic leukemia zinc finger protein, also known as MYST3 and KAT6A) and MORF (MOZ-related factor, also known as MYST4 and KAT6B), while the C-terminal EPC motif binds to Inhibitor of Growth Family Member 5 (ING5) and MYST/ Esa1 Associated Factor 6 (EAF6), so BRPF1 can form a tetrameric complex with MOZ/MORF, ING5 and EAF6. MOZ and MORF are vertebrate lysine acetyltransferases, while ING5 and EAF6 are co-factors for transcriptional activation or repression. Afterwards, BRPF1 can form an alternative tetrameric complex, which replaces MOZ/MORF with histone acetyltransferases bound to ORC1 (HBO1, also known as KAT7), another lysine acetyltransferase that switches its substrate from H4 to H3 upon the interaction with BRPF1 (Figure 15). In addition to its reader function, BRPF1 acts also as a chromatin writer/regulator inducing the modification of chromatin state, for example promoting the acetylation of lysine 23 in H3 (H3K23Ac), and working as a scaffold for transcription factors which need to interact with the modified chromatin region (Yan et al., 2017; X. J. Yang, 2015; You, Zou, et al., 2015).
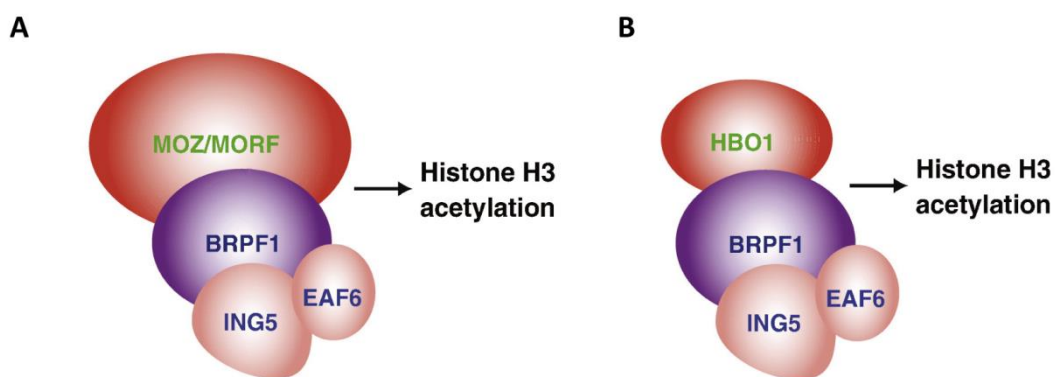
Figure 15: Architecture of BRPF1 complexes and domain organization of BRPF1, MOZ/MORF and HBO1. (A) Cartoon showing a tetrameric complex composed of MOZ (orMORF), BRPF1, ING5 and EAF6. BRPF1 serves as a scaffold to promote complex formation and stimulate acetylation of nucleosomal histone H3. (B) Same as (A) except that the catalytic subunit is HBO1 instead of MOZ or MORF (X. J. Yang, 2015).

Regarding spatial-temporal distribution, BRPF1 is expressed in several embryonic tissues such as placenta, limb buds, brain, spinal cord, retina, nose, bone and brown fat and this wide diffusion explains its determining role during embryogenesis. Otherwise, in post-natal life Brpf1 expression is restricted to testis and adult brain regions, such as neocortex, hippocampus and cerebellum (You, Chen, Penney, Miao, & Yang, 2014).

BRPF1, due to its adult spatial expression (cerebellum) and its function as chromatin regulator, represents a perfect candidate to investigate in order to find new molecular mechanisms that specifically mark the adult form of SHH MB. Indeed, several adult SHH MB patients present BRPF1

co-mutated with SMO (Figure 16). BRPF1 mutations mostly consist in an insertion of a premature stop codon, which generates a truncated protein lacking of bromodomain and PWWP domain. Unfortunately, up to now, it is still unknown if this truncated form can interact with the physiological BRPF1 or whether it has a completely new function (Kool et al., 2014; X. J. Yang, 2015).
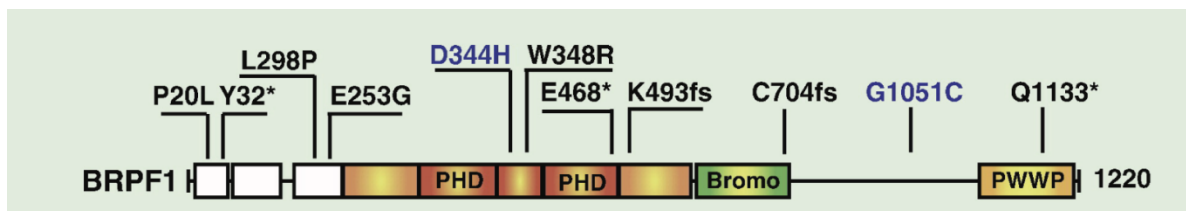
Figure 16: Recurrent mutations of BRPF1 gene in childhood leukemia and adult SHH medulloblastoma. The mutations present in adult medulloblastoma are indicated with dark letters, whereas those found in pediatric leukemia are shown in blue. fs, Reading frame shift; (*) translational termination (X. J. Yang, 2015). The mutations are composed from data published in two recent studies (Huether et al., 2014; Kool et al., 2014).

2. Aim of project

Starting from the common opinion that the cells of origin should possess a proliferative capacity (Blanpain, 2013; Visvader, 2011) and that the transition of neural progenitors to differentiated postmitotic neurons is considered irreversible in physiological and pathological conditions, my PhD project aims to demonstrate the opposite concept, investigating the field of neuron dedifferentiation. Indeed, after the discovery of Yamanaka et al., that shown how terminally differentiated cells can be reprogrammed up to their original pluripotent state (Takahashi & Yamanaka, 2006), the idea of terminal differentiation/commitment has changed, indicating that all cells still retain the ability to retrace their past, undergoing a process of dedifferentiation. The adult SHH MB represents a model to study neurons reprograming. Indeed, Human SHH medulloblastoma (MB) is a brain tumor mainly found in adults and infants that is thought to originate from cerebellar granule neuron progenitors. These progenitors are present in infants and newborn mice, but they seem not to be present in adult humans and mice (Biran, Verney, & Ferriero, 2012; Marzban et al., 2014; Z.-J. Yang et al., 2008). Furthermore, it was recently discovered that the two different forms of SHH MB are distinguished by different transcriptome/methylome levels suggesting that the adult SHH MB may originate from a different cell of origin (Cavalli et al., 2017; Kool et al., 2014). Relying on these data, this project has essentially three specific aims:

1 To test if SmoM2 over-expression in cerebellar granule neurons promotes neurons dedifferentiation and Shh medulloblastoma *in vivo*.

2 To mimic human adult SHH MB by exploring SmoM2 and mutant BRPF1 cooperation.

3 To define the contribution of chromatin changes of granule neurons in response to SmoM2 activation alone or in cooperation with truncated BRPF1 overexpression.

3.Experimental design

Mice and humans own similar cerebellar tissue in terms of development and neuronal populations and furthermore, they share the same pathways which regulate both physiological and pathological conditions of the cerebellum. Moreover, mice are characterised by a rapid life cycle, high breeding capabilities and longer life expectancy compared to other animal models. For these reasons, *Mus musculus* stands as the perfect animal model to study SHH medulloblastoma in order to solve open questions related to this pathology, as the possible existence of other cells of origin between SHH MB subtypes, or to reveal new and interesting pathways, which have not yet been disclosed. Here are shown and summarized the experimental approaches used to demonstrates different aims of the project.

AIM 1 : To demonstrate that SmoM2 over-expression in cerebellar granule neurons promotes neurons dedifferentiation and Shh medulloblastoma *in vivo*.

A possible strategy to verify the contribution of mature granule neurons in the MB development consists in combining a conditional Cre allele able to direct the expression of recombinase only in post-mitotic cerebellar granule neurons with an allele encoding for a constitutive active form of Smoothened (*Smo*), which has already been applied in literature to generate SHH MB mouse model. Furthermore, Smoothened mutations are enriched in adult SHH MB patients, in which the probability to observe tumors induced by neuronal dedifferentiation should be increased compared to infants, due to the physiological absence of CGNPs after the first years of life (Kool et al., 2014). In particular, SmoM2 encodes a mutant form of *Smo*. In this allele, an activating mutation in the seventh transmembrane domain results in ligand-independent constitutive activation of Hh signalling in target tissues. This point mutation has been discovered in basal cell carcinoma and results in a non-synonymous substitution of a tryptophan with a leucine (W535L) (Lau et al., 2012). Taking advantage of a conditional Cre-Lox recombination system, SmoM2 expression (LSL-SmoM2 mice) would be induced only in postmitotic neurons using Gabra6-cre transgenic mouse (Figure 17), demonstrating that post-migratory mature granule neurons upon SmoM2 overexpression can dedifferentiate and give rise to SHH MB in vivo. Gamma-aminobutyric acid receptor subunit alpha-6 is a well-known transmitter-gated chloride ion channel, which is activated upon the interaction with GABA (γ-aminobutyric acid), a neurotransmitter that usually induces an inhibitory post-synaptic potential in the receiving cell. In particular, GABAA receptor is composed of different class of subunits (α, β, γ and δ), which aggregate in pentamers and are widely diffused in all regions of adult human and mouse brains.

A particular class of α subunit was identified by Kato in 1990 and called α6 subunit. This particular class is expressed only in cerebellar granule neurons of adult mouse brain, revealing the first neuroreceptor subunit specifically expressed in a single neuronal population (Kato, 1990).

Another study reported *Gabra6* expression not only in cerebellar granule neurons, but also in the same neuronal populations present in cochlear nuclei. However, thanks to the effort of Bahn et al. in 1997 was generated a truncated form of Gabra6 promoter lacking of cochlear nucleus regulatory elements, triggering gene expression solely to cerebellar granule neurons. In detail, transgenic Gabra6 promoter was generated using the 5' 6kb-long fragment that corresponds to exons 1-8 of its coding gene, which overall is called Δα6 promoter (Bahn, Jones, & Wisden, 1997). This sequence is able to guide target gene expression in postmitotic granule neurons, avoiding progenitors contribution. The reliability of this truncated promoter was tested by Aller et al. in 2003, by generating knock-in mice through homologous recombination of IRES-cre cassette or a LacZ operon, downstream to the exon 8 of Gabra6 promoter, in order to create Δα6-cre and Δα6-LacZ mice, respectively. Both immunohistochemistry for Cre and staining for β-galactosidase revealed that Δα6 promoter can drive gene expression in cerebellar granule neurons, but also at lower levels in other brain regions, such as neocortex, hippocampus, thalamus, brain stem and deep cerebellar nuclei (Aller et al., 2003).
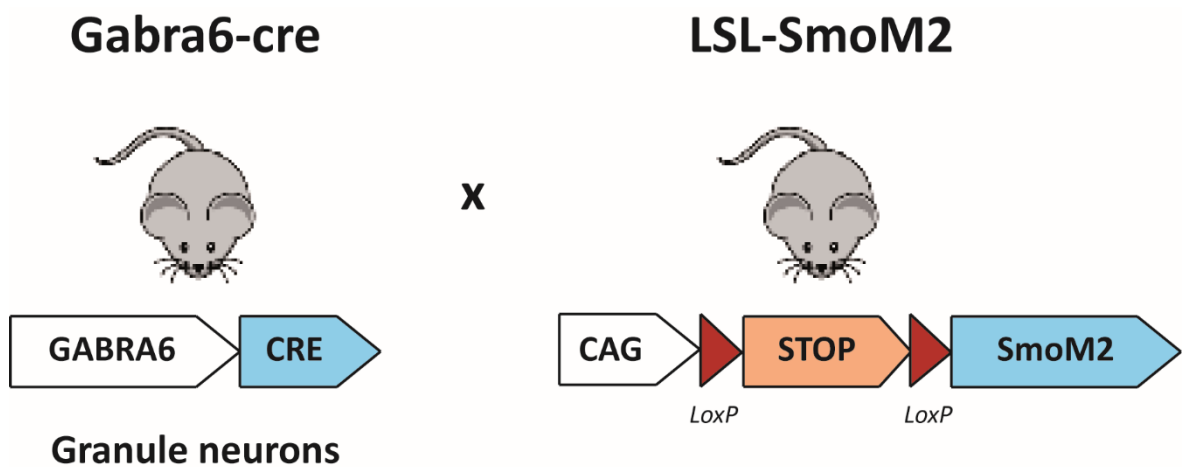
Figure 17: Schematic representation of Gabra6-cre;LSL-SmoM2 transgenic mice used to test neuronal contribution in MB development. Abbreviations: LSL, lox-stop-lox cassette.

The possibility that granule neurons might undergo a dedifferentiation process and give rise to SHH MB would be validated using also different neuronal promoters and different strategies. Indeed, Neuronal Differentiation 1 (*NeuroD1*) is a gene that encodes for a bHLH transcription factor, involved in neuronal fate specification as observed in Xenopus embryos. The expression of

NeuroD1 was detected in neurons of adult brain structures, such as olfactory bulbs, hippocampus and cerebellum, but also during the differentiation of pancreatic β cells. In the mouse cerebellum, *NeuroD1* is highly expressed in CGNPs and pre-migratory post-mitotic neurons, which reside in the inner EGL (Cho & Tsai, 2006; Huang et al., 2011; Miyata, Maeda, & Lee, 1999). Moreover, *NeuroD1* expression has already been exploited in literature to drive the expression of specific genes both in intermediate progenitors and post-mitotic neurons of hippocampal sub-ventricular zone (SVZ) (Guerrier et al., 2009). In order to avoid the CGNP and pre-migratory post-mitotic granule neurons contribution, it is necessary to induce the transient expression of NeuroD1-Cre recombinase after postnatal day 21, when CGNPs are completely absent(Figure 18)(Leto et al., 2016; V. Y. Wang & Zoghbi, 2001).
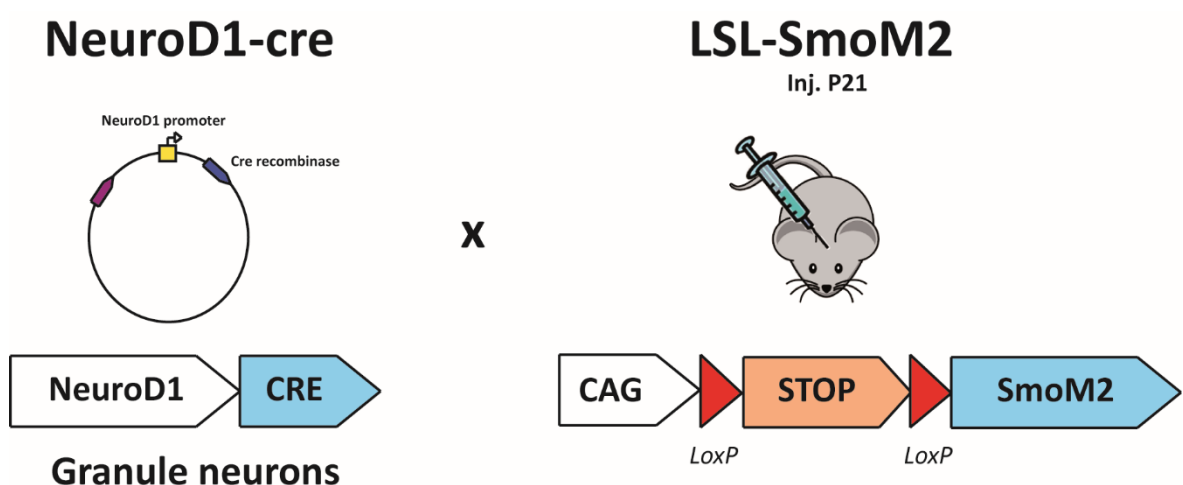
Figure 18: Schematic representation of NeuroD1-cre transfection in P21 LSL-SmoM2 transgenic mice. Abbreviations: LSL, lox-stop-lox cassette.

AIM 2 : To mimic human adult SHH MB by exploring SmoM2 and mutant BRPF1 cooperation.

Human adult SHH MB patients present inactivating mutations of the chromatin reader BRPF1 that are associated with SMO mutations and absent in pediatric and adolescent patients (Kool et al., 2014). Starting from human patients, in order to recapitulate their mutational background, a truncated form of BRPF1 would be co-transfected together with hSynI-cre plasmid in adult LSL-SmoM2 mice. Human Synapsin I (hSynI) is another neuronal promoter that can be exploited to verify the neuron dedifferentiation process and its involvement in tumor progression. Indeed, the development of synaptic compartment and the establishment of neurotransmission is one of the last events during neuronal maturation. The Synapsins' family of genes is involved in the establishment of the presynaptic compartment; indeed, it contains neuronal phosphoproteins enriched in the synaptic vesicle-associated domains. In particular, the synapsins' protein family is

encoded by three genes (*SYN1*, *SYN2* and *SYN3*), which undergo several alternative splicing events to generate 10 isoforms (synapsin Ia–b, IIa–b, IIIa–f) with several roles including vesicle pre and post-docking, short-term facilitation and potentiation of synaptic transmission and long-term plasticity (Cesca, Baldelli, Valtorta, & Benfenati, 2010). Synapsin I and II are widely distributed in adult nerve terminals of mature neurons, in order to promote the accumulation of cholinergic neurotransmitters and, at a minor level, of glutamatergic and GABAergic signals (Bogen, Haug, Roberg, Fonnum, & Walaas, 2009), while the expression of synapsin III isoforms is down-regulated in mature neurons and not confined to synaptic terminals. Indeed, its expression is mainly frequent in developing neurons and non-neuronal tissue, exhibiting non-canonical functions of these proteins (Cesca et al., 2010; Fornasiero, Bonanomi, Benfenati, & Valtorta, 2010; Kao et al., 1998). hSynI promoter is considered a reliable tool to drive the expression of target genes only in post-mitotic neurons (Kim et al., 2015; Kugler, Kilic, & Bahr, 2003) and transient expression of hSynI-cre in LSL-SmoM2 background can be used to model SHH MB. In order to recapitulate the human adult SHH MB scenario, a truncated form of BRPF1 would be co-transfected together with the hSynI-cre plasmid in adult LSL-SmoM2 mice (Figure 19).
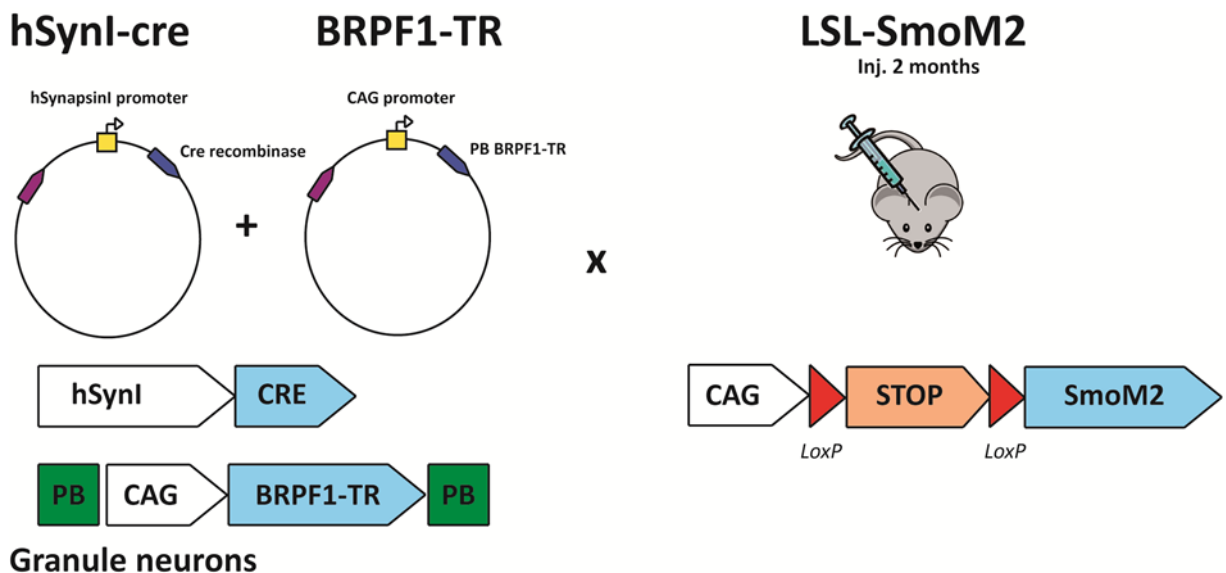
Figure 19: Schematic representation of hSynI-cre and pPB BRPF1-TR transfection in 2 months-old LSL-SmoM2 transgenic mice. Abbreviations: PB, piggyback transposon system; TR, Truncated; LSL, lox-stop-lox cassette.

Moreover, to overcome leakiness of neuronal promoters and consequential CGNPs contribution in the development of adult SHH MB mouse model, another strategy consists in driving the expression of the gene of interest selectively in postmitotic neurons by using an inducible recombination system, taking advantage of Etv1-CreERT2 transgenic mice (figure 20).

ETS Variant transcription factor 1 (*Etv1*) is a gene encoding for a transcription factor which is expressed in the cerebellum, specifically in CGNPs at the moment in which they start to migrate radially towards the IGL and to differentiate in mature GCs. Transcriptomic analysis of postnatal cerebellar development revealed Etv1 expression both in EGL and IGL at P7 while at later timepoints (P15, P22), its expression was found only in the IGL (Schuller, Kho, Zhao, Ma, & Rowitch, 2006).
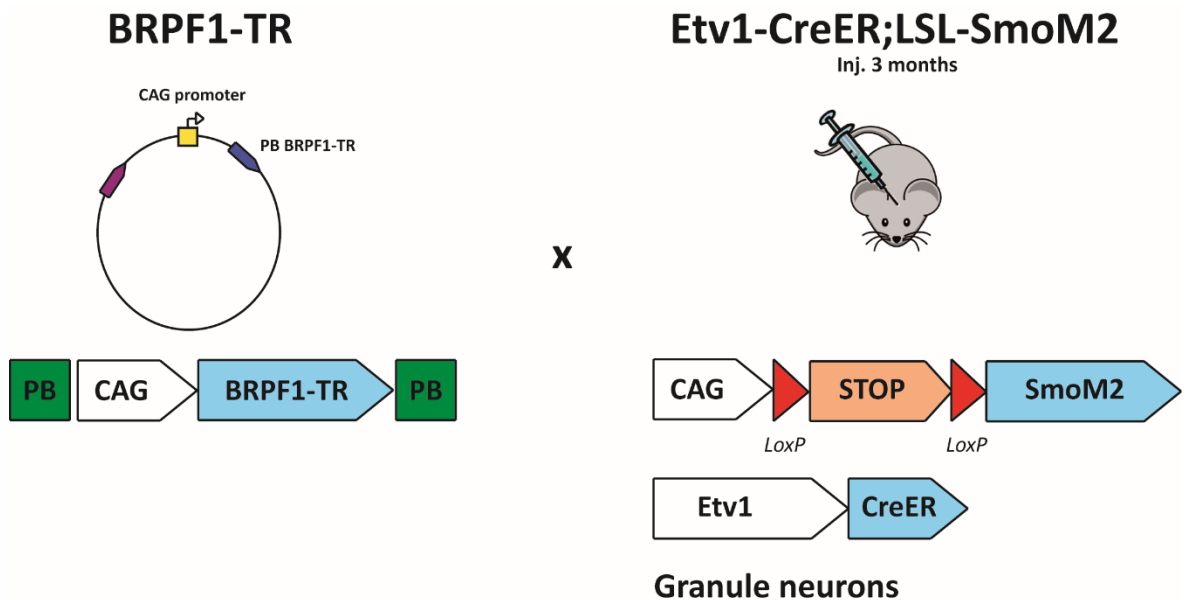
Figure 20: Schematic representation of pPB BRPF1-TR transfection in 3 months-old Etv1-creERLSL-SmoM2 transgenic mice. Abbreviations: PB, piggyback transposon system; TR, Truncated; LSL, lox-stop-lox cassette.

Finally, the role of BRPF1 in neuron dedifferentiation process would be verified by performing an *ex vivo* cerebellar assay. Cerebellar *ex vivo* primary culture will be established from P7 LSL-SmoM2 mice and nucleofected with hSynI-cre plasmid in order to find neurons which express simultaneously neuronal and stemness markers (Figure 21).
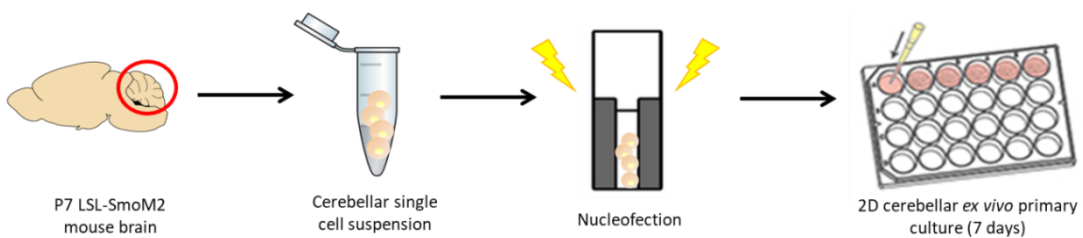
Figure 21: Schematic representation of *ex vivo* cerebellar assay.

AIM 3: To define the contribution of chromatin changes of granule neurons in response to SmoM2 activation alone or in cooperation with truncated BRPF1 overexpression.

ATAC-seq profiling would allowed to retrieve chromatin accessibility changes both in mouse tissue samples and in human neurons, unveiling cis-regulatory elements and their relative changes in response to SmoM2 and BRPF1 TR expression. The SmoM2 effect in modifying the epigenetic landscape of granule neurons will be checked by profiling chromatin accessibility on four cerebella samples retrieved from Gabra6-cre;LSL-SmoM2 and the control Gabra6-cre, respectively. Furthermore, the role of truncated BRPF1 and its cooperativity with smoM2 activation in driving chromatin plasticity will be verified by performing ATAC-seq in iPSC-derived human cerebellar neurons that possess hindbrain fate.

The following results are published in the paper: "Truncated BRPF1 Cooperates with Smoothened to Promote Adult Shh Medulloblastoma." *Cell Rep, 29*(12), 4036-4052 e4010. doi: 10.1016/j.celrep.2019.11.046 (Aiello et al., 2019)

4. Results

4.1 SmoM2 expression in granule neurons promotes medulloblastoma

In the present work, we investigated if postmitotic neurons could dedifferentiate *in vivo* and if this process could lead to Shh MB in mice. To do so, we induced Shh pathway activation through the expression of a constitutively active Smo mutant (SmoM2) to mimic the SMO gain of function mutations present in human adult SHH MB (Kool et al., 2014; Northcott et al., 2012). In particular, to examine if neurons can dedifferentiate *in vivo*, we conditionally induced SmoM2-EYFP expression (LSL-SmoM2 mice) in postmitotic neurons using Gabra6-cre mouse (Aller et al., 2003). Indeed, GABAA receptor α6 subunit (*Gabra6*) is expressed only in postmitotic neurons and it has already been shown that Gabra6-cre mouse induces recombination in neurons of the cerebellum, midbrain and cortex. As shown in Figure 22 A and 22 B Gabra6-cre;LSL-SmoM2 mice developed MB (7 and 4 months) and showed signs of ataxia, frequent falls and weight loss (n=9). Moreover, Kaplan-Meier survival analysis showed that less than 50% of the mice were still alive after 300 days (Figure 22 C). Notably, we found cerebellum aberrations and presence of tumor cells expressing PCNA, a marker of cell proliferation, as early as in 4-week-old mice (Figure 22 D). The tumor localization suggests that it could originate from neurons of the EGL (external granular layer), IGL (internal granular layer) or the Molecular Layer. Several cells within the tumor were also Sox9 (Figure S1 A, B and E) and Sox2 positive (Figure S1 C, D and E), two cell markers present in mouse and human SHH MB (Sutter et al., 2010; Swartling et al., 2012; Vanner et al., 2014) and expressed at higher levels in human adult SHH MB, compared to the infant form (Al-Halabi et al., 2011). Notably, Sox2 and Sox9 proteins are also expressed in mouse neural stem cells, Bergmann glia cells and at low levels in granule neuron progenitors during cerebellum development (Ahlfeld et al., 2013; Sutter et al., 2010; Vong, Leung, Behringer, & Kwan, 2015). The tumors were also positive for Doublecortin (DCX), a marker for highly proliferative progenitors present in mouse Shh MB (Figure S1F). The tumors were EYFP positive (GFP antibody), thus confirming that SmoM2-EYFP is expressed in cancer cells (Figure S1G). Furthermore, histopathological and immunophenotypical analyses confirmed that tumors in Gabra6-cre;LSL-SmoM2 mice are Shh MB (YAP1 and GAB1 positive and with cytoplasmic beta-catenin Figure S1I-R (Ellison et al., 2011)). In search for putative genes required for neuron dedifferentiation, we crossed Gabra6-cre;LSL-SmoM2 mice with Sox9^{flox} mice. In fact, it has already been shown that SmoM2 requires Sox9 to induce basal cell carcinoma (skin cancer)(Larsimont et al., 2015). Interestingly, we obtained MB also in Gabra6-cre;LSL-SmoM2;Sox9$^{flox/flox}$ mice (3/3 mice, Figure S1H), indicating that Sox9 functions are not conserved between skin and brain cancer. To further confirm the tumorigenicity

of Gabra6-cre;LSL-SmoM2 MB cells, we performed tumor transplantation experiments. Specifically, we isolated cells from 4-month-old tumor-bearing Gabra6-cre;LSL-SmoM2 cerebella and then we injected the cells into the cerebellum of 4-month-old nude mice (Foxn1nu). Our results showed that all 4 mice injected with Gabra6-cre;LSL-SmoM2 MB cells, generated tumors populated by PCNA, NeuN and Ph3 positive cells (Figure 22 E,F and data not shown). To further characterize our mouse model, we examined the expression profiles of five different Gabra6-cre;LSL-SmoM2 MB and compared them to wild type cerebellar tissue obtained from CD1 mice. In particular after determining the differential expressed genes (Supplementary Table 1), we performed functional annotation procedures using the Database for Annotation, Visualization and Integrated Discovery (DAVID) and Gene set enrichment analysis (GSEA). As shown in Figure S1 S and S1 T, the tumor samples presented an increase in the expression of genes linked to cell cycle, DNA replication and as expected to the Shh Pathway. Consistently, we observed a decreased expression of genes related to normal neuron functions like the synaptic vesicles cycle (Figure S1 T). We then compared our model to several types of MB mouse models using publicly available datasets (GSE11859, GSE24628, GSE33199). PCA analysis showed that the gene expression profile of tumors retrieved from Gabra6-cre;LSL-SmoM2 clustered with SmoM2 and Ptch1$^{+/-}$ Shh MB mouse models (Figure 22 G). Finally, we compared our model to human SHH MB gene expression dataset (GSE85217), respect to the enrichment of SHH pathway signature. This analysis showed that Gabra6-cre;LSL-SmoM2 (G6) samples activated the SHH pathway to the same extent as human SHH MB (Figure 22 H). Together these results are consistent with the hypothesis that Gabra6-cre;LSL-SmoM2 represents a putative Shh MB mouse model. Bioinformatics analysis was performed by Silvano Piazza of the bioinformatics core facility.
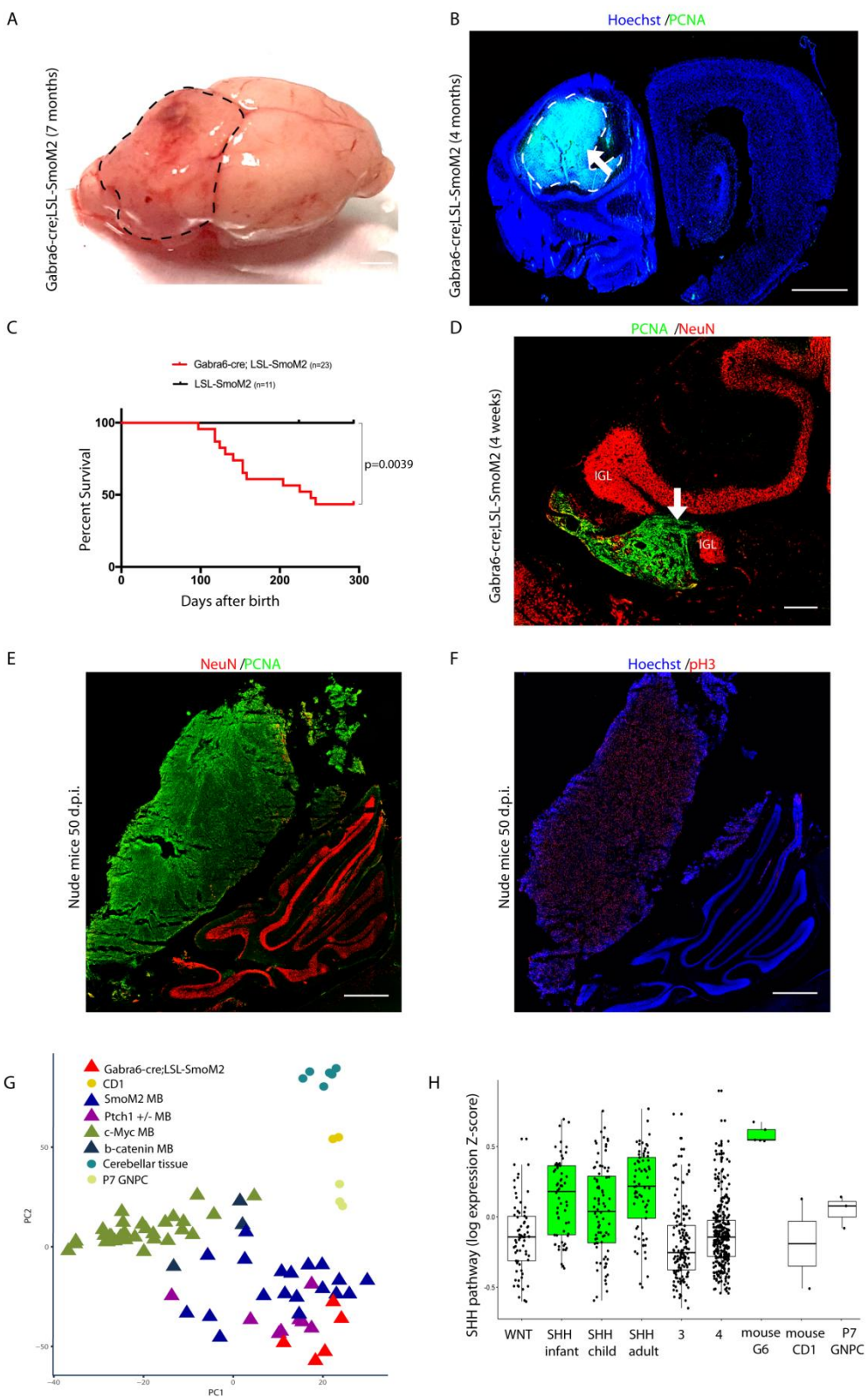
Figure 22 SmoM2 expression in granule neurons promotes Shh MB. (A) Image of 7-month-old Gabra6-cre;LSL-SmoM2 MB. **(B)** Hoechst and PCNA staining of brain section of 4-month-old Gabra6-cre;LSL-SmoM2 mouse. Arrow points to the tumor. **(C)** Kaplan-Meier survival curves of LSL-SmoM2 and Gabra6-cre;LSL-SmoM2 mice. **(D-E)** PCNA and NeuN staining of brain sections of 4-week-old Gabra6-cre;LSL-SmoM2 mouse **(D)** and 4-month-old nude mice, 50 d.p.i. with Gabra6-

cre;LSL-SmoM2 MB cells **(E)**, arrow points to the tumor. Lower and higher magnification of **D** in Figure S1AK-AL. **(F)** Hoechst and pH3 staining of brain sections of 4-month-old nude mice, 50 d.p.i. with Gabra6-cre;LSL-SmoM2 MB cells. **(G)** Multidimensional Scaling of several MB mouse models, plotting the results of the two principal coordinates. Original GEO dataset entries (GSE11859, GSE24628, GSE33199). **(H)** Boxplots of the median values of the Shh genes for the human samples (GSE85217) and Gabra6-cre;LSL-SmoM2 MB. Scale bar 2mm **(A)** 1mm **(B,E,F)** , 250μm **(D)**. IGL, Internal Granular Layer. The dashed lines in A,B mark the tumors. d.p.i. days post injection. **(G)** PC1 and PC2, principal coordinates 1 and 2. **(H)** WNT, WNT subgroup. SHH, SHH subgroup. 3, Group3. 4, Group4. G6, Gabra6-cre;LSL-SmoM2. CD1, normal cerebellum tissue. P7 GNPC, P7 granule neuron progenitors cells.

4.2 SmoM2 promotes dedifferentiation of granule neurons

Our data suggest that Smo gain of function in postmitotic neurons is sufficient to induce MB formation and reinforce the possibility that neurons are dedifferentiating. To clarify if the granule neurons started dedifferentiating at early stages of tumor formation, we analyzed Gabra6-cre;LSL-SmoM2 mice at postnatal day 14 (P14). As shown in Figure 23 A and 23 B, few PCNA and NeuN double positive cells can be detected at this stage in mouse cerebellum (33±8 cells in 3 sections for each brain, Mean±S.D, n=4 brains), indicating that neurons have started to proliferate without losing NeuN expression. Notably, we did not observe PCNA and NeuN double positive cells in control mice (LSL-SmoM2) (Figure S1H and data not shown), therefore indicating that SmoM2 induction upon cre expression was responsible for this proliferation burst. This suggests that the PCNA and NeuN double positive cells could represent the cell of origin of Shh MB. Interestingly, we also identified Sox9/Sox2 and NeuN double positive cells, indicating that some neurons while dedifferentiating start expressing markers of neuronal progenitors (Figure 23 C and 23 D and Figure S1 U and S1 V). Of notice the same phenotype was not observed in control mice (Figure S1H). Indeed, it has been published that rare Sox2-expressing cells are the founding cancer stem cell population driving cancer initiation and therapy resistance (Vanner et al., 2014) in mouse models of infant Shh MB. Based on this knowledge, we analyzed the Gabra6-cre;LSL-SmoM2 mice at different timepoints and we detected Sox9/PCNA and NeuN double positive cells at P7, P14, P21 and P28 (Figure S1 W-AD and figure S1 AE-AL). Notably, at P21 we already observed small clusters of PCNA positive cells (Figure S1 AI-AJ) and aberrant Sox9 expression (Figure S1 AA-AB). SmoM2 expression was confirmed by immunofluorescence using a GFP antibody that recognizes the YFP fused to SmoM2 (Figure S1 AM-AP). To better detect and identify dedifferentiated neurons, we crossed the Gabra6-cre;LSL-SmoM2 mice with LSL-tdTomato mice that express tdTomato only upon cre recombination (Madisen et al., 2010). As shown in Figure S2 A-L, we did not observe tdTomato expression in mice embryos at E16.5 (Gabra6-cre;LSL-SmoM2;LSL-tdTomato) but we detected PCNA/Sox9 and tdTomato double positive cells in the IGL at P7 and P14, when granule neurons are already present. Since Gabra6-cre mice express cre recombinase

also in few Deep Cerebellar Nuclei (DCN) cells (Aller et al., 2003), we analyzed PCNA expression in Gabra6-cre;LSL-tdTomato and Gabra6-cre;LSL-SmoM2 in DCN. Notably we did not detect any aberrant PCNA staining at P21 in both mice (Figure S2 M-P). Therefore, we postulate that the tumors should not originate from dedifferentiated neurons of DCN. Taken together, these data suggest that the Sox2/Sox9 and NeuN double positive cells identified in the cerebellum of Gabra6-cre;LSL-SmoM2 mice could be dedifferentiated granule neurons that originate Shh MB. To further confirm our hypothesis, we injected EdU in Gabra6-cre;LSL-SmoM2 mice at P19 to avoid EdU incorporation in progenitors (that are not present at this timepoint) and to label only neurons that re-enter in the cell cycle. As shown in Figure 23 E,F and Figure S2 Q, we observed small clusters of EdU positive cells in the IGL in P21 Gabra6-cre;LSL-SmoM2 mice and not in Gabra6-cre;LSL-tdTomato mice (Figure S2 R and Figure S2 S-AC). Therefore, we speculate that the EdU positive cells could be dedifferentiated neurons. Since *Ptch1* ablation in cerebellar progenitors is able to induce Shh MB in few months (Northcott et al., 2012), we analyzed the effect of *Ptch1* loss in postmitotic neurons in Gabra6-cre;Ptch1$^{flox/flox}$ and Gabra6-cre;Ptch1$^{flox/+}$ mice, but we did not observe MB development (Figure S1 H). To understand the reason why SmoM2 overexpression, unlike *Ptch1* deletion, leads to tumor formation we analyzed their cerebella at P14 by qRT-PCR. As shown previously, at this stage most of the granule neurons have been produced and in Gabra6-cre;LSL-SmoM2 there is no tumor formation yet. Gene expression analysis revealed that *Math1* and *Gli1* genes are upregulated specifically in Gabra6-cre;LSL-SmoM2 mice, but not in Gabra6-cre;Ptch1$^{flox/flox}$ (Figure S3 A). These data suggest that SmoM2 overexpression induces a much stronger activation of Shh signaling and *Math1* (specific marker for granule neuron progenitors) as compared to Ptch1 loss and could explain the presence of Shh MB in Gabra6-cre;LSL-SmoM2 and its absence in Gabra6-cre;Ptch1$^{flox/flox}$ mice. It has also been shown that Ptch1^{flox} mice are able to induce MB when crossed with mice expressing recombinase in cerebellar progenitors (GFAP-cre) (Wu et al., 2017) and we validated the effect of *Ptch1* deletion in Math1-creER;Ptch1$^{flox/+}$ mice, observing the induction of progenitors overproliferation (Figure S3 B and S3 C).
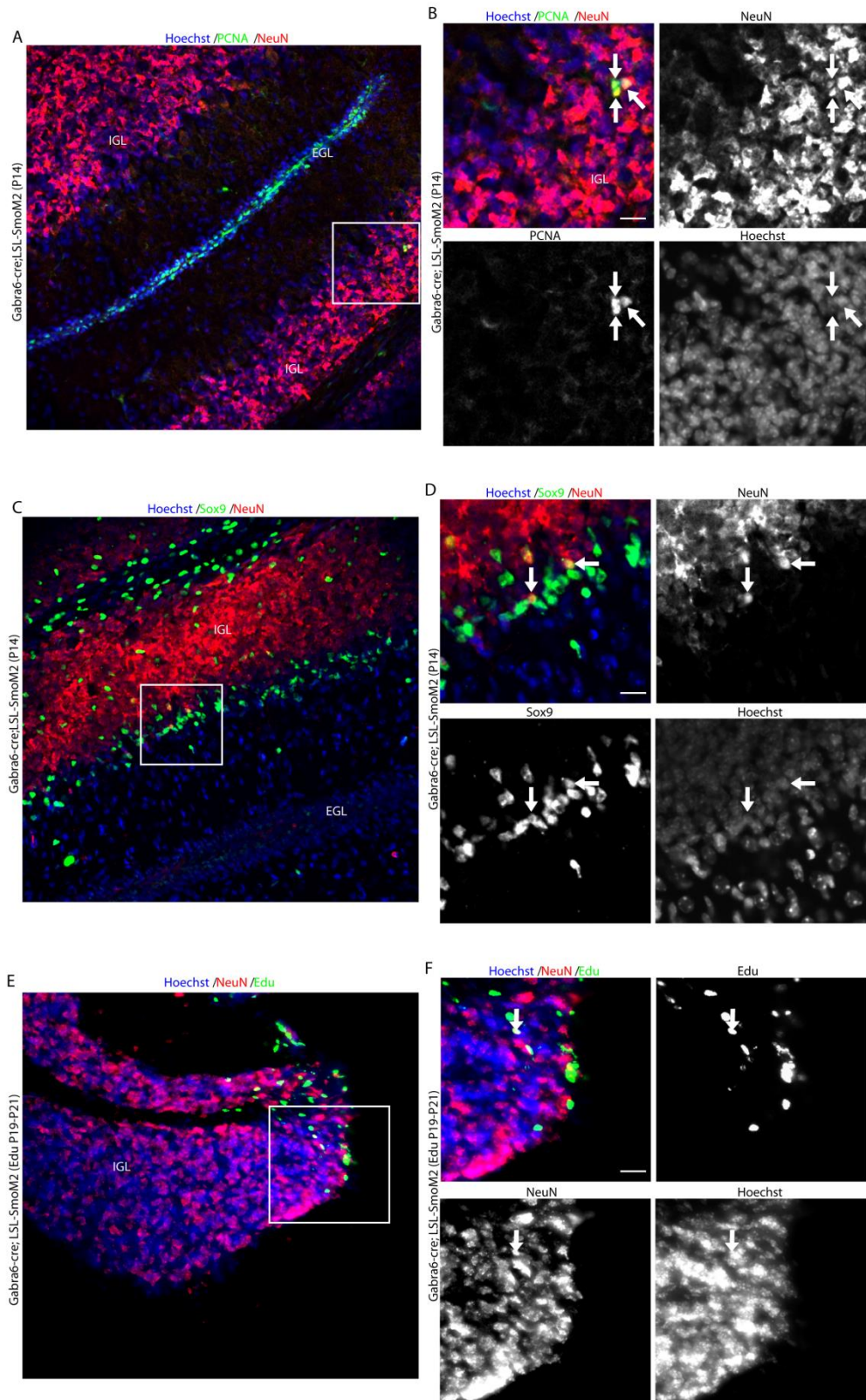
Figure 23: SmoM2 promotes dedifferentiation of granule neurons. (**A,B**) Hoechst, PCNA and NeuN staining of brain sections of P14 Gabra6-cre;LSL-SmoM2 mouse. Square in **A** marks the region shown at higher magnification in **B**. Arrows point to PCNA/NeuN double positive cells. (**C,D**) Hoechst, Sox9 and NeuN staining of brain sections of P14 Gabra6-cre;LSL-SmoM2 mouse. Square in **C** marks the region shown at higher magnification in **D**. Arrows point to Sox9/NeuN double positive cells. (**E,F**) Hoechst, EdU and NeuN staining of brain sections of P21 Gabra6-cre;LSL-SmoM2 mouse, injected with EdU at P19. Square in **E** marks the region shown at higher magnification in **F**. Lower magnification

of **E** in Figure S2Q. Arrows point to EdU/NeuN double positive cells. Scale bars 25 μm (**B,D,F**). EGL, External Granular Layer. IGL, Internal Granular Layer.

4.3 Gabra6-cre mice express cre recombinase in neurons

To exclude that Gabra6-cre mice induce recombination in cerebellar progenitors, we crossed them with LSL-tdTomato mice that express tdTomato only upon cre recombination. We then analyzed if tdTomato was expressed in progenitors at different postnatal timepoints. We quantified several thousand tdTomato positive cells (see Materials and Methods) and all of them were negative for progenitors, glial or proliferation markers such as PCNA, pH3, Sox2 and Sox9 (Figure S3 D-L). Moreover, almost all tdTomato cells were positive for the neuronal marker NeuN at postnatal day 4,7,10 and 14 (Figure S3 L). Finally, to confirm the specificity of Gabra6-cre;LSL-tdTomato mice, we crossed them with Math1-GFP mice that express a Math1 protein fused with GFP (Rose et al., 2009) only in granule neuron progenitors. As shown in Figure S4 A-E, tdTomato positive cells were GFP negative. Interestingly, in Gabra6-cre;LSL-tdTomato mice, tdTomato was expressed in several brain regions such as cortex, hippocampus, ventral thalamus and hypothalamus (Figure S4 F-J). Taken together, these data indicate that our genetic model allows manipulation of post-mitotic neurons only. Moreover, these data suggest that only cerebellar neurons are able to dedifferentiate into cancer cells, since we have never observed tumor masses in other regions of the brain.

4.4 Transient Cre recombinase expression promotes dedifferentiation of granule neurons in LSL-SmoM2 mice

To prove that Shh MB originates from postmitotic neurons, we transfected granule neurons of LSL-SmoM2 mice at P21/24 with a plasmid expressing cre recombinase under the control of NeuroD1 promoter (pNeuroD1-cre)(Guerrier et al., 2009). *NeuroD1* is expressed in granule neurons and progenitors (Cho & Tsai, 2006), but at the selected timepoints granule neuron progenitors are not present anymore(Tiberi et al., 2014; Z.-J. Yang et al., 2008) (Figure S4 K). As shown in Figure 24 A, four days after *in vivo* transfection of pNeuroD1-cre-IRES-GFP, we detected GFP positive cells in the cerebellum IGL, but we did not detect Sox9/Sox2/PCNA and GFP double positive cells (Figure 24 B and figure S4L-O). These data suggest that we can specifically transfect cerebellar neurons. Anyhow, it has been shown by other groups that Shh pathway activation in granule neuron progenitors after P12-14 does not lead to MB formation (Z.-J. Yang et al., 2008). We have confirmed these data by induction of SmoM2 with a granule neuron progenitor specific promoter (Math1-creER) at P21 and we did not obtain MB (Figure S1 H). On the contrary, as

shown in Figure 24 C, 60 days after pNeuroD1-cre transfection at P21, we observed MB in only one mouse (n=16). Furthermore, we noticed the formation of PCNA, DCX, pH3, Sox2 and Sox9 positive cells clusters in the IGL of five other mice (Figure 24 D-F and figure S4 P-R). These data suggest that SmoM2 expression driven by pNeuroD1-cre in mouse cerebellum (when granule neuron progenitors are not present) can rarely induce Shh MB. In addition, we investigated the possibility to dedifferentiate neurons in adult mice. We transfected 2-month-old LSL-SmoM2 mice with a plasmid expressing cre recombinase under the control of human SynapsinI promoter (phSynI-cre). This promoter has been shown to induce expression of desired genes in postmitotic neurons and not in glial cells (Kugler et al., 2003). Indeed, 4 days after *in vivo* transfection of phSynI-cre together with pPB-LSL-tdTomato in 2-month-old LSL-SmoM2 mice, we did not detect Sox9/Sox2/PCNA/pH3 and tdTomato double positive cells (Figure S4 S-U). As shown in Figure S5 A-B, we obtained formation of abnormal PCNA and Sox9 clusters in cerebellum IGL (upon SmoM2 expression) in 2 out of 7 transfected adult mice. These clusters are positive for GFP staining, indicating that transfected cells are expressing SmoM2-YFP. Taken together, these data suggest that SmoM2 is able to dedifferentiate granule neurons also in adult mice.
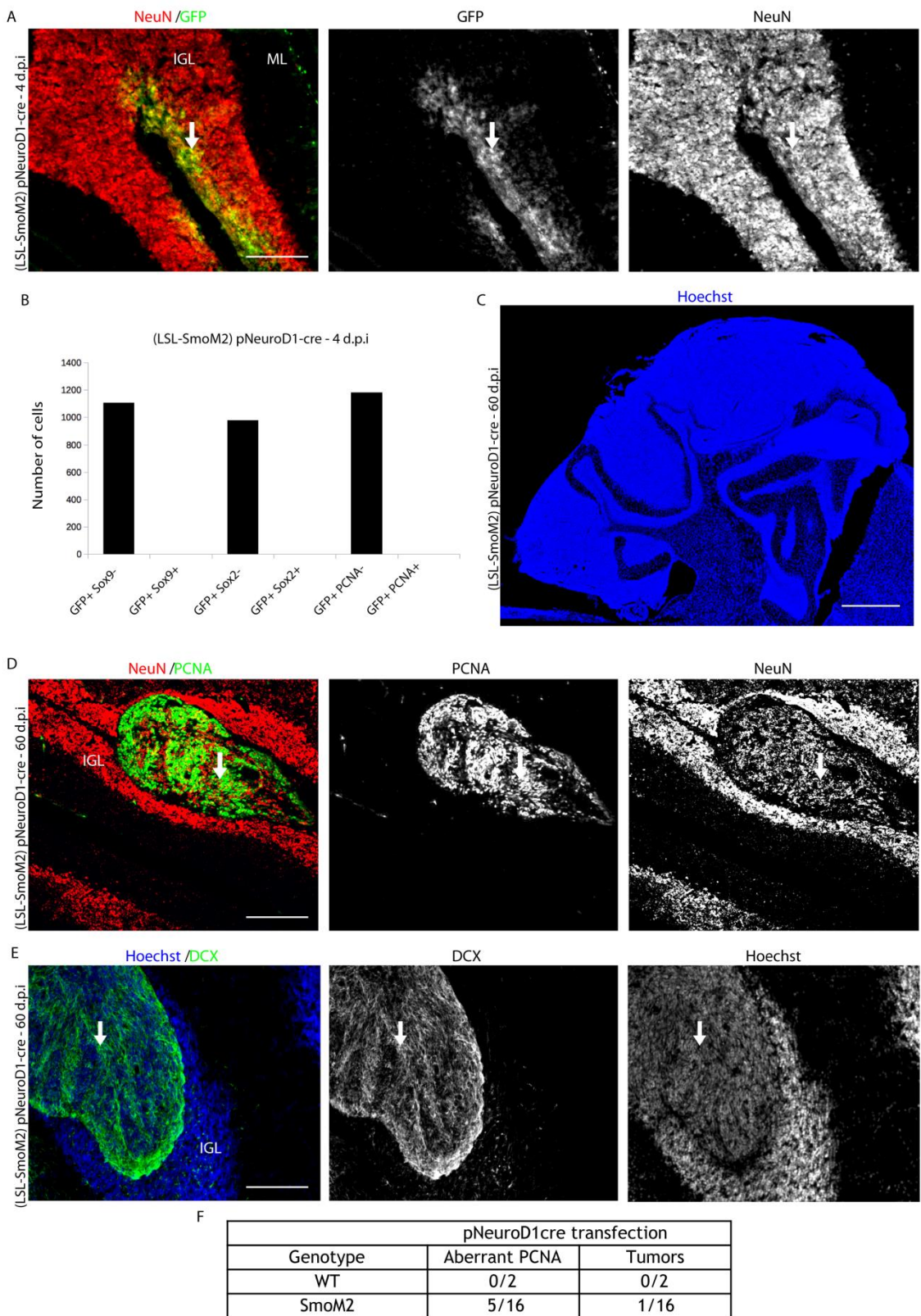
Figure 24: Transient cre recombinase expression promotes dedifferentiation of granule neurons and Shh MB in LSL-SmoM2 mice. (A) GFP and NeuN staining of brain sections of LSL-SmoM2 mice, 4 d.p.i. at P21 with pNeuroD1-cre . Arrow points to GFP and NeuN positive cells. (**B**) Quantification of GFP and Sox9/Sox2/PCNA double positive cells in LSL-SmoM2 mice, 4 d.p.i. at P21 with pNeuroD1-cre (n=3). (**C**) Hoechst staining of brain sections of LSL-SmoM2 mice, 60 d.p.i. at P21 with pNeuroD1-cre. (**D**) PCNA and NeuN staining of brain sections of LSL-SmoM2 mice, 60 d.p.i. at P21 with

pNeuroD1-cre. Arrow points to a tumorigenic cell cluster within the IGL. (**E**) Hoechst and DCX staining of brain sections of LSL-SmoM2 mice, 60 d.p.i. at P21 with pNeuroD1-cre. Arrow points to a tumorigenic cell cluster within the IGL. (**F**) Mice with abnormal PCNA+ cell clusters or tumors. Scale bar 1 mm (**C**), 150μm (**A,D,E**). IGL, Internal Granular Layer. ML, Molecular Layer. d.p.i. days post injection.

4.5 Mutant BRPF1 promotes adult Shh medulloblastoma formation

Looking for a molecular mechanism by which SmoM2 induces neuron dedifferentiation, we exploited already published data of human SHH MB exome sequencing. Interestingly, recurrent mutated genes have been identified in adult SHH MB that were absent or very rare in pediatric SHH MB, such as *BRPF1*, *KIAA0182*, *TCF4*, *CREBBP*, *NEB*, *LRP1B*, *PIK3CA*, *FBXW7*, *KDM3B*, *XPO1*, *PRKAR1A*, and *PDE4D* (Kool et al., 2014; Merk et al., 2018). For instance, nonsense and frameshift *BRPF1* mutations have been found associated with SMO mutations and absent in pediatric and adolescent SHH MB (samples ID:AdRep_MB107, MB101, MB143). The presence of a premature stop codon could generate truncated forms of BRPF1 proteins lacking several domains. Brpf1 has been previously shown to be expressed in granule neurons and Purkinje cells in newborn mice (You et al., 2014) and we found that Brpf1 is expressed in mouse cerebellum in P7 and 4-week-old mice (Figure S5 C-D). We also analyzed the expression of Brpf1 in adult brains and in Gabra6-cre;LSL-SmoM2 tumors. As shown in Figure 25 A, Brpf1 was found expressed in cerebellar IGL and in few cells within Gabra6-cre;LSL-SmoM2 MB. This indicates that Brpf1 protein is expressed at low levels in these tumors. Based on the described association of BRPF1 and SMO mutations in adult SHH MB, we tested its function in tumor formation. We co-transfected pNeuroD1-cre with a plasmid that allows constitutive expression of wild-type BRPF1 in LSL-SmoM2 mice (pPB-BRPF1 WT, Figure 25 B). Notably, we detected no sign of tumor/dysplasia in any of the 19 mice injected with pNeuroD1-cre and pPB-BRPF1 WT (Figure 25 C, Figure S5 E), suggesting that BRPF1 overexpression blocks SmoM2 ability to induce neuron dedifferentiation. To mimic the mutational background of a subset of human patients, we generated a truncated form of BRPF1 lacking the bromodomain and PWWP motif (Figure 25 B). Interestingly, we observed tumor formation when we co-transfected this truncated form of human BRPF1 (pPB-BRPF1 TR, Figure 25 C) and a significant decrease in mouse survival compared to BRPF1 WT transfection (Figure 25 D). We observed MB formation in 50 % of the transfected mice (3 out of 6, Figure 25 C) and the tumors were DCX, Sox9 and PCNA positive (Figure 25 E-G and Figure S5 F-G). These data indicate that truncated BRPF1, as found in patients, is able to induce adult SHH MB. Next, we performed an *ex vivo* assay to test if BRPF1 has also a role in neuron dedifferentiation. Cerebellar cells from P7 LSL-SmoM2 mice were nucleofected with phSynI-cre alone or together with pPB-BRPF1 WT. After 7 days of *ex vivo* culture, we detected several GFP/Sox9/NeuN triple positive cells in cerebellar cells

nucleofected with phSynI-cre alone (Figure S5 H-I), but fewer with co-overexpression of BRPF1 WT, suggesting that BRPF1 WT blocks neuron dedifferentiation. Moreover, in the same experimental setup Gli1 co-overexpression, was able to rescue the repressive effect of BRPF1 WT, indicating that Shh pathway and BRPF1 WT could have antagonistic roles in the dedifferentiation process. Interestingly, the nucleofection of phSynI-cre and a plasmid expressing truncated BRPF1 did not block neuron dedifferentiation, rather increased it compared to phSynI-cre alone (Figure S5 J). This suggests that truncated BRPF1 could have a dominant negative effect in promoting neuron dedifferentiation. Notably, Gli1/2 knockdown was able to completely block SmoM2 and truncated BRPF1 functions suggesting that they require Gli1/2 expression to induce neuron dedifferentiation. Finally, to prove that also neurons of adult mice can give rise to adult Shh MB, we transfected adult LSL-SmoM2 animals (2-month-old) with phSynI-cre and pPB-BRPF1 TR (truncated BRPF1) plasmids. We obtained MB formation in 3 mice out of 5 (Figure 26 A-E) containing cancer cells positive for GFP, PCNA and DCX. Furthermore, Kaplan-Meier survival analysis showed that less than 50% of the mice survived 100 days after transfection (Figure 26 F). As previously shown in Figure S5A-B, phSynI-cre transfection alone induced dedifferentiation of granule neurons, but did not lead to MB formation. This confirms that Shh pathway and BRPF1 functions should be altered together in adult mice during adult Shh MB tumorigenesis. Notably, we did not obtain Shh MB (n=11) transfecting truncated BRPF1 alone in 2-month-old CD1 mice (data not shown). To better characterize the BRPF1-induced MB, we performed gene expression profiling of one phSynI-cre+BRPF1 TR and one pNeuroD1-cre+BRPF1 TR tumors (Mouse BRPF1). Interestingly, the activation level of Shh signaling pathway in the SmoM2+BRPF1 TR induced tumors was similar to human adult SHH MB (Figure 26 G). To evaluate if phSynI-cre+BRPF1 TR and pNeuroD1-cre+BRPF1 TR tumors mimic human adult SHH MB, we further compared their gene expression profiles with mouse and human MB samples. Based on the genes reported in Al-Halabi et al., 2011 as differentially expressed in human adult versus human infant SHH MB, pNeuroD1-cre+BRPF1 TR and phSynI-cre+BRPF1 TR mouse models resulted similar to human adult SHH MB (Figure 26 H). Gabra6-cre;LSL-SmoM2 mice (1 out of 5 samples) showed limited similarity to human adult SHH MB, while no similarity was observed for Math1-cre;LSL-SmoM2 mice (GSE11859). These data suggest that BRPF1 TR and SmoM2 co-overexpression in adult granule neurons gives rise to mouse tumors with a gene expression profile resembling human adult SHH MB. On the other hand, the tumors obtained from granule neuron progenitors are more similar to human infant SHH MB (Math1-cre;LSL-SmoM2 mice, GSE11859). In addition, we performed immunofluorescence for p-AKT and p-S6 that have already been shown to be co-markers only for human adult SHH MB (Kool et al., 2014). In fact, few human infant SHH MB are marked by p-AKT and p-S6 and always in a mutually exclusive way. The tumors generated upon transfection of pNeuroD1-cre+BRPF1 TR and phSynI-cre+BRPF1 TR in LSL-SmoM2 showed both p-AKT and p-S6,

similar to human adult patients (Figure S5K-N and data not shown) while Math1-creER;LSL-SmoM2 mice present only p-S6 (Figure S5O-R). Taken together, these data suggest that our mouse models resemble human adult SHH MB. To validate the cooperativity of SmoM2 and truncated BRPF1 in inducing adult Shh MB, we expressed in adult mice an inducible cre recombinase under the control of the Etv1 promoter in postmitotic neurons (Schuller et al., 2006; Taniguchi et al., 2011). We transfected Etv1-creER;LSL-SmoM2 mice with pPB-BRPF1 TR at P90 and then we induced the recombination with tamoxifen (n=9). Notably, only one mouse developed MB (Figure S5S-T) and aberrant small clusters of cells were observed in other two mice (data not shown). We also tested the specificity of Etv1-creER recombination, transfecting Etv1cre-ER;LSL-SmoM2 mice at P90 with pPB-LSL-tdTomato. In these animals, we did not detect any tdTomato and Sox9/Sox2/PCNA/pH3 double positive cells (Figure S5U). This confirms the role of SmoM2 and truncated BRPF1 in promoting MB formation from postmitotic neurons in adult mice. Finally, we assessed BRPF1 expression in human adult SHH MB derived from 6 different patients. In all the tumors (Figure S5V-W and data not shown) we observed few BRPF1 positive cells within the PCNA positive tumor cells, confirming that BRPF1 protein is downregulated in human adult SHH MB. Bioinformatics analysis was performed by Alessandro Romanel of the laboratory of bioinformatics and computational genomics.
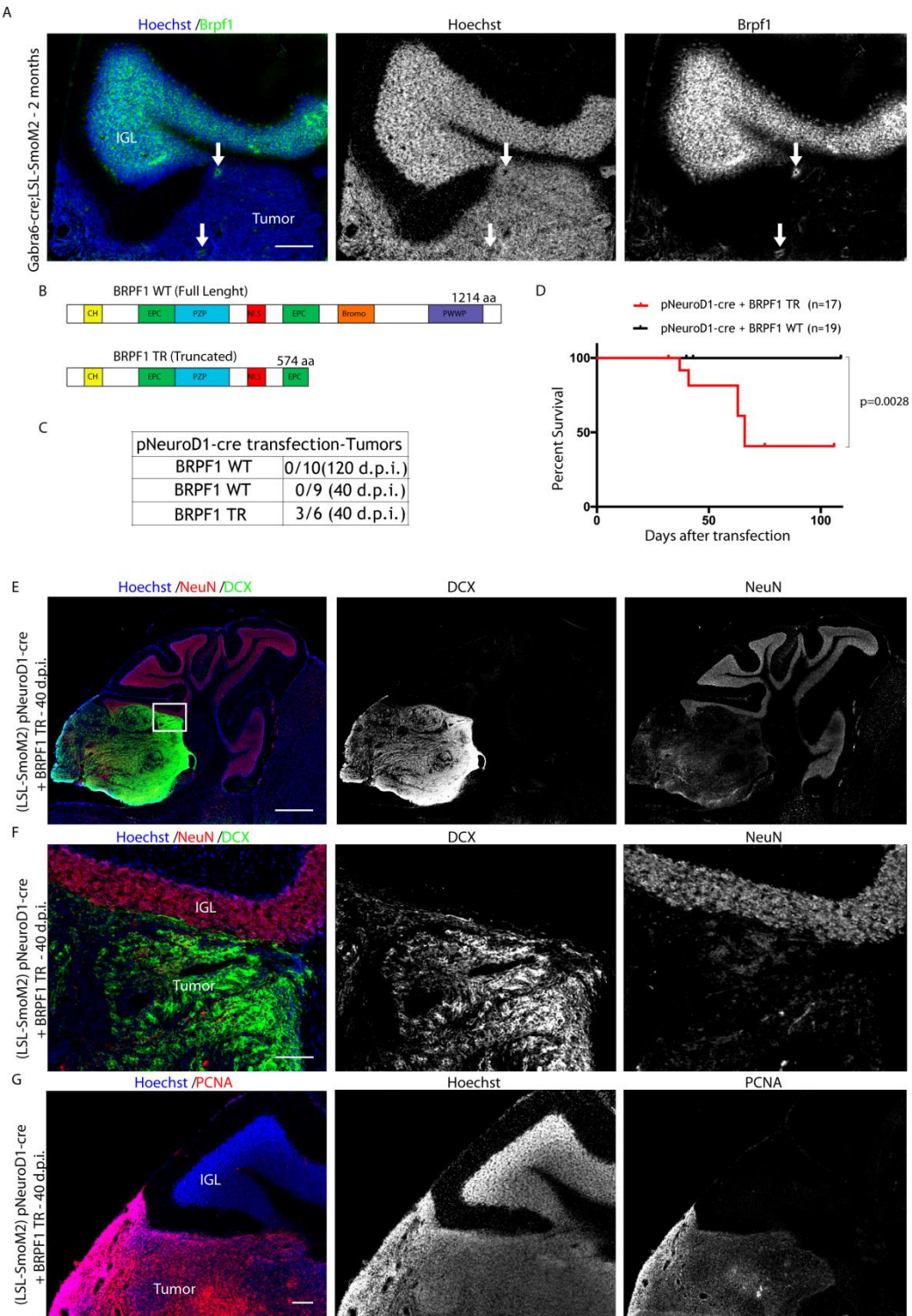
Figure 25: Wild type BRPF1 is required to block Shh MB formation in LSL-SmoM2 mice. (**A**) Hoechst and Brpf1 staining of brain sections of 2-month-old Gabra6-cre;LSL-SmoM2 mouse. Arrows point to Brpf1 positive cells. (**B**) Representation of human wildtype BRPF1 and truncated BRPF1. CH, C2H2 zinc finger. EPC, enhancer of polycomb-like motif. PZP, PHD finger–zinc knuckle–PHD finger motif. NLS, nuclear localization signal. Bromo, bromodomain. PWWP, Pro-TrpTrp-Pro motif. Truncated BRPF1 lacks the bromodomain and the PWWP motif. (**C**) Mice with Shh MB after transfection at P21 with pNeuroD1-cre and BRPF1 WT or BRPF1 TR. (**D**) Kaplan-Meier survival curves of LSL-SmoM2 mice transfected at P21

with either pNeuroD1-cre+BRPF1 WT or pNeuroD1-cre+BRPF1 TR. (**E,F**) Hoechst, NeuN and DCX staining of brain sections of LSL-SmoM2 mouse, 40 d.p.i. at P21 with pNeuroD1-cre + BRPF1 TR. Square in **E** marks the region shown at higher magnification in **F**. (**G**) Hoechst and PCNA staining of brain sections of LSL-SmoM2 mouse, 40 d.p.i. at P21 with pNeuroD1-cre + BRPF1 TR. Scale bar 200 μm (**A**), 1 mm (**E**), 500 μm (**G**), 150μm (**F**). IGL, Internal Granular Layer. d.p.i. days post injection.
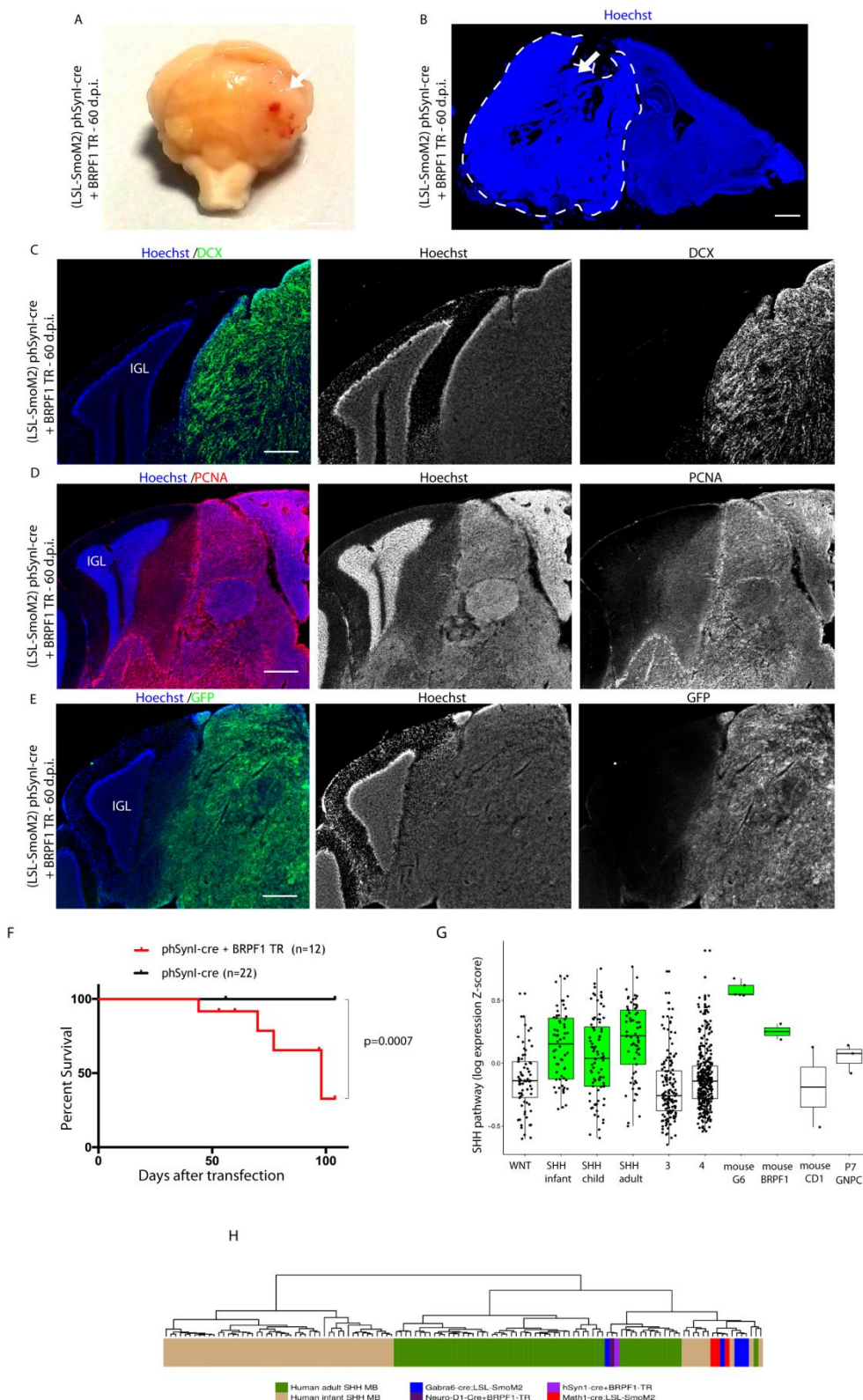
Figure 26: Truncated BRPF1 promotes adult Shh MB. (A) Image of LSL-SmoM2 mouse, 60 d.p.i. at 2 months with phSynI-cre+BRPF1 TR. Arrow points to tumoral mass. **(B)** Hoechst staining of brain section of LSL-SmoM2 mouse, 60 d.p.i. at 2 months with phSynI-cre+BRPF1 TR. The dashed lines and arrow in **B** mark the tumor **(C,D,E)** Hoechst, DCX **(C)**, PCNA **(D)** and GFP **(E)** staining of brain sections of LSL-SmoM2 mouse, 60 d.p.i. at 2 months with phSynI-cre+BRPF1 TR. **(F)** Kaplan-Meier survival curves of LSL-SmoM2 mice transfected at 2 months with either phSynI-cre or phSynI-cre+BRPF1 TR. Scale bar 2 mm **(A)**, 1 mm **(B)**, 500 μm **(C-E)**. **(G)** Boxplots of the median values of the SHH pathway for the human samples (GSE85217) and our samples. WNT, WNT subgroup. SHH, SHH subgroup. 3, Group3. 4, Group4. G6, Gabra6-cre;LSL-SmoM2. BRPF1, 40 d.p.i pNeuroD1-cre+BRPF1 TR and 60 d.p.i. phSynI-cre+BRPF1 TR. CD1, normal cerebellum tissue. P7 GNPC, P7 granule neuron progenitor cells. **(H)** Hierarchical clustering of different Shh MB mouse models data and human adult/infant SHH MB data on both samples distances and samples gene expression profiles using 108 differentially expressed genes in human adult versus human infant SHH MB. IGL, Internal Granular Layer. d.p.i. days post injection.

4.6 SmoM2 expression in granule neurons promotes widespread chromatin plasticity

Considering that dedifferentiation of postmitotic cells requires to overcome those epigenetic barriers that are established to maintain cell identity (Fagnocchi, Poli, & Zippo, 2018; Poli et al., 2018), we investigated whether SmoM2 expression in granule neurons was sufficient to alter the chromatin state. To this end, we profiled changes in chromatin accessibility by ATAC-seq in P14 cerebella of Gabra6-cre;LSL-SmoM2 and Gabra6-cre control mice. ATAC-seq analyses defined approximately 130000 open chromatin regions which were equally enriched at promoters (TSS), introns and intergenic sites, independently from the genetic background (Figure 27 A). Although most of the peaks were shared between the analysed samples, we retrieved 4029 and 6025 open regions which were enriched in Gabra6-cre and Gabra6-cre;LSL-SmoM2, respectively (Figure 27 B and Figure S6 A). Of importance, the differential enrichment of these regions was conserved among tissue samples obtained from independent mice (Figure 27 C). The enriched regions for ATAC-seq signals showed a typical profile with narrow peaks, resembling nucleosome depleted regions, occupied by TFs (Figure 27 D). We confirmed that the ATAC-seq profiling on cerebella tissue enables the identification of cis-regulatory elements as we identified specific DNA binding motifs enriched on the specific ATAC-seq peaks (Figure 27 E). In Gabra6-cre samples we found binding motifs for neural-specific TFs and architectural proteins such as CTCF, which are normally enriched at sites of chromatin looping including enhancers (Rada-Iglesias, Grosveld, & Papantonis, 2018). On Gabra6-cre;LSL-SmoM2 ATAC-seq peaks, we identified DNA binding motifs of lineage-specifying TFs which are expressed during cerebellum development, such as Sox2 and Math1 (Figure 27 E and figure S6B). These data were corroborated by Gene ontology analysis on the genes annotated on specific ATAC-seq peaks highlighting the enrichment of specific signatures associated with stem cell-like features and cancer pathways in Gabra6-cre;LSL-SmoM2 (Figure 27

F and figure S6C). This pattern was further confirmed by comparing the identified chromatin open regions with those that specified distinct stages of developing cerebellum (Frank et al., 2015). By quantifying the ATAC-seq signals on the previously identified chromatin accessible sites enriched at P14 and P60 (compared to P7) of developing cerebellum, we determined decreased in chromatin accessibility in Gabra6-cre;LSL-SmoM2, respect to Gabra6-cre (Figure 27 G and figure S6 D-E). In sum, these results showed that activation of SmoM2 in granule neurons induced changes in chromatin accessibility at cis-regulatory elements. These data suggest an increment of chromatin plasticity by means of favouring diversity in the chromatin contexts, priming for the activation of progenitor-associated transcriptional programs. ATAC-seq analysis was performed by Luca Fagnocchi and Alessio Zippo of the laboratory of chromatin biology & epigenetics.
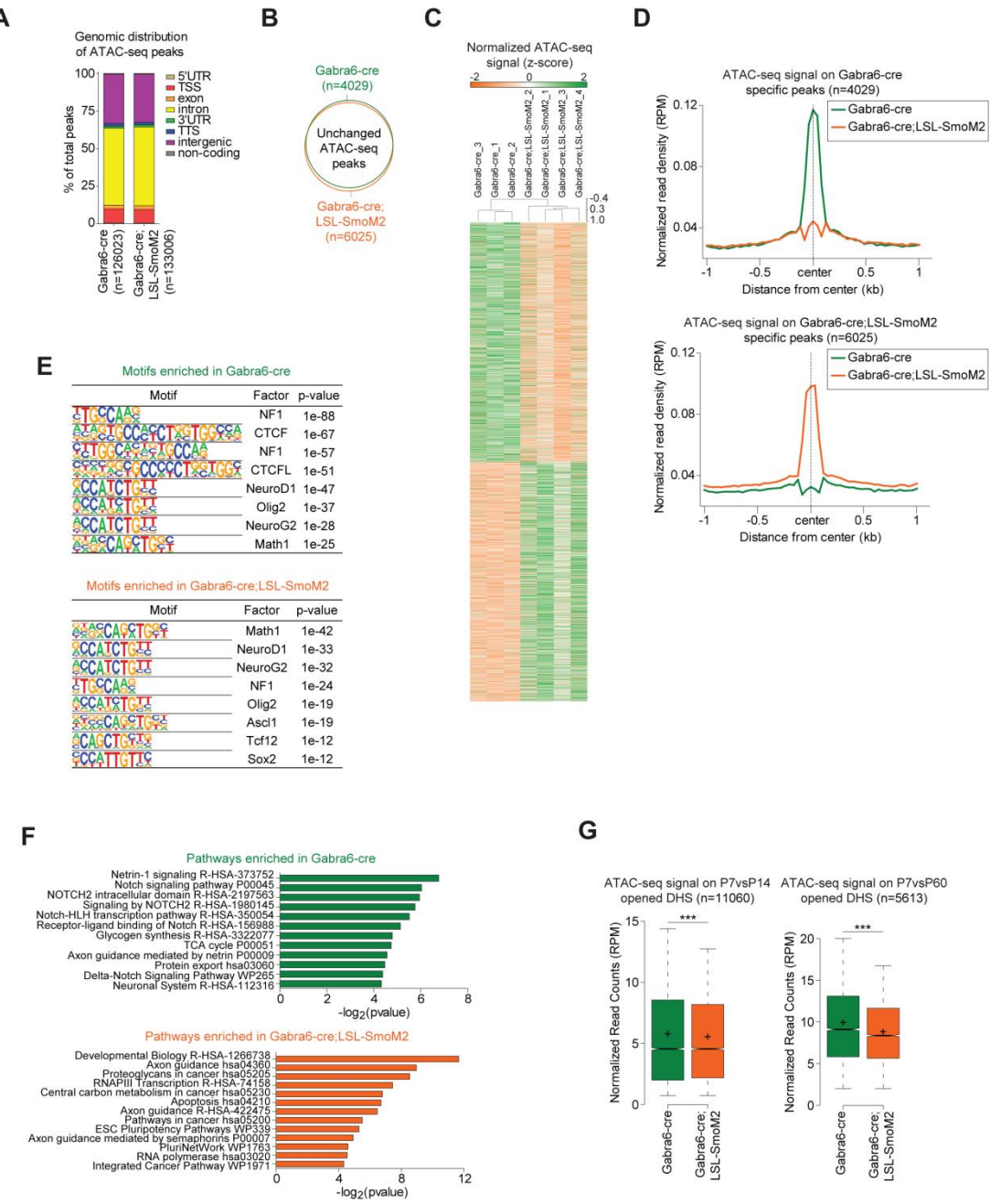
Figure 27: SmoM2 expression in granule neurons favors widespread chromatin plasticity and activation of stem/progenitor-associated genes. (A) Box plots showing the genomic distribution of ATAC-seq peaks, with respect to Transcription Start Sites (TSS), Transcription Termination Sites (TTS), 5'UTR, 3'UTR, exons, introns, intergenic regions and non-coding genes. **(B)** Venn diagram showing the overlap between ATAC-seq peaks in Gabra6-cre and Gabra6-cre;LSL-SmoM2 cells. **(C)** Heatmap representing the normalized ATAC-seq signal (Z-score) on the top 2000 most differentially enriched peaks in either Gabra6-cre or Gabra6-cre;LSL-SmoM2 cells. **(D)** Average tag density plot of the

normalized (RPM) ATAC-seq signal on the differential peaks, enriched either in Gabra6-cre (upper panel) or Gabra6-cre;LSL-SmoM2 (lower panel) cells. **(E)** Motif enrichment analysis on the specific ATAC-seq peaks in Gabra6-cre (left panel) or Gabra6-cre;LSL-SmoM2 (right panel) cells. **(F)** Gene ontology analysis on the genes annotated to specific ATAC-seq peaks in Gabra6-cre (upper panel) or Gabra6-cre;LSL-SmoM2 (lower panel) cells. Pathway from Reactome, Panther, WikiPathways and KEGG databases were analyzed. **(G)** Boxplots showing the normalized reads count of ATAC-seq signals in Gabra6-cre and Gabra6-cre;LSL-SmoM2 cells, on previously reported DNase Hypersensitive Sites (DHS), which resulted more accessible in P14 (left) or P60 (right) cerebella, when compared to P7 cerebellum. *** = p-value < 0.001, as assessed by a 2-tailed, unpaired Student's t-test. P14 Gabra6-cre (n=3) and Gabra6-cre;LSL-SmoM2 (n=4) cerebella.

4.7 Truncated Brpf1 expression elicits chromatin plasticity by activating super-enhancers

As we showed that, upon SmoM2 activation the truncated BRPF1 protein induced MB in adult mice and considering its presumed function in chromatin regulation (Yan et al., 2017), we investigated whether it could favour tumorigenesis by promoting chromatin plasticity and neuronal dedifferentiation. To this end, we profiled the chromatin accessibility changes occurring in post-mitotic neurons, in response to SmoM2 activation alone or in cooperation with truncated BRPF1. We took advantage of the human neuroepithelial-like stem cells AF22, that have a gene expression pattern resembling hindbrain fate and committed to generate post-mitotic neurons *in vitro* (Falk et al., 2012; Tailor et al., 2013)(Figure S6F). Indeed, qRT-PCR analysis showed that differentiated AF22 cells expressed high levels of ZIC1 gene, a specific marker for cerebellar granule neurons (Aruga et al., 1998)(Figure S6G). To resemble the scenario already analyzed in mouse, we nucleofected AF22 with pPB-hSynI-creER as control (Ctrl), and with pPB-hSynI-creER+pPB-LSL-SmoM2 (SmoM2) or pPB-hSynI-creER+pPB-LSL-SmoM2+pPB-LSL-BRPF1 TR (SmoM2+BRPF1 TR) to measure their cooperativity. Moreover, we tested the nucleofection with pPB-hSynI-creER+pPB-LSL-BRPF1 TR (BRPF1 TR) to assess if truncated BRPF1 alone was sufficient per se to alter chromatin accessibility. Of importance, qRT-PCR analysis confirmed that SmoM2 overexpression increases GLI1 mRNA levels in differentiated AF22 neurons (Figure S6H), as observed in Gabra6-cre;LSL-SmoM2 mice (Figure S3A). Thereafter, we profiled changes in chromatin accessibility by ATAC-seq in AF22 neurons expressing the different combinations of SmoM2 and BRPF1 (Figure 28 A). ATAC-seq analyses defined comparable numbers of open chromatin regions which were similarly distributed within the genome (Figure 28 A and figure S7 A-C). At first we confirmed that SmoM2 activation determined an increment in chromatin accessibility at specific cis-regulatory elements which were enriched for stem cells and Sox-family transcription factors (Figure S7D-G). Of importance, GSEA analysis confirmed that expression of SmoM2 in human neurons negatively correlated with neuron chromatin accessible sites enriched at P14 and P60 (Figure S7H-I). Together, these results showed that we recapitulated the

chromatin accessibility pattern found in mouse cerebella in response to SmoM2, also in human neurons. Thereafter, we investigated the contribution of truncated BRPF1 to alter chromatin landscape. Differential analyses retrieved specific ATAC-seq regions enriched in BPRF1 TR and SmoM2+BRPF1 TR conditions (Figure 28 B-C), which showed a profile resembling accessible cis-regulatory elements, similar to the ones detected in the mouse models (Figure 28 D and figure S9J). GSEA analysis on the ATAC-seq signals showed that SmoM2 activation correlated with cerebellum development, SHH pathways and stem cell signatures, while we concurrently measured a decreased in chromatin accessibility on those regions associated with genes related to mature neuron functions (Figure 28 E). These analyses indicate that, independently from the genetic background, SmoM2 activation increased chromatin accessibility at stem/progenitor genes associated loci in neurons. Importantly, these features were further elicited by truncated BRPF1 (Figure S7K). Considering that cell fate specification and maintenance of cell identity are regulated by the activation of enhancers (also in human MB)(Lin et al., 2016), we asked whether the measured changes in chromatin accessibility were associated with enhancers modulation. By measuring the ATAC-seq tag density on annotated human enhancers (Shen, Shao, Liu, & Nestler, 2014), we determined that, while BRPF1 TR per se did not alter chromatin accessibility (Figure S7L), its co-expression with SmoM2 induced and increment of chromatin opening (Figure 28 F). Given the relative spread pattern of the retrieved ATAC-seq signal distribution on these enhancers (Figure 28 F), we asked whether the expression of SmoM2+BRPF1 TR could augment chromatin accessibility to lineage-specifying clustered enhancers, referred as super-enhancers (Loven et al., 2013). By clustering ATAC-seq peaks which reside in proximity in a given locus, we identified super-enhancers in all the analysed conditions (Figure 28 G and figure S7 M). Independently from the genetic background we noticed that the expression of BRPF1 TR increased the number of unique super-enhancers (Figure 28 G and figure S7 M). Of importance, in the SmoM2+BRPF1 TR neurons we defined 241 clusters of enhancers with an average size spanning over 33kb (Figure 28 G-H). By measuring the relative enrichment of ATAC-seq signal we depicted a clear increase of chromatin accessibility associated with the concomitant expression of SmoM2 and BRPF1 TR (Figure 28 H). Moreover, we found that the identified super-enhancers were linked to key genes involved in cerebellum development (GBX2, LMX1B) (Guo et al., 2007; Wassarman et al., 1997) and chromatin remodelling (KDM6B, KDM4B, KMT2C). Gene ontology analyses confirmed that the SmoM2+BRPF1 TR super-enhancers were specifically associated with chromatin-modifying enzymes, but also with base-excision repair, suggesting a possible involvement of DNA damage response (Figure 28 I and figure S7 N). Finally, to assess whether the identified cis-regulatory elements in neurons expressing SmoM2+BRPF1 TR resembled specific chromatin features of human SHH MB, we measured changes of chromatin accessibility on the previously annotated SHH MB enhancers (Lin et al., 2016). This analysis showed that BRPF1 TR expression induced an

increment of chromatin opening on SHH enhancers (Figure 28 J) and also on SHH associates super-enhancers (Figure 28 K). Of importance, the contribution of BRPF1 TR to increase chromatin accessibility was specifically dependent on SmoM2 activation, as the same changes were not detected in truncated BRPF1 alone (Figure S7O-P). Taken together these data showed that truncated BRPF1 cooperates with SmoM2 by promoting chromatin accessibility at clustered enhancers that are linked to genes involved in chromatin remodelling. ATAC-seq analysis was performed by Luca Fagnocchi and Alessio Zippo of the laboratory of chromatin biology & epigenetics.

Figure 28: Truncated Brpf1 potentiates the effect of SmoM2, by reprogramming the super-enhancers landscape. (A) Box plots showing the genomic distribution of ATAC-seq peaks, with respect to Transcription Start Sites (TSS), Transcription Termination Sites (TTS), 5'UTR, 3'UTR, exons, introns, intergenic regions and non-coding genes, in the indicated cell lines. **(B)** Venn diagram showing the overlap between ATAC-seq peaks in hSynI-creER+LSL-BRPF1 TR and hSynI-creER+LSL-SmoM2+LSL-BRPF1 TR cells. **(C)** Heatmap representing the normalized ATAC-seq signal (Z-score) on the

top 2000 most differentially enriched peaks in either hSynI-creER+LSL-BRPF1 TR or hSynI-creER+LSL-SmoM2+LSL-BRPF1 TR cells. **(D)** Average tag density plot of the normalized (RPM) ATAC-seq signal on the differential peaks, enriched either in hSynI-creER+LSL-BRPF1 TR (upper panel) or hSynI-creER+LSL-SmoM2+LSL-BRPF1 TR (lower panel) cells. **(E)** GSEA of indicated gene lists, in hSynI-creER+LSL-BRPF1 TR versus hSynI-creER+LSL-SmoM2+LSL-BRPF1 TR cells. All gene lists are enriched with a statistical p-value < 0.05. **(F)** Average tag density plot of the normalized (RPM) ATAC-seq signals in hSynI-creER+LSL-SmoM2 and hSynI-creER+LSL-SmoM2+LSL-BRPF1 TR cells, on annotated enhancer regions of human genome hg19/GRCh37. **(G)** Distribution of the ATAC-seq signal across hSynI-creER+LSL-SmoM2+LSL-BRPF1 TR enhancers, showing the presence of 241 super-enhancers. Representative super-enhancers are highlighted along with their associated genes. **(H)** Average tag density plot of the normalized (RPM) ATAC-seq signals in indicated cell lines, hSynI-creER+LSL-SmoM2+LSL-BRPF1 TR-specific super-enhancers. **(I)** Gene ontology analysis on the genes associated to hSynI-creER+LSL-SmoM2+LSL-BRPF1 TR-specific super-enhancers. Pathway from Reactome, Panther, WikiPathways and KEGG databases were analyzed. **(J-K)** Average tag density plot of the normalized (RPM) ATAC-seq signals in hSynI-creER+LSL-SmoM2 and hSynI-creER+LSL-SmoM2+LSL-BRPF1 TR cells, on previously reported enhancers **(J)** and super-enhancers **(K)**, which characterize the SHH MB. Analyses are performed on 2 biological replicates for each cell line.

5. Discussion

Cancer is viewed as an evolutionary conserved process that results from the accumulation of somatic mutations in the progeny of a normal cell and it is a common opinion that the cells of origin should possess a proliferative capacity (Blanpain, 2013; Visvader, 2011). Interestingly, few groups have attempted to induce cancer from neurons using full KO mice for cell cycle regulators or by genetic modification of mice and *Drosophila melanogaster,* although rare targeting of progenitors cannot be excluded (S. R. Alcantara Llaguno & Parada, 2016; Arlotta & Berninger, 2014). Notably, adult SHH MB arises when progenitors are not present anymore and for this reason postmitotic neurons could represent the cell of origin. In the present work, we showed that constitutive activation of Shh pathway induced by SmoM2 mutation, specifically in mouse cerebellar granule neurons, promotes the expression of progenitor and proliferation markers, enabling postmitotic neurons to re-enter in the cell cycle and give rise to Shh MB.

5.1 SmoM2 over-expression in cerebellar granule neurons promotes neurons dedifferentiation and Shh MB *in vivo*

The model system adopted exploits the Gabra6 promoter, that guides gene expression in mature neurons but not in progenitors. A time course analysis on Gabra6cre;LSL-tdTomato mice allowed to verify the reliability of the promoter. Gabra6 expression, distinguished by the expression of the reporter (tdTomato positive cells), never co-localized with all the proliferation/stemness markers used (PCNA, pH3, Sox2, Sox9, Math1), suggesting that all recombinant cells are mature neurons. The time course analysis indicates Gabra6 to be a suitable promoter to show that upon Shh pathway activation (SmoM2 expression), postmitotic granule neurons can be reprogrammed into cancer cells that express stem cells markers (Sox2, Sox9) and originate medulloblastoma. Interestingly, Gabra6-cre;LSL-tdTomato mice showed the presence of recombinant cells in several other brain regions, such as the occipital cortex, the hypothalamus, the frontal cortex and the hippocampus, as it was reported previously by Aller et al in 2003. However, all Gabra6-Cre;LSL-SmoM2 mice developed tumors only in cerebellum, suggesting that the oncogenic effect of Smo constitutive activation requires a cerebellar granule lineage identity. A tumorigenesis time course by staining (E16.5, P7, P14, P21, P28) Gabra6-cre;LSL-SmoM2 mice showed that the tumor does not simply surround the cerebellum, but spreads through the molecular layer, going inside the IGL, generally populated by postmitotic cells. This led to speculate that it might arise from the IGL and that granule neurons could be the tumor-initiating cells. The process of dedifferentiation was analyzed when the tumor was not yet present. Indeed at P14, neurons positive for NeuN were found co-expressing the proliferation markers PCNA and Sox9, suggesting that those cells were

starting to dedifferentiate, eventually developing in cancer cells. Notably, the deletion of oncosuppressor gene *Ptch1* in granule neurons was not able to recapitulate Shh MB development, as observed with the overexpression of SmoM2. Indeed, *Gli1* and *Math1* (a well-known marker for granule neuron progenitors) expression levels are higher in Gabra6-cre;LSL-SmoM2 compared to Gabra6-cre;Ptch1$^{flox/flox}$ mice cerebella. These data suggest that SmoM2 overexpression induces a much stronger activation of Shh signaling as compared to *Ptch1* loss and could explain the presence of Shh MB in Gabra6-cre;LSL-SmoM2 and its absence in Gabra6-cre;Ptch1$^{flox/flox}$ mice.

The lower induction of Shh signalling in *Ptch1* deletion suggests that other mutational hits could be required. In line with our observation, it has been recently found that tumor suppressors deletion in neurons (cerebral cortex) leads to extended cell division but no glioma formation (S. Alcantara Llaguno et al., 2019).

5.2 SmoM2 and mutant BRPF1 cooperation mimics human adult SHH MB

The exploitation of already published data of human SHH MB exome sequencing revealed that several adult SHH MB patients present truncated mutations of the chromatin reader BRPF1, that are often associated with SMO mutations and absent in paediatric and adolescent patients (Kool et al., 2014). To mimic the mutational background of a subset of human patients, a truncated form of BRPF1 was overexpressed together with SmoM2, exploiting the neuronal promoters NeuroD1 and hSynI. Truncated BRPF1 and SmoM2 co-overexpression led to neuronal dedifferentiation and Shh MB in adult mice. Our data show that a second mutational hit is essential to faithfully recapitulate the adult condition, because constitutive activation of Shh pathway alone rarely induced MB, while, the co-overexpression of SmoM2 and truncated BRPF1 in adult mice is able to promote adult Shh MB development. Notably, transcriptome data obtained through Affymetrix microarrays on our samples, allowed to associate "cerebellar granule progenitors-derived MB" with the human infant form while "truncated BRPF1-induced tumors" clustered with human adult SHH MB. Nowadays, the best MB diagnosis is verified using a molecular classification approach based on DNA methylation arrays (Hovestadt et al., 2014; Hovestadt et al., 2013). Unfortunately, human and mouse MB comparison result impossible at the moment due to the absence of human CpG islands from the homologous mouse genes (Antequera & Bird, 1993), resulting in a huge limitation for MB mouse modelling. Indeed, in literature, current molecular characterization of murine Shh MB cannot distinguish between adult and infant forms, in particular, all murine Shh MB are similar to human adult MB (Poschl et al., 2014). However, our molecular investigation, based on the genes reported in Al-Halabi et al. as differentially expressed in human adult versus human infant SHH MB allowed to discriminate the murine adult and pediatric forms. Anyhow, microarray analysis cannot provide a deep

investigation of the transcriptome and RNA-Seq analysis is required to elucidate intrinsic feature of the "truncated BRPF1-induced tumors" . Indeed, unlike arrays, RNA-Seq can detect SNPs and small indels as well as gene fusions and novel transcripts (Z. Wang, Gerstein, & Snyder, 2009; Wilhelm & Landry, 2009).

Moreover, "truncated BRPF1-induced tumors" are positive for both p-AKT and p-S6, while "cerebellar granule progenitors-derived MB" present only p-S6. These two markers have already been shown to be present only in human adult SHH MB while few human infant SHH MB are positive for either p-AKT or p-S6 and always in a mutually exclusive way (Kool et al., 2014). These data further confirm that our mouse model, based on the co-overexpression of SmoM2 and truncated BRPF1 resemble human adult SHH MB. Although the expression of human Synapsin I and NeuroD1 has been reported only in post-mitotic neurons in the adult brain (Kugler et al., 2003; Schwab et al., 1998), and the activity of hSynI and NeuroD1 promoters for their specific expression in postmitotic neurons was verified by excluding their co-expression with several proliferation markers, the above described experiments cannot certainly exclude the potential promoters leakiness or their expression in other cerebellar postmitotic cells. Indeed, human Synapsin I is not specific for cerebellar granule neurons, but can also target GABAergic interneurons (Kuhn, Ozden, Lampi, Hasan, & Wang, 2012), not excluding their contribution in tumor progression. Furthermore, unlike hSynI and NeuroD1, "Gabra6 induced-tumor" only requires the Smo constitutive activation, as a single mutational hit, to give rise to the tumor. The difference in "Gabra6 induced-tumor" and the "truncated BRPF1-induced tumors" lead us to speculate that different maturity of post-mitotic cells, can make the neurons more prone to dedifferentiate. Therefore, single cell analysis on recombinant cells of Gabra6cre transgenic mice (Gabra6cre;LSL-SmoM2;LSL-tdTomato) and on "truncated BRPF1-induced tumors" at early stages of tumorigenesis, would potentially elucidate the contribution of the different cell populations.

Furthermore, the role of BRPF1 in neuron dedifferentiation process has been verified by performing an *ex vivo* cerebellar assay. This has been useful to demonstrate that BRPF1 alteration can promote neuronal dedifferentiation and increase the number of cancer cell of origin for SHH MB. In addition, it allowed to prove its putative role as an oncosuppressor, even though the precise molecular mechanisms still need to be investigated and clarified.

5.3 SmoM2 activation alone or in cooperation with truncated BRPF1 overexpression determine chromatin changes of granule neurons

To define the contribution of chromatin changes in granule neurons dedifferentiation in response to SmoM2 activation and truncated BRPF1 overexpression, ATAC-seq analysis was profiled both in mouse tissue samples and in human neurons. ATAC-seq was used to unveil cis-regulatory

elements and their relative changes in response to SmoM2 and BRPF1 TR expression. Starting from the mouse model, we profiled chromatin accessibility by ATAC-seq on four cerebella samples retrieved from Gabra6-cre;LSL-SmoM2 and the control Gabra6-cre, respectively. The comparative analyses showed that ATAC-seq on cerebella tissues retrieved cis-regulatory elements that were enriched at TSS, introns and intergenic regions, as expected. The same distribution pattern was retrieved in both conditions, thereby permitting to define specific enriched regions. The distribution of ATAC-seq taq density showed enrichment at cis-regulatory elements which have been characterized for the presence of transcription factor binding motifs and the associated genes. We identified in Gabra6-cre;LSL-SmoM2 mice specific sites of increased chromatin accessibility, which are associated with neural precursor and stem cell states. These results support the phenotypic characterization of the MB models used in this study, providing further explanation on the possible role of SmoM2 activation in favouring dedifferentiation of granule neurons. We further investigated the role of truncated BRPF1 and its cooperativity with SmoM2 activation in driving chromatin accessibility. Since we could not perform the same analyses using mouse models (due to the few cells transfected *in vivo*), we adopted a system in which we fully differentiated the human AF22 neuroepithelial-like stem cells into post-mitotic neurons. We recapitulated the *in vivo* experimental conditions by nucleofecting plasmids in different combinations, to retrieve the role of BRPF1 in altering chromatin accessibility, in presence or absence of SmoM2 activation. We found that BRPF1 expression reinforced the SmoM2-associated chromatin pattern, favouring an increase of chromatin accessibility at *cis*-regulatory elements associated with stem cell pathways. Moreover, we found that truncated BPRF1 specifically favours the activation of enhancers and super-enhancers (with SmoM2). By assessing the linked genes, we showed that BPRF1 could support neural dedifferentiation by facilitating the reactivation of developmental TFs such as GBX2, LMX1B and also by deregulating chromatin modifying enzymes such as KMT6B (Jmjd3), which collaborate with SHH signalling to regulate gene activation both during development and in medulloblastoma (Guo et al., 2007; Wassarman et al., 1997). Overall, the performed experiments demonstrated the role of truncated BRPF1 in altering the chromatin landscape of cis-regulatory elements. Although we did not define the direct molecular mechanism through which truncated BRPF1 impinges on chromatin accessibility, our data highlighted its contribution in activating a specific subset of super-enhancers linked to chromatin modifiers and DNA damage genes. We believe that these findings could open new roads towards understanding the link between chromatin reshaping and cell dedifferentiation occurring in human patients, that could eventually lead to tumor formation.

6. Future perspectives

Our new mouse model for adult SHH MB can be considered as a significant breakthrough for cancer development theory. Indeed, it has been shown that, upon the right mutational hits, granule neurons can undergo a dedifferentiation process, unveiling for the first time BRPF1's key role in the pathogenesis of the adult SHH MB. However, the timing of BRPF1 mutation and the precise molecular mechanisms are missing points that we aim to clarify in the future, in order to have a deeper knowledge on adult SHH MB onset and possibly, put the basis for new therapeutic strategies. On this context, few alternatives could explain how mutations on BRPF1 can lead to tumorigenesis. One possibility is that BRPF1 mutations are acquired during neuronal development, but their effects would emerge only when the maturation process ends, uncovering a possible function in the maintenance of mature neurons identity; alternatively, BRPF1 could be a putative master regulator in SHH MB onset, showing that mutated BRPF1 alone during neuronal maturation could be sufficient to promote SHH MB. Indeed, mutated BRPF1 function has never been tested in granule neuron progenitors and whole genome sequencing of human patients showed 2 out of 10 adult SHH MB patients displaying mutation in BRPF1 protein but not in the main SHH pathway regulator genes (*PTCH1* or *SMO*) (Kool et al., 2014). Since little is known about BRPF1, the use of cerebellar organoids could be a new and effective way to investigate its function and model the dedifferentiation process. As stated by Lancaster and Knoblich in 2014: "a 3D organotypic culture, also called organoid, is a collection of organ-specific cell types that develops from stem cells or organ progenitors and self-organize through cell-sorting and spatially restricted lineage commitment in a manner similar to the *in vivo* counterpart" (Lancaster & Knoblich, 2014). Organoids have a relevant application also in cancer research, as they combine the possibility to study tumorigenesis and at the same time, to easily screen for new therapeutic drugs. Moreover, Ballabio et al., 2020 have already demonstrated that organoids represent a reliable tool to model MB (Ballabio et al., 2020) ; therefore, this method could be applied to investigate more closely the role of BRPF1, thereby cutting the distance between research and human patients. Indeed, a new diagnostic approach based on the analysis of the tumor methylation profile has been recently developed. DNA methylation changes in the process of tumor formation reflect features of tumorigenesis and the analysis of these epigenetic changes provide a safer diagnosis and classification of the tumor (Hovestadt et al., 2014). Unfortunately, sequence comparison showed that more than 20% of human CpG islands are absent from the homologous mouse genes and their comparison result at the moment impossible (Antequera & Bird, 1993). For this reason, organoids would be used to recapitulate the *in vivo* condition and, subsequently, injected in nude mice (Foxn1nu). DNA methylation profile from organoids-derived

tumors would be compared with SHH patients with the aim to define the first effective human adult SHH MB 3D *in vitro* model. Furthermore, the ease of handling and the higher percentage of cell transfection compared to mouse cerebellum would facilitate to discover and investigate the physiological molecular role of BRPF1 and its involvement in the dedifferentiation process and cancer development. Live imaging on single transfected neurons will be performed to follow the dedifferentiation process from the early steps in order to verify even the small morphological changes of the transforming cells (such as decrease in the number of dendrites and axonal branching or loss of growth cones). Moreover, molecular analysis on transfected neurons would be also performed at different timepoints and their sorting and subsequent single cell analysis could clarify the putative genes involved in neurons dedifferentiation process. Furthermore, ChIP-seq analysis on full-length and truncated BRPF1 will allow to clarify the still unknown binding sites and, eventually, the alterations in a mutated condition. Analysis will be performed only in transfected and sorted organoids cells, thus avoiding the noise due to non-transfected cells. ChIP-seq analysis, but also the already published ATAC-seq data, will provide a list of putative genes involved in the tumor formation process. By interpolating ChIP-seq and ATAC-seq data with each other, and with the already published human RNA-seq data, it will be possible both to determine new BRPF1 targets and new candidate tumor-involved genes. Indeed, performing a cut-off of these genes based on human RNA-seq data, will clarify their involvement in adult tumorigenesis, thus maintaining a strong connection with human patients. Validation of those putative targets will be achieved in organoids; indeed, gain of function or loss of function of selected genes should hind tumor formation, rescuing the carcinogenic phenotype. All these experiments are aimed at discovering key genes for tumor development, therefore finalizing research for a therapeutic purpose. Organoids can be used as an effective tool for drug screening and targeted therapy. Finally, adult SHH MB differs from the infant subgroup based on the enrichment of genetic mutations in chromatin modifiers and/or transcription regulators such as BRPF1, KIAA0182, TCF4, CREBBP, NEB, LRP1B, PIK3CA, FBXW7, KDM3B, XPO1, PRKAR1A, and PDE4D. However, only the tumorigenic role of BRPF1 has been explored, even if there are other regulators, such as DDX3X or KDM3B, strongly mutated in adult subgroup compared to the infant one (Figure 13 D) (Kool et al., 2014). Using the same BRPF1 project experimental setup for those genes could clarify their involvement in adult SHH MB; conversely, it could increase the importance of the BRPF1 model, indicating it as the only model that recapitulates the same conditions as the adult human patient.

7. Material and methods

7.1 Key resources table

REAGENT or RESOURCE	SOURCE	IDENTIFIER
Antibodies		
Anti-NeuN (1:2000)	Millipore	Cat# ABN78, RRID:AB_10807945
Anti-PCNA (1:2000)	Millipore	Cat# MAB424, RRID:AB_95106
Anti-Sox9 (1:2000)	Millipore	Cat# AB5535, RRID:AB_2239761
Anti-Sox2 (1:500)	Abcam	Cat# ab97959, RRID:AB_2341193
Anti-posphoH3 (1:500)	Abcam	Cat# ab97959, RRID:AB_2341193
Anti-Green Fluorescent Protein (1:200)	Thermo Fisher Scientific	Cat# A-11122, RRID:AB_221569
Anti-Doublecortin (1:500)	Millipore	Cat# AB2253, RRID:AB_1586992
Anti-Brpf1 (1:500)	Thermo Fisher Scientific	Cat# PA5-27783, RRID:AB_2545259
Anti-DYKDDDDK Tag (1:500)	Thermo Fisher Scientific	Cat# PA1-984B, RRID:AB_347227
Anti-Neuro D (A-10) (1:100)	Santa Cruz Biotechnology	Cat# sc-46684, RRID:AB_671759
Anti-Phospho-S6 Ribosomal Protein Ser235/236 (1:100)	Cell Signaling Technology	Cat# 2211, RRID:AB_331679
Anti-Phospho-Akt Ser473 (1:100).	Cell Signaling Technology	Cat# 4058, RRID:AB_331168
Alexa Fluor 488 goat anti-mouse (1:500)	Thermo Fisher Scientific	Cat# A28175, RRID:AB_2536161
Alexa Fluor 546 goat anti-rabbit (1:500)	Thermo Fisher Scientific	Cat# A-11010, RRID:AB_2534077
Alexa Fluor 647 goat anti-rabbit (1:500)	SouthernBiotech	Cat# 4030-31, RRID:AB_2795939

Alexa Fluor 488 goat anti-rabbit (1:500)	Thermo Fisher Scientific	Cat# A-11008, RRID:AB_143165
Alexa Fluor 488 goat anti-rat (1:500)	Thermo Fisher Scientific	Cat# A-11006, RRID:AB_2534074
Mouse IgG-heavy and light chain Biotinylated (1:250)	Bethyl	Cat# A90-116B, RRID:AB_309457
Anti-Synaptophysin - Clone 27G12	Leica Biosystems	Cat# NCL-L-SYNAP-299, RRID:AB_564017
Anti-Glial Fibrillary Acidic Protein (GFAP) - Clone GA5	Leica Biosystems	Cat# NCL-GFAP-GA5, RRID:AB_563739
Mouse Anti-Catenin, beta - Clone 14/Beta-Catenin	BD Transduction Laboratories	Cat# 610154, RRID:AB_397555
Anti-YAP1 (63.7)	Santa Cruz Biotechnology	Cat# sc-101199, RRID:AB_1131430
Anti-GAB1	Abcam	Cat# ab59362, RRID:AB_941700
Bacterial and Virus Strains		
10-beta Competent E. coli (High Efficiency)	NEB	Cat# C3019H
One Shot Stbl3 Chemically Competent E. coli	Invitrogen	Cat# C737303
Biological Samples		
Human adult SHH MB (nodular/desmoplastic) brain section from a 44-year-old female patient	Dr. Felice Giangaspero (University Sapienza of Rome)	N/A
Human adult SHH MB (nodular/desmoplastic) brain section from a 40-year-old male patient	Dr. Felice Giangaspero (University Sapienza of Rome)	N/A
Chemicals, Peptides, and Recombinant Proteins		
Poly-D-lysine	Sigma-Aldrich	Cat# P0899-50MG
Neurobasal medium	Thermo Fisher Scientific	Cat# 21103-049
Fetal Bovine Serum	Thermo Fisher Scientific	Cat# 10270106
D-(+)-Glucose	Sigma-Aldrich	Cat# G5767

Penicillin-Streptomycin (10,000 U/mL)	Thermo Fisher Scientific	Cat# 15140122
L-glutamine	Gibco 100x	Cat# 25030081
Paraformaldehyde	Acros Organics	Cat#AC169650010
DMEM/F12	Thermo Fisher Scientific	Cat# 31330038
N-2 Supplement (100X)	Thermo Fisher Scientific	Cat# 17502048
B-27™ Supplement (50X), serum free	Thermo Fisher Scientific	Cat# 17504044
EGF Recombinant Human Protein	Thermo Fisher Scientific	Cat# PHG0313
FGF2-Basic Recombinant Human Protein	Thermo Fisher Scientific	Cat# PHG0264
8-Bromo-cAMP	Santa cruz	Cat# Sc-201564a
4-Hydroxytamoxifen	Sigma-Aldrich	Cat# H7904
Tamoxifen, 98% (50 mg/Kg)	Alfa Aesar	Cat# J63509
NucleoBond® Xtra Midi kits	Macherey-Nagel	Cat# 740410.50
NucleoSpin® Gel and PCR Clean-up	Macherey-Nagel	Cat# 740609.250
NucleoSpin® Plasmid (NoLid)	Macherey-Nagel	Cat# 740499.250
T4 DNA ligase (5 U/µL)	Thermo Fisher Scientific	Cat# EL0011
T4 DNA ligase Buffer (10X)	Thermo Fisher Scientific	Cat# B69
in vivo-jetPEI transfection reagent	Polyplus-transfection	Cat# 201-50G
Sucrose	Biosigma	Cat# S5016
bovine serum albumin (BSA)	SEQENS IVD / H2B	Cat# 1000-70
TritonX-100	Sigma-Aldrich	Cat# T8787
Normal Goat Serum	Sigma-Aldrich	Cat# S26
Hoechst	Abcam	Cat# 33258
Vectastain Elite ABC Kit Standard	Vector Labs	Cat# PK-6100
DAB Peroxidase Substrate Kit	Vector Labs	Cat# SK-4100
Hematoxylin	Abcam	Cat# ab220365
TRIzol™ Reagent	Invitrogen	Cat# 15596018
iScript cDNA synthesis kit	Biorad	Cat# 1708891

Power SYBR™ Green PCR Master Mix	Thermo Fisher Scientific	Cat# 4367659
OptiPrep™ Density Gradient Medium (60% Iodixanol)	Sigma-Aldrich	Cat# D1556
Tween-20	Sigma-Aldrich	Cat# P9416
IGEPAL® CA-630	Sigma-Aldrich	Cat# I3021
Digitonin	Promega	Cat# G9441
2x TD reaction buffer from Nextera kit	Illumina	Cat# FC-121-1030
Nextera Tn5 Transposase	Illumina	Cat# FC-121-1030
MinElute PCR Purification Kit	Qiagen	Cat# 28004
Next High-Fidelity 2× PCR Master Mix	NEB	Cat# M0541L
Critical Commercial Assays		
Click-iT™ EdU imaging kit	Invitrogen	Cat# C10632
Deposited Data		
Raw and analyzed data (ATAC-seq)	This paper	GEO: GSE127733
Experimental Models: Cell Lines		
Primary *ex-vivo* cerebellar cell culture from P7 mice	This paper	N/A
Human AF22 neuroepithelial-like stem cells	(Falk et al., 2012)	N/A
Experimental Models: Organisms/Strains		
M. musculus: Rosa26-LSL-SmoM2-EYFP	The Jackson Laboratory	Cat# JAX:005130, RRID:IMSR_JAX:005130
M. Musculus: Rosa26-LSL-tdTomato	The Jackson Laboratory	Cat# JAX:007908, RRID:IMSR_JAX:007908
M. musculus: Ptch1 flox/flox	The Jackson Laboratory	Cat# JAX:012457, RRID:IMSR_JAX:012457
M. musculus: Math1-creER	The Jackson Laboratory	Cat# JAX:007684, RRID:IMSR_JAX:007684
M. musculus: Sox9 flox/flox	The Jackson Laboratory	Cat# JAX:013106, RRID:IMSR_JAX:013106

M. musculus: Math1-GFP	The Jackson Laboratory	Cat# JAX:013593, RRID:IMSR_JAX:013593
M. musculus: Etv1-creER	The Jackson Laboratory	Cat# JAX:013048, RRID:IMSR_JAX:013048
M. musculus: Foxn1 nude mice	The Jackson Laboratory	Cat# JAX:002019, RRID:IMSR_JAX:002019
M. musculus: Gabra6-cre	Dr. William Wisden (Imperial College London)	N/A
Oligonucleotides		
PCR primers and shRNA target sequences are in Table S2	N/A	N/A
Recombinant DNA		
pNeuroD1-IRES-GFP	(Guerrier et al., 2009)	RRID:Addgene_61403
pNeuroD1-cre-IRES-GFP	This paper	N/A
pAAV-hsyn-flex-dsRed-shvgat	(Yu et al., 2015)	RRID:Addgene_67845
pAAV-hSynI-cre	This paper	N/A
pPB CAG rtTA-IN	(Takashima et al., 2014)	RRID:Addgene_60612
pRCF-Brpf1	Dr. Jacques Côté (Laval University Cancer Research Center)	N/A
pPB-CAG-3xFlag-BRPF1-IRES-GFP	This paper	N/A
pPB-CAG-3xFlag-BRPF1-TR-IRES-GFP	This paper	N/A
pDZ264	(Larson, Zenklusen, Wu, Chao, & Singer, 2011)	RRID:Addgene_35193
pPB-CAG-LSL-MCS-IRES-GFP	This paper	N/A
pPB-CAG-LSL-tdTomato	This paper	N/A

pPB-CAG-LSL-BRPF1 TR-IRES-GFP	This paper	N/A
SmoM2 (W535L)-pcw107-V5	(Martz et al., 2014)	RRID:Addgene_64628
pPB-CAG-LSL-MCS-IRES-Venus	This paper	N/A
pPB-LSL-SmoM2-IRES-Venus	This paper	N/A
pR275 lenti-NeuroD1prom-CreERT2-WPRE	Dr. Franck Polleux (Columbia University)	N/A
pPB-hSynI-MCS-IRES-Venus	This paper	N/A
pPB-hSynI-creER-IRES-Venus	This paper	N/A
pCMVHahyPBase	(Yusa, Zhou, Li, Bradley, & Craig, 2011)	N/A
pCAG-GLI1	(Tiberi et al., 2014)	N/A
pSilencer2.1-CAG-Venus (pSCV2)	Dr. Franck Polleux (Columbia University)	N/A
pSCV2-sh1Gli1	This paper	N/A
pSCV2-sh1Gli2	This paper	N/A
pPB-CAG-Venus	This paper	N/A
pPB-CAG-MCS-IRES-GFP	This paper	N/A
Software and Algorithms		
ImageJ	NIH	https://imagej.nih.gov/ij/
Prism 6	GraphPad Software	https://www.graphpad.com/
Adobe Illustrator	Adobe	https://www.adobe.com/it/products/illustrator.html
Adobe Photoshop	Adobe	https://www.adobe.com/it/products/photoshop.html
FastQC	Brabaham Bioinformatics	https://www.bioinformatics.babraham.ac.uk/projects/fastqc/

Trimmomatic	(Bolger, Lohse, & Usadel, 2014)	N/A
Bowtie2	(Langmead & Salzberg, 2012)	N/A
SAMtools	(Li et al., 2009)	N/A
BEDtools version 2.24.0	(Quinlan & Hall, 2010)	https://bedtools.readthedocs.io/en/latest/
bedGraphToBigWig program	ENCODE	https://www.encodeproject.org/software/bedgraphtobigwig/
UCSC Genome Browser	N/A	http://genome.ucsc.edu/
HOMER software	(Heinz et al., 2010)	N/A
TM4 MeV v4.9 software	MeV	http://mev.tm4.org/
BoxPlotR	N/A	http://shiny.chemgrid.org/boxplotr/
ngsplot 2.47	(Shen et al., 2014)	N/A
Enrichr	(Chen et al., 2013; Kuleshov et al., 2016)	N/A
GREAT	(McLean et al., 2010)	N/A
Gene set enrichment analysis (GSEA)	(Subramanian et al., 2005)	N/A
Rank Ordering Of Super-Enhancers (ROSE) tool	(Loven et al., 2013; Whyte et al., 2013)	N/A
AffyQC module tool	(Eijssen et al., 2013)	N/A
affy package	(Gautier, Cope, Bolstad, & Irizarry, 2004)	N/A
BrainArray custom CDF (mouse4302mmengcdf version 22)	(Dai et al., 2005)	N/A
rma normalization method	(Irizarry et al., 2003)	N/A

org.Mm.eg.db	Bioconductor	https://bioconductor.org/packages/release/data/annotation/html/org.Mm.eg.db.html./
limma package	(Ritchie et al., 2015)	N/A
Database for Annotation, Visualization and Integrated Discovery (DAVID) Bioinformatics Resources v6.8	(Huang da, Sherman, & Lempicki, 2009)	N/A
fgsea package (GSEA)	(Subramanian et al., 2005) (Sergushichev, 2016)	N/A
KEGG Pathways dataset (mouse profile, accessed in January 2018)	N/A	https://www.genome.jp/kegg/
Gene Set Knowledgebase (GSKB)	Bioconductor	http://ge-lab.org/gskb
COMBAT normalization (inSilicoMerging package)	COMBAT	N/A
Gene Expression Omnibus (GEO)	NCBI	https://www.ncbi.nlm.nih.gov/geo/
Custom CDF (HuGene11stv1_Hs_ENTREZID, ver 22)	BrainArray	http://brainarray.mbni.med.umich.edu/Brainarray/Database/CustomCDF/CDF_download.asp
org.Hs.eg.db	Bioconductor	N/A
Ensembl database (accessed in January 2018)	N/A	https://www.ensembl.org/index.html
mouse4302.db	Bioconductor	N/A
hugene11sttranscriptcluster.db	Bioconductor	N/A
HOM_MouseHumanSequence.rpt	N/A	http://www.informatics.jax.org/
library(oligo)	Bioconductor	N/A
library(pd.mouse430.2)	Bioconductor	N/A
library(mouse4302.db)	Bioconductor	N/A
library(genefilter)	Bioconductor	N/A
library(pd.hugene.1.1.st.v1)	Bioconductor	N/A

library(hugene11sttranscriptcluster.db)	Bioconductor	N/A
library(sva)	Bioconductor	N/A
library(data.table)	CRAN	N/A
library(factoextra)	CRAN	N/A
library(pheatmap)	CRAN	N/A

7.2 Experimental model and subject details

7.2.1 Mice

Rosa26-LSL-SmoM2 (#005130), Rosa26-LSL-tdTomato (#007908), Ptch1$^{flox/flox}$ (#012457), Math1-creER (#007684), Sox9 $^{flox/flox}$ (#013106), Math1-GFP (#013593), Etv1-creER (#013048), nude mice (#002019) were purchased from The Jackson Laboratory. Males and females Gabra6-cre;LSL-SmoM2 mice were analysed at E16.5, P7, P14, P21, P28, 3 months, > 5 months. Males and females Gabra6-cre;LSL-tdTomato mice were analysed at P0, P4, P7, P10, P14, P21. Males and females Gabra6-cre;Ptch1$^{flox/+}$ mice were analysed at 3 months and > 5 months whereas males and females Gabra6-cre;Ptch1$^{flox/flox}$ mice were analysed at P14, 3 months and > 5 months. Males and females Gabra6-cre;LSL-SmoM2;Sox9$^{flox/flox}$ mice were analysed at 4 weeks and 3 months. Males and females Gabra6-cre;LSL-tdTomato;Math1-GFP mice were analysed at P0 and P7. Males and females Math1creER;LSL-SmoM2 mice were injected with tamoxifen at P5 or P21 and then analysed at 1 months, 3 months and > 5 months. Males and females Math1creER;Ptch1$^{flox/+}$ mice were injected with tamoxifen at P5 and analysed at 4 months. Males and females Etv1-creER;LSL-SmoM2 mice were transfected with pPB-BRPF1 TR at P90 and then injected with tamoxifen. Those mice where analysed at 138 days post injection. Males and females LSL-SmoM2 mice were analysed at P14, P28, 3 months and >5 months. Males and females LSL-SmoM2 mice were transfected with pNeuroD1-cre, pNeuroD1-cre + BRPF1 TR or pNeuroD1-cre + BRPF1 WT, phSynI-cre or phSynI-cre + BRPF1 TR and analysed at 40, 60 and 100 days post injection. We thank Prof. William Wisden for providing us with Gabra6-cre mice. Mice were housed in a certified Animal Facility in accordance with European Guidelines. Mice were monitored daily for neurological symptoms of brain tumors: weight loss, hydrocephalus, kyphosis, altered gait, lethargy; and euthanized immediately when recommended by veterinary and biological services staff members. The experiments were approved by the Italian Ministry of Health as confirming to the relevant regulatory standards.

7.2.2 Human adult SHH medulloblastoma samples

Human adult medulloblastoma brain sections from a 44-year-old female patient and a 40-year-old male patient have been provided by prof. Giangaspero from Dept. of Radiologic, Oncologic and Anatomo Pathological Sciences, University Sapienza of Rome, Rome, Italy and IRCCS Neuromed , Pozzilli, Isernia, Italy.

7.2.3 Primary *ex vivo* cerebellar cell cultures

Cerebella were dissected from P7 LSL-SmoM2 mice (males and females) and cells were dissociated by pipetting in dissociation medium (81,8 mM Na2SO4, 30 mM K2SO4, 5,8 mM MgCl2, 0,25 mM CaCl2, 1 mM Hepes pH 7,4, 20 mM Glucose, 0,2 mM NaOH). Cells were nucleofected with 10 µg of total DNA in 100 µl of nucleofection buffer (5mM KCl, 15mM MgCl2, 10 mM Glucose, 120 mM K2HPO4/KH2PO4, pH7.2), using the A-033 program and a Nucleofector 2b Device (Amaxa). For the nucleofection ten different combinations of plasmids were used.

Combination 1: pPB CAG-IRES-GFP, pPB CAG-Venus, pPBase;

Combination 2: pPB CAG-BRPF1 WT-IRES-GFP, pPB CAG-Venus, pPBase;

Combination 3: pPB CAG-BRPF1 TR-IRES-GFP, pPB CAG-Venus, pPBase;

Combination 4: phSynI-cre, pPB CAG-IRES-GFP, pPB CAG-Venus, pPBase;

Combination 5: phSynI-cre, pPB CAG-BRPF1 WT-IRES-GFP, pPB CAG-Venus, pPBase;

Combination 6: phSynI-cre, pPB CAG-BRPF1 TR-IRES-GFP, pPB CAG-Venus, pPBase;

Combination 7: phSynI-cre, pCAG-GLI1, pPB CAG-IRES-GFP, pPB CAG-Venus, pPBase;

Combination 8: phSynI-cre, pPB CAG-BRPF1 WT-IRES-GFP, pPB CAG-Venus, pCAG-GLI1, pPBase;

Combination 9: phSynI-cre, pPB CAG-IRES-GFP, pPB CAG-Venus, psh1-Gli1, psh1-Gli2, pPBase;

Combination 10: phSynI-cre, pPB CAG-BRPF1 TR-IRES-GFP, pPB CAG-Venus, psh1-Gli1, psh1-Gli2, pPBase.

Nucleofected cells were plated in poly-D-lysine coated 24-well plates (each cerebellum was used to fill 4 wells) and grown in Neurobasal medium supplemented with: 20% FBS, 3 mM KCl, 2,1 mg/ml glucose, penicillin/streptomycin and 2mM L-glutamine. Medium was partially changed every 3 days. Cells were fixed after 7 days of growth using PFA 4%.

7.2.4 AF22 cell cultures

Human iPSC-derived neuroepithelial-like stem cells AF22 at passage 30, were cultured in a 1:1 ratio mixture of Neurobasal and DMEM/F12 media supplemented with N2 (1:100), B27 (1 µl/ml), 10 ng/ml EGF and 10 ng/ml FGF2. 2x10^6 AF22 cells were nucleofected with 20 µg plasmid DNA in

200 μl nucleofection buffer using the T-020 program and a Nucleofector 2b device (Amaxa). AF22 cells were differentiated into neurons as previously described (Falk A et al, PLOS One, 2012). Briefly, neurons were induced culturing the cells for three weeks in a 1:1 ratio mixture of Neurobasal and DMEM/F12 media supplemented with N2 (1:100), B27 (1:50) and 300 ng/ml cAMP. After 19 days of differentiation, 500 ng/ml 4-Hydroxytamoxifen was added to the differentiation media. Two days later, neurons were collected for downstream analyses. Four nucleofection plasmid combination were tested.

Combination 1: pPB-hSynI-creER, pPB-CAG-LSL-tdTomato, pPBase;

Combination 2: pPB-hSynI-creER, pPB-CAG-LSL-tdTomato, pPB-LSL-SmoM2, pPBase;

Combination 3: pPB-hSynI-creER, pPB-CAG-LSL-tdTomato, pPB-LSL-BRPF1 TR, pPBase;

Combination 4: pPB-hSynI-creER, pPB-CAG-LSL-tdTomato, pPB-LSL-SmoM2, pPB-LSL-BRPF1 TR, pPBase.

7.3 Method details

7.3.1 Plasmids

The coding sequence of Cre recombinase was cloned into pNeuroD1-IRES-GFP creating pNeuroD1-cre-IRES-GFP. pNeuroD1-IRES-GFP is a gift from Franck Polleux (Guerrier et al., 2009) (Addgene plasmid # 61403). The coding sequence of cre recombinase was cloned into pAAV-hsyn-flex-dsRed-shvgat (Yu et al., 2015)(Addgene#67845), forming pAAV-hSynI-cre (phSynI-cre). The coding sequence of human BRPF1 was amplified by PCR from a plasmid of Dr. Jacques Côté (Laval University Cancer Research Center, Canada) and cloned into pPB CAG rtTA-IN (Takashima et al., 2014)(Addgene #60612), forming pPB-CAG-3xFlag-BRPF1-IRES-GFP (pPB-BRPF1 WT). Truncated human BRPF1 was amplified by PCR from WT 3xFlag-BRPF1 (1-574aa) and cloned into pPB-CAG rtTA-IN (Takashima et al., 2014)(Addgene #60612) forming pPB-CAG-3xFlag-BRPF1-TR-IRES-GFP (pPB-BRPF1 TR). The coding sequence of tdTomato was amplified by PCR from pDZ264 (Larson et al., 2011)(Addgene#35193) and cloned into pPB-CAG-LSL-MCS-IRES-GFP, forming pPB-CAG-LSL-tdTomato. Truncated human BRPF1 was amplified by PCR from pPB-CAG-3xFlag-Brpf1-TR-IRES-GFP and cloned into pPB-CAG-LSL-MCS-IRES-GFP, forming pPB-CAG-LSL-BRPF1 TR-IRES-GFP (pPB-LSL-BRPF1 TR). The coding sequence of human SmoM2 was amplified by PCR from SmoM2 (W535L)-pcw107-V5 (Martz et al., 2014)(Addgene#64628) and cloned into pPB-CAG-LSL-MCS-IRES-Venus, forming pPB-LSL-SmoM2-IRES-Venus (pPB-LSL-SmoM2). The coding sequence of creER^{T2} was cloned from pR275 lenti-NeuroD1prom-CreERT2-WPRE (gift from Franck Polleux) and cloned into pPB-hSynI-MCS-IRES-Venus, forming pPB-hSynI-creER-IRES-Venus (pPB-hSynI-creER). The plasmid encoding a hyperactive form of the piggyBac transposase, pCMVHahyPBase (PBase) was provided

from the Wellcome Sanger Institute, Cambridge UK. The plasmid encoding the overexpression of GLI1 transcription factor (pCAG-GLI1) was provided by Tiberi et al, 2014. Double-stranded oligonucleotides coding for mouse Gli1 shRNA (target sequence, 5'- TCGGAGTTCAGTCAAATTA -3') (Tiberi et al., 2014), mouse Gli2 shRNA (target sequence, 5'- AATGATGCCAACCAGAACAAG -3') (Tiberi et al., 2014) were cloned downstream of the U6 promoter into the pSilencer2.1-CAG-Venus (pSCV2) (gift from Franck Polleux) according to the pSilencer instructions from Ambion, forming pSCV2-sh1Gli1 and pSCV2-sh1Gli2. Venus was amplified from pSCV2, to generate pPB-CAG-Venus plasmid (pPB-Venus). The backbone pPB-CAG-MCS-IRES-GFP (pPB-GFP) was used as read-out of nucleofection efficiency in *ex vivo* cerebellar assay. All plasmid used for *in vivo* transfection, *ex vivo* nucleofection and AF22 cell culture; pNeuroD1-cre-IRES-GFP (pNeuroD1-cre), pAAV-hSynI-cre (phSynI-cre), pPB-CAG-3xFlag-Brpf1-IRES-GFP (pPB-BRPF1 WT), pPB-CAG-3xFlag-Brpf1-TR-IRES-GFP (pPB-BRPF1 TR), pPB-CAG-LSL-BRPF1-TR-IRES-GFP (pPB-LSL-BRPF1 TR), pPB-LSL-SmoM2-IRES-Venus (pPB-LSL-SmoM2), pPB-hSynI-creER-IRES-Venus (pPB-hSynI-creER), pPB-CAG-LSL-tdTomato, pPB-CAG-IRES-GFP (pPB-GFP), pPB-CAG-Venus (pPB-Venus), pCAG-GLI1, pSCV2-sh1Gli1 (psh1-Gli1), pSCV2-sh1GLI2 (psh2-Gli2), pCMV-HahyPBase (PBase) are purified using the NucleoBond® Xtra Midi kits (Macherey-Nagel).

7.3.2 *In vivo* transfection of granule neurons

A mix of plasmid DNA (0,5 µg/µl) and *in vivo*-jetPEI transfection reagent (Polyplus-transfection) was prepared according to the manufacturer's instructions. pPBase and piggyBac donor plasmids were mixed at a 1:4 ratio. P21-24 and 2, 3-month-old LSL-SmoM2 mice (males and females) were anaesthetised with 2% isoflurane and medially injected at -1.6 mm rostral to lambda, 0 mm midline, and 1 mm ventral to the skull surface, with 10 µl of DNA transfection reagent mix using a Syringe with a 30-gauge needle.

7.3.3 Transplantation of tumor cells in nude mice

Tumor of 4-month-old Gabra6-cre;LSL-SmoM2 mouse was single cell dissociated in trypsin and resuspended in Neurobasal medium at a concentration of $3,2x10^4$ cells/µl. For transplantation, 4-month- old nude mice (males and females) were anaesthetised with 2% isoflurane and medially injected at -1.6 mm rostral to lambda, 0 mm midline, and 1 mm ventral to the skull surface, with 10 µl of freshly isolated tumor cells using a 26s-gauge Hamilton syringe. The cells were injected slowly, and the incision was sutured with one or two drops of medical glue. Animals were monitored for 50 days post-transplantation; brains were fixed by perfusion with 4% paraformaldehyde and then appropriate cryoprotected in 30% sucrose (wt/vol, Merck).

7.3.4 Histopathological evaluation

Three Gabra6-cre;LSL-SmoM2 tumors were diagnosed by neuropathologists Francesca Gianno and Felice Giangaspero. In addition to standard hematoxylin and eosin staining, immunostaining was done on formalin-fixed paraffin-embedded tumors after dewaxing and rehydrating slides. Antigen retrieval was performed by incubating slices for 30 min in retrieval solution (10 mM Sodium Citrate, 0.5% Tween-20 (v/v), pH 6.0) at 98°C. Primary antibodies were incubated overnight at 4°C and secondary antibodies for 1 hour at room temperature in Antibody solution. ABC solution was used 2 hours at room temperature (Vectastain Elite ABC Kit Standard PK-6100). The sections were incubated with the substrate at room temperature until suitable staining was observed (DAB Peroxidase Substrate Kit, SK-4100). Nuclei were counterstained with Hematoxylin (Abcam, ab220365).

7.3.5 Immunofluorescence

E16.5, P0, P4, P7, P10, P14, P21, P28, 3, 4, 7-month-old mice (males and females) were perfused with 4% paraformaldehyde and then brains were cryoprotected in 30% sucrose (wt/vol, Merck). Immunofluorescence staining was performed on slides, 20/30-µm-thick cryosections. Blocking and Antibody solutions consisted of PBS supplemented with 3% goat serum, 0.3% Triton X-100 (Sigma). Primary antibodies were incubated overnight at 4 °C and secondary antibodies for 1 h at 15–25 °C. Nuclei were stained with bisbenzimide (Hoechst#33258, Sigma). Sections and coverslips were mounted with Permanent Mounting Medium (PMT030).

7.3.6 EdU staining

P19 Gabra6-cre;LSL-SmoM2 and Gabra6-cre;LSL-tdTomato mice (males and females) were i.p. injected with 50 mg/kg EdU and sacrificed at P21. EdU staining was conducted on brain slices, using Click-iT™ EdU imaging kit (Invitrogen, Carlsbad, CA), according to the manufacturer's protocol. This protocol was adapted for histological staining of brain tissue as follows. Slides containing mounted frozen brain sections were fixed with 4% paraformaldehyde in phosphate buffer saline (PBS) for 15 min. Fixation step is required to maintain previous staining since EdU labelling has to be performed later. Slides were washed with 3% bovine serum albumin (BSA) in PBS and then permeabilized with 0.5% TritonX-100 in PBS for 20 min. The sections were again washed with 3% BSA in PBS and then incubated with a Click-iT™ reaction cocktail containing PBS 1X, 4 mM CuSO4, Alexa Fluor® 488 Azide, and reaction buffer additive for 30 min, while protected

from light. The sections were washed once more with 3% BSA in PBS and the incubated with Hoechst (#33258) for DNA staining.

7.3.7 Imaging

Images were acquired with a Zeiss Axio Imager M2 (Axiocam MRc, Axiocam MRm), and Zeiss Axio Observer Z1 equipped with Colibri 1, ApoTome 1 and Cell Observer modules. Confocal imaging was performed with either Leica TCS Sp5 or NIKON Eclipse TI2 Spinning Disk confocal Imager optical. Images were processed using ImageJ software. Figures were prepared using Adobe Photoshop (Adobe).

7.3.8 Cell Quantification

For quantification of Sox9/Sox2/PCNA positive cells in 4-week-old Gabra6-cre;LSL-SmoM2 mice, we used at least three sections of each brain (three brains for each marker), quantified cells: 101 $Sox9^+$/Hoechst$^+$ cells within 2700 Hoechst positive cells, 119 $Sox2^+$/Hoechst$^+$ cells within 2700 Hoechst positive cells, 2672 $PCNA^+$/Hoechst$^+$ cells within 2700 Hoechst positive cells. For quantification of Edu and NeuN double positive cells, we used at least three sections in three different brains, quantified cells: 79 Edu^+/NeuN$^+$ cells within 900 Edu positive cells in Gabra6-cre;LSL-SmoM2 mice, 0 Edu^+/NeuN$^+$ cells within 477 Edu positive cells in Gabra6-cre;LSL-tdTomato mice. For quantification of Edu and tdTomato double positive cells, we used at least three sections in three different brains of Gabra6-cre;LSL-tdTomato, quantified cells: 0 Edu^+/tdTomato$^+$ cells within 368 Edu positive cells. For quantification of tdTomato and PCNA double positive cells we have used at least six sections of each brain (three brains for each timepoint), we quantified: P4=927 tomato positive cells, P7=9145 tomato positive cells, P10=42940 tomato positive cells, P14=106090 tomato positive cells. For quantification of tdTomato and pH3 double positive cells we have used at least six sections of each brain (three brains for each timepoint), we quantified: P4=4786 ph3 positive cells , P7=842 ph3 positive cells, P10=1676 ph3 positive cells, P14=350 ph3 positive cells. For quantification of tdTomato and Sox2 double positive cells we have used at least six sections of each brain (three brains for each timepoint), we quantified: P10=8905 sox2 positive cells, P14=8422 sox2 positive cells. For quantification of tdTomato and Sox9 double positive cells we have used at least six sections of each brain (three brains for each timepoint), we quantified: P10 =7953 sox9 positive cells, P14=8061 sox9 positive cells. To identify the tomato positive cells mice Rosa26-CAG-LSL-tdTomato without cre have been used to detect background levels. For quantification of tdTomato and GFP double positive cells in Gabra6-cre;Math1-GFP;LSL-tdTomato mice, we used at least three sections of each brain (three brains for each timepoint), quantified

cells: P0=0 GFP$^+$/tdTomato$^+$ cells within 41 tdTomato positive cells, P7=0 GFP$^+$/tdTomato$^+$ cells within 1805 tdTomato positive cells. For quantification of Sox9/Sox2/PCNA and GFP double positive cells in P21 Rosa26-CAG-LSL-SmoM2 mice transfected with pNeuroD1-cre-IRES-GFP at least three sections of each brain have been used (three brains for each marker), quantified cells: GFP$^+$/Sox9$^+$ = 0 cells, GFP$^+$/Sox9$^-$ = 1105 cells, GFP$^+$/Sox2$^+$ = 0 cells, GFP$^+$/Sox2$^-$ = 978 cells, GFP$^+$/PCNA$^+$ = 0 cells, GFP$^+$/PCNA$^-$ = 1182 cells. For quantification of Sox9/Sox2/PCNA/pH3 and tdTomato double positive cells in 2-month-old Rosa26-CAG-LSL-SmoM2 mice transfected with phSynI-cre and pPB-CAG-LSL-tdTomato at least three sections of each brain have been used (three brains for each marker), quantified cells: tdTomato$^+$/Sox9$^+$ = 0 cells, tdTomato$^+$/Sox9$^-$ = 2361 cells, tdTomato$^+$/Sox2$^+$ = 0 cells, tdTomato$^+$/Sox2$^-$ = 819 cells, tdTomato$^+$/PCNA$^+$ = 0 cells, tdTomato$^+$/PCNA$^-$ = 1139 cells, tdTomato$^+$/pH3$^+$ = 0 cells, tdTomato$^+$/pH3$^-$ = 2005 cells. For quantification of Sox9/Sox2/PCNA/pH3 and tdTomato double positive cells in 3-month-old Etv1cre-ER;LSL-SmoM2 mice transfected with pPB-CAG-LSL-tdTomato at least three sections of each brain have been used (three brains for each marker), quantified cells: tdTomato$^+$/Sox9$^+$ = 0 cells, tdTomato$^+$/Sox9$^-$ = 390 cells, tdTomato$^+$/Sox2$^+$ = 0 cells, tdTomato$^+$/Sox2$^-$ = 532 cells, tdTomato$^+$/PCNA$^+$ = 0 cells, tdTomato$^+$/PCNA$^-$ = 410 cells, tdTomato$^+$/pH3$^+$ = 0 cells, tdTomato$^+$/pH3$^-$ = 570 cells. For the quantification of the nucleofected *ex vivo* cerebellar cells, we quantified at least 300 cells GFP+NeuN+ cells for each condition from three biological repeats. The background levels of GFP/YFP have been detected in cerebellar cells nucleofected without plasmids.

7.3.9 RNA isolation and Real-Time PCR analysis

Total RNA from samples were isolated with TRIzol™ Reagent (Invitrogen) and reverse transcribed using iScript cDNA synthesis kit (Biorad) according to the manufacturer's instructions. Quantitative PCR was performed using Power SYBR™ Green PCR Master Mix (Applied Biosystems). Primer sequences used for real-time analysis are shown:

7.3.10 PCR primers and shRNA target sequences

Gene	Forward primer (5'-3')	Reverse primer (5'-3')
Mouse Math1	GAGTGGGCTGAGGTAAAAGAGT	GGTCGGTGCTATCCAGGAG
Mouse Sox9	GAGCCGGATCTGAAGAAGGA	GCTTGACGTGTGGCTTGTTC
Mouse Sox2	GAGTGGAAACTTTTGTCCGAGA	GAAGCGTGTACTTATCCTTCTTCAT
Mouse Ccnd1	GTTCATTTCCAACCCACCCTC	AGAAAGTGCGTTGTGCGGTAG
Mouse Gli1	CCAAGCCAACTTTATGTCAGGG	AGCCCGCTTCTTTGTTAATTTGA

Mouse Brpf1	CAGTAAGATCACCAACCGCC	GAGGAAAGGGGTCAGCTGCA
Mouse Gapdh	TGTGTCCGTCGTGGATCTGA	CCTGCTTCACCACCTTCTTGA
Human ZIC1	AAGATCCACAAAAGGACGCA	CACGTGCATGTGCTTCTTG
Human GLI1	ACCCCCTGGACTCTCTTGAT	GGAATTCTGTTTCCCCAGGT
Human GAPDH	CCACTCCTCCACCTTTGAC	ACCCTGTTGCTGTAGCCA

Gene (shRNA)	Target sequence (5'-3')
Mouse Gli1 shRNA	5'- TCGGAGTTCAGTCAAATTA -3'
Mouse Gli2 shRNA	5'- AATGATGCCAACCAGAACAAG -3'

Plasmid cloning primer	Primer (5'-3')
Forward Human SalI-3xFlag-BRPF1 TR	5'- CATCATGTCGACATGGACTACAAAGACCATGACGGTGATTATAAAGATCATGACAT CGATTACAAGGATGACGGGGTGGACTTTGATGTGAAGAC- 3'
Reverse Human BRPF1 TR-EcoRI	5'- CATCATGAATTCTCATCATCACCCAACTTGGTCACAGTTCCTCT- 3'

7.3.11 Survival analysis

Survival analysis was performed calculating the lifespan in days of every Rosa26-LSL-SmoM2, Gabra6-cre; Rosa26-LSL-SmoM2 and Rosa26-LSL-SmoM2 mouse transfected with each specific combination of plasmids. Kaplan-Meier survival curves (Figure 4D and 5F) do not take in consideration LSL-SmoM2 mice transfected with pNeuroD1-cre+BRPF1-TR (Figure 4C) and phSynI-cre+BRPF1-TR which were sacrificed at a fixed experimental endpoint. Mice died due to undetermined causes during the study were censored in the analysis.

7.4 ATAC-seq

7.4.1 ATAC-seq samples preparation

ATAC-seq analysis was performed by Luca Fagnocchi and Alessio Zippo of the laboratory of chromatin biology & epigenetics. We performed ATAC-seq on frozen cerebella from P14 Gabra6-cre;LSL-SmoM2 and control Gabra6-cre mice and on hSynI-creER+LSL-tdTomato, hSynI-creER+LSL-

BRPF1 TR, hSynI-creER+LSL-SmoM2 and hSynI-creER+LSL-SmoM2+LSL-BRPF1 TR nucleofected AF22 neuroephitilial-like stem cells, as previously described(Corces et al., 2017). Briefly, we first dounced frozen cerebella in 2 ml cold homogenization buffer (0.017 mM PMSF, 0.17 mM β-mercaptoethanol, 320 mM sucrose, 0.1 mM EDTA, 0.1% NP40, 5 mM CaCl2, 3 mM Mg(Ac)2, 10 mM Tris pH 7.8) and pelleted at 100 RCF for 1 min. We next isolated nuclei by transferring 400 ul of supernatant in a plastic tube and sequentially added 400 ul of 50% Iodixanol solution (homogenization buffer and 50% Iodixanol solution), 600 ul of 29% Iodixanol (homogenization buffer, 160 mM and 29% Iodixanol solution) and 600 ul of 35% Iodixanol solution (homogenization buffer, 160 mM and 35% Iodixanol solution) to the bottom of the tube, avoiding mixture of layers. At this point cell lines were also processed in order to isolate their nuclei. We centrifuged for 20 min at 3,000 RCF and we discarded upper layers of the gradient in order to collect 200 ul from the nuclei band. We counted nuclei and transferred 50.000 into a tube with 1 ml of ATAC-Resuspension Buffer (RSB) + 0.1% Tween-20 (10 mM Tris-HCl pH 7.4, 10 mM NaCl, 3 mM MgCl2, 0.1% Tween-20). We pelleted nuclei by centrifuging for 10 minutes at 500 RCF and resuspended in 50 ul cold ATAC-RSB containing 0.1% NP40, 0.1% Tween-20, and 0.01% Digitonin,. We lysed for 3 minutes on ice and washed with 1 ml of cold ATAC-RSB + 0.1% Tween-20. We then transposed the samples by resuspending in 50 ul of transposition mix (25 ul 2x TD buffer, 100nM transposase, 16.5 ul PBS, 0.5 ul 1% digitonin, 0.5 ul 10% Tween-20, 5 ul H2O) and incubated at 37°C for 30 minutes. We purified the transposed DNA using the Qiagen MinElute PCR Purification Kit (cat. # 28004) and eluted in 10 μl elution buffer. Next we amplified the transposed DNA fragments in the PCR mix (10 μl transposed DNA, 10 μl nuclease-free H2O, 2.5 μl 25 μM PCR Primer 1, 2.5 μl 25 μM Barcoded PCR Primer 2 and 25 μl NEB Next High-Fidelity 2× PCR Master Mix cat. # M0541L). The final ATAC-seq libraries were purified using the Qiagen MinElute PCR Purification Kit, quantified at the Qubit Fluorometer (Invitrogen, cat. #Q33226) and quality controlled with the High Sensitivity DNA Assay at the 2100 Bioanalyzer (Agilent, cat. # G2939BA). Four and three independent biological replicates, sequenced as independent libraries, were performed for Gabra6-cre;LSL-SmoM2 and control Gabra6-cre, respectively. Two independent biological replicates, sequenced as independent libraries, were performed for hSynI-creER+LSL-tdTomato, hSynI-creER+LSL-BRPF1 TR, hSynI-creER+LSL-SmoM2 and hSynI-creER+LSL-SmoM2+LSL-BRPF1 TR cell lines. All libraries were sequenced as single reads of 50 bp with the Illumina HiSeq2500.

7.4.2 ATAC-seq data processing

Sequenced reads from all independent sequenced libraries were quality assessed by using fastQC (https://www.bioinformatics.babraham.ac.uk/projects/fastqc/) and trimmed with Trimmomatic(Bolger et al., 2014). Reads from biological replicates were merged for all analysis,

unless differentially stated in figure legends. Total reads were aligned to either the mouse genome NCBI37/mm9 or the human genome GRCh37/hg19 using Bowtie2(Langmead and Salzberg, 2012), using the parameters '--very-sensitive -k 1', thus discarding ambiguous reads mapping at multiple sites. Duplicated reads and reads mapping on mitochondrial DNA were discarded for further analysis with SAMtools(Li et al., 2009). Normalized BigWig tracks of ATAC-seq signals were generated with BEDtools 2.24.0 (https://bedtools.readthedocs.io/en/latest/)(Quinlan and Hall, 2010) and the bedGraphToBigWig program (https://www.encodeproject.org/software/bedgraphtobigwig/) and visualized on the UCSC Genome Browser (http://genome.ucsc.edu/). The HOMER software(Heinz et al., 2010) was further used to analyze ATAC-seq data. The command 'findPeaks' was used for peak calling with these parameters '-size 150 -minDist 1000'; the command 'get-DifferentialPeaks' was used to find peaks with differential ATAC-seq signals between two conditions ('-F 2 -P 0.001'); the command 'findMotifsGenome.pl' was used for motifs enrichment analysis; the command 'annotatePeaks.pl' was used to annotate peaks to related genes and genomic regions and to count the number of normalized reads on specific regions. Tag counts were then used to produce heatmaps with TM4 MeV v4.9 software (http://mev.tm4.org/) and boxplots with with BoxPlotR (http://shiny.chemgrid.org/boxplotr/). Average tag density plot of the normalized (RPM) ATAC-seq signals were generated with the ngsplot 2.47(Shen et al., 2014) command ngs.plot.r and plotted with GraphPad Prism (GraphPad Software, San Diego, California, USA, www.graphpad.com). Annotated genes were checked for biological processes and pathways enrichment using both Enrichr(Chen et al., 2013; Kuleshov et al., 2016) and GREAT(Mclean et al., 2010). Gene set enrichment analysis was performed with GSEA(Subramanian et al., 2005) on publicly available gene sets. Super-enhancers were called with the Rank Ordering Of Super-Enhancers (ROSE) tool(Lovén et al., 2013; Whyte et al., 2013), using the ATAC-seq signal and with default parameters.

7.5 Microarray analysis

Bioinformatics analyses were performed by Silvano Piazza of the bioinformatics core facility and by Alessandro Romanel of the laboratory of bioinformatics and computational genomics.

7.5.1 Differential gene expression analysis and functional annotation

As a first step, we checked the quality of the raw data file (CEL file) using the AffyQC module tool(Eijssen et al., 2013) observing that the quality indicator values were within the recommended thresholds. Then we follow the quantification procedures using a standard workflow: raw data files were processed with affy package(Gautier et al., 2004) using BrainArray custom CDF(Dai et al.,

2005) (mouse4302mmengcdf version 22) and normalized/summarized using rma method(Irizarry et al., 2003). The additional gene annotation was retrieved using org.Mm.eg.db package (https://bioconductor.org/packages/release/data/annotation/html/org.Mm.eg.db.html.).

To obtain the differential gene list, we used the principles of linear models and empirical bayes methods as implemented in the limma package(Ritchie et al., 2015). In this way we obtained a list of 1183 differential expressed genes (absolute log fold change greater than 1.5 and multiple-testing adjusted p-values< 0.05(Benjamini and Hochberg, 1995). The functional annotation was performed using two approaches: a) the up-regulated genes or downregulated genes(Huang et al., 2009) were analysed separately through the Database for Annotation, Visualization and Integrated Discovery (DAVID) Bioinformatics Resources v6.8 using the stringent parameter set equal to "high" and the background parameter set to match the actual microarray platform. b) Gene set enrichment analysis was performed using the version implemented in fgsea package(Sergushichev, 2016; Subramanian et al., 2005) performing 10000 permutations and using as database the combination of the KEGG Pathways dataset (mouse profile, accessed in January 2018) and the Gene Set Knowledgebase (GSKB), a comprehensive knowledgebase for pathway analysis in mouse (for detail see http://ge-lab.org/gskb).

7.5.2 Gene expression comparison

Mouse comparison. We download from Gene Expression Omnibus the raw data from different datasets (GSE11859, GSE24628, GSE33199) comprehending several types of Medulloblastoma mouse models as well normal cerebellum tissues. The low level analysis was performed as described above. To remove the possible batch bias and compare these samples to our data, we performed COMBAT normalization as implemented in inSilicoMerging package(Johnson et al., 2007). Then we performed Classical Multidimensional Scaling of all merged datasets, plotting the results of the two principal coordinates.

Human comparison. We download from Gene Expression Omnibus the raw data of the GSE85217 dataset. The low level analysis was performed as described above with the differences of the used custom CDF (HuGene11stv1_Hs_ENTREZID, ver 22) and the annotation package (org.Hs.eg.db). Then we used the human-mouse orthologues mapping information from the Ensembl database (accessed in January 2018) to re-annotate the mouse dataset into human identifiers. Also in this case, we used the COMBAT normalization method to reduce the differences between platforms and organisms. Then we calculated the median values of the Sonic Hedgehog Pathway genes using the human gene list from KEGG database.

7.5.3 Similarity of mouse models to human adult SHH MB

Our pNeuroD1-cre+BRPF1 TR, phSynI-cre+BRPF1 TR and Gabra6-cre;LSL-SmoM2 mice data and Math1-cre;LSL-SmoM2 mice data (GSE11859) were combined with human adult and infant SHH MB data (GSE85217). As previously described, data was normalized using rma method and COMBAT was used to remove potential batch bias. Annotation for mouse data was obtained using mouse4302.db package while annotation for human data was obtained using hugene11sttranscriptcluster.db package. Human-mouse orthologues mapping was performed using HOM_MouseHumanSequence.rpt table available from www.informatics.jax.org. Hierarchical clustering using differential expressed genes from Al-Halabi et al. *Acta Neuropathol.* **121,** 229–239 (2011), with observed absolute log2 fold change greater than 2 was performed using Pearson's correlation coefficient as distance measure. Clustering analysis was performed on samples.

7.6 Quantification and statistical analysis

7.6.1 qRT-PCR analysis

Data are presented as mean + s.e.m. of three biologically independent P14 cerebella (Figure S3A) or differentiated AF22 cells (Figure S6H). Two-tailed Student's t test was used for calculating significance values.

7.6.2 *Ex vivo* cerebellar cell cultures

Data are presented as mean + s.e.m. of three biologically independent *ex vivo* experiments. Two-tailed Student's t test was used for calculating significance values. PiggyBac n=1733 cells, BRPF1 WT n=1841 cells, BRPF1 TR n=1637 cells, hSynI-cre n=1185 cells, hSynI-cre+BRPF1 WT=1321 cells, hSynI-cre+BRPF1 TR=837 cells, hSynI-cre+BRPF1 WT+GLI1 n=4238 cells, hSynI-cre+GLI1 n=2156 cells, hSynI-cre+shGli1+shGli2 n=3796, hSynI-cre+BRPF1 TR+shGli1+shGLi2 n=3505 (Figure S5J).

7.6.3 Survival statistical analysis

Data were displayed using the Kaplan-Meier format and statistical significance of the results was tested using the Log-rank (Mantel-Cox) test. Gabra6-cre;LSL-SmoM2 n=23 mice, LSL-SmoM2 n=11 mice (Figure 22C); pNeuroD1-cre + BRPF1 TR n=17 mice, pNeuroD1-cre + BRPF1 WT n=19 mice (Figure 25D); phSynI-cre + BRPF1 TR n= 12 mice, phSynI-cre n=22 mice (Figure 26F).

7.7 Data and code availability

The data discussed in this publication have been deposited in NCBI's Gene Expression Omnibus (GEO). The accession number for the ATAC-seq data reported in this paper is GSE127733.

8. Contributions

I would like to thank Luca Fagnocchi and Alessio Zippo of the laboratory of chromatin biology & epigenetics who performed ATAC-seq analysis; Silvano Piazza of the bioinformatics core facility and Alessandro Romanel of the laboratory of bioinformatics and computational genomics who performed the bioinformatics analysis; Francesca Gianno and Felice Giangaspero (Department of Radiologic, Oncologic and Anatomo Pathological Sciences, University Sapienza of Rome) that performed histopathological analysis of Gabra6-cre;LSL-SmoM2 MB.

Furthermore, I would like to thank the Lab members that made a great contribution for the project. Indeed, Claudio Ballabio for the *in vitro* differentiation of the human neuroepithelial-like stem cells AF22; Riccardo Ruggeri, Ilaria Morassut and Francesca Garilli for the *in vivo* experiments. Davide Caron for the cryostat cutting and Marica Anderle for the revision of the manuscript. In particular, I would like to thank Prof. Luca Tiberi with whom we designed and analysed all the experiments and wrote the manuscript.

9. References

Ahlfeld, J., Favaro, R., Pagella, P., Kretzschmar, H. A., Nicolis, S., & Schuller, U. (2013). Sox2 requirement in sonic hedgehog-associated medulloblastoma. *Cancer Res, 73*(12), 3796-3807. doi: 10.1158/0008-5472.CAN-13-0238

Aiello, G., Ballabio, C., Ruggeri, R., Fagnocchi, L., Anderle, M., Morassut, I., . . . Tiberi, L. (2019). Truncated BRPF1 Cooperates with Smoothened to Promote Adult Shh Medulloblastoma. *Cell Rep, 29*(12), 4036-4052 e4010. doi: 10.1016/j.celrep.2019.11.046

Ajioka, I., Martins, R. A., Bayazitov, I. T., Donovan, S., Johnson, D. A., Frase, S., . . . Dyer, M. A. (2007). Differentiated horizontal interneurons clonally expand to form metastatic retinoblastoma in mice. *Cell, 131*(2), 378-390. doi: 10.1016/j.cell.2007.09.036

Al-Halabi, H., Nantel, A., Klekner, A., Guiot, M. C., Albrecht, S., Hauser, P., . . . Jabado, N. (2011). Preponderance of sonic hedgehog pathway activation characterizes adult medulloblastoma. *Acta Neuropathol, 121*(2), 229-239. doi: 10.1007/s00401-010-0780-0

Alcantara Llaguno, S., Sun, D., Pedraza, A. M., Vera, E., Wang, Z., Burns, D. K., & Parada, L. F. (2019). Cell-of-origin susceptibility to glioblastoma formation declines with neural lineage restriction. *Nat Neurosci, 22*(4), 545-555. doi: 10.1038/s41593-018-0333-8

Alcantara Llaguno, S. R., & Parada, L. F. (2016). Cell of origin of glioma: biological and clinical implications. *Br J Cancer, 115*(12), 1445-1450. doi: 10.1038/bjc.2016.354

Aller, M. I., Jones, A., Merlo, D., Paterlini, M., Meyer, A. H., Amtmann, U., . . . Wisden, W. (2003). Cerebellar granule cell Cre recombinase expression. *Genesis, 36*(2), 97-103. doi: 10.1002/gene.10204

Antequera, F., & Bird, A. (1993). Number of CpG islands and genes in human and mouse. *Proc Natl Acad Sci U S A, 90*(24), 11995-11999. doi: 10.1073/pnas.90.24.11995

Arlotta, P., & Berninger, B. (2014). Brains in metamorphosis: reprogramming cell identity within the central nervous system. *Curr Opin Neurobiol, 27*, 208-214. doi: 10.1016/j.conb.2014.04.007

Aruga, J., Minowa, O., Yaginuma, H., Kuno, J., Nagai, T., Noda, T., & Mikoshiba, K. (1998). Mouse Zic1 is involved in cerebellar development. *J Neurosci, 18*(1), 284-293.

Bahn, S., Jones, A., & Wisden, W. (1997). Directing gene expression to cerebellar granule cells using gamma-aminobutyric acid type A receptor alpha6 subunit transgenes. *Proc Natl Acad Sci U S A, 94*(17), 9417-9421. doi: 10.1073/pnas.94.17.9417

Ballabio, C., Anderle, M., Gianesello, M., Lago, C., Miele, E., Cardano, M., . . . Tiberi, L. (2020). Modeling medulloblastoma in vivo and with human cerebellar organoids. *Nat Commun, 11*(1), 583. doi: 10.1038/s41467-019-13989-3

Berger, C., Renner, S., Luer, K., & Technau, G. M. (2007). The commonly used marker ELAV is transiently expressed in neuroblasts and glial cells in the Drosophila embryonic CNS. *Dev Dyn, 236*(12), 3562-3568. doi: 10.1002/dvdy.21372

Biran, V., Verney, C., & Ferriero, D. M. (2012). Perinatal cerebellar injury in human and animal models. *Neurol Res Int, 2012*, 858929. doi: 10.1155/2012/858929

Blanpain, C. (2013). Tracing the cellular origin of cancer. *Nat Cell Biol, 15*(2), 126-134. doi: 10.1038/ncb2657

Bogen, I. L., Haug, K. H., Roberg, B., Fonnum, F., & Walaas, S. I. (2009). The importance of synapsin I and II for neurotransmitter levels and vesicular storage in cholinergic, glutamatergic and GABAergic nerve terminals. *Neurochem Int, 55*(1-3), 13-21. doi: 10.1016/j.neuint.2009.02.006

Bolger, A. M., Lohse, M., & Usadel, B. (2014). Trimmomatic: a flexible trimmer for Illumina sequence data. *Bioinformatics, 30*(15), 2114-2120. doi: 10.1093/bioinformatics/btu170

Butts, T., Green, M. J., & Wingate, R. J. (2014). Development of the cerebellum: simple steps to make a 'little brain'. *Development, 141*(21), 4031-4041. doi: 10.1242/dev.106559

Capper, D., Jones, D. T. W., Sill, M., Hovestadt, V., Schrimpf, D., Sturm, D., . . . Pfister, S. M. (2018). DNA methylation-based classification of central nervous system tumours. *Nature, 555*(7697), 469-474. doi: 10.1038/nature26000

Cavalli, F. M. G., Remke, M., Rampasek, L., Peacock, J., Shih, D. J. H., Luu, B., . . . Taylor, M. D. (2017). Intertumoral Heterogeneity within Medulloblastoma Subgroups. *Cancer Cell, 31*(6), 737-754 e736. doi: 10.1016/j.ccell.2017.05.005

Cesca, F., Baldelli, P., Valtorta, F., & Benfenati, F. (2010). The synapsins: key actors of synapse function and plasticity. *Prog Neurobiol, 91*(4), 313-348. doi: 10.1016/j.pneurobio.2010.04.006

Chen, E. Y., Tan, C. M., Kou, Y., Duan, Q., Wang, Z., Meirelles, G. V., . . . Ma'ayan, A. (2013). Enrichr: interactive and collaborative HTML5 gene list enrichment analysis tool. *BMC Bioinformatics, 14*, 128. doi: 10.1186/1471-2105-14-128

Cho, J. H., & Tsai, M. J. (2006). Preferential posterior cerebellum defect in BETA2/NeuroD1 knockout mice is the result of differential expression of BETA2/NeuroD1 along anterior-posterior axis. *Dev Biol, 290*(1), 125-138. doi: 10.1016/j.ydbio.2005.11.024

Choudhry, Z., Rikani, A. A., Choudhry, A. M., Tariq, S., Zakaria, F., Asghar, M. W., . . . Mobassarah, N. J. (2014). Sonic hedgehog signalling pathway: a complex network. *Ann Neurosci, 21*(1), 28-31. doi: 10.5214/ans.0972.7531.210109

Cobaleda, C., Jochum, W., & Busslinger, M. (2007). Conversion of mature B cells into T cells by dedifferentiation to uncommitted progenitors. *Nature, 449*(7161), 473-477. doi: 10.1038/nature06159

Dai, M., Wang, P., Boyd, A. D., Kostov, G., Athey, B., Jones, E. G., . . . Meng, F. (2005). Evolving gene/transcript definitions significantly alter the interpretation of GeneChip data. *Nucleic Acids Res, 33*(20), e175. doi: 10.1093/nar/gni179

De Luca, A., Cerrato, V., Fuca, E., Parmigiani, E., Buffo, A., & Leto, K. (2016). Sonic hedgehog patterning during cerebellar development. *Cell Mol Life Sci, 73*(2), 291-303. doi: 10.1007/s00018-015-2065-1

Deneris, E. S., & Hobert, O. (2014). Maintenance of postmitotic neuronal cell identity. *Nat Neurosci, 17*(7), 899-907. doi: 10.1038/nn.3731

Eberhart, C. G. (2008). Even cancers want commitment: lineage identity and medulloblastoma formation. *Cancer Cell, 14*(2), 105-107. doi: 10.1016/j.ccr.2008.07.011

Eijssen, L. M., Jaillard, M., Adriaens, M. E., Gaj, S., de Groot, P. J., Muller, M., & Evelo, C. T. (2013). User-friendly solutions for microarray quality control and pre-processing on ArrayAnalysis.org. *Nucleic Acids Res, 41*(Web Server issue), W71-76. doi: 10.1093/nar/gkt293

Ellison, D. W., Dalton, J., Kocak, M., Nicholson, S. L., Fraga, C., Neale, G., . . . Gilbertson, R. J. (2011). Medulloblastoma: clinicopathological correlates of SHH, WNT, and non-SHH/WNT molecular subgroups. *Acta Neuropathol, 121*(3), 381-396. doi: 10.1007/s00401-011-0800-8

Fagnocchi, L., Poli, V., & Zippo, A. (2018). Enhancer reprogramming in tumor progression: a new route towards cancer cell plasticity. *Cell Mol Life Sci, 75*(14), 2537-2555. doi: 10.1007/s00018-018-2820-1

Falk, A., Koch, P., Kesavan, J., Takashima, Y., Ladewig, J., Alexander, M., . . . Brustle, O. (2012). Capture of neuroepithelial-like stem cells from pluripotent stem cells provides a versatile system for in vitro production of human neurons. *PLoS One, 7*(1), e29597. doi: 10.1371/journal.pone.0029597

Fornasiero, E. F., Bonanomi, D., Benfenati, F., & Valtorta, F. (2010). The role of synapsins in neuronal development. *Cell Mol Life Sci, 67*(9), 1383-1396. doi: 10.1007/s00018-009-0227-8

Frank, C. L., Liu, F., Wijayatunge, R., Song, L., Biegler, M. T., Yang, M. G., . . . West, A. E. (2015). Regulation of chromatin accessibility and Zic binding at enhancers in the developing cerebellum. *Nat Neurosci, 18*(5), 647-656. doi: 10.1038/nn.3995

Friedmann-Morvinski, D., Bushong, E. A., Ke, E., Soda, Y., Marumoto, T., Singer, O., . . . Verma, I. M. (2012). Dedifferentiation of neurons and astrocytes by oncogenes can induce gliomas in mice. *Science, 338*(6110), 1080-1084. doi: 10.1126/science.1226929

Fuccillo, M., Joyner, A. L., & Fishell, G. (2006). Morphogen to mitogen: the multiple roles of hedgehog signalling in vertebrate neural development. *Nat Rev Neurosci, 7*(10), 772-783. doi: 10.1038/nrn1990

Gautier, L., Cope, L., Bolstad, B. M., & Irizarry, R. A. (2004). affy--analysis of Affymetrix GeneChip data at the probe level. *Bioinformatics, 20*(3), 307-315. doi: 10.1093/bioinformatics/btg405

Guerrier, S., Coutinho-Budd, J., Sassa, T., Gresset, A., Jordan, N. V., Chen, K., . . . Polleux, F. (2009). The F-BAR domain of srGAP2 induces membrane protrusions required for neuronal migration and morphogenesis. *Cell, 138*(5), 990-1004. doi: 10.1016/j.cell.2009.06.047

Guo, C., Qiu, H. Y., Huang, Y., Chen, H., Yang, R. Q., Chen, S. D., . . . Ding, Y. Q. (2007). Lmx1b is essential for Fgf8 and Wnt1 expression in the isthmic organizer during tectum and cerebellum development in mice. *Development, 134*(2), 317-325. doi: 10.1242/dev.02745

Heinz, S., Benner, C., Spann, N., Bertolino, E., Lin, Y. C., Laslo, P., . . . Glass, C. K. (2010). Simple combinations of lineage-determining transcription factors prime cis-regulatory elements required for macrophage and B cell identities. *Mol Cell, 38*(4), 576-589. doi: 10.1016/j.molcel.2010.05.004

Herrup, K., & Yang, Y. (2007). Cell cycle regulation in the postmitotic neuron: oxymoron or new biology? *Nat Rev Neurosci, 8*(5), 368-378. doi: 10.1038/nrn2124

Hovestadt, V., Ayrault, O., Swartling, F. J., Robinson, G. W., Pfister, S. M., & Northcott, P. A. (2019). Medulloblastomics revisited: biological and clinical insights from thousands of patients. *Nat Rev Cancer*. doi: 10.1038/s41568-019-0223-8

Hovestadt, V., Jones, D. T., Picelli, S., Wang, W., Kool, M., Northcott, P. A., . . . Lichter, P. (2014). Decoding the regulatory landscape of medulloblastoma using DNA methylation sequencing. *Nature, 510*(7506), 537-541. doi: 10.1038/nature13268

Hovestadt, V., Remke, M., Kool, M., Pietsch, T., Northcott, P. A., Fischer, R., . . . Jones, D. T. (2013). Robust molecular subgrouping and copy-number profiling of medulloblastoma from small amounts of archival tumour material using high-density DNA methylation arrays. *Acta Neuropathol, 125*(6), 913-916. doi: 10.1007/s00401-013-1126-5

Huang da, W., Sherman, B. T., & Lempicki, R. A. (2009). Systematic and integrative analysis of large gene lists using DAVID bioinformatics resources. *Nat Protoc, 4*(1), 44-57. doi: 10.1038/nprot.2008.211

Huang, P., Kishida, S., Cao, D., Murakami-Tonami, Y., Mu, P., Nakaguro, M., . . . Kadomatsu, K. (2011). The neuronal differentiation factor NeuroD1 downregulates the neuronal repellent factor Slit2 expression and promotes cell motility and tumor formation of neuroblastoma. *Cancer Res, 71*(8), 2938-2948. doi: 10.1158/0008-5472.CAN-10-3524

Huether, R., Dong, L., Chen, X., Wu, G., Parker, M., Wei, L., . . . Downing, J. R. (2014). The landscape of somatic mutations in epigenetic regulators across 1,000 paediatric cancer genomes. *Nat Commun, 5*, 3630. doi: 10.1038/ncomms4630

Irizarry, R. A., Bolstad, B. M., Collin, F., Cope, L. M., Hobbs, B., & Speed, T. P. (2003). Summaries of Affymetrix GeneChip probe level data. *Nucleic Acids Res, 31*(4), e15. doi: 10.1093/nar/gng015

Jones, D. T., Jager, N., Kool, M., Zichner, T., Hutter, B., Sultan, M., . . . Lichter, P. (2012). Dissecting the genomic complexity underlying medulloblastoma. *Nature, 488*(7409), 100-105. doi: 10.1038/nature11284

Kao, H. T., Porton, B., Czernik, A. J., Feng, J., Yiu, G., Haring, M., . . . Greengard, P. (1998). A third member of the synapsin gene family. *Proc Natl Acad Sci U S A, 95*(8), 4667-4672. doi: 10.1073/pnas.95.8.4667

Kato, K. (1990). Novel GABAA receptor alpha subunit is expressed only in cerebellar granule cells. *J Mol Biol, 214*(3), 619-624. doi: 10.1016/0022-2836(90)90276-r

Kim, Y., Kim, T., Rhee, J. K., Lee, D., Tanaka-Yamamoto, K., & Yamamoto, Y. (2015). Selective transgene expression in cerebellar Purkinje cells and granule cells using adeno-associated viruses together with specific promoters. *Brain Res, 1620*, 1-16. doi: 10.1016/j.brainres.2015.05.015

Kool, M., Jones, D. T., Jager, N., Northcott, P. A., Pugh, T. J., Hovestadt, V., . . . Project, I. P. T. (2014). Genome sequencing of SHH medulloblastoma predicts genotype-related response to smoothened inhibition. *Cancer Cell, 25*(3), 393-405. doi: 10.1016/j.ccr.2014.02.004

Kugler, S., Kilic, E., & Bahr, M. (2003). Human synapsin 1 gene promoter confers highly neuron-specific long-term transgene expression from an adenoviral vector in the adult rat brain depending on the transduced area. *Gene Ther, 10*(4), 337-347. doi: 10.1038/sj.gt.3301905

Kuhn, B., Ozden, I., Lampi, Y., Hasan, M. T., & Wang, S. S. (2012). An amplified promoter system for targeted expression of calcium indicator proteins in the cerebellar cortex. *Front Neural Circuits, 6*, 49. doi: 10.3389/fncir.2012.00049

Kuleshov, M. V., Jones, M. R., Rouillard, A. D., Fernandez, N. F., Duan, Q., Wang, Z., . . . Ma'ayan, A. (2016). Enrichr: a comprehensive gene set enrichment analysis web server 2016 update. *Nucleic Acids Res, 44*(W1), W90-97. doi: 10.1093/nar/gkw377

Lancaster, M. A., & Knoblich, J. A. (2014). Organogenesis in a dish: modeling development and disease using organoid technologies. *Science, 345*(6194), 1247125. doi: 10.1126/science.1247125

Langmead, B., & Salzberg, S. L. (2012). Fast gapped-read alignment with Bowtie 2. *Nat Methods, 9*(4), 357-359. doi: 10.1038/nmeth.1923

Larsimont, J. C., Youssef, K. K., Sanchez-Danes, A., Sukumaran, V., Defrance, M., Delatte, B., . . . Blanpain, C. (2015). Sox9 Controls Self-Renewal of Oncogene Targeted Cells and Links Tumor Initiation and Invasion. *Cell Stem Cell, 17*(1), 60-73. doi: 10.1016/j.stem.2015.05.008

Larson, D. R., Zenklusen, D., Wu, B., Chao, J. A., & Singer, R. H. (2011). Real-time observation of transcription initiation and elongation on an endogenous yeast gene. *Science, 332*(6028), 475-478. doi: 10.1126/science.1202142

Lau, J., Schmidt, C., Markant, S. L., Taylor, M. D., Wechsler-Reya, R. J., & Weiss, W. A. (2012). Matching mice to malignancy: molecular subgroups and models of medulloblastoma. *Childs Nerv Syst, 28*(4), 521-532. doi: 10.1007/s00381-012-1704-1

Laue, K., Daujat, S., Crump, J. G., Plaster, N., Roehl, H. H., Tubingen Screen, C., . . . Hammerschmidt, M. (2008). The multidomain protein Brpf1 binds histones and is required for Hox gene expression and segmental identity. *Development, 135*(11), 1935-1946. doi: 10.1242/dev.017160

Leto, K., Arancillo, M., Becker, E. B., Buffo, A., Chiang, C., Ding, B., . . . Hawkes, R. (2016). Consensus Paper: Cerebellar Development. *Cerebellum, 15*(6), 789-828. doi: 10.1007/s12311-015-0724-2

Lewis, P. M., Gritli-Linde, A., Smeyne, R., Kottmann, A., & McMahon, A. P. (2004). Sonic hedgehog signaling is required for expansion of granule neuron precursors and patterning of the mouse cerebellum. *Dev Biol, 270*(2), 393-410. doi: 10.1016/j.ydbio.2004.03.007

Li, H., Handsaker, B., Wysoker, A., Fennell, T., Ruan, J., Homer, N., . . . Genome Project Data Processing, S. (2009). The Sequence Alignment/Map format and SAMtools. *Bioinformatics, 25*(16), 2078-2079. doi: 10.1093/bioinformatics/btp352

Lin, C. Y., Erkek, S., Tong, Y., Yin, L., Federation, A. J., Zapatka, M., . . . Northcott, P. A. (2016). Active medulloblastoma enhancers reveal subgroup-specific cellular origins. *Nature, 530*(7588), 57-62. doi: 10.1038/nature16546

Loven, J., Hoke, H. A., Lin, C. Y., Lau, A., Orlando, D. A., Vakoc, C. R., . . . Young, R. A. (2013). Selective inhibition of tumor oncogenes by disruption of super-enhancers. *Cell, 153*(2), 320-334. doi: 10.1016/j.cell.2013.03.036

Madisen, L., Zwingman, T. A., Sunkin, S. M., Oh, S. W., Zariwala, H. A., Gu, H., . . . Zeng, H. (2010). A robust and high-throughput Cre reporting and characterization system for the whole mouse brain. *Nat Neurosci, 13*(1), 133-140. doi: 10.1038/nn.2467

Martz, C. A., Ottina, K. A., Singleton, K. R., Jasper, J. S., Wardell, S. E., Peraza-Penton, A., . . . Wood, K. C. (2014). Systematic identification of signaling pathways with potential to confer anticancer drug resistance. *Sci Signal, 7*(357), ra121. doi: 10.1126/scisignal.aaa1877

Marzban, H., Del Bigio, M. R., Alizadeh, J., Ghavami, S., Zachariah, R. M., & Rastegar, M. (2014). Cellular commitment in the developing cerebellum. *Front Cell Neurosci, 8*, 450. doi: 10.3389/fncel.2014.00450

McLean, C. Y., Bristor, D., Hiller, M., Clarke, S. L., Schaar, B. T., Lowe, C. B., . . . Bejerano, G. (2010). GREAT improves functional interpretation of cis-regulatory regions. *Nat Biotechnol, 28*(5), 495-501. doi: 10.1038/nbt.1630

Merk, D. J., Ohli, J., Merk, N. D., Thatikonda, V., Morrissy, S., Schoof, M., . . . Schuller, U. (2018). Opposing Effects of CREBBP Mutations Govern the Phenotype of Rubinstein-Taybi Syndrome and Adult SHH Medulloblastoma. *Dev Cell, 44*(6), 709-724 e706. doi: 10.1016/j.devcel.2018.02.012

Millard, N. E., & De Braganca, K. C. (2016). Medulloblastoma. *J Child Neurol, 31*(12), 1341-1353. doi: 10.1177/0883073815600866

Miterko, L. N., Lackey, E. P., Heck, D. H., & Sillitoe, R. V. (2018). Shaping Diversity Into the Brain's Form and Function. *Front Neural Circuits, 12*, 83. doi: 10.3389/fncir.2018.00083

Miyata, T., Maeda, T., & Lee, J. E. (1999). NeuroD is required for differentiation of the granule cells in the cerebellum and hippocampus. *Genes Dev, 13*(13), 1647-1652. doi: 10.1101/gad.13.13.1647

Nguyen, L., Besson, A., Roberts, J. M., & Guillemot, F. (2006). Coupling cell cycle exit, neuronal differentiation and migration in cortical neurogenesis. *Cell Cycle, 5*(20), 2314-2318. doi: 10.4161/cc.5.20.3381

Northcott, P. A., Hielscher, T., Dubuc, A., Mack, S., Shih, D., Remke, M., . . . Taylor, M. D. (2011). Pediatric and adult sonic hedgehog medulloblastomas are clinically and molecularly distinct. *Acta Neuropathol, 122*(2), 231-240. doi: 10.1007/s00401-011-0846-7

Northcott, P. A., Jones, D. T., Kool, M., Robinson, G. W., Gilbertson, R. J., Cho, Y. J., . . . Pfister, S. M. (2012). Medulloblastomics: the end of the beginning. *Nat Rev Cancer, 12*(12), 818-834. doi: 10.1038/nrc3410

Northcott, P. A., Korshunov, A., Witt, H., Hielscher, T., Eberhart, C. G., Mack, S., . . . Taylor, M. D. (2011). Medulloblastoma comprises four distinct molecular variants. *J Clin Oncol, 29*(11), 1408-1414. doi: 10.1200/JCO.2009.27.4324

Pan, S., Wu, X., Jiang, J., Gao, W., Wan, Y., Cheng, D., . . . Dorsch, M. (2010). Discovery of NVP-LDE225, a Potent and Selective Smoothened Antagonist. *ACS Med Chem Lett, 1*(3), 130-134. doi: 10.1021/ml1000307

Petrova, R., & Joyner, A. L. (2014). Roles for Hedgehog signaling in adult organ homeostasis and repair. *Development, 141*(18), 3445-3457. doi: 10.1242/dev.083691

Poli, V., Fagnocchi, L., Fasciani, A., Cherubini, A., Mazzoleni, S., Ferrillo, S., . . . Zippo, A. (2018). MYC-driven epigenetic reprogramming favors the onset of tumorigenesis by inducing a stem cell-like state. *Nat Commun, 9*(1), 1024. doi: 10.1038/s41467-018-03264-2

Poschl, J., Stark, S., Neumann, P., Grobner, S., Kawauchi, D., Jones, D. T., . . . Schuller, U. (2014). Genomic and transcriptomic analyses match medulloblastoma mouse models to their human counterparts. *Acta Neuropathol, 128*(1), 123-136. doi: 10.1007/s00401-014-1297-8

Pugh, T. J., Weeraratne, S. D., Archer, T. C., Pomeranz Krummel, D. A., Auclair, D., Bochicchio, J., . . . Cho, Y. J. (2012). Medulloblastoma exome sequencing uncovers subtype-specific somatic mutations. *Nature, 488*(7409), 106-110. doi: 10.1038/nature11329

Quinlan, A. R., & Hall, I. M. (2010). BEDTools: a flexible suite of utilities for comparing genomic features. *Bioinformatics, 26*(6), 841-842. doi: 10.1093/bioinformatics/btq033

Rada-Iglesias, A., Grosveld, F. G., & Papantonis, A. (2018). Forces driving the three-dimensional folding of eukaryotic genomes. *Mol Syst Biol, 14*(6), e8214. doi: 10.15252/msb.20188214

Raffel, C. (2004). Medulloblastoma: molecular genetics and animal models. *Neoplasia, 6*(4), 310-322. doi: 10.1593/neo.03454

Remke, M., Ramaswamy, V., Peacock, J., Shih, D. J., Koelsche, C., Northcott, P. A., . . . Taylor, M. D. (2013). TERT promoter mutations are highly recurrent in SHH subgroup medulloblastoma. *Acta Neuropathol, 126*(6), 917-929. doi: 10.1007/s00401-013-1198-2

Ritchie, M. E., Phipson, B., Wu, D., Hu, Y., Law, C. W., Shi, W., & Smyth, G. K. (2015). limma powers differential expression analyses for RNA-sequencing and microarray studies. *Nucleic Acids Res, 43*(7), e47. doi: 10.1093/nar/gkv007

Rose, M. F., Ren, J., Ahmad, K. A., Chao, H. T., Klisch, T. J., Flora, A., . . . Zoghbi, H. Y. (2009). Math1 is essential for the development of hindbrain neurons critical for perinatal breathing. *Neuron, 64*(3), 341-354. doi: 10.1016/j.neuron.2009.10.023

Schroeder, K., & Gururangan, S. (2014). Molecular variants and mutations in medulloblastoma. *Pharmgenomics Pers Med, 7*, 43-51. doi: 10.2147/PGPM.S38698

Schuller, U., Heine, V. M., Mao, J., Kho, A. T., Dillon, A. K., Han, Y. G., . . . Ligon, K. L. (2008). Acquisition of granule neuron precursor identity is a critical determinant of progenitor cell competence to form Shh-induced medulloblastoma. *Cancer Cell, 14*(2), 123-134. doi: 10.1016/j.ccr.2008.07.005

Schuller, U., Kho, A. T., Zhao, Q., Ma, Q., & Rowitch, D. H. (2006). Cerebellar 'transcriptome' reveals cell-type and stage-specific expression during postnatal development and tumorigenesis. *Mol Cell Neurosci, 33*(3), 247-259. doi: 10.1016/j.mcn.2006.07.010

Schwab, M. H., Druffel-Augustin, S., Gass, P., Jung, M., Klugmann, M., Bartholomae, A., . . . Nave, K. A. (1998). Neuronal basic helix-loop-helix proteins (NEX, neuroD, NDRF): spatiotemporal expression and targeted disruption of the NEX gene in transgenic mice. *J Neurosci, 18*(4), 1408-1418.

Schwitalla, S., Fingerle, A. A., Cammareri, P., Nebelsiek, T., Goktuna, S. I., Ziegler, P. K., . . . Greten, F. R. (2013). Intestinal tumorigenesis initiated by dedifferentiation and acquisition of stem-cell-like properties. *Cell, 152*(1-2), 25-38. doi: 10.1016/j.cell.2012.12.012

Sergushichev, A. A. (2016). An algorithm for fast preranked gene set enrichment analysis using cumulative statistic calculation. *bioRxiv*, 060012. doi: 10.1101/060012

Shen, L., Shao, N., Liu, X., & Nestler, E. (2014). ngs.plot: Quick mining and visualization of next-generation sequencing data by integrating genomic databases. *BMC Genomics, 15*, 284. doi: 10.1186/1471-2164-15-284

Southall, T. D., Davidson, C. M., Miller, C., Carr, A., & Brand, A. H. (2014). Dedifferentiation of neurons precedes tumor formation in Lola mutants. *Dev Cell, 28*(6), 685-696. doi: 10.1016/j.devcel.2014.01.030

Subramanian, A., Tamayo, P., Mootha, V. K., Mukherjee, S., Ebert, B. L., Gillette, M. A., . . . Mesirov, J. P. (2005). Gene set enrichment analysis: a knowledge-based approach for interpreting genome-wide expression profiles. *Proc Natl Acad Sci U S A, 102*(43), 15545-15550. doi: 10.1073/pnas.0506580102

Sutter, R., Shakhova, O., Bhagat, H., Behesti, H., Sutter, C., Penkar, S., . . . Marino, S. (2010). Cerebellar stem cells act as medulloblastoma-initiating cells in a mouse model and a neural stem cell signature characterizes a subset of human medulloblastomas. *Oncogene, 29*(12), 1845-1856. doi: 10.1038/onc.2009.472

Swartling, F. J., Savov, V., Persson, A. I., Chen, J., Hackett, C. S., Northcott, P. A., . . . Weiss, W. A. (2012). Distinct neural stem cell populations give rise to disparate brain tumors in response to N-MYC. *Cancer Cell, 21*(5), 601-613. doi: 10.1016/j.ccr.2012.04.012

Tailor, J., Kittappa, R., Leto, K., Gates, M., Borel, M., Paulsen, O., . . . Smith, A. (2013). Stem cells expanded from the human embryonic hindbrain stably retain regional specification and high neurogenic potency. *J Neurosci, 33*(30), 12407-12422. doi: 10.1523/JNEUROSCI.0130-13.2013

Takacs, J., Markova, L., Borostyankoi, Z., Gorcs, T. J., & Hamori, J. (1999). Metabotrop glutamate receptor type 1a expressing unipolar brush cells in the cerebellar cortex of different species: a comparative quantitative study. *J Neurosci Res, 55*(6), 733-748. doi: 10.1002/(SICI)1097-4547(19990315)55:6<733::AID-JNR8>3.0.CO;2-8

Takahashi, K., & Yamanaka, S. (2006). Induction of pluripotent stem cells from mouse embryonic and adult fibroblast cultures by defined factors. *Cell, 126*(4), 663-676. doi: 10.1016/j.cell.2006.07.024

Takashima, Y., Guo, G., Loos, R., Nichols, J., Ficz, G., Krueger, F., . . . Smith, A. (2014). Resetting transcription factor control circuitry toward ground-state pluripotency in human. *Cell, 158*(6), 1254-1269. doi: 10.1016/j.cell.2014.08.029

Taniguchi, H., He, M., Wu, P., Kim, S., Paik, R., Sugino, K., . . . Huang, Z. J. (2011). A resource of Cre driver lines for genetic targeting of GABAergic neurons in cerebral cortex. *Neuron, 71*(6), 995-1013. doi: 10.1016/j.neuron.2011.07.026

Taylor, M. D., Northcott, P. A., Korshunov, A., Remke, M., Cho, Y. J., Clifford, S. C., . . . Pfister, S. M. (2012). Molecular subgroups of medulloblastoma: the current consensus. *Acta Neuropathol, 123*(4), 465-472. doi: 10.1007/s00401-011-0922-z

Tiberi, L., Bonnefont, J., van den Ameele, J., Le Bon, S. D., Herpoel, A., Bilheu, A., . . . Vanderhaeghen, P. (2014). A BCL6/BCOR/SIRT1 complex triggers neurogenesis and suppresses medulloblastoma by repressing Sonic Hedgehog signaling. *Cancer Cell, 26*(6), 797-812. doi: 10.1016/j.ccell.2014.10.021

Tschaharganeh, D. F., Xue, W., Calvisi, D. F., Evert, M., Michurina, T. V., Dow, L. E., . . . Lowe, S. W. (2014). p53-dependent Nestin regulation links tumor suppression to cellular plasticity in liver cancer. *Cell, 158*(3), 579-592. doi: 10.1016/j.cell.2014.05.051

Vanner, R. J., Remke, M., Gallo, M., Selvadurai, H. J., Coutinho, F., Lee, L., . . . Dirks, P. B. (2014). Quiescent sox2(+) cells drive hierarchical growth and relapse in sonic hedgehog subgroup medulloblastoma. *Cancer Cell, 26*(1), 33-47. doi: 10.1016/j.ccr.2014.05.005

Visvader, J. E. (2011). Cells of origin in cancer. *Nature, 469*(7330), 314-322. doi: 10.1038/nature09781

Visvader, J. E., & Lindeman, G. J. (2012). Cancer stem cells: current status and evolving complexities. *Cell Stem Cell, 10*(6), 717-728. doi: 10.1016/j.stem.2012.05.007

Vong, K. I., Leung, C. K., Behringer, R. R., & Kwan, K. M. (2015). Sox9 is critical for suppression of neurogenesis but not initiation of gliogenesis in the cerebellum. *Mol Brain, 8*, 25. doi: 10.1186/s13041-015-0115-0

Waddington, C. H. (1956). Genetic Assimilation of the Bithorax Phenotype. *Evolution, 10*(1), 1-13. doi: 10.2307/2406091

Wang, V. Y., & Zoghbi, H. Y. (2001). Genetic regulation of cerebellar development. *Nat Rev Neurosci, 2*(7), 484-491. doi: 10.1038/35081558

Wang, Y., Yang, J., Zheng, H., Tomasek, G. J., Zhang, P., McKeever, P. E., . . . Zhu, Y. (2009). Expression of mutant p53 proteins implicates a lineage relationship between neural stem cells and malignant astrocytic glioma in a murine model. *Cancer Cell, 15*(6), 514-526. doi: 10.1016/j.ccr.2009.04.001

Wang, Z., Gerstein, M., & Snyder, M. (2009). RNA-Seq: a revolutionary tool for transcriptomics. *Nat Rev Genet, 10*(1), 57-63. doi: 10.1038/nrg2484

Wassarman, K. M., Lewandoski, M., Campbell, K., Joyner, A. L., Rubenstein, J. L., Martinez, S., & Martin, G. R. (1997). Specification of the anterior hindbrain and establishment of a normal mid/hindbrain organizer is dependent on Gbx2 gene function. *Development, 124*(15), 2923-2934.

Whyte, W. A., Orlando, D. A., Hnisz, D., Abraham, B. J., Lin, C. Y., Kagey, M. H., . . . Young, R. A. (2013). Master transcription factors and mediator establish super-enhancers at key cell identity genes. *Cell, 153*(2), 307-319. doi: 10.1016/j.cell.2013.03.035

Wilhelm, B. T., & Landry, J. R. (2009). RNA-Seq-quantitative measurement of expression through massively parallel RNA-sequencing. *Methods, 48*(3), 249-257. doi: 10.1016/j.ymeth.2009.03.016

Wu, C. C., Hou, S., Orr, B. A., Kuo, B. R., Youn, Y. H., Ong, T., . . . Han, Y. G. (2017). mTORC1-Mediated Inhibition of 4EBP1 Is Essential for Hedgehog Signaling-Driven Translation and Medulloblastoma. *Dev Cell, 43*(6), 673-688 e675. doi: 10.1016/j.devcel.2017.10.011

Yam, P. T., & Charron, F. (2013). Signaling mechanisms of non-conventional axon guidance cues: the Shh, BMP and Wnt morphogens. *Curr Opin Neurobiol, 23*(6), 965-973. doi: 10.1016/j.conb.2013.09.002

Yan, K., Rousseau, J., Littlejohn, R. O., Kiss, C., Lehman, A., Rosenfeld, J. A., . . . Yang, X. J. (2017). Mutations in the Chromatin Regulator Gene BRPF1 Cause Syndromic Intellectual Disability and Deficient Histone Acetylation. *Am J Hum Genet, 100*(1), 91-104. doi: 10.1016/j.ajhg.2016.11.011

Yang, X. J. (2015). MOZ and MORF acetyltransferases: Molecular interaction, animal development and human disease. *Biochim Biophys Acta, 1853*(8), 1818-1826. doi: 10.1016/j.bbamcr.2015.04.014

Yang, Z.-J., Ellis, T., Markant, S. L., Read, T.-A., Kessler, J. D., Bourboulas, M., . . . Wechsler-Reya, R. J. (2008). Medulloblastoma Can Be Initiated by Deletion of Patched in Lineage-Restricted Progenitors or Stem Cells. *Cancer Cell, 14*(2), 135-145. doi: https://doi.org/10.1016/j.ccr.2008.07.003

Yao, K. M., & White, K. (1994). Neural specificity of elav expression: defining a Drosophila promoter for directing expression to the nervous system. *J Neurochem, 63*(1), 41-51. doi: 10.1046/j.1471-4159.1994.63010041.x

You, L., Chen, L., Penney, J., Miao, D., & Yang, X. J. (2014). Expression atlas of the multivalent epigenetic regulator Brpf1 and its requirement for survival of mouse embryos. *Epigenetics, 9*(6), 860-872. doi: 10.4161/epi.28530

You, L., Li, L., Zou, J., Yan, K., Belle, J., Nijnik, A., . . . Yang, X. J. (2016). BRPF1 is essential for development of fetal hematopoietic stem cells. *J Clin Invest, 126*(9), 3247-3262. doi: 10.1172/JCI80711

You, L., Yan, K., Zou, J., Zhao, H., Bertos, N. R., Park, M., . . . Yang, X. J. (2015). The lysine acetyltransferase activator Brpf1 governs dentate gyrus development through neural stem cells and progenitors. *PLoS Genet, 11*(3), e1005034. doi: 10.1371/journal.pgen.1005034

You, L., Zou, J., Zhao, H., Bertos, N. R., Park, M., Wang, E., & Yang, X. J. (2015). Deficiency of the chromatin regulator BRPF1 causes abnormal brain development. *J Biol Chem, 290*(11), 7114-7129. doi: 10.1074/jbc.M114.635250

Yu, X., Ye, Z., Houston, C. M., Zecharia, A. Y., Ma, Y., Zhang, Z., . . . Wisden, W. (2015). Wakefulness Is Governed by GABA and Histamine Cotransmission. *Neuron, 87*(1), 164-178. doi: 10.1016/j.neuron.2015.06.003

Yusa, K., Zhou, L., Li, M. A., Bradley, A., & Craig, N. L. (2011). A hyperactive piggyBac transposase for mammalian applications. *Proc Natl Acad Sci U S A, 108*(4), 1531-1536. doi: 10.1073/pnas.1008322108

Zhang, C., Williams, E. H., Guo, Y., Lum, L., & Beachy, P. A. (2004). Extensive phosphorylation of Smoothened in Hedgehog pathway activation. *Proc Natl Acad Sci U S A, 101*(52), 17900-17907. doi: 10.1073/pnas.0408093101

10. Annexes

10.1 Supplementary figures
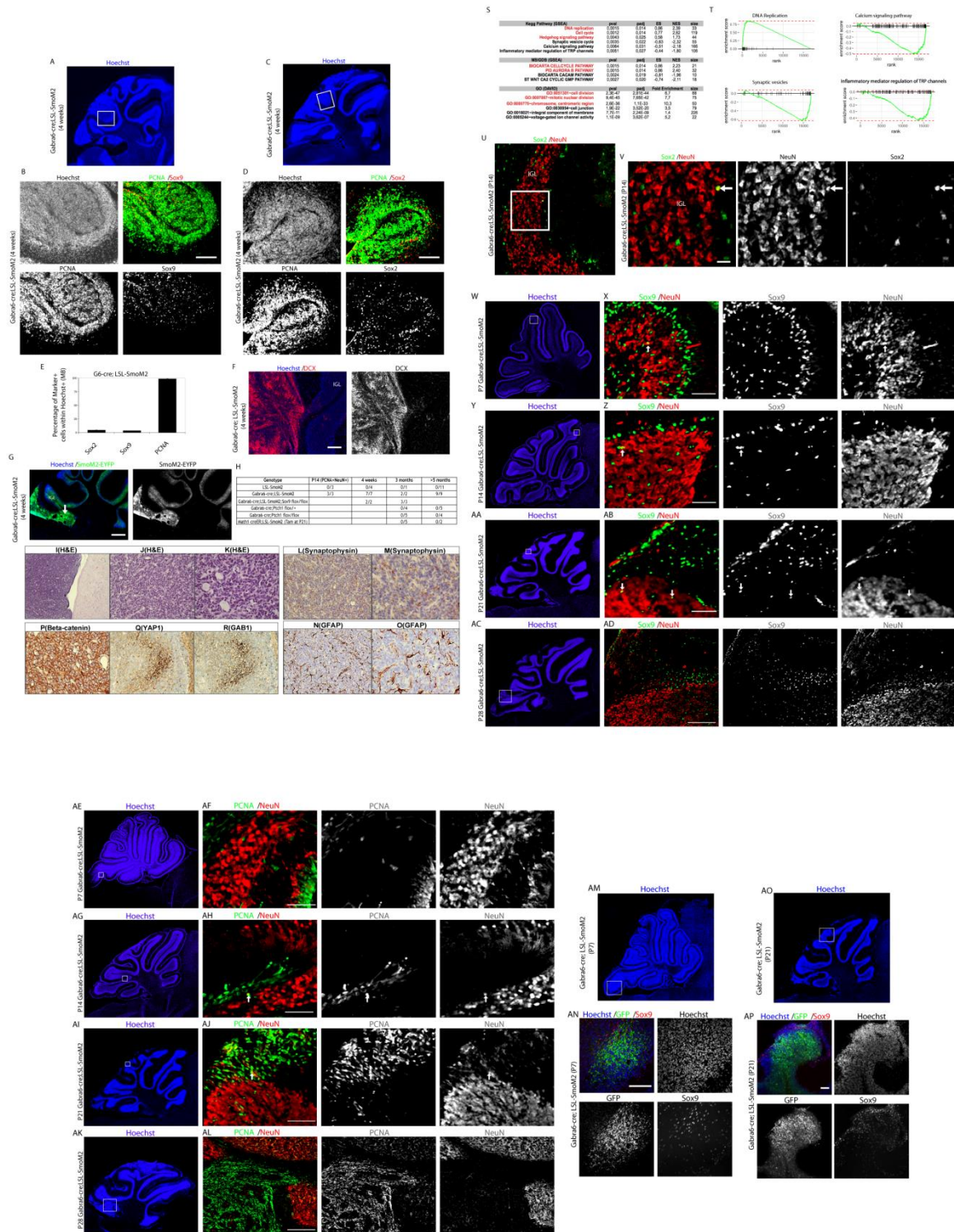
Figure S1

Figure S1, related to Figure 22 and 23 | SmoM2 expression promotes dedifferentiation of granule neurons and Shh MB.

(**A**) Hoechst staining of sagittal brain sections of 4-week-old Gabra6-cre;LSL-SmoM2 mouse. Square in **A** marks the region shown at higher magnification in **B**. (**B**) Hoechst staining and immunofluorescence for PCNA and Sox9 of sagittal brain sections of 4-week-old Gabra6-cre;LSL-SmoM2 mouse. (**C**) Hoechst staining of sagittal brain sections of 4-week-old Gabra6-cre;LSL-SmoM2 mouse. Square in **C** marks the region shown at higher magnification in **D**. (**D**) Hoechst staining and immunofluorescence for PCNA and Sox2 of sagittal brain sections of 4-week-old Gabra6-cre;LSL-SmoM2 mouse. (**E**) Quantification of Sox2, Sox9 and PCNA positive cells of sagittal brain sections of 4-week-old Gabra6-cre;LSL-SmoM2 mice. Mean±S.E.M. n=3. (**F**) Hoechst staining and immunofluorescence for Doublecortin (DCX) of sagittal brain sections of 4-week-old Gabra6-cre;LSL-SmoM2 mouse. (**G**) Hoechst staining and immunofluorescence for GFP of sagittal brain sections of 4-week-old Gabra6-cre;LSL-SmoM2 mouse. Arrow points to the tumor. (**H**) Genotypes and number of mice that display abnormal PCNA+ cell cluster/tumors. (**I-K**) H&E stained section. Shh MB in Gabra6-cre; LSL-SmoM2 mice at different magnification. (**I**) In the left side of the figure the tumor is characterized by high cellularity consisting of monomorphic small round blue cells with hyperchromatic nuclei. Normal brain tissue is present in the right side (10X magnification). (**J**) Higher magnification showing primitive-appearance cells with high N:C ratio and some Homer Wright rosettes (tumor cells grouped around a central region containing neuropil) (20X magnification). (**K**) Presence of some nuclear molding and apoptotic cells. A couple of mitotic figures are visible in this image (40X magnification). (**L,M**) Positive staining for Synaptophysin in the cytoplasm of cells with granular pattern (20X and 40X magnification). (**N,O**) Negative staining for GFAP in neoplastic cells. Isolated strongly positive elements with multiple long processes represent reactive glial cells (20X and 40X magnification). (**P**) Beta-catenin immunoreactivity restricted to the plasma membrane and cytoplasm identify non-WNT medulloblastoma (40X magnification). (**Q**) Strong expression of YAP1 protein in the plasma membrane and cytoplasm of neoplastic cells (20X magnification) (**R**) GAB1 protein expression in the same field showing the same pattern of YAP1 (20X magnification). (**S**) Table showing some of the relevant terms/pathways of the Functional Annotation analysis using GSEA and DAVID tool. (**T**) GSEA plots for relevant pathways. (**U,V**) Confocal images of immunofluorescence for Sox2 and NeuN of sagittal brain sections of P14 Gabra6-cre;LSL-SmoM2 mouse. Square in **U** marks the region shown at higher magnification in **V**. Arrows point to Sox2/NeuN double positive cells. (**W,Y,AA,AC**) Hoechst stainings of P7 (**W**), P14 (**Y**), P21 (**AA**), P28 (**AC**) of Gabra6-cre;LSL-SmoM2 mice. (**X,Z,AB,AD**) Confocal images of immunofluorescence for Sox9 and NeuN of sagittal brain sections of Gabra6-cre;LSL-SmoM2 mouse. Square in **W,Y,AA,AC** marks the region shown at higher magnification in **X,Z,AB,AD**. Arrows point to Sox9/NeuN double positive cells. (**AE,AG,AI,AK**) Hoechst stainings of P7 (**AE**), P14 (**AG**), P21 (**AI**), P28 (**AK**) of Gabra6-cre;LSL-SmoM2 mice. (**AF,AH,AJ,AL**) Confocal images of immunofluorescence for PCNA and NeuN of sagittal brain sections of Gabra6-cre;LSL-SmoM2 mouse. Square in **AE,AG,AI,AK** marks the region shown at higher magnification in **AF,AH,AJ,AL**. Arrows point to PCNA/NeuN double positive cells. (**AM, AO**) Hoechst stainings of P7 (**AM**), P21 (**AO**) of Gabra6-cre;LSL-SmoM2 mice. (**AN,AP**) Confocal images of immunofluorescence for Sox9 and GFP of sagittal brain sections of Gabra6-cre;LSL-SmoM2 mouse. Square in **AM,AO** marks the region shown at higher magnification in **AN,AP**. Scale bars 25 μm (**AF,AH**) 50 μm (**V,X,AJ,AL,AN**), 100μm (**Z,AB,AD,AP**), 200 μm (**B,D,F**), 500 μm (**G**). IGL, Internal Granular Layer.
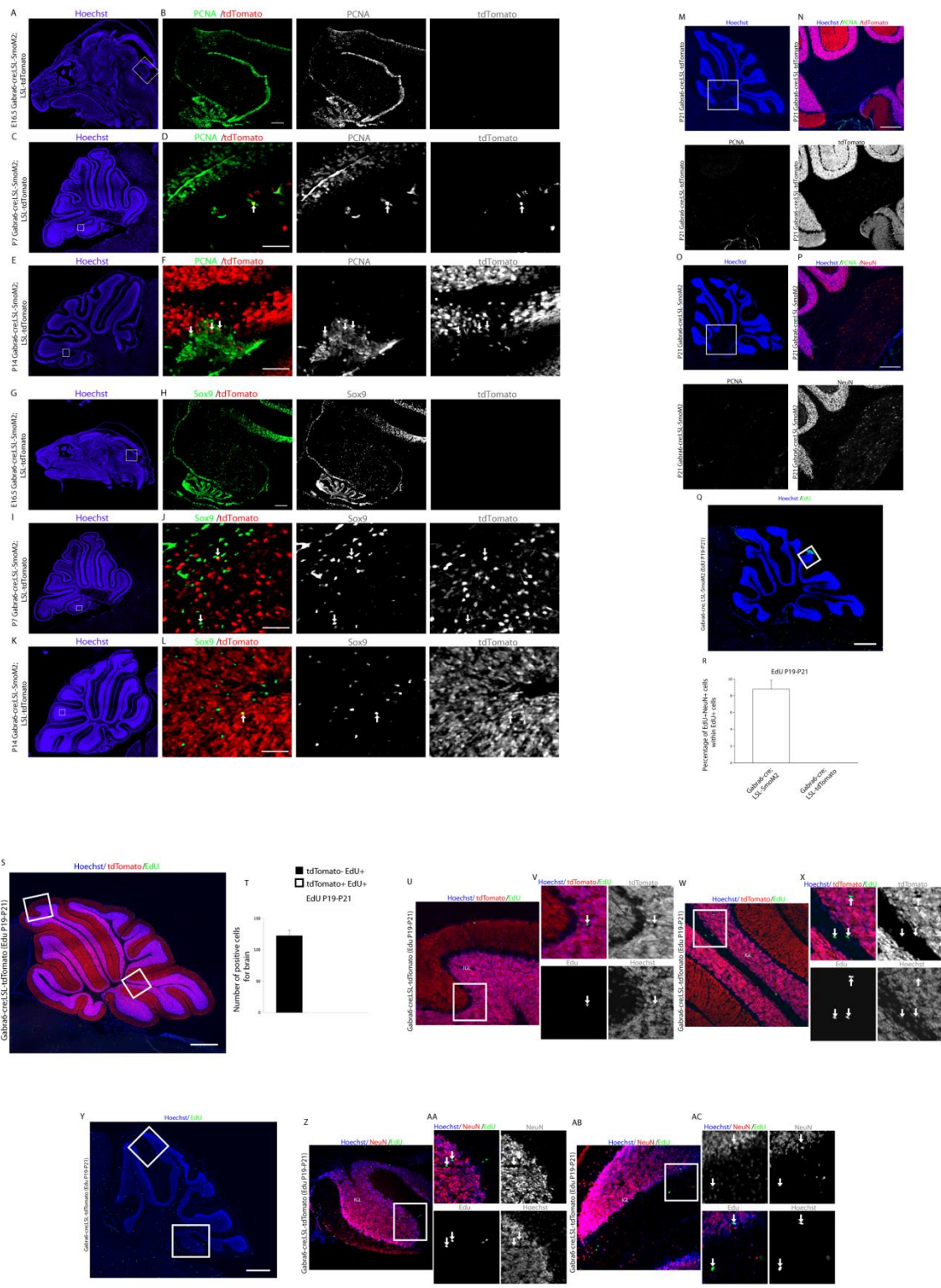
Figure S2

Figure S2, related to Figure 22 and 23 | Presence of tdTomato and PCNA/Sox9 double positive cells in Gabra6-cre;LSL-SmoM2;LSL-tdTomato mice and cerebellum analysis of EdU injection in Gabra6-cre;LSL-SmoM2 or Gabra6-cre;LSL-tdTomato mice.

(**A,C,E**) Hoechst stainings of E16.5 (**A**), P7 (**C**), P14 (**E**) of Gabra6-cre;LSL-SmoM2;LSL-tdTomato mice. (**B,D,F**) Confocal images of immunofluorescence for PCNA and tdTomato of sagittal brain sections of Gabra6-cre;LSL-SmoM2;LSL-tdTomato mice. Square in **A,C,E** marks the region shown at higher magnification in **B,D,F**. (**G,I,K**) Hoechst stainings of E16.5 (**G**), P7 (**I**), P14 (**K**) of Gabra6-cre;LSL-SmoM2;LSL-tdTomato mice. (**H,J,L**) Confocal images of immunofluorescence for Sox9 and tdTomato of sagittal brain sections of Gabra6-cre;LSL-SmoM2;LSL-tdTomato mice. Square in **G,I,K** marks the region shown at higher magnification in **H,J,L**. Arrows point to PCNA/Sox9 and tdTomato double positive cells. (**M**) Hoechst staining of P21 Gabra6-cre;LSL-tdTomato mouse. (**N**) Confocal images of immunofluorescence for PCNA and tdTomato of sagittal brain sections of Gabra6-cre;LSL-tdTomato mouse. Square in **M** marks the region shown at higher magnification in **N**. (**O**) Hoechst staining of P21 Gabra6-cre;LSL-SmoM2 mouse. (**P**) Confocal images of immunofluorescence for PCNA and NeuN of sagittal brain sections of Gabra6-cre;LSL-SmoM2 mouse. Square in **O** marks the region shown at higher magnification in **P**. (**Q**) Hoechst staining and immunofluorescence for EdU of P21 Gabra6-cre;LSL-SmoM2 mouse, injected with EdU at P19. Square in **Q** marks the region shown at higher magnification in **Figure 2E**. (**R**) Quantification of EdU/NeuN double positive cells within EdU+ cells of sagittal brain sections of P21 Gabra6-cre;LSL-SmoM2 and Gabra6-cre;LSL-tdTomato mice (EdU injection at P19). Mean±S.E.M. n=3. (**S**) Hoechst staining and immunofluorescence for tdTomato and EdU of sagittal brain sections of P21 Gabra6-cre;LSL-tdTomato, injected with EdU at P19. Squares in **S** marks the region shown at higher magnification in **U,X**. (**T**) Quantification of tdTomato/EdU double positive cells of P21 Gabra6-cre;LSL-tdTomato mice, injected with EdU at P19, Mean±S.E.M. n=3. (**U**) Hoechst staining and immunofluorescence for tdTomato and EdU of sagittal brain sections of P21 Gabra6-cre;LSL-tdTomato, injected with EdU at P19. Squares in **U** marks the region shown at higher magnification in **V**. (**W**) Hoechst staining and immunofluorescence for tdTomato and EdU of sagittal brain sections of P21 Gabra6-cre;LSL-tdTomato, injected with EdU at P19. Squares in **W** marks the region shown at higher magnification in **X**. (**Y**) Hoechst staining and immunofluorescence for EdU of sagittal brain sections of P21 Gabra6-cre;LSL-tdTomato, injected with EdU at P19. Squares in **Y** marks the region shown at higher magnification in **Z,AB**. (**Z**) Hoechst staining and immunofluorescence for EdU and NeuN of sagittal brain sections of P21 Gabra6-cre;LSL-tdTomato, injected with EdU at P19. Squares in **Z** marks the region shown at higher magnification in **AA**. (**AB**) Hoechst staining and immunofluorescence for EdU and NeuN of sagittal brain sections of P21 Gabra6-cre;LSL-tdTomato, injected with EdU at P19. Squares in **AB** marks the region shown at higher magnification in **AC**. Arrows point to EdU positive cells. Scale bars 50 µm (**D,F,J,L**), 100µm (**B,H,N,P**), 1 mm (**Q,S,Y**).
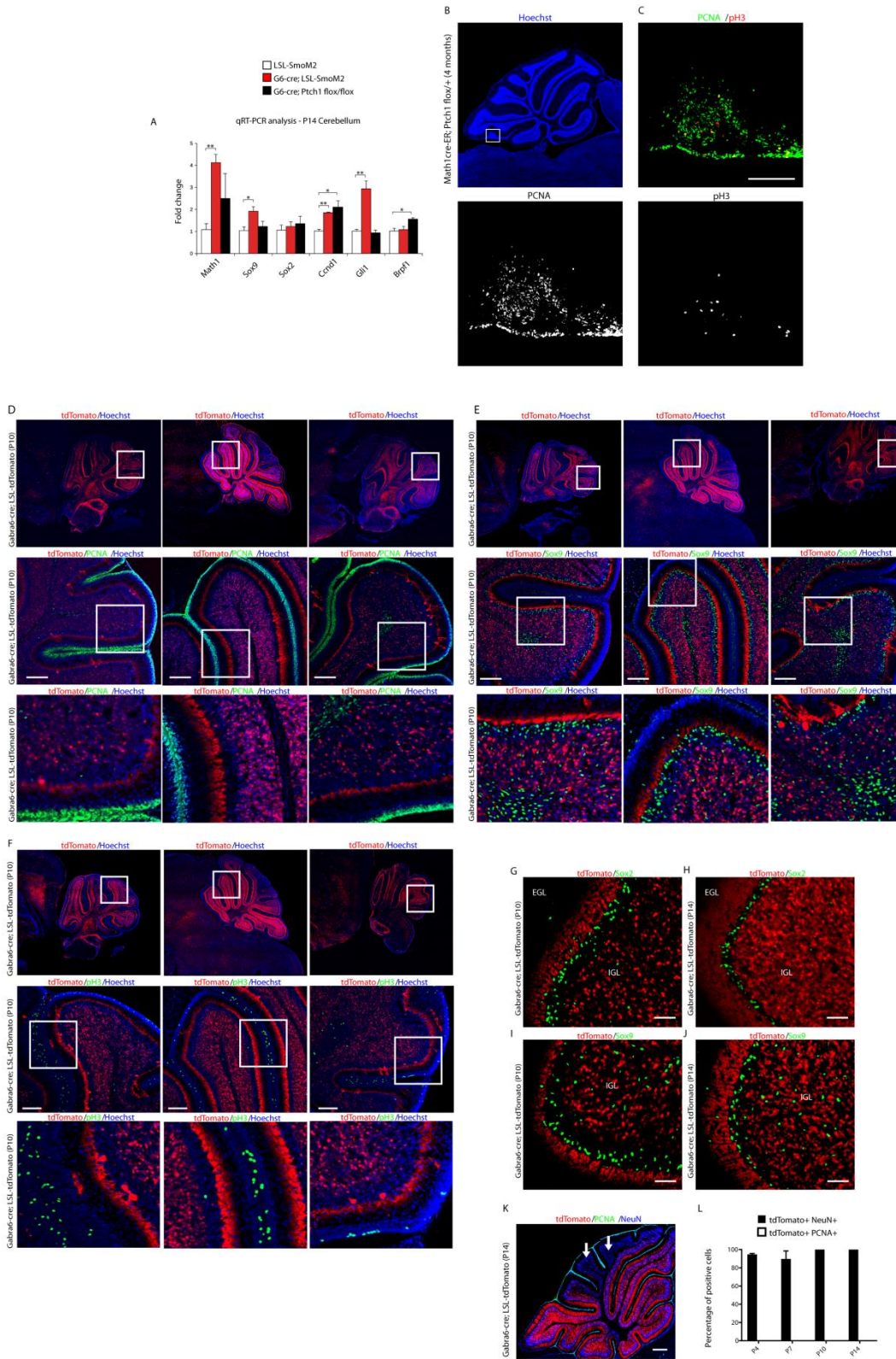
Figure S3

Figure S3, related to Figure 22 | Gene expression comparison between Gabra6-cre;LSL-SmoM2 and Gabra6-cre;Ptch1 flox/flox mice, characterization of Math1-creER;Ptch1 flox/+ mice and Gabra6-cre expression in neurons.

(**A**) qRT-PCR analysis for Math1, Sox9, Sox2, Ccnd1, Gli1, Brpf1 genes expression in LSL-SmoM2, Gabra6-cre;LSL-SmoM2 and Gabra6-cre;Ptch1 flox/flox mice at P14. Mean±S.E.M. n=3. *p value<0.05. **p value<0.01. (**B**) Hoechst staining of sagittal brain sections of Math1-creER;Ptch1 flox/+ mouse injected with Tamoxifen at P5. Square in **B** marks the region shown at higher magnification in **C**. (**C**) Immunofluorescence for PCNA and pH3 of sagittal brain sections of Math1-creER;Ptch1 flox/+ mouse injected with Tamoxifen at P5. (**D**) Hoechst stainings and immunofluorescence for tdTomato and PCNA in Gabra6-cre;LSL-tdTomato mice at P10 at three different sagittal planes: lateral left, medial, lateral right. Squares mark the region shown at higher magnification in the images below. (**E**) Hoechst stainings and immunofluorescence for tdTomato and Sox9 in Gabra6-cre;LSL-tdTomato mice at P10 at three different sagittal planes: lateral left, medial, lateral right. Squares mark the region shown at higher magnification in the images below. (**F**) Hoechst stainings and immunofluorescence for pH3 and tdTomato in Gabra6-cre;LSL-tdTomato mice at P10 at three different sagittal planes: lateral left, medial, lateral right. Squares mark the region shown at higher magnification in the images below. (**G,H**) Confocal images of immunofluorescence for Sox2 and tdTomato of sagittal brain sections of P10 (**G**) and P14 (**H**) in Gabra6-cre;LSL-tdTomato mice. (**I,J**) Confocal images of immunofluorescence for Sox9 and tdTomato of sagittal brain sections of P10 (**I**) and P14 (**J**) in Gabra6-cre;LSL-tdTomato mice. (**K**) Immunofluorescence for tdTomato, PCNA and NeuN of sagittal brain sections of P14 Gabra6-cre;LSL-tdTomato mouse. Arrows point to cerebellar lobules VI and VII expressing less tdTomato than other lobules. (**L**) Quantification of tdTomato and either PCNA or NeuN double positive cells of sagittal brain sections of P4, P7, P10, P14 Gabra6-cre;LSL-tdTomato mice. Mean±S.D. n=3. Scale bar 50 µm (**G-J**), 100 µm (**C,D,E,F**), 1 mm (**K**). IGL, Internal Granular Layer. EGL, External Granular Layer.
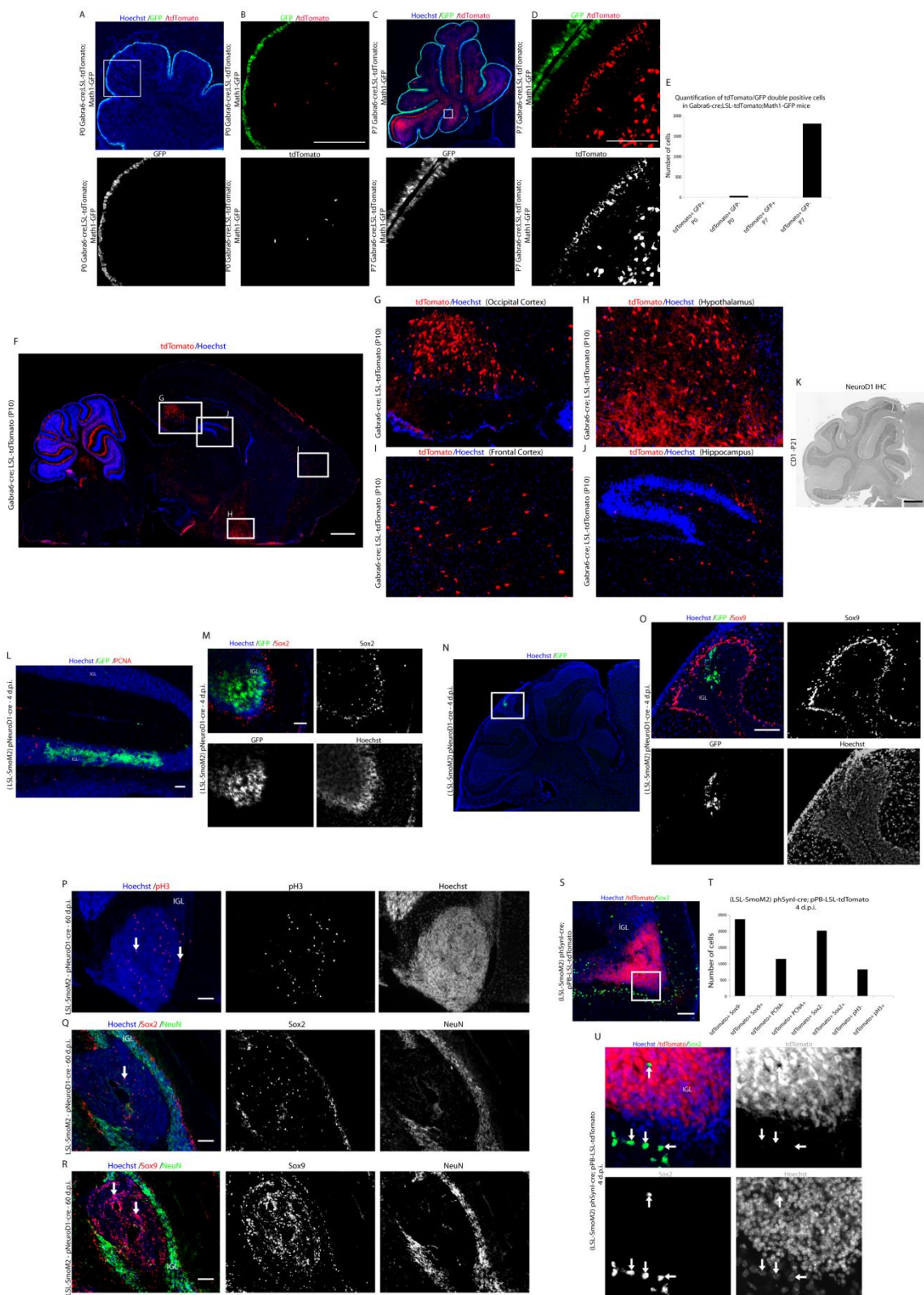
Figure S4

Figure S4, related to Figure 22, 24 and 26 | Gabra6, NeuroD1 and hSynI promoters specificity

(**A**) Hoechst staining and immunofluorescence for GFP and tdTomato of sagittal brain sections of P0 Gabra6-cre;Math1-GFP;LSL-tdTomato mouse. Square in **A** marks the region shown at higher magnification in **B**. (**B**) Hoechst staining and immunofluorescence for GFP and tdTomato of sagittal brain sections of P0 Gabra6-cre;Math1-GFP;LSL-tdTomato mouse. (**C**) Hoechst staining and immunofluorescence for GFP and tdTomato of sagittal brain sections of P7 Gabra6-cre;Math1-GFP;LSL-tdTomato mouse. Square in **C** marks the region shown at higher magnification in **D**. (**D**) Hoechst staining and immunofluorescence for GFP and tdTomato of sagittal brain sections of P7 Gabra6-cre;Math1-GFP;LSL-tdTomato mouse. (**E**) Quantification of tdTomato+/GFP+ and tdTomato+/GFP- cells in Gabra6-cre;Math1-GFP;LSL-tdTomato mouse, at P0 and P7. (**F**) Hoechst staining and immunofluorescence for tdTomato of sagittal brain section in P10 Gabra6-cre;LSL-tdTomato mouse. Squares in **F** mark the regions shown at higher magnification in **G-J**. (**K**) Immunohistochemistry for NeuroD1 in a P21 CD1 mouse. (**L**) Hoechst staining and immunofluorescence for GFP and PCNA of sagittal brain sections of LSL-SmoM2 mice, 4 d.p.i. at P21 with pNeuroD1-cre. (**M**) Hoechst staining and immunofluorescence for GFP and Sox2 of sagittal brain sections, 4 d.p.i. at P21 with pNeuroD1-cre. (**N**) Hoechst staining and immunofluorescence for GFP of sagittal brain sections of LSL-SmoM2 mouse, 4 d.p.i. at P21 with pNeuroD1-cre. Square in **N** marks the region shown at higher magnification in **O**. (**O**) Hoechst staining and immunofluorescence for GFP and Sox9 of sagittal brain sections, 4 d.p.i. at P21 with pNeuroD1-cre. (**P**) Hoechst staining and immunofluorescence for pH3 of sagittal brain sections of LSL-SmoM2 mouse, 60 d.p.i. at P21 with pNeuroD1-cre. Arrows point to pH3 positive cells within the tumor. (**Q**) Hoechst staining and immunofluorescence for Sox2 and NeuN of sagittal brain sections of LSL-SmoM2 mouse, 60 d.p.i. at P21 with pNeuroD1-cre. Arrow points to Sox2 positive cell within the tumor. (**R**) Hoechst staining and immunofluorescence for Sox9 and NeuN of sagittal brain sections of LSL-SmoM2 mouse, 60 d.p.i. at P21 with pNeuroD1-cre. Arrows point to Sox9 positive cells within the tumor. (**S**) Hoechst staining and immunofluorescence for Sox2 and tdTomato of sagittal brain sections of LSL-SmoM2 mouse, 4 d.p.i. at 2 months with phSynI-cre+pPB-CAG-LSL-tdTomato. Square in **S** marks the region shown at higher magnification in **U**. (**T**) Quantification of tdTomato and Sox9/PCNA/Sox2/pH3 double positive cells in LSL-SmoM2 mice, 4 d.p.i. at 2 months with phSynI-cre+pPB-LSL-tdTomato. (**U**) Hoechst staining and immunofluorescence for Sox2 and tdTomato of sagittal brain sections of LSL-SmoM2 mouse, 4 d.p.i. at 2 months with phSynI-cre+pPB-CAG-LSL-tdTomato. Arrows point to Sox2 positive cells. Scale bar 100 μm (**B,D,O**), 150 μm (**L,M,P,Q,R,S**), 1 mm (**F,K**). IGL, Internal Granular Layer. d.p.i. days post injection.

Figure S5

112
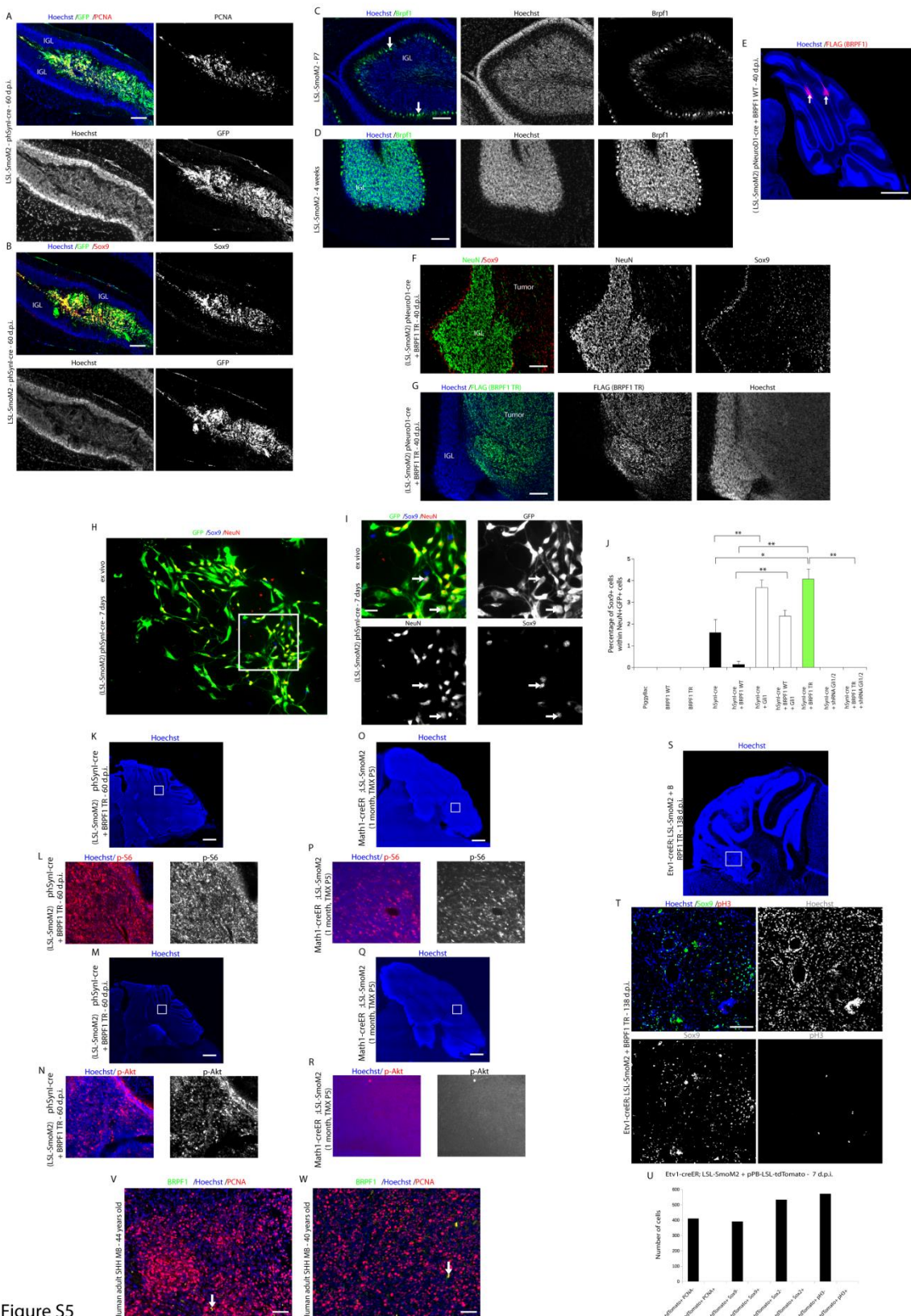
Figure S5, related Figure 24,25 and 26 | pNeuroD1-cre/phSynI-cre + BRPF1 TR transfection promotes adult Shh MB formation in LSL-SmoM2 mice, while wild type BRPF1 blocks cancer formation from postmitotic neurons. BRPF1 and Shh pathway cooperation analysis in *ex vivo* cerebellar assay, specific co-expression of human adult SHH MB markers in LSL-SmoM2 mice transfected with phSynI-cre+BRPF1 TR and MB development in Etv1-creER;LSL-SmoM2 mice after transfection with BRPF1 TR.

(**A**) Hoechst staining and immunofluorescence for GFP and PCNA of sagittal brain sections of LSL-SmoM2 mouse, 60 d.p.i. at 2 months with phSynI-cre. (**B**) Hoechst staining and immunofluorescence for GFP and Sox9 of sagittal brain sections of LSL-SmoM2 mouse, 60 d.p.i. at 2 months with phSynI-cre. (**C,D**) Hoechst staining and immunofluorescence for Brpf1 of sagittal brain sections of P7 (**C**) and 4-week-old (**D**) LSL-SmoM2 mice. Arrows point to single Brpf1 positive cells. (**E**) Hoechst staining and immunofluorescence for FLAG (BRPF1) of sagittal brain sections of LSL-SmoM2 mouse, 40 d.p.i. at P21 with pNeuroD1-cre+BRPF1 WT. Arrows point to BRPF1 WT positive cell clusters. (**F**) Immunofluorescence for NeuN and Sox9 of sagittal brain sections of LSL-SmoM2 mice, 40 d.p.i. at P21 with pNeuroD1-cre+BRPF1 TR. (**G**) Hoechst staining and immunofluorescence for FLAG (BRPF1) of sagittal brain sections of LSL-SmoM2 mouse, 40 d.p.i. at P21 with pNeuroD1-cre+BRPF1 TR. (**H**) Immunofluorescence for GFP, Sox9 and NeuN 7 days after nucleofection with phSynI-cre, pPB-GFP, pPB-Venus, PBase of *ex vivo* cultured cerebellar cells from P7 LSL-SmoM2 mice. Square in **H** marks the region shown at higher magnification in **I**. (**I**) Immunofluorescence staining for GFP, Sox9 and NeuN 7 days after nucleofection with phSynI-cre, pPB-GFP, pPB-Venus, PBase of *ex vivo* cultured cerebellar cells from P7 LSL-SmoM2 mice. Arrows point to GFP/NeuN/Sox9 triple positive cells. (**J**) Histograms show the percentage of cells expressing Sox9+ among all NeuN+GFP+ double positive cells 7 days after nucleofection with PiggyBac , BRPF1 WT, BRPF1 TR, phSynI-cre, phSynI-cre+BRPF1 WT, phSynI-cre+Gli1, phSynI-cre+BRPF1 WT+Gli1, phSynI-cre+BRPF1 TR, phSynI-cre+shRNAGli1/2 and phSynI-cre+BRPF1 TR+shRNAGli1/2 of *ex vivo* cultured cerebellar cells from P7 LSL-SmoM2 mice (see Materials and Methods). *Ex-vivo* data are presented as mean + s.e.m. of three biologically independent *ex vivo* experiments. Two-sided Student's t test was used for calculating significance values. PiggyBac n=1733 cells, BRPF1 WT n=1841 cells, BRPF1 TR n=1637 cells, phSynI-cre n=1185 cells, phSynI+BRPF1 WT=1321 cells, phSynI-cre+Gli1 n=2156 cells, phSynIcre+BRPF1 WT+Gli1 n=4238 cells, phSynI+BRPF1 TR=837 cells, phSynIcre+shGli1+shGli2 n=3796 cells, phSynIcre+BRPF1 TR+shGli1+shGli2 n=3505 cells. *p value<0.05. **p value<0.01. (**K**) Hoechst staining of sagittal brain sections of MB in LSL-SmoM2 mouse, 60 d.p.i. at 2 months with phSynI-cre+BRPF1 TR. Square in **K** marks the region shown at higher magnification in **L**. (**L**) Hoechst staining and immunofluorescence for p-S6 of sagittal brain sections of MB in LSL-SmoM2 mouse, 60 d.p.i. at 2 months with phSynI-cre+BRPF1 TR. (**M**) Hoechst staining of sagittal brain sections of MB in LSL-SmoM2 mouse, 60 d.p.i. at 2 months with phSynI-cre+BRPF1 TR. Square in **M** marks the region shown at higher magnification in **N**. (**N**) Hoechst staining and immunofluorescence for p-Akt of sagittal brain sections of MB in LSL-SmoM2 mouse 60 d.p.i. at 2 months with phSynI-cre+BRPF1 TR. (**O**) Hoechst staining of sagittal brain sections of MB in 1-month-old Math1-creER;LSL-SmoM2 mouse injected with Tamoxifen at P5. Square in **O** marks the region shown at higher magnification in **P**. (**P**) Hoechst staining and immunofluorescence for p-S6 of sagittal brain sections of MB in 1-month-old Math1-creER;LSL-SmoM2 mouse injected with Tamoxifen at P5. (**Q**) Hoechst staining of sagittal brain sections of MB in 1-month-old Math1-creER;LSL-SmoM2 mouse injected with Tamoxifen at P5. Square in **Q** marks the region shown at higher magnification in **R**. (**R**) Hoechst staining and immunofluorescence for p-Akt of sagittal brain sections of MB in 1-month-old Math1-creER;LSL-SmoM2 mouse injected with Tamoxifen at P5. (**S**) Hoechst staining of sagittal brain sections of 138 d.p.i. Etv1-creER;LSL-SmoM2 mouse, transfected with BRPF1 TR (at 3 months) and then injected with tamoxifen. Square in **S** marks the region shown at higher magnification in **T**. (**T**) Hoechst staining and immunofluorescence for Sox9 and pH3 of sagittal brain sections of 138 d.p.i. Etv1-creER;LSL-SmoM2 mouse transfected with BRPF1 TR (at 3 months) and then injected with tamoxifen. (**U**) Quantification of tdTomato and PCNA/Sox9/Sox2/pH3 double positive cells in 7 d.p.i. Etv1-creER;LSL-SmoM2 mice transfected with pPB-CAG-LSL-tdTomato (at 3 months) and then injected with tamoxifen. (**V**) Hoechst staining and immunofluorescence for BRPF1 and

PCNA of human adult SHH MB (nodular/desmoplastic) brain section from a 44-year-old female patient. (**W**) Hoechst staining and immunofluorescence for BRPF1 and PCNA of human adult SHH MB (nodular/desmoplastic) brain section from a 40-year-old male patient. Arrows point to BRPF1 positive cells. Scale bar 25 μm (**I**), 100 μm (**T,V,W**), 150 μm (**A,B**), 200 μm (**C,D,F,G**), 1 mm (**E,K,M,O,Q**). d.p.i. days post injection.

A ATAC-seq signal on total genes

B

C
Biological processes enriched in Gabra6-cre

Biological processes enriched in Gabra6-cre (GREAT annotation)

Biological processes enriched in Gabra6-cre;LSL-SmoM2

Biological processes enriched in Gabra6-cre;LSL-SmoM2 (GREAT annotation)

D ATAC-seq signal on P14 opened DHS (n=11060)

ATAC-seq signal on P60 opened DHS (n=5613)

E P14 up-regulated genes (n=513)

P60 up-regulated genes (n=476)

F Venus

G qRT-PCR analysis - differentiated AF22

H qRT-PCR analysis - differentiated AF22

Figure S6

115

Figure S6, related to Figure 27 and 28 | SmoM2 expression in murine granule neurons favors widespread chromatin plasticity.

(**A**) Average tag density plot of the normalized (RPM) ATAC-seq signal along the gene bodies of all genes in Gabra6-cre and Gabra6-cre;LSL-SmoM2 cells. (**B**) Genomic snapshot showing the *Math1* locus and the normalized ATAC-seq signals in Gabra6-cre and Gabra6-cre;LSL-SmoM2 cells. (**C**) Gene ontology analysis on the genes annotated to specific ATAC-seq peaks in Gabra6-cre (upper panels) or Gabra6-cre;LSL-SmoM2 (lower panels) cells. The biological processes enriched in either condition are reported. The peaks were annotated to relative genes with either the Homer command 'annotatePeaks.pl' or with the Genomic Regions Enrichment of Annotations Tool (GREAT). (**D**) Average tag density plot of the normalized (RPM) ATAC-seq signal in Gabra6-cre and Gabra6-cre;LSL-SmoM2 cells, on previously reported DNase Hypersensitive Sites (DHS), which resulted more accessible in P14 (left) or P60 (right) cerebella, when compared to P7 cerebellum. (**E**) Gene Set Enrichment Analysis (GSEA) of genes, which previously resulted to be up-regulated in P14 (upper panel) or P60 (lover panel) cerebella, when compared to P7 cerebellum. NES = Normalized Enrichment Score; FDR = False Discovery Rate. All analysis are performed on 3 and 4 biological replicates for P14 Gabra6-cre and Gabra6-cre;LSL-SmoM2 cerebella, respectively. (**F**) Venus expression in human AF22 cells, differentiated in postmitotic neurons and nucleofected with pPBhSynI-creER-IRES-Venus+pPB-LSL-BRPF1 TR+pPB-LSL-SmoM2, 48h after tamoxifen. (**G**) qRT-PCR analysis for ZIC1 gene expression in hiPSC and AF22 cells, differentiated in postmitotic neurons and nucleofected with pPBhSynI-creER-IRES-Venus, 48h after tamoxifen. (**H**) qRT-PCR analysis for GLI1 gene expression in differentiated AF22 cells, after nucleofection with pPBhSynI-creER-IRES-Venus, pPBhSynI-creER-IRES-Venus+pPB-LSL-SmoM2, pPBhSynI-creER-IRES-Venus+pPB-LSL-BRPF1 TR, pPBhSynI-creER-IRES-Venus+pPB-LSL-SmoM2+pPB-LSL-BRPF1 TR, 48h after tamoxifen. Mean + s.e.m. n=3. **p value<0.01. Scale bars 100 µm (**F**).
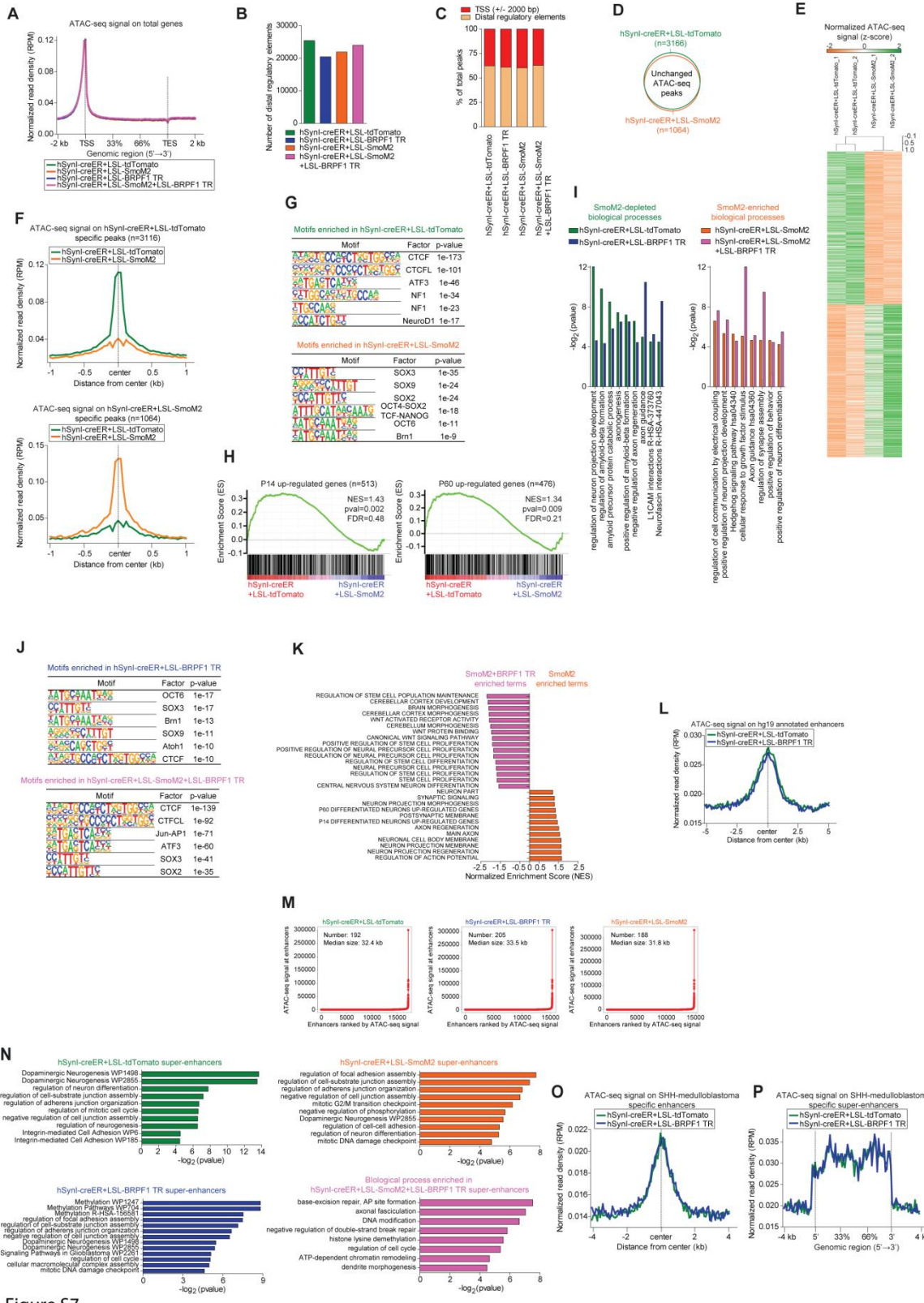
Figure S7

Figure S7, related to Figure 28 | Truncated BRPF1, in synergy with SmoM2, reprograms the super-enhancers landscape, thus favoring medulloblastoma disruption.

(A) Average tag density plot of the normalized (RPM) ATAC-seq signal along the gene bodies of all genes in indicated cell lines. **(B)** Barplot showing the number of distal regulatory elements (excluded from TSS ± 2 kb) in indicated cell lines. **(C)** Barplot showing the percentage of ATAC-seq peaks locating on either TSS (± 2 kb) or distal regulatory elements in indicated cell lines. **(D)** Venn diagram showing the overlap between ATAC-seq peaks in hSynI-creER+LSL-tdTomato and hSynI-creER+LSL-SmoM2 cells. **(E)** Heatmap representing the normalized ATAC-seq signal (Z-score) on the top 2000 most differentially enriched peaks in either hSynI-creER+LSL-tdTomato or hSynI-creER+LSL-SmoM2 cells. **(F)** Average tag density plot of the normalized (RPM) ATAC-seq signal on the differential peaks, enriched either in hSynI-creER+LSL-tdTomato (upper panel) or hSynI-creER+LSL-SmoM2 (lower panel) cells. **(G)** Motif enrichment analysis on the specific ATAC-seq peaks in indicated cells. Analysis are performed on 2 biological replicates for each cell line. **(H)** Gene Set Enrichment Analysis (GSEA) of genes, which previously resulted to be up-regulated in P14 (left panels) or P60 (right panels) cerebella, when compared to P7 cerebellum, in the indicated comparisons. NES = Normalized Enrichment Score; FDR = False Discovery Rate. **(I)** Gene ontology analysis on genes annotated to specific ATAC-seq peaks in hSynI-creER+LSL-tdTomato and hSynI-creER+LSL-BRPF1 TR (left panel) or hSynI-creER+LSL-SmoM2 cells and hSynI-creER+LSL-SmoM2+LSL-BRPF1 TR (right panel) cells. The SmoM2-depleted or -enriched biological processed are reported. **(J)** Motif enrichment analysis on the specific ATAC-seq peaks in indicated cells. **(K)** Gene Set Enrichment Analysis (GSEA) of indicated gene lists, in hSynI-creER+LSL-SmoM2 versus hSynI-creER+LSL-SmoM2+LSL-BRPF1 TR cells. All gene lists are enriched with a statistical p-value < 0.05. **(L)** Average tag density plot of the normalized (RPM) ATAC-seq signals in hSynI-creER+LSL-tdTomato and hSynI-creER+LSL-BRPF1 TR cells, on annotated enhancer regions of human genome hg19/GRCh37. **(M)** Distribution of the ATAC-seq signal across hSynI-creER+LSL-tdTomato, hSynI-creER+LSL-BRPF1 TR, hSynI-creER+LSL-SmoM2 enhancers, showing the presence of 192, 205 and 188 super-enhancers, respectively. The median length of super-enhancers is reported. **(N)** Gene ontology analysis on the genes associated to hSynI-creER+LSL-tdTomato (green), hSynI-creER+LSL-BRPF1 TR (blue), hSynI-creER+LSL-SmoM2 (orange) and hSynI-creER+LSL-SmoM2+LSL-BRPF1 TR (purple) super-enhancers. Biological processes and pathways from Reactome, Panther, WikiPathways and KEGG databases were analyzed. **(O-P)** Average tag density plot of the normalized (RPM) ATAC-seq signals in hSynI-creER+LSL-tdTomato and hSynI-creER+LSL-BRPF1 TR cells, on previously reported enhancers (**O**) and super-enhancers (**P**), which characterize the SHH MB. Analysis are performed on 2 biological replicates for each cell line.

10.2 Table S1, related to Figure 22| Differential expressed gene list between Gabra6-cre;LSL-SmoM2 and CD1 mice

Differential expressed gene list as a results of the comparison between the Gabra6-cre;LSL-SmoM2 samples and the CD1, normal cerebellum tissue. Several gene annotations are reported. The statistical column are the standard output of limma topTable function.

Download link:
https://www.cell.com/cell-reports/fulltext/S2211-1247(19)31528-1?_returnURL=https%3A%2F%2Flinkinghub.elsevier.com%2Fretrieve%2Fpii%2FS2211124719315281%3Fshowall%3Dtrue#secsectitle0265

Cell Reports

Truncated BRPF1 Cooperates with Smoothened to Promote Adult Shh Medulloblastoma

Graphical Abstract
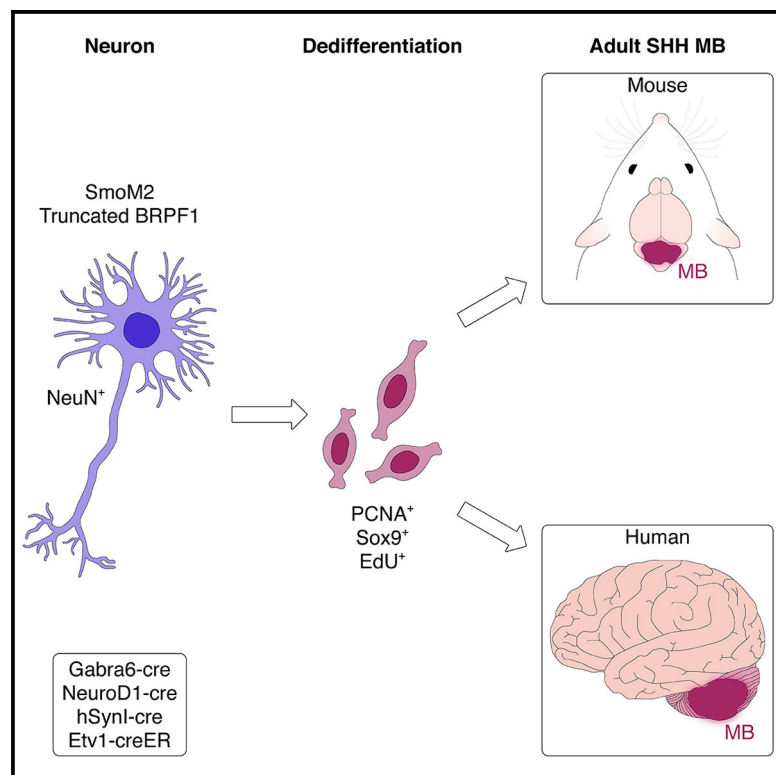
Authors

Giuseppe Aiello, Claudio Ballabio,
Riccardo Ruggeri, ...,
Alessandro Romanel, Alessio Zippo,
Luca Tiberi

Correspondence

luca.tiberi@unitn.it

In Brief

Medulloblastoma is a brain tumor affecting the cerebellum of infants and adults. Aiello et al. establish a mouse model for adult onset, which allows investigation of the pathogenesis of the disease and identifies neurons as putative cells of origin.

Highlights

- SmoM2 overexpression promotes cerebellar granule neurons dedifferentiation *in vivo*

- SmoM2 and mutant BRPF1 cooperation *in vivo* mimics human adult SHH MBs

- Granule neurons are putative cells of origin of adult SHH MBs

- Truncated BRPF1 increases the accessibility of a subset of super-enhancers

CellPress

Truncated BRPF1 Cooperates with Smoothened to Promote Adult Shh Medulloblastoma

Giuseppe Aiello,[1] Claudio Ballabio,[1] Riccardo Ruggeri,[1] Luca Fagnocchi,[2] Marica Anderle,[1] Ilaria Morassut,[1] Davide Caron,[1] Francesca Garilli,[1] Francesca Gianno,[3,4] Felice Giangaspero,[3,4] Silvano Piazza,[5] Alessandro Romanel,[6] Alessio Zippo,[2] and Luca Tiberi[1,7,*]

[1]Armenise-Harvard Laboratory of Brain Disorders and Cancer, CIBIO, University of Trento, Via Sommarive 9, 38123 Trento, Italy
[2]Laboratory of Chromatin Biology & Epigenetics, CIBIO, University of Trento, Via Sommarive 9, 38123 Trento, Italy
[3]Department of Radiologic, Oncologic and Anatomo Pathological Sciences, University Sapienza of Rome, Rome, Italy
[4]IRCCS Neuromed, Pozzilli, Isernia, Italy
[5]Bioinformatics Core Facility, CIBIO, University of Trento, Via Sommarive 9, 38123 Trento, Italy
[6]Laboratory of Bioinformatics and Computational Genomics, CIBIO, University of Trento, Via Sommarive 9, 38123 Trento, Italy
[7]Lead Contact
*Correspondence: luca.tiberi@unitn.it
https://doi.org/10.1016/j.celrep.2019.11.046

SUMMARY

The transition of neural progenitors to differentiated postmitotic neurons is mainly considered irreversible in physiological conditions. In the present work, we show that Shh pathway activation through SmoM2 expression promotes postmitotic neurons dedifferentiation, re-entering in the cell cycle and originating medulloblastoma *in vivo*. Notably, human adult patients present inactivating mutations of the chromatin reader BRPF1 that are associated with SMO mutations and absent in pediatric and adolescent patients. Here, we found that truncated BRPF1 protein, as found in human adult patients, is able to induce medulloblastoma in adult mice upon SmoM2 activation. Indeed, postmitotic neurons re-entered the cell cycle and proliferated as a result of chromatin remodeling of neurons by BRPF1. Our model of brain cancer explains the onset of a subset of human medulloblastoma in adult individuals where granule neuron progenitors are no longer present.

INTRODUCTION

Tumors are composed of proliferating cells that invade healthy tissue and grow over time. Even though it is still unclear, it is a common opinion that the cells of origin should possess a proliferative capacity (Blanpain, 2013; Visvader, 2011). The transition of neural progenitors to differentiated postmitotic neurons is considered irreversible in physiological and pathological conditions (Deneris and Hobert, 2014; Nguyen et al., 2006). Therefore, postmitotic neurons have not been considered as suitable cells of origin of brain cancer. Interestingly, few groups have attempted to induce cancer from neurons using full knockout (KO) mice for cell-cycle regulators or by genetic modification of mice and *Drosophila melanogaster* (Ajioka et al., 2007; Friedmann-Morvinski et al., 2012; Southall et al., 2014). Furthermore, it is still unclear whether this process could be relevant to human brain cancer formation. For instance, human SHH medulloblastoma (MB) is a brain tumor found in adults and infants that is thought to originate from cerebellar granule neuron progenitors. Notably, several groups have shown that Shh pathway activation (SmoM2 overexpression) in mouse granule neuron progenitors is able to induce Shh MB (Schüller et al., 2008; Yang et al., 2008). These progenitors are present in infants and newborn mice, but they seem not to be present in adult humans and mice (Marzban et al., 2015; Yang et al., 2008), therefore suggesting that adult MB could originate from a different subset of cells. Based on these data, we speculate that postmitotic neurons are the cells of origin of adult SHH MBs. Interestingly, several adult SHH MB patients present truncated mutations of the chromatin reader BRPF1 that are often associated with Smoothened (SMO) mutations and completely absent in pediatric and adolescent patients (Kool et al., 2014). Therefore, we investigate whether BRPF1 mutations could be required to allow tumor formation in adult patients.

RESULTS

SmoM2 Expression in Granule Neurons Promotes MB

In the present work, we investigated if postmitotic neurons could dedifferentiate *in vivo* and if this process could lead to Shh MB in mice. To do so, we induced Shh pathway activation through the expression of a constitutively active Smo mutant (SmoM2) to mimic the SMO gain of function mutations present in human adult SHH MB (Kool et al., 2014; Northcott et al., 2012). In particular, to examine if neurons can dedifferentiate *in vivo*, we conditionally induced SmoM2-EYFP expression (*LSL-SmoM2* mice) in postmitotic neurons using *Gabra6-cre* mouse (Aller et al., 2003). Indeed, GABAA receptor α6 subunit (Gabra6) is expressed only in postmitotic neurons and it has already been shown that *Gabra6-cre* mouse induces recombination in neurons of the cerebellum, midbrain, and cortex. As shown in Figures 1A and 1B, *Gabra6-cre;LSL-SmoM2* mice developed MBs (7 and 4 months) and showed signs of ataxia, frequent falls, and weight loss (n = 9). Moreover, Kaplan-Meier survival analysis showed that less than 50% of the mice were still alive after 300 days (Figure 1C). Notably, we found
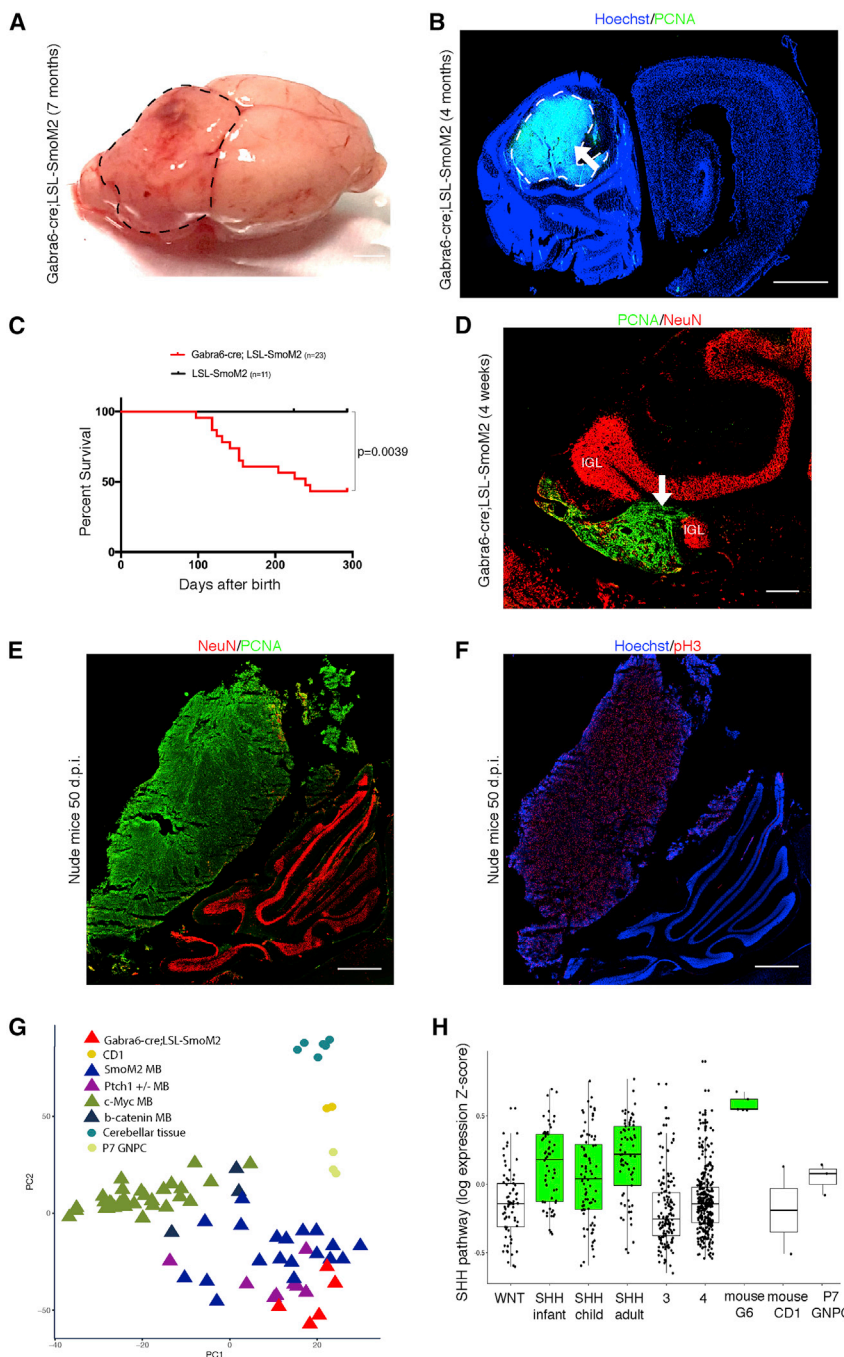
Figure 1. SmoM2 Expression in Granule Neurons Promotes Shh MB

(A) Image of 7-month-old *Gabra6-cre;LSL-SmoM2* MB.

(B) Hoechst and PCNA staining of brain section of 4-month-old *Gabra6-cre;LSL-SmoM2* mouse. The arrow points to the tumor.

(C) Kaplan-Meier survival curves of *LSL-SmoM2* and *Gabra6-cre;LSL-SmoM2* mice.

(D and E) PCNA and NeuN staining of brain sections of 4-week-old *Gabra6-cre;LSL-SmoM2* mouse (D) and 4-month-old nude mice, 50 days post injection (d.p.i.), with *Gabra6-cre;LSL-SmoM2* MB cells (E); arrow points to the tumor. Lower and higher magnifications of (D) are shown in Figures S1AK and S1AL.

(F) Hoechst and pH3 staining of brain sections of 4-month-old nude mice, 50 d.p.i., with *Gabra6-cre;LSL-SmoM2* MB cells.

(G) Multidimensional scaling of several MB mouse models, plotting the results of the two principal coordinates. Original GEO dataset entries (GEO: GSE11859, GSE24628, and GSE33199). PC1, principal coordinate 1; PC2, principal coordinate 2.

(H) Boxplots of the median values of the Shh genes for the human samples (GEO: GSE85217) and *Gabra6-cre;LSL-SmoM2* MB. *CD1*, normal cerebellum tissue; G6, *Gabra6-cre;LSL-SmoM2*; SHH, SHH subgroup; WNT, WNT subgroup; 3, group 3; 4, group 4; P7 GNPC, P7 granule neuron progenitors cell.

Scale bars, 2 mm in (A), 1 mm in (B), (E), and (F), and 250 μm in (D). The dashed lines in (A) and (B) mark the tumors. d.p.i., days post injection.

at higher levels in human adult SHH MBs, compared to the infant form (Al-Halabi et al., 2011). Notably, Sox2 and Sox9 proteins are also expressed in mouse neural stem cells, Bergmann glia cells, and at low levels in granule neuron progenitors during cerebellum development (Ahlfeld et al., 2013; Sutter et al., 2010; Vong et al., 2015). The tumors were also positive for doublecortin (Dcx), a marker for highly proliferative progenitors present in mouse Shh MBs (Figure S1F). The tumors were EYFP positive (GFP antibody), thus confirming that SmoM2-EYFP is expressed in cancer cells (Figure S1G). Furthermore, histopathological and immunophenotypical analyses confirmed that tumors in *Gabra6-cre;LSL-SmoM2* mice are Shh MBs (Yap1 and Gab1 positive and with cytoplasmic beta-catenin) (Ellison et al., 2011) (Figures S1I–S1R). In our search for putative genes required for neuron dedifferentiation, we crossed *Gabra6-cre;LSL-SmoM2* mice with *Sox9*flox mice. In fact, it has already been shown that SmoM2 requires Sox9 to induce basal cell carcinoma (skin cancer) (Larsimont et al., 2015). Interestingly, we also obtained MBs in *Gabra6-cre;LSL-SmoM2;Sox9*flox/flox mice (3/3 mice; Figure S1H),

cerebellum aberrations and presence of tumor cells expressing PCNA, a marker of cell proliferation, as early as in 4-week-old mice (Figure 1D). The tumor localization suggests that it could originate from neurons of the EGL (external granular layer), IGL (internal granular layer), or the molecular layer. Several cells within the tumor were also Sox9 (Figures S1A, S1B, and S1E) and Sox2 positive (Figures S1C, S1D, and S1E), two cell markers present in mouse and human SHH MBs (Sutter et al., 2010; Swartling et al., 2012; Vanner et al., 2014) and expressed

Figure 2. SmoM2 Promotes Dedifferentiation of Granule Neurons

(A and B) Hoechst, PCNA, and NeuN staining of brain sections of P14 *Gabra6-cre;LSL-SmoM2* mouse. Square in (A) marks the region shown at higher magnification in (B). Arrows point to PCNA/NeuN double-positive cells.

(C and D) Hoechst, Sox9, and NeuN staining of brain sections of P14 *Gabra6-cre;LSL-SmoM2* mouse. Square in (C) marks the region shown at higher magnification in (D). Arrows point to Sox9/NeuN double-positive cells.

(E and F) Hoechst, EdU, and NeuN staining of brain sections of P21 *Gabra6-cre;LSL-SmoM2* mouse, injected with EdU at P19. Square in (E) marks the region shown at higher magnification in (F). Lower magnification of (E) is shown in Figure S2Q. Arrows point to EdU/NeuN double-positive cells.

Scale bars, 25 μm in (B), (D), and (F). EGL, external granular layer; IGL, internal granular layer.

(Figures 1E and 1F; data not shown). To further characterize our mouse model, we examined the expression profiles of five different *Gabra6-cre;LSL-SmoM2* MBs and compared them to wild-type (WT) cerebellar tissue obtained from CD1 mice. In particular after determining the differentially expressed genes (Table S1), we performed functional annotation procedures using the Database for Annotation, Visualization and Integrated Discovery (DAVID) and gene set enrichment analysis (GSEA). As shown in Figures S1S and S1T, the tumor samples presented an increase in the expression of genes linked to cell cycle, DNA replication, and as expected to the Shh pathway. Consistently, we observed a decreased expression of genes related to normal neuron functions like the synaptic vesicles cycle (Figure S1T). We then compared our model to several types of MB mouse models using publicly available datasets (GEO: GSE11859, GSE24628, and GSE33199). PCA analysis showed that the gene expression profile of tumors retrieved from *Gabra6-cre;LSL-SmoM2* clustered with *SmoM2*

indicating that Sox9 functions are not conserved between skin and brain cancer. To further confirm the tumorigenicity of *Gabra6-cre;LSL-SmoM2* MB cells, we performed tumor transplantation experiments. Specifically, we isolated cells from 4-month-old tumor-bearing *Gabra6-cre;LSL-SmoM2* cerebella and then we injected the cells into the cerebellum of 4-month-old nude mice (*Foxn1^nu*). Our results showed that all four mice injected with *Gabra6-cre;LSL-SmoM2* MB cells generated tumors populated by PCNA, NeuN, and pH 3 positive cells

and *Ptch1^{+/−}* Shh MB mouse models (Figure 1G). Finally, we compared our model to human SHH MB gene expression dataset (GEO: GSE85217), with respect to the enrichment of the SHH pathway signature. This analysis showed that *Gabra6-cre;LSL-SmoM2* (G6) samples activated the SHH pathway to the same extent as human SHH MBs (Figure 1H). Together, these results are consistent with the hypothesis that Gabra6-cre;LSL-SmoM2 represents a putative Shh MB mouse model.

SmoM2 Promotes Dedifferentiation of Granule Neurons

Our data suggest that Smo gain of function in postmitotic neurons is sufficient to induce MB formation and reinforce the possibility that neurons are dedifferentiating. To clarify if the granule neurons started dedifferentiating at early stages of tumor formation, we analyzed *Gabra6-cre;LSL-SmoM2* mice at postnatal day 14 (P14). As shown in Figures 2A and 2B, few PCNA and NeuN double-positive cells can be detected at this stage in mouse cerebellum (33 ± 8 cells in three sections for each brain, mean ± SD, n = 4 brains), indicating that neurons have started to proliferate without losing NeuN expression. Notably, we did not observe PCNA and NeuN double-positive cells in control mice (*LSL-SmoM2*) (Figure S1H; data not shown), therefore indicating that SmoM2 induction upon cre expression was responsible for this proliferation burst. This suggests that the PCNA and NeuN double-positive cells could represent the cell of origin of Shh MBs. Interestingly, we also identified Sox9/Sox2 and NeuN double-positive cells, indicating that some neurons while dedifferentiating start expressing markers of neuronal progenitors (Figures 2C, 2D, S1U, and S1V). Of notice, the same phenotype was not observed in control mice (Figure S1H). Indeed, it has been published that rare Sox2-expressing cells are the founding cancer stem cell population driving cancer initiation and therapy resistance (Vanner et al., 2014) in mouse models of infant Shh MBs. Based on this knowledge, we analyzed the *Gabra6-cre;LSL-SmoM2* mice at different time points and we detected Sox9/PCNA and NeuN double-positive cells at P7, P14, P21, and P28 (Figures S1W–S1AD and S1AE–S1AL). Notably, at P21 we already observed small clusters of PCNA-positive cells (Figures S1AI and S1AJ) and aberrant Sox9 expression (Figures S1AA and S1AB). SmoM2 expression was confirmed by immunofluorescence using a GFP antibody that recognizes the YFP fused to SmoM2 (Figures S1AM–S1AP). To better detect and identify dedifferentiated neurons, we crossed the *Gabra6-cre;LSL-SmoM2* mice with *LSL-tdTomato* mice that express tdTomato only upon cre recombination (Madisen et al., 2010). As shown in Figures S2A–S2L, we did not observe tdTomato expression in mice embryos at embryonic day 16.5 (E16.5) (*Gabra6-cre;LSL-SmoM2;LSL-tdTomato*), but we detected PCNA/Sox9 and tdTomato double-positive cells in the IGL at P7 and P14, when granule neurons are already present. Since *Gabra6-cre* mice express cre recombinase also in few deep cerebellar nuclei (DCN) cells (Aller et al., 2003), we analyzed PCNA expression in *Gabra6-cre;LSL-tdTomato* and *Gabra6-cre;LSL-SmoM2* in DCN. Notably, we did not detect any aberrant PCNA staining at P21 in both mice (Figures S2M–S2P). Therefore, we postulate that the tumors should not originate from dedifferentiated neurons of DCN. Taken together, these data suggest that the Sox2/Sox9 and NeuN double-positive cells identified in the cerebellum of *Gabra6-cre;LSL-SmoM2* mice could be dedifferentiated granule neurons that originate Shh MB. To further confirm our hypothesis, we injected EdU in *Gabra6-cre;LSL-SmoM2* mice at P19 to avoid EdU incorporation in progenitors (that are not present at this time point) and to label only neurons that re-enter in the cell cycle. As shown in Figures 2E, 2F, and S2Q, we observed small clusters of EdU-positive cells in the IGL in P21 *Gabra6-cre;LSL-SmoM2* mice and not in *Gabra6-cre;LSL-tdTomato* mice (Figures S2R and S2S–S2AC). Therefore, we

speculate that the EdU-positive cells could be dedifferentiated neurons. Since Ptch1 ablation in cerebellar progenitors is able to induce Shh MB in a few months (Northcott et al., 2012), we analyzed the effect of Ptch1 loss in postmitotic neurons in *Gabra6-cre;Ptch1*^{flox/flox} and *Gabra6-cre;Ptch1*^{flox/+} mice, but we did not observe MB development (Figure S1H). To understand the reason why SmoM2 overexpression, unlike Ptch1 deletion, leads to tumor formation, we analyzed their cerebella at P14 by quantitative real-time PCR. As shown previously, at this stage most of the granule neurons have been produced and in *Gabra6-cre;LSL-SmoM2* there is no tumor formation yet. Gene expression analysis revealed that *Math1* and *Gli1* genes are upregulated specifically in *Gabra6-cre;LSL-SmoM2* mice, but not in *Gabra6-cre;Ptch1*^{flox/flox} (Figure S3A). These data suggest that SmoM2 overexpression induces a much stronger activation of Shh signaling and Math1 (specific marker for granule neuron progenitors) as compared to Ptch1 loss and could explain the presence of Shh MBs in *Gabra6-cre;LSL-SmoM2* and its absence in *Gabra6-cre;Ptch1*^{flox/flox} mice. It has also been shown that *Ptch1*^{flox} mice are able to induce MB when crossed with mice expressing recombinase in cerebellar progenitors (*GFAP-cre*) (Wu et al., 2017) and we validated the effect of Ptch1 deletion in *Math1-creER;Ptch1*^{flox/+} mice, observing the induction of progenitors overproliferation (Figures S3B and S3C).

Gabra6-Cre Mice Express Cre Recombinase in Neurons

To exclude that *Gabra6-cre* mice induce recombination in cerebellar progenitors, we crossed them with *LSL-tdTomato* mice that express tdTomato only upon cre recombination. We then analyzed if tdTomato was expressed in progenitors at different postnatal time points. We quantified several thousand tdTomato positive cells (see STAR Methods) and all of them were negative for progenitors, glial or proliferation markers such as PCNA, pH3, Sox2, and Sox9 (Figures S3D–S3L). Moreover, almost all tdTomato cells were positive for the neuronal marker NeuN at P4, P7, P10, and P14 (Figure S3L). Finally, to confirm the specificity of *Gabra6-cre;LSL-tdTomato* mice, we crossed them with *Math1-GFP* mice that express a Math1 protein fused with GFP (Rose et al., 2009) only in granule neuron progenitors. As shown in Figures S4A–S4E, tdTomato-positive cells were GFP negative. Interestingly, in *Gabra6-cre;LSL-tdTomato* mice, tdTomato was expressed in several brain regions such as the cortex, hippocampus, ventral thalamus, and hypothalamus (Figures S4F–S4J). Taken together, these data indicate that our genetic model allows manipulation of postmitotic neurons only. Moreover, these data suggest that only cerebellar neurons are able to dedifferentiate into cancer cells, since we have never observed tumor masses in other regions of the brain.

Transient Cre Recombinase Expression Promotes Dedifferentiation of Granule Neurons in *LSL-SmoM2* Mice

To prove that Shh MB originates from postmitotic neurons, we transfected granule neurons of *LSL-SmoM2* mice at P21/P24 with a plasmid expressing cre recombinase under the control of NeuroD1 promoter (pNeuroD1-cre) (Guerrier et al., 2009). NeuroD1 is expressed in granule neurons and progenitors (Cho and Tsai, 2006), but at the selected time points granule neuron

A NeuN/GFP | GFP | NeuN

(LSL-SmoM2) pNeuroD1-cre - 4 d.p.i

IGL   ML

B

(LSL-SmoM2) pNeuroD1-cre - 4 d.p.i

Number of cells

GFP+ Sox9- | GFP+ Sox9+ | GFP+ Sox2- | GFP+ Sox2+ | GFP+ PCNA- | GFP+ PCNA+

C Hoechst

(LSL-SmoM2) pNeuroD1-cre - 60 d.p.i

D NeuN/PCNA | PCNA | NeuN

(LSL-SmoM2) pNeuroD1-cre - 60 d.p.i

IGL

E Hoechst/DCX | DCX | Hoechst

(LSL-SmoM2) pNeuroD1-cre - 60 d.p.i

IGL

F

	pNeuroD1cre transfection	
Genotype	Aberrant PCNA	Tumors
WT	0/2	0/2
SmoM2	5/16	1/16
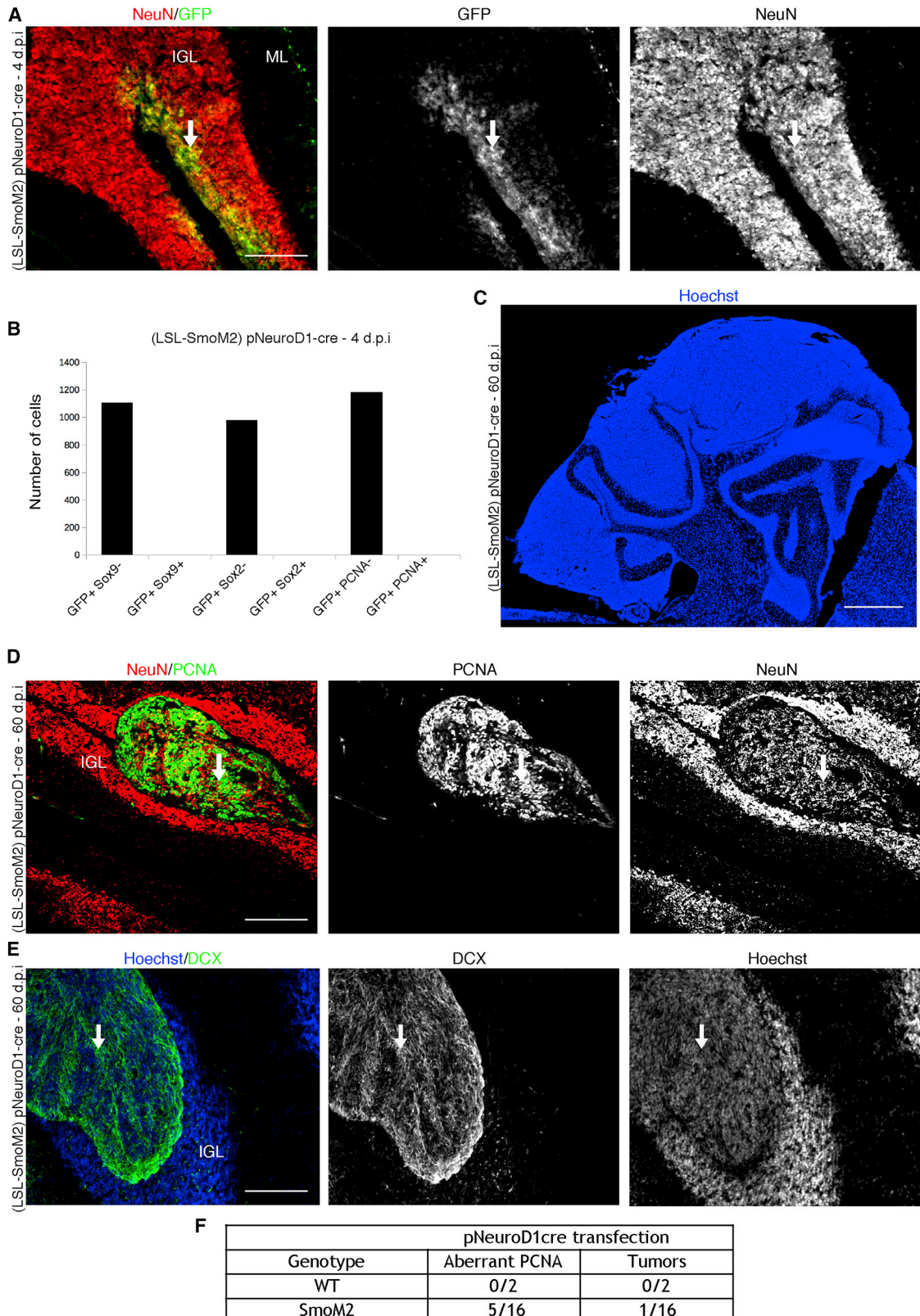
(legend on next page)

progenitors are no longer present (Tiberi et al., 2014; Yang et al., 2008) (Figure S4K). As shown in Figure 3A, 4 days after *in vivo* transfection of pNeuroD1-cre-IRES-GFP, we detected GFP-positive cells in the cerebellum IGL, but we did not detect Sox9/Sox2/PCNA and GFP double-positive cells (Figures 3B and S4L–S4O). These data suggest that we can specifically transfect cerebellar neurons. Anyhow, it has been shown by other groups that Shh pathway activation in granule neuron progenitors after P12-P14 does not lead to MB formation (Yang et al., 2008). We have confirmed these data by induction of SmoM2 with a granule neuron progenitor specific promoter (*Math1-creER*) at P21 and we did not obtain MB (Figure S1H). On the contrary, as shown in Figure 3C, 60 days after pNeuroD1-cre transfection at P21, we observed MB in only one mouse (n = 16). Furthermore, we noticed the formation of PCNA, DCX, pH3, Sox2, and Sox9 positive cells clusters in the IGL of five other mice (Figures 3D–3F and S4P–S4R). These data suggest that SmoM2 expression driven by pNeuroD1-cre in mouse cerebellum (when granule neuron progenitors are not present) can rarely induce Shh MB. In addition, we investigated the possibility to dedifferentiate neurons in adult mice. We transfected 2-month-old *LSL-SmoM2* mice with a plasmid expressing cre recombinase under the control of human SynapsinI promoter (phSynI-cre). This promoter has been shown to induce expression of desired genes in postmitotic neurons and not in glial cells (Kügler et al., 2003). Indeed, 4 days after *in vivo* transfection of phSynI-cre together with pPB-LSL-tdTomato in 2-month-old *LSL-SmoM2* mice, we did not detect Sox9/Sox2/PCNA/pH3 and tdTomato double-positive cells (Figures S4S–S4U). As shown in Figures S5A and S5B, we obtained formation of abnormal PCNA and Sox9 clusters in cerebellum IGL (upon SmoM2 expression) in two out of seven transfected adult mice. These clusters are positive for GFP staining, indicating that transfected cells are expressing SmoM2-YFP. Taken together, these data suggest that SmoM2 is also able to dedifferentiate granule neurons in adult mice.

Mutant BRPF1 Promotes Adult Shh MB Formation

Looking for a molecular mechanism by which SmoM2 induces neuron dedifferentiation, we exploited already published data of human SHH MB exome sequencing. Interestingly, recurrent mutated genes have been identified in adult SHH MBs that were absent or very rare in pediatric SHH MBs, such as BRPF1, KIAA0182, TCF4, CREBBP, NEB, LRP1B, PIK3CA, FBXW7, KDM3B, XPO1, PRKAR1A, and PDE4D (Kool et al., 2014; Merk et al., 2018). For instance, nonsense and frameshift BRPF1 mutations have been found to be associated with SMO

mutations and absent in pediatric and adolescent SHH MBs (samples ID: AdRep_MB107, MB101, and MB143). The presence of a premature stop codon could generate truncated forms of BRPF1 proteins lacking several domains. Brpf1 has been previously shown to be expressed in granule neurons and Purkinje cells in newborn mice (You et al., 2014) and we found that Brpf1 is expressed in mouse cerebellum in P7 and 4-week-old mice (Figures S5C and S5D). We also analyzed the expression of Brpf1 in adult brains and in *Gabra6-cre;LSL-SmoM2* tumors. As shown in Figure 4A, Brpf1 was found to be expressed in cerebellar IGL and in a few cells within *Gabra6-cre;LSL-SmoM2* MBs. This indicates that Brpf1 protein is expressed at low levels in these tumors. Based on the described association of BRPF1 and SMO mutations in adult SHH MB, we tested its function in tumor formation. We co-transfected pNeuroD1-cre with a plasmid that allows constitutive expression of WT BRPF1 in *LSL-SmoM2* mice (pPB-BRPF1 WT; Figure 4B). Notably, we detected no sign of tumor/dysplasia in any of the 19 mice injected with pNeuroD1-cre and pPB-BRPF1 WT (Figures 4C and S5E), suggesting that BRPF1 overexpression blocks SmoM2's ability to induce neuron dedifferentiation. To mimic the mutational background of a subset of human patients, we generated a truncated form of BRPF1 lacking the bromodomain and PWWP motif (Figure 4B). Interestingly, we observed tumor formation when we co-transfected this truncated form of human BRPF1 (pPB-BRPF1 TR; Figure 4C) and a significant decrease in mouse survival compared to BRPF1 WT transfection (Figure 4D). We observed MB formation in 50% of the transfected mice (three out of six; Figure 4C) and the tumors were DCX, Sox9, and PCNA positive (Figures 4E-4G, S5F, and S5G). These data indicate that truncated BRPF1, as found in patients, is able to induce adult SHH MB. Next, we performed an *ex vivo* assay to test if BRPF1 also has a role in neuron dedifferentiation. Cerebellar cells from P7 *LSL-SmoM2* mice were nucleofected with phSynI-cre alone or together with pPB-BRPF1 WT. After 7 days of *ex vivo* culture, we detected several GFP/Sox9/NeuN triple-positive cells in cerebellar cells nucleofected with phSynI-cre alone (Figures S5H and S5I), but fewer with co-overexpression of BRPF1 WT, suggesting that BRPF1 WT blocks neuron dedifferentiation. Moreover, in the same experimental setup Gli1 co-overexpression was able to rescue the repressive effect of BRPF1 WT, indicating that the Shh pathway and BRPF1 WT could have antagonistic roles in the dedifferentiation process. Interestingly, the nucleofection of phSynI-cre and a plasmid-expressing truncated BRPF1 did not block neuron dedifferentiation but rather increased it compared to phSynI-cre alone (Figure S5J). This suggests that truncated BRPF1

Figure 3. Transient Cre Recombinase Expression Promotes Dedifferentiation of Granule Neurons and Shh MB in *LSL-SmoM2* Mice

(A) GFP and NeuN staining of brain sections of *LSL-SmoM2* mice, 4 d.p.i. at P21 with pNeuroD1-cre. The arrow points to GFP and NeuN positive cells.

(B) Quantification of GFP and Sox9/Sox2/PCNA double-positive cells in *LSL-SmoM2* mice, 4 d.p.i. at P21 with pNeuroD1-cre (n = 3).

(C) Hoechst staining of brain sections of *LSL-SmoM2* mice, 60 d.p.i. at P21 with pNeuroD1-cre.

(D) PCNA and NeuN staining of brain sections of *LSL-SmoM2* mice, 60 d.p.i. at P21 with pNeuroD1-cre. The arrow points to a tumorigenic cell cluster within the IGL.

(E) Hoechst and DCX staining of brain sections of *LSL-SmoM2* mice, 60 d.p.i. at P21 with pNeuroD1-cre. The arrow points to a tumorigenic cell cluster within the IGL.

(F) Mice with abnormal PCNA⁺ cell clusters or tumors.

Scale bars, 1 mm in (C) and 150 μm in (A), (D), and (E). d.p.i. days post injection; IGL, internal granular layer; ML, molecular layer.
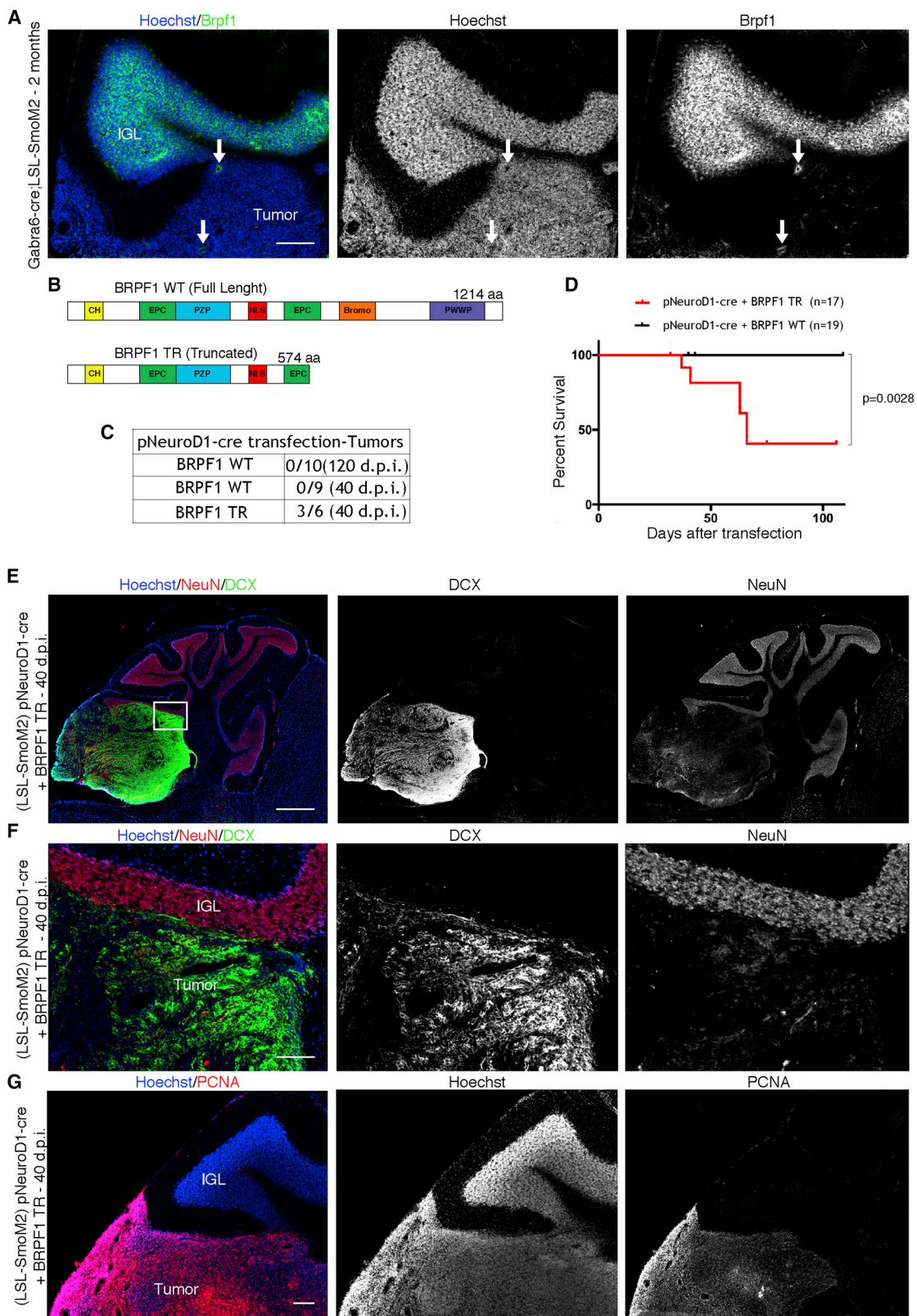
could have a dominant-negative effect in promoting neuron dedifferentiation. Notably, Gli1/2 knockdown was able to completely block SmoM2 and truncated BRPF1 functions, suggesting that they require Gli1/2 expression to induce neuron dedifferentiation. Finally, to prove that neurons of adult mice can also give rise to adult Shh MBs, we transfected adult *LSL-SmoM2* animals (2 months old) with phSynI-cre and pPB-BRPF1 TR (truncated BRPF1) plasmids. We obtained MB formation in three mice out of five (Figures 5A–5E) containing cancer cells positive for GFP, PCNA, and DCX. Furthermore, Kaplan-Meier survival analysis showed that less than 50% of the mice survived 100 days after transfection (Figure 5F). As previously shown in Figures S5A and S5B, phSynI-cre transfection alone induced dedifferentiation of granule neurons, but did not lead to MB formation. This confirms that the Shh pathway and BRPF1 functions should be altered together in adult mice during adult Shh MB tumorigenesis. Notably, we did not obtain Shh MB (n = 11) transfecting truncated BRPF1 alone in 2-month-old CD1 mice (data not shown). To better characterize the BRPF1-induced MB, we performed gene expression profiling of single phSynI-cre+BRPF1 TR and pNeuroD1-cre+BRPF1 TR tumors (Mouse BRPF1). Interestingly, the activation level of the Shh signaling pathway in the SmoM2+BRPF1 TR induced tumors was similar to human adult SHH MBs (Figure 5G). To evaluate if phSynI-cre+BRPF1 TR and pNeuroD1-cre+BRPF1 TR tumors mimic human adult SHH MBs, we further compared their gene expression profiles with mouse and human MB samples. Based on the genes reported in Al-Halabi et al. (2011) as differentially expressed in human adult versus human infant SHH MB, pNeuroD1-cre+BRPF1 TR and phSynI-cre+BRPF1 TR mouse models showed results similar to those for human adult SHH MB (Figure 5H). *Gabra6-cre;LSL-SmoM2* mice (one out of five samples) showed limited similarity to human adult SHH MB, while no similarity was observed for *Math1-cre;LSL-SmoM2* mice (GEO: GSE11859). These data suggest that BRPF1 TR and SmoM2 co-overexpression in adult granule neurons gives rise to mouse tumors with a gene expression profile resembling human adult SHH MB. On the other hand, the tumors obtained from granule neuron progenitors are more similar to human infant SHH MB (*Math1-cre;LSL-SmoM2* mice; GEO: GSE11859). In addition, we performed immunofluorescence for p-AKT and p-S6 and the results have already been shown to be co-markers only for human adult SHH MB (Kool et al., 2014). In fact, few human infant SHH MBs are marked by p-AKT and p-S6 and always in a mutually exclusive way. The tumors generated upon transfection of pNeuroD1-cre+BRPF1 TR and phSynI-cre+BRPF1 TR in *LSL-SmoM2*

showed both p-AKT and p-S6, similar to human adult patients (Figures S5K–S5N; data not shown), while *Math1-creER;LSL-SmoM2* mice present only p-S6 (Figures S5O–S5R). Taken together, these data suggest that our mouse models resemble human adult SHH MB. To validate the cooperativity of SmoM2 and truncated BRPF1 in inducing adult Shh MB, we expressed in adult mice an inducible cre recombinase under the control of the Etv1 promoter in postmitotic neurons (Schüller et al., 2006; Taniguchi et al., 2011). We transfected *Etv1-creER;LSL-SmoM2* mice with pPB-BRPF1 TR at P90 and then we induced the recombination with tamoxifen (n = 9). Notably, only one mouse developed MB (Figures S5S and S5T) and aberrant small clusters of cells were observed in two other mice (data not shown). We also tested the specificity of Etv1-creER recombination, transfecting *Etv1cre-ER;LSL-SmoM2* mice at P90 with pPB-LSL-tdTomato. In these animals, we did not detect any tdTomato and Sox9/Sox2/PCNA/pH3 double-positive cells (Figure S5U). This confirms the role of SmoM2 and truncated BRPF1 in promoting MB formation from postmitotic neurons in adult mice. Finally, we assessed BRPF1 expression in human adult SHH MBs derived from six different patients. In all of the tumors (Figures S5V and S5W; data not shown) we observed few BRPF1-positive cells within the PCNA-positive tumor cells, confirming that BRPF1 protein is downregulated in human adult SHH MBs.

SmoM2 Expression in Granule Neurons Promotes Widespread Chromatin Plasticity

Considering that dedifferentiation of postmitotic cells requires overcoming those epigenetic barriers that are established to maintain cell identity (Fagnocchi et al., 2018; Poli et al., 2018), we investigated whether SmoM2 expression in granule neurons was sufficient to alter the chromatin state. To this end, we profiled changes in chromatin accessibility by ATAC-seq in P14 cerebella of *Gabra6-cre;LSL-SmoM2* and *Gabra6-cre* control mice. ATAC-seq analyses defined approximately 130,000 open chromatin regions which were equally enriched at promoters (transcription start sites; TSSs), introns, and intergenic sites, independently from the genetic background (Figure 6A). Although most of the peaks were shared between the analyzed samples, we retrieved 4,029 and 6,025 open regions that were enriched in *Gabra6-cre* and *Gabra6-cre;LSL-SmoM2*, respectively (Figures 6B and S6A). Of importance, the differential enrichment of these regions was conserved among tissue samples obtained from independent mice (Figure 6C). The enriched regions for ATAC-seq signals showed a typical profile with narrow peaks, resembling nucleosome-depleted regions,

---

Figure 4. WT BRPF1 Is Required to Block Shh MB Formation in *LSL-SmoM2* Mice

(A) Hoechst and Brpf1 staining of brain sections of 2-month-old *Gabra6-cre;LSL-SmoM2* mouse. The arrows point to Brpf1-positive cells.

(B) Representation of human WT BRPF1 and truncated BRPF1. Truncated BRPF1 lacks the bromodomain and the PWWP motif. Bromo, bromodomain; CH, C2H2 zinc finger; EPC, enhancer of polycomb-like motif; NLS, nuclear localization signal; PWWP, Pro-Trp-Trp-Pro motif; PZP, PHD finger-zinc knuckle-PHD finger motif.

(C) Mice with Shh MB after transfection at P21 with pNeuroD1-cre and BRPF1 WT or BRPF1 TR.

(D) Kaplan-Meier survival curves of *LSL-SmoM2* mice transfected at P21 with pNeuroD1-cre+BRPF1 WT or pNeuroD1-cre+BRPF1 TR.

(E and F) Hoechst, NeuN, and DCX staining of brain sections of *LSL-SmoM2* mouse, 40 d.p.i. at P21, with pNeuroD1-cre+BRPF1 TR. Square in (E) marks the region shown at higher magnification in (F).

(G) Hoechst and PCNA staining of brain sections of *LSL-SmoM2* mouse; 40 d.p.i. at P21 with pNeuroD1-cre+BRPF1 TR.

Scale bars, 200 μm in (A), 1 mm in (E), 500 μm in (G), and 150 μm in (F). IGL, internal granular layer. d.p.i. days post injection.
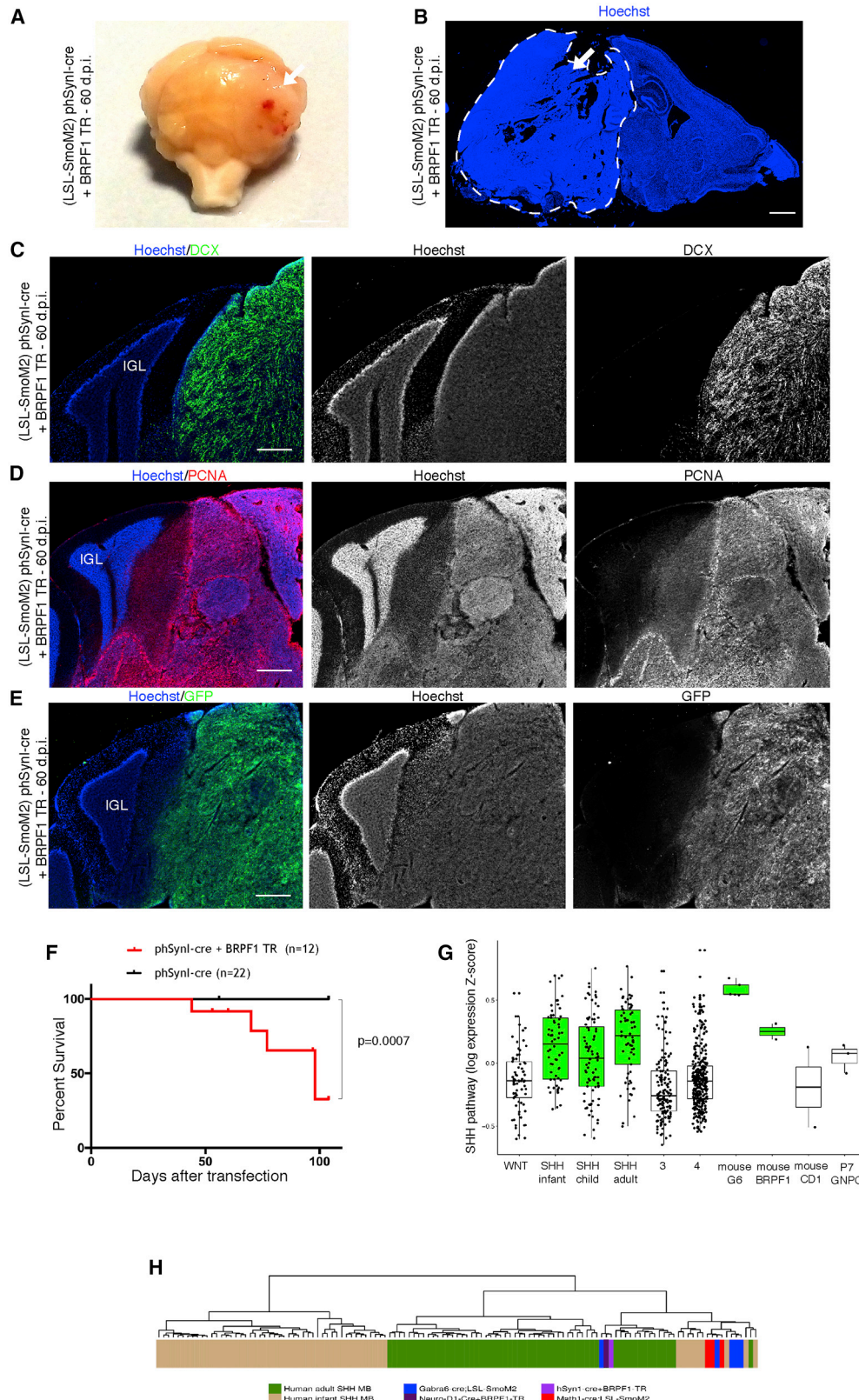
(legend on next page)

occupied by transcription factors (TFs) (Figure 6D). We confirmed that the ATAC-seq profiling on cerebella tissue enables the identification of cis-regulatory elements as we identified specific DNA-binding motifs enriched on the specific ATAC-seq peaks (Figure 6E). In Gabra6-cre samples we found binding motifs for neural-specific TFs and architectural proteins such as CTCF, which are normally enriched at sites of chromatin looping including enhancers (Rada-Iglesias et al., 2018). On Gabra6-cre;LSL-SmoM2 ATAC-seq peaks, we identified DNA-binding motifs of lineage-specifying TFs, which are expressed during cerebellum development, such as Sox2 and Math1 (Figures 6E and S6B). These data were corroborated by Gene Ontology analysis on the genes annotated on specific ATAC-seq peaks highlighting the enrichment of specific signatures associated with stem-cell-like features and cancer pathways in Gabra6-cre;LSL-SmoM2 (Figures 6F and S6C). This pattern was further confirmed by comparing the identified chromatin open regions with those that specified distinct stages of developing cerebellum (Frank et al., 2015). By quantifying the ATAC-seq signals on the previously identified chromatin accessible sites enriched at P14 and P60 (compared to P7) of developing cerebellum, we determined decreases in chromatin accessibility in Gabra6-cre;LSL-SmoM2, respect to Gabra6-cre (Figures 6G, S6D, and S6E). In sum, these results showed that activation of SmoM2 in granule neurons induced changes in chromatin accessibility at cis-regulatory elements. These data suggest an increment of chromatin plasticity by means of favoring diversity in the chromatin contexts, priming for the activation of progenitor-associated transcriptional programs.

Truncated Brpf1 Expression Elicits Chromatin Plasticity by Activating Super-Enhancers

As we showed that upon SmoM2 activation the truncated BRPF1 protein induced MB in adult mice and considering its presumed function in chromatin regulation (Yan et al., 2017), we investigated whether it could favor tumorigenesis by promoting chromatin plasticity and neuronal dedifferentiation. To this end, we profiled the chromatin accessibility changes occurring in postmitotic neurons, in response to SmoM2 activation alone or in cooperation with truncated BRPF1. We took advantage of the human neuroepithelial-like stem cells AF22, that have a gene expression pattern resembling hindbrain fate and committed to generate postmitotic neurons in vitro (Falk et al., 2012; Tailor et al., 2013) (Figure S6F). Indeed, quantitative real-time PCR analysis showed that differentiated AF22 cells expressed high levels of ZIC1 gene, a specific

marker for cerebellar granule neurons (Aruga et al., 1998) (Figure S6G). To resemble the scenario already analyzed in mouse, we nucleofected AF22 with pPB-hSynI-creER as control (Ctrl), and with pPB-hSynI-creER+pPB-LSL-SmoM2 (SmoM2) or pPB-hSynI-creER+pPB-LSL-SmoM2+pPB-LSL-BRPF1 TR (SmoM2+BRPF1 TR) to measure their cooperativity. Moreover, we tested the nucleofection with pPB-hSynI-creER+pPB-LSL-BRPF1 TR (BRPF1 TR) to assess if truncated BRPF1 alone was sufficient per se to alter chromatin accessibility. Of importance, quantitative real-time PCR analysis confirmed that SmoM2 overexpression increases GLI1 mRNA levels in differentiated AF22 neurons (Figure S6H), as observed in Gabra6-cre;LSL-SmoM2 mice (Figure S3A). Thereafter, we profiled changes in chromatin accessibility by ATAC-seq in AF22 neurons expressing the different combinations of SmoM2 and BRPF1 (Figure 7A). ATAC-seq analyses defined comparable numbers of open chromatin regions that were similarly distributed within the genome (Figures 7A and S7A–S7C). At first we confirmed that SmoM2 activation determined an increment in chromatin accessibility at specific cis-regulatory elements that were enriched for stem cells and Sox-family transcription factors (Figures S7D–S7G). Of importance, GSEA analysis confirmed that expression of SmoM2 in human neurons negatively correlated with neuron chromatin accessible sites enriched at P14 and P60 (Figures S7H and S7I). Together, these results showed that we recapitulated the chromatin accessibility pattern found in mouse cerebella in response to SmoM2, also in human neurons. Thereafter, we investigated the contribution of truncated BRPF1 to alter the chromatin landscape. Differential analyses retrieved specific ATAC-seq regions enriched in BPRF1 TR and SmoM2+BRPF1 TR conditions (Figures 7B and 7C), which showed a profile resembling accessible cis-regulatory elements, similar to the ones detected in the mouse models (Figures 7D and S7J). GSEA analysis on the ATAC-seq signals showed that SmoM2 activation correlated with cerebellum development, SHH pathways, and stem cell signatures, while we concurrently measured a decreased in chromatin accessibility on those regions associated with genes related to mature neuron functions (Figure 7E). These analyses indicate that, independent from the genetic background, SmoM2 activation increased chromatin accessibility at stem/progenitor genes associated loci in neurons. Importantly, these features were further elicited by truncated BRPF1 (Figure S7K). Considering that cell fate specification and maintenance of cell identity are regulated by the activation of enhancers (also in human MBs)

Figure 5. Truncated BRPF1 Promotes Adult Shh MB

(A) Image of LSL-SmoM2 mouse; 60 d.p.i. at 2 months, with phSynI-cre+BRPF1 TR. The arrow points to tumoral mass.

(B) Hoechst staining of brain section of LSL-SmoM2 mouse; 60 d.p.i. at 2 months, with phSynI-cre+BRPF1 TR. The dashed lines and arrow in (B) mark the tumor.

(C–E) Hoechst, DCX (C), PCNA (D), and GFP (E) staining of brain sections of LSL-SmoM2 mouse; 60 d.p.i. at 2 months, with phSynI-cre+BRPF1 TR.

(F) Kaplan-Meier survival curves of LSL-SmoM2 mice transfected at 2 months with either phSynI-cre or phSynI-cre+BRPF1 TR. Scale bars, 2 mm in (A), 1 mm in (B), and 500 μm in (C)–(E).

(G) Boxplots of the median values of the SHH pathway for the human samples (GEO: GSE85217) and our samples. BRPF1, 40 d.p.i. pNeuroD1-cre+BRPF1 TR and 60 d.p.i. phSynI-cre+BRPF1 TR. CD1, normal cerebellum tissue. 3, group 3; 4, group 4; G6, Gabra6-cre;LSL-SmoM2; P7 GNPC, P7 granule neuron progenitor cells; SHH, SHH subgroup; WNT, WNT subgroup.

(H) Hierarchical clustering of different Shh MB mouse models data and human adult/infant SHH MB data on both samples distances and samples gene expression profiles using 108 differentially expressed genes in human adult versus human infant SHH MB.

d.p.i., days post injection; IGL, internal granular layer.
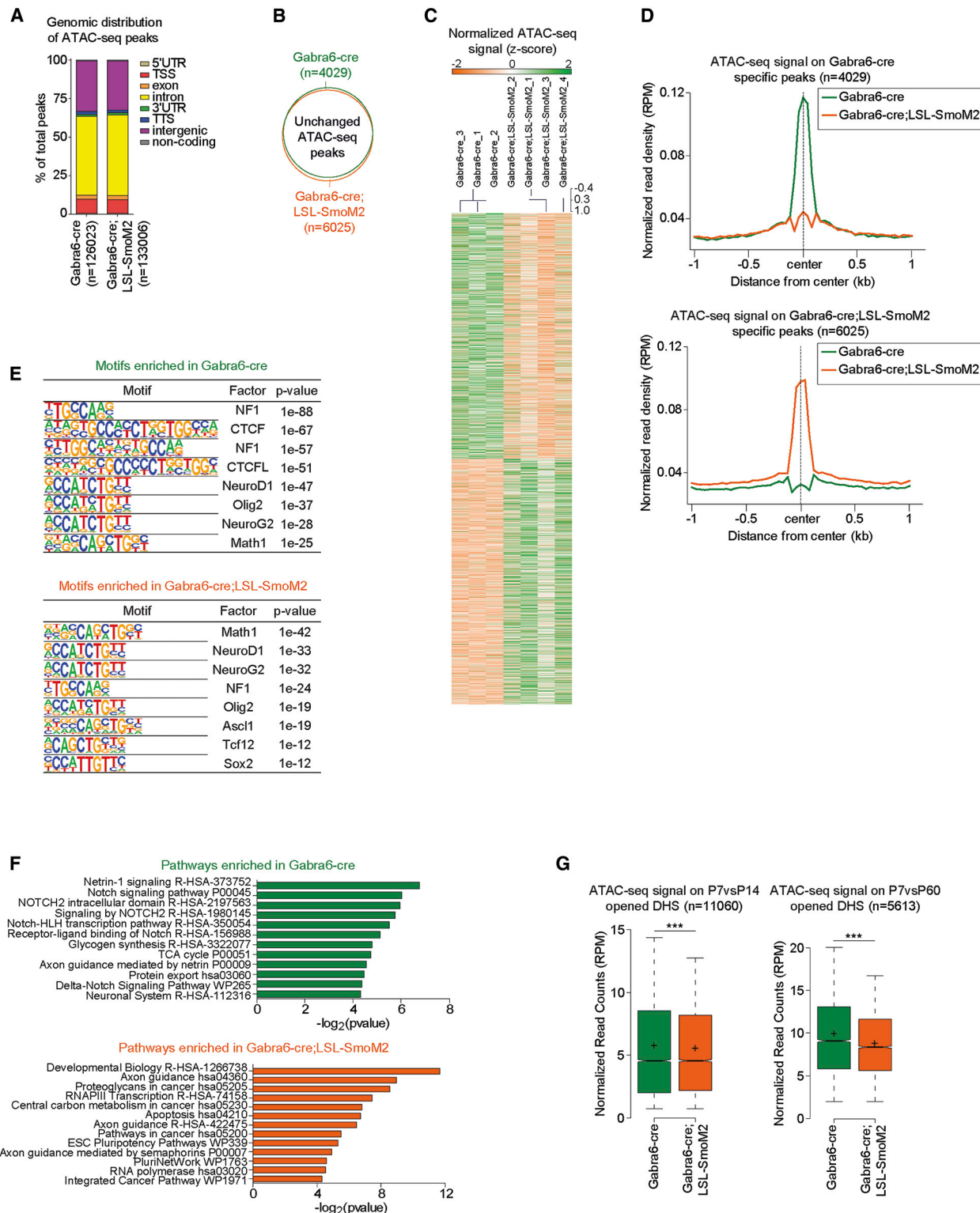
**Figure 6. SmoM2 Expression in Granule Neurons Favors Widespread Chromatin Plasticity and Activation of Stem/Progenitor-Associated Genes**

(A) Boxplots showing the genomic distribution of ATAC-seq peaks, with respect to transcription start sites (TSSs), transcription termination sites (TTSs), 5′UTR, 3′UTR, exons, introns, intergenic regions, and non-coding genes.

(legend continued on next page)

(Lin et al., 2016), we asked whether the measured changes in chromatin accessibility were associated with enhancers modulation. ATAC-seq analysis on annotated human enhancers (Shen et al., 2014) showed that, while BRPF1 TR per se did not alter chromatin accessibility (Figure S7L), its co-expression with SmoM2 induced an increment of chromatin opening (Figure 7F). Given the relative spread pattern of the retrieved ATAC-seq signal distribution on these enhancers (Figure 7F), we asked whether the expression of SmoM2+BRPF1 TR could augment chromatin accessibility to lineage-specifying clustered enhancers, referred as super-enhancers (Lovén et al., 2013). By clustering ATAC-seq peaks, which reside in proximity in a given locus, we identified super-enhancers in all the analyzed conditions (Figures 7G and S7M). Independently from the genetic background, we noticed that the expression of BRPF1 TR increased the number of unique super-enhancers (Figures 7G and S7M). Of importance, in the SmoM2+BRPF1 TR neurons we defined 241 clusters of enhancers with an average size spanning over 33 kb (Figures 7G and 7H). By measuring the relative enrichment of the ATAC-seq signal, we depicted a clear increase in chromatin accessibility associated with the concomitant expression of SmoM2 and BRPF1 TR (Figure 7H). Moreover, we found that the identified super-enhancers were linked to key genes involved in cerebellum development (GBX2 and LMX1B) (Wassarman et al., 1997; Guo et al., 2007) and chromatin remodeling (KDM6B, KDM4B, KMT2C). Gene Ontology analyses confirmed that the SmoM2+BRPF1 TR super-enhancers were specifically associated with chromatin-modifying enzymes, but also with base-excision repair, suggesting a possible involvement of DNA damage response (Figures 7I and S7N). Finally, to assess whether the identified *cis*-regulatory elements in neurons expressing SmoM2+BRPF1 TR resembled specific chromatin features of human SHH MBs, we measured changes of chromatin accessibility on the previously annotated SHH MB enhancers (Lin et al., 2016). This analysis showed that BRPF1 TR expression induced an increment of chromatin opening on SHH enhancers (Figure 7J) and also on SHH associates super-enhancers (Figure 7K). Of importance, the contribution of BRPF1 TR to increased chromatin accessibility was specifically dependent on SmoM2 activation, as the same changes were not detected in truncated BRPF1 alone (Figures S7O and S7P). Taken together, these data showed that truncated BRPF1 cooperates with SmoM2 by promoting chromatin accessibility at clustered enhancers that are linked to genes involved in chromatin remodeling.

DISCUSSION

Cancer is viewed as an evolutionary conserved process that results from the accumulation of somatic mutations in the progeny of a normal cell and it is a common opinion that the cells of origin should possess a proliferative capacity (Blanpain, 2013; Visvader, 2011). Interestingly, few groups have attempted to induce cancer from neurons using full KO mice for cell-cycle regulators or by genetic modification of mice and *Drosophila melanogaster* although rare targeting of progenitors cannot be excluded (Alcantara Llaguno and Parada, 2016; Arlotta and Berninger, 2014). Notably, adult SHH MB arises when progenitors are no longer present and for this reason postmitotic neurons could represent the cell of origin. In the present work we showed that constitutive activation of Shh pathway induced by SmoM2 mutation, specifically in mouse cerebellar granule neurons, promotes the expression of progenitor- and proliferation-associated markers, enabling postmitotic neurons to re-enter in the cell cycle and give rise to Shh MB. Interestingly, activation of the Shh pathway in other CNS neurons does not induce cancer, suggesting that granule neurons have defined intrinsic characteristics that allow the dedifferentiation process. Notably, the deletion of oncosuppressor Ptch1 in granule neurons was not able to recapitulate Shh MB development, as observed with the overexpression of SmoM2. Indeed, Ptch1 deletion led to a lower induction of Shh signaling as compared to SmoM2 constitutive activation, suggesting that other mutational hits could be required. In line with our observations, it has been recently found that tumor suppressors deletion in neurons (cerebral cortex) leads to extended cell division but no glioma formation (Alcantara Llaguno et al., 2019). On the other hand, we performed oncogene overexpression (smoothened gain of function) and we checked for co-mutated genes in the adult SHH MB. Several adult SHH MB patients present truncated mutations of the chromatin reader BRPF1 that are often associated with SMO mutations and absent in pediatric and adolescent patients (Kool et al., 2014). To mimic the mutational background of a subset of human patients, a truncated form of BRPF1 was overexpressed together with SmoM2, exploiting the neuronal promoters NeuroD1 and hSynI. Truncated BRPF1 and SmoM2 co-overexpression led to neuronal dedifferentiation and Shh MB in adult mice. Our data show that a second mutational hit is essential to faithfully recapitulate the adult condition, because constitutive activation of the Shh pathway alone rarely induced MB; otherwise, the co-overexpression of SmoM2 and truncated BRPF1 in adult mice is

(B) Venn diagram showing the overlap between ATAC-seq peaks in *Gabra6-cre* and *Gabra6-cre;LSL-SmoM2* cells.

(C) Heatmap representing the normalized ATAC-seq signal (Z score) on the top 2,000 most differentially enriched peaks in either *Gabra6-cre* or *Gabra6-cre;LSL-SmoM2* cells.

(D) Average tag density plot of the normalized (RPM) ATAC-seq signal on the differential peaks, enriched in *Gabra6-cre* (top panel) or *Gabra6-cre;LSL-SmoM2* (bottom panel) cells.

(E) Motif enrichment analysis on the specific ATAC-seq peaks in *Gabra6-cre* (left panel) or *Gabra6-cre;LSL-SmoM2* (right panel) cells.

(F) Gene Ontology analysis on the genes annotated to specific ATAC-seq peaks in *Gabra6-cre* (top panel) or *Gabra6-cre;LSL-SmoM2* (bottom panel) cells. Pathways from Reactome, Panther, WikiPathways, and KEGG databases were analyzed.

(G) Boxplots showing the normalized read counts of ATAC-seq signals in *Gabra6-cre* and *Gabra6-cre;LSL-SmoM2* cells, on previously reported DNase hypersensitive sites (DHSs), resulting in more accessibility in P14 (left) or P60 (right) cerebella, when compared to P7 cerebella.

***p < 0.001, as assessed by a two-tailed, unpaired Student's t test. P14 *Gabra6-cre* (n = 3) and *Gabra6-cre;LSL-SmoM2* (n = 4) cerebella.

A

Genomic distribution
of ATAC-seq peaks

5'UTR
TSS
exon
intron
3'UTR
TTS
intergenic
non-coding

% of total peaks

hSynI-creER+LSL-tdTomato(n=38431)
hSynI-creER+LSL-SmoM2 TR(n=33825)
hSynI-creER+LSL-BRPF1 TR(n=35867)
hSynI-creER+LSL-SmoM2+LSL-BRPF1 TR (n=40361)

B

hSynI-creER+LSL-BRPF1 TR
(n=1268)

Unchanged
ATAC-seq
peaks

hSynI-creER+LSL-SmoM2
+LSL-BRPF1 TR
(n=2321)

C

Normalized ATAC-seq
signal (z-score)

−2   0   2

hSynI-creER+LSL-BRPF1 TR_1
hSynI-creER+LSL-BRPF1 TR_2
hSynI-creER+LSL-SmoM2+LSL-BRPF1 TR_1
hSynI-creER+LSL-SmoM2+LSL-BRPF1 TR_2

−0.8
0.1
1.0

D

ATAC-seq signal on hSynI-creER+LSL-BRPF1 TR
specific peaks (n=1268)

hSynI-creER+LSL-BRPF1 TR
hSynI-creER+LSL-BRPF1 TR+LSL-SmoM2

Normalized read density (RPM)

Distance from center (kb)

ATAC-seq signal on hSynI-creER+LSL-BRPF1 TR
+LSL-SmoM2 specific peaks (n=2321)

hSynI-creER+LSL-BRPF1 TR
hSynI-creER+LSL-BRPF1 TR+LSL-SmoM2

Normalized read density (RPM)

Distance from center (kb)

E

Normalized Enrichment Score (NES)

SmoM2-enriched
terms

SmoM2-depleted
terms

WT background
BRPF1 TR background

PID_HEDGEHOG 2 PATHWAY
CEREBELLAR CORTEX MORPHOGENESIS
CEREBELLAR CORTEX DEVELOPMENT
PID_HEDGEHOG GLI PATHWAY
WNT ACTIVATED RECEPTOR ACTIVITY
REGULATION OF STEM CELL POPULATION MAINTENANCE
BIOCARTA_SHH PATHWAY
KEGG_HEDGEHOG SIGNALING PATHWAY
REGULATION OF CEREBELLAR GRANULE CELL PRECURSOR PROLIFERATION
CEREBELLUM MORPHOGENESIS
POSITIVE REGULATION OF STEM CELL PROLIFERATION
WNT PROTEIN BINDING
CANONICAL WNT SIGNALING PATHWAY
POSITIVE REGULATION OF NEURAL PRECURSOR CELL PROLIFERATION
REGULATION OF NEURAL PRECURSOR CELL PROLIFERATION
REGULATION OF STEM CELL DIFFERENTIATION
NEURAL PRECURSOR CELL PROLIFERATION
P60 DIFFERENTIATED NEURONS UP-REGULATED GENES
P14 DIFFERENTIATED NEURONS UP-REGULATED GENES
KEGG_NEUROACTIVE LIGAND RECEPTOR INTERACTION
AXON REGENERATION
REGULATION OF ACTION POTENTIAL
DENDRITE MEMBRANE
NEURON CELL CELL ADHESION
NEURON PROJECTION MEMBRANE
EURON PROJECTION REGENERATION
NEURONAL CELL BODY MEMBRANE

F

ATAC-seq signal on hg19 annotated enhancers

hSynI-creER+LSL-SmoM2
hSynI-creER+LSL-SmoM2+LSL-BRPF1 TR

Normalized read density (RPM)

Distance from center (kb)

G

hSynI-creER+LSL-SmoM2
+LSL-BRPF1 TR

Number: 241
Median size: 33.5 kb

ATAC-seq signal at enhancers

ZFHX3
KDM6B
KMT2C
LMX1B
KDM4B
ATF4
GBX2
NCOR2

Enhancers ranked by ATAC-seq signal

H

ATAC-seq signal on hSynI-creER+LSL-SmoM2
+LSL-BRPF1 TR specific super-enhancers

hSynI-creER+LSL-tdTomato
hSynI-creER+LSL-SmoM2
hSynI-creER+LSL-BRPF1 TR
hSynI-creER+LSL-SmoM2+LSL-BRPF1 TR

Normalized read density (RPM)

Genomic region (5'→3')

I

Pathways enriched in
hSynI-creER+LSL-SmoM2+LSL-BRPF1 TR super-enhancers

Methylation WP1247
Methylation Pathways WP704
Base-Excision Repair, AP Site Formation R-HSA-73929
Methylation R-HSA-156581
Chromatin organization R-HSA-4839726
Chromatin modifying enzymes R-HSA-3247509
PluriNetWork WP1763
Signaling Pathways in Glioblastoma WP2261
Notch Signaling Pathway WP61
HDMs demethylate histones R-HSA-3214842
Dopaminergic Neurogenesis WP1498
Dopaminergic Neurogenesis WP2855
Axon guidance hsa04360
Resolution of Abasic Sites (AP sites) R-HSA-73933
Base Excision Repair R-HSA-73884

−log₂(pvalue)

J

ATAC-seq signal on SHH-medulloblastoma
specific enhancers

hSynI-creER+LSL-SmoM2
hSynI-creER+LSL-SmoM2+LSL-BRPF1 TR

Normalized read density (RPM)

Distance from center (kb)

K

ATAC-seq signal on SHH-medulloblastoma
specific super-enhancers

hSynI-creER+LSL-SmoM2
hSynI-creER+LSL-SmoM2+LSL-BRPF1 TR

Normalized read density (RPM)

Genomic region (5'→3')

(legend on next page)

able to promote adult Shh MB development. Gene expression analysis confirmed the similarity between human adult SHH MBs and the tumors originated by truncated BRPF1 and SmoM2 co-overexpression. Notably, only the oldest Gabra6-associated MB resembles the transcriptomic level of human adult SHH MB, probably due to its late onset. In addition, tumors generated upon transfection of truncated BRPF1 exhibited p-Akt and p-S6 markers that are exclusively associated to human adult SHH MB patients. Finally, ATAC-seq analysis revealed that SmoM2 overexpression reshaped the chromatin structure of granule neurons, enriching the number of open chromatin regions associated with stem/progenitor-like genes. Moreover, it pointed out a synergistic mechanism between SmoM2 and truncated BRPF1 in modifying the chromatin accessibility of postmitotic neurons, increasing the number of super-enhancers associated with chromatin organization/modification genes. Overall, the performed experiments demonstrated the role of truncated BRPF1 in altering the chromatin landscape of *cis*-regulatory elements. We believe that these findings could open new roads toward understanding the link between chromatin reshaping and cell dedifferentiation occurring in human patients and leading to tumor formation. Our work establishes a mouse model for human adult SHH MB, showing that postmitotic granule neurons own the capability to re-enter in the cell cycle and give rise to tumors upon the proper oncogenic mutational hit. Remarkably, we uncover that BRPF1 might be one of the key genes involved in adult Shh MB formation and its truncated form could be relevant to mimicking neuronal dedifferentiation and adult Shh MB development.

STAR★METHODS

Detailed methods are provided in the online version of this paper and include the following:

- ● KEY RESOURCES TABLE
- ● LEAD CONTACT AND MATERIALS AVAILABILITY

- ● EXPERIMENTAL MODEL AND SUBJECT DETAILS
  - ○ Mice
  - ○ Human Adult SHH Medulloblastoma Samples
  - ○ Cell Lines and Primary Cell Cultures
- ● METHOD DETAILS
  - ○ Plasmids
  - ○ *In Vivo* Transfection of Granule Neurons
  - ○ Transplantation of Tumor Cells in Nude Mice
  - ○ Histopathological Evaluation
  - ○ Immunofluorescence
  - ○ EdU Staining
  - ○ Imaging
  - ○ Cell Quantification
  - ○ RNA Isolation and Real-Time PCR Analysis
  - ○ Survival Analysis
  - ○ ATAC-Seq
  - ○ Microarray Analysis
- ● QUANTIFICATION AND STATISTICAL ANALYSIS
  - ○ Statistical Analysis
- ● DATA AND CODE AVAILABILITY

SUPPLEMENTAL INFORMATION

Supplemental Information can be found online at https://doi.org/10.1016/j.celrep.2019.11.046.

Figure 7. Truncated Brpf1 Potentiates the Effect of SmoM2, by Reprogramming the Super-Enhancers Landscape

(A) Boxplots showing the genomic distribution of ATAC-seq peaks, with respect to TSSs, TTSs, 5′UTR, 3′UTR, exons, introns, intergenic regions, and non-coding genes, in the indicated cell lines.

(B) Venn diagram showing the overlap between ATAC-seq peaks in hSynI-creER+LSL-BRPF1 TR and hSynI-creER+LSL-SmoM2+LSL-BRPF1 TR cells.

(C) Heatmap representing the normalized ATAC-seq signal (Z score) on the top 2,000 most differentially enriched peaks in either hSynI-creER+LSL-BRPF1 TR or hSynI-creER+LSL-SmoM2+LSL-BRPF1 TR cells.

(D) Average tag density plot of the normalized (RPM) ATAC-seq signal on the differential peaks, enriched either in hSynI-creER+LSL-BRPF1 TR (top panel) or hSynI-creER+LSL-SmoM2+LSL-BRPF1 TR (bottom panel) cells.

(E) GSEA of indicated gene lists, in hSynI-creER+LSL-BRPF1 TR versus hSynI-creER+LSL-SmoM2+LSL-BRPF1 TR cells. All gene lists are enriched with a statistical p < 0.05.

(F) Average tag density plot of the normalized (RPM) ATAC-seq signals in hSynI-creER+LSL-SmoM2 and hSynI-creER+LSL-SmoM2+LSL-BRPF1 TR cells, on annotated enhancer regions of human genome hg19/GRCh37.

(G) Distribution of the ATAC-seq signal across hSynI-creER+LSL-SmoM2+LSL-BRPF1 TR enhancers, showing the presence of 241 super-enhancers. Representative super-enhancers are highlighted along with their associated genes.

(H) Average tag density plot of the normalized (RPM) ATAC-seq signals in indicated cell lines, hSynI-creER+LSL-SmoM2+LSL-BRPF1 TR-specific super-enhancers.

(I) Gene Ontology analysis on the genes associated to hSynI-creER+LSL-SmoM2+LSL-BRPF1 TR-specific super-enhancers. Pathways from Reactome, Panther, WikiPathways, and KEGG databases were analyzed.

(J and K) Average tag density plot of the normalized (RPM) ATAC-seq signals in hSynI-creER+LSL-SmoM2 and hSynI-creER+LSL-SmoM2+LSL-BRPF1 TR cells, on previously reported enhancers (J) and super-enhancers (K), which characterize the SHH MB. Analyses are performed on two biological replicates for each cell line.

AUTHOR CONTRIBUTIONS

DECLARATION OF INTERESTS

REFERENCES

Ahlfeld, J., Favaro, R., Pagella, P., Kretzschmar, H.A., Nicolis, S., and Schüller, U. (2013). Sox2 requirement in sonic hedgehog-associated medulloblastoma. Cancer Res. *73*, 3796–3807.

Ajioka, I., Martins, R.A.P., Bayazitov, I.T., Donovan, S., Johnson, D.A., Frase, S., Cicero, S.A., Boyd, K., Zakharenko, S.S., and Dyer, M.A. (2007). Differentiated horizontal interneurons clonally expand to form metastatic retinoblastoma in mice. Cell *131*, 378–390.

Alcantara Llaguno, S.R., and Parada, L.F. (2016). Cell of origin of glioma: biological and clinical implications. Br. J. Cancer *115*, 1445–1450.

Alcantara Llaguno, S., Sun, D., Pedraza, A.M., Vera, E., Wang, Z., Burns, D.K., and Parada, L.F. (2019). Cell-of-origin susceptibility to glioblastoma formation declines with neural lineage restriction. Nat. Neurosci. *22*, 545–555.

Al-Halabi, H., Nantel, A., Klekner, A., Guiot, M.C., Albrecht, S., Hauser, P., Garami, M., Bognar, L., Kavan, P., Gerges, N., et al. (2011). Preponderance of sonic hedgehog pathway activation characterizes adult medulloblastoma. Acta Neuropathol. *121*, 229–239.

Aller, M.I., Jones, A., Merlo, D., Paterlini, M., Meyer, A.H., Amtmann, U., Brickley, S., Jolin, H.E., McKenzie, A.N.J., Monyer, H., et al. (2003). Cerebellar granule cell Cre recombinase expression. Genesis *36*, 97–103.

Arlotta, P., and Berninger, B. (2014). Brains in metamorphosis: reprogramming cell identity within the central nervous system. Curr. Opin. Neurobiol. *27*, 208–214.

Aruga, J., Minowa, O., Yaginuma, H., Kuno, J., Nagai, T., Noda, T., and Mikoshiba, K. (1998). Mouse Zic1 is involved in cerebellar development. J. Neurosci. *18*, 284–293.

Benjamini, Y., and Hochberg, Y. (1995). Controlling the False Discovery Rate: A Practical and Powerful Approach to Multiple Testing. J. R. Stat. Soc. Series B Stat. Methodol. *57*, 289–300.

Blanpain, C. (2013). Tracing the cellular origin of cancer. Nat. Cell Biol. *15*, 126–134.

Bolger, A.M., Lohse, M., and Usadel, B. (2014). Trimmomatic: a flexible trimmer for Illumina sequence data. Bioinformatics *30*, 2114–2120.

Chen, E.Y., Tan, C.M., Kou, Y., Duan, Q., Wang, Z., Meirelles, G.V., Clark, N.R., and Ma'ayan, A. (2013). Enrichr: interactive and collaborative HTML5 gene list enrichment analysis tool. BMC Bioinformatics *14*, 128.

Cho, J.H., and Tsai, M.J. (2006). Preferential posterior cerebellum defect in BETA2/NeuroD1 knockout mice is the result of differential expression of BETA2/NeuroD1 along anterior-posterior axis. Dev. Biol. *290*, 125–138.

Corces, M.R., Trevino, A.E., Hamilton, E.G., Greenside, P.G., Sinnott-Armstrong, N.A., Vesuna, S., Satpathy, A.T., Rubin, A.J., Montine, K.S., Wu, B., et al. (2017). An improved ATAC-seq protocol reduces background and enables interrogation of frozen tissues. Nat. Methods *14*, 959–962.

Dai, M., Wang, P., Boyd, A.D., Kostov, G., Athey, B., Jones, E.G., Bunney, W.E., Myers, R.M., Speed, T.P., Akil, H., et al. (2005). Evolving gene/transcript definitions significantly alter the interpretation of GeneChip data. Nucleic Acids Res. *33*, e175.

Deneris, E.S., and Hobert, O. (2014). Maintenance of postmitotic neuronal cell identity. Nat. Neurosci. *17*, 899–907.

Eijssen, L.M.T., Jaillard, M., Adriaens, M.E., Gaj, S., de Groot, P.J., Müller, M., and Evelo, C.T. (2013). User-friendly solutions for microarray quality control and pre-processing on. Nucleic Acids Res. *41*, W71–W76. ArrayAnalysis.org.

Ellison, D.W., Dalton, J., Kocak, M., Nicholson, S.L., Fraga, C., Neale, G., Kenney, A.M., Brat, D.J., Perry, A., Yong, W.H., et al. (2011). Medulloblastoma: clinicopathological correlates of SHH, WNT, and non-SHH/WNT molecular subgroups. Acta Neuropathol. *121*, 381–396.

Fagnocchi, L., Poli, V., and Zippo, A. (2018). Enhancer reprogramming in tumor progression: a new route towards cancer cell plasticity. Cell. Mol. Life Sci. *75*, 2537–2555.

Falk, A., Koch, P., Kesavan, J., Takashima, Y., Ladewig, J., Alexander, M., Wiskow, O., Tailor, J., Trotter, M., Pollard, S., et al. (2012). Capture of neuroepithelial-like stem cells from pluripotent stem cells provides a versatile system for in vitro production of human neurons. PLoS ONE *7*, e29597.

Frank, C.L., Liu, F., Wijayatunge, R., Song, L., Biegler, M.T., Yang, M.G., Vockley, C.M., Safi, A., Gersbach, C.A., Crawford, G.E., and West, A.E. (2015). Regulation of chromatin accessibility and Zic binding at enhancers in the developing cerebellum. Nat. Neurosci. *18*, 647–656.

Friedmann-Morvinski, D., Bushong, E.A., Ke, E., Soda, Y., Marumoto, T., Singer, O., Ellisman, M.H., and Verma, I.M. (2012). Dedifferentiation of neurons and astrocytes by oncogenes can induce gliomas in mice. Science *338*, 1080–1084.

Gautier, L., Cope, L., Bolstad, B.M., and Irizarry, R.A. (2004). affy–analysis of Affymetrix GeneChip data at the probe level. Bioinformatics *20*, 307–315.

Guerrier, S., Coutinho-Budd, J., Sassa, T., Gresset, A., Jordan, N.V., Chen, K., Jin, W.L., Frost, A., and Polleux, F. (2009). The F-BAR domain of srGAP2 induces membrane protrusions required for neuronal migration and morphogenesis. Cell *138*, 990–1004.

Guo, C., Qiu, H.Y., Huang, Y., Chen, H., Yang, R.Q., Chen, S.D., Johnson, R.L., Chen, Z.-F., and Ding, Y.Q. (2007). Lmx1b is essential for Fgf8 and Wnt1 expression in the isthmic organizer during tectum and cerebellum development in mice. Development *134*, 317–325.

Heinz, S., Benner, C., Spann, N., Bertolino, E., Lin, Y.C., Laslo, P., Cheng, J.X., Murre, C., Singh, H., and Glass, C.K. (2010). Simple combinations of lineage-determining transcription factors prime cis-regulatory elements required for macrophage and B cell identities. Mol. Cell *38*, 576–589.

Huang, W., Sherman, B.T., and Lempicki, R.A. (2009). Systematic and integrative analysis of large gene lists using DAVID bioinformatics resources. Nat. Protoc. *4*, 44–57.

Irizarry, R.A., Bolstad, B.M., Collin, F., Cope, L.M., Hobbs, B., and Speed, T.P. (2003). Summaries of Affymetrix GeneChip probe level data. Nucleic Acids Res. *31*, e15.

Johnson, W.E., Li, C., and Rabinovic, A. (2007). Adjusting batch effects in microarray expression data using empirical Bayes methods. Biostatistics *8*, 118–127.

Kool, M., Jones, D.T.W., Jäger, N., Northcott, P.A., Pugh, T.J., Hovestadt, V., Piro, R.M., Esparza, L.A., Markant, S.L., Remke, M., et al.; ICGC PedBrain Tumor Project (2014). Genome sequencing of SHH medulloblastoma predicts genotype-related response to smoothened inhibition. Cancer Cell *25*, 393–405.

Kügler, S., Kilic, E., and Bähr, M. (2003). Human synapsin 1 gene promoter confers highly neuron-specific long-term transgene expression from an adenoviral vector in the adult rat brain depending on the transduced area. Gene Ther. *10*, 337–347.

Kuleshov, M.V., Jones, M.R., Rouillard, A.D., Fernandez, N.F., Duan, Q., Wang, Z., Koplev, S., Jenkins, S.L., Jagodnik, K.M., Lachmann, A., et al.

(2016). Enrichr: a comprehensive gene set enrichment analysis web server 2016 update. Nucleic Acids Res. 44 (W1), W90–W97.

Langmead, B., and Salzberg, S.L. (2012). Fast gapped-read alignment with Bowtie 2. Nat. Methods 9, 357–359.

Larsimont, J.C., Youssef, K.K., Sánchez-Danés, A., Sukumaran, V., Defrance, M., Delatte, B., Liagre, M., Baatsen, P., Marine, J.C., Lippens, S., et al. (2015). Sox9 Controls Self-Renewal of Oncogene Targeted Cells and Links Tumor Initiation and Invasion. Cell Stem Cell 17, 60–73.

Larson, D.R., Zenklusen, D., Wu, B., Chao, J.A., and Singer, R.H. (2011). Real-time observation of transcription initiation and elongation on an endogenous yeast gene. Science 332, 475–478.

Li, H., Handsaker, B., Wysoker, A., Fennell, T., Ruan, J., Homer, N., Marth, G., Abecasis, G., and Durbin, R.; 1000 Genome Project Data Processing Subgroup (2009). The Sequence Alignment/Map format and SAMtools. Bioinformatics 25, 2078–2079.

Lin, C.Y., Erkek, S., Tong, Y., Yin, L., Federation, A.J., Zapatka, M., Haldipur, P., Kawauchi, D., Risch, T., Warnatz, H.J., et al. (2016). Active medulloblastoma enhancers reveal subgroup-specific cellular origins. Nature 530, 57–62.

Lovén, J., Hoke, H.A., Lin, C.Y., Lau, A., Orlando, D.A., Vakoc, C.R., Bradner, J.E., Lee, T.I., and Young, R.A. (2013). Selective inhibition of tumor oncogenes by disruption of super-enhancers. Cell 153, 320–334.

Madisen, L., Zwingman, T.A., Sunkin, S.M., Oh, S.W., Zariwala, H.A., Gu, H., Ng, L.L., Palmiter, R.D., Hawrylycz, M.J., Jones, A.R., et al. (2010). A robust and high-throughput Cre reporting and characterization system for the whole mouse brain. Nat. Neurosci. 13, 133–140.

Martz, C.A., Ottina, K.A., Singleton, K.R., Jasper, J.S., Wardell, S.E., Peraza-Penton, A., Anderson, G.R., Winter, P.S., Wang, T., Alley, H.M., et al. (2014). Systematic identification of signaling pathways with potential to confer anti-cancer drug resistance. Sci. Signal. 7, ra121.

Marzban, H., Del Bigio, M.R., Alizadeh, J., Ghavami, S., Zachariah, R.M., and Rastegar, M. (2015). Cellular commitment in the developing cerebellum. Front. Cell. Neurosci. 8, 450.

McLean, C.Y., Bristor, D., Hiller, M., Clarke, S.L., Schaar, B.T., Lowe, C.B., Wenger, A.M., and Bejerano, G. (2010). GREAT improves functional interpretation of cis-regulatory regions. Nat. Biotechnol. 28, 495–501.

Merk, D.J., Ohli, J., Merk, N.D., Thatikonda, V., Morrissy, S., Schoof, M., Schmid, S.N., Harrison, L., Filser, S., Ahlfeld, J., et al. (2018). Opposing Effects of CREBBP Mutations Govern the Phenotype of Rubinstein-Taybi Syndrome and Adult SHH Medulloblastoma. Dev. Cell 44, 709–724.e6.

Nguyen, L., Besson, A., Roberts, J.M., and Guillemot, F. (2006). Coupling cell cycle exit, neuronal differentiation and migration in cortical neurogenesis. Cell Cycle 5, 2314–2318.

Northcott, P.A., Jones, D.T.W., Kool, M., Robinson, G.W., Gilbertson, R.J., Cho, Y.J., Pomeroy, S.L., Korshunov, A., Lichter, P., Taylor, M.D., and Pfister, S.M. (2012). Medulloblastomics: the end of the beginning. Nat. Rev. Cancer 12, 818–834.

Poli, V., Fagnocchi, L., Fasciani, A., Cherubini, A., Mazzoleni, S., Ferrillo, S., Miluzio, A., Gaudioso, G., Vaira, V., Turdo, A., et al. (2018). MYC-driven epigenetic reprogramming favors the onset of tumorigenesis by inducing a stem cell-like state. Nat. Commun. 9, 1024.

Quinlan, A.R., and Hall, I.M. (2010). BEDTools: a flexible suite of utilities for comparing genomic features. Bioinformatics 26, 841–842.

Rada-Iglesias, A., Grosveld, F.G., and Papantonis, A. (2018). Forces driving the three-dimensional folding of eukaryotic genomes. Mol. Syst. Biol. 14, e8214.

Ritchie, M.E., Phipson, B., Wu, D., Hu, Y., Law, C.W., Shi, W., and Smyth, G.K. (2015). limma powers differential expression analyses for RNA-sequencing and microarray studies. Nucleic Acids Res. 43, e47.

Rose, M.F., Ren, J., Ahmad, K.A., Chao, H.T., Klisch, T.J., Flora, A., Greer, J.J., and Zoghbi, H.Y. (2009). Math1 is essential for the development of hindbrain neurons critical for perinatal breathing. Neuron 64, 341–354.

Schüller, U., Kho, A.T., Zhao, Q., Ma, Q., and Rowitch, D.H. (2006). Cerebellar 'transcriptome' reveals cell-type and stage-specific expression during postnatal development and tumorigenesis. Mol. Cell. Neurosci. 33, 247–259.

Schüller, U., Heine, V.M., Mao, J., Kho, A.T., Dillon, A.K., Han, Y.G., Huillard, E., Sun, T., Ligon, A.H., Qian, Y., et al. (2008). Acquisition of granule neuron precursor identity is a critical determinant of progenitor cell competence to form Shh-induced medulloblastoma. Cancer Cell 14, 123–134.

Sergushichev, A.A. (2016). An algorithm for fast preranked gene set enrichment analysis using cumulative statistic calculation. bioRxiv. https://doi.org/10.1101/060012.

Shen, L., Shao, N., Liu, X., and Nestler, E. (2014). ngs.plot: Quick mining and visualization of next-generation sequencing data by integrating genomic databases. BMC Genomics 15, 284.

Southall, T.D., Davidson, C.M., Miller, C., Carr, A., and Brand, A.H. (2014). Dedifferentiation of neurons precedes tumor formation in Lola mutants. Dev. Cell 28, 685–696.

Subramanian, A., Tamayo, P., Mootha, V.K., Mukherjee, S., Ebert, B.L., Gillette, M.A., Paulovich, A., Pomeroy, S.L., Golub, T.R., Lander, E.S., and Mesirov, J.P. (2005). Gene set enrichment analysis: a knowledge-based approach for interpreting genome-wide expression profiles. Proc. Natl. Acad. Sci. USA 102, 15545–15550.

Sutter, R., Shakhova, O., Bhagat, H., Behesti, H., Sutter, C., Penkar, S., Santuccione, A., Bernays, R., Heppner, F.L., Schüller, U., et al. (2010). Cerebellar stem cells act as medulloblastoma-initiating cells in a mouse model and a neural stem cell signature characterizes a subset of human medulloblastomas. Oncogene 29, 1845–1856.

Swartling, F.J., Savov, V., Persson, A.I., Chen, J., Hackett, C.S., Northcott, P.A., Grimmer, M.R., Lau, J., Chesler, L., Perry, A., et al. (2012). Distinct neural stem cell populations give rise to disparate brain tumors in response to N-MYC. Cancer Cell 21, 601–613.

Tailor, J., Kittappa, R., Leto, K., Gates, M., Borel, M., Paulsen, O., Spitzer, S., Karadottir, R.T., Rossi, F., Falk, A., and Smith, A. (2013). Stem cells expanded from the human embryonic hindbrain stably retain regional specification and high neurogenic potency. J. Neurosci. 33, 12407–12422.

Takashima, Y., Guo, G., Loos, R., Nichols, J., Ficz, G., Krueger, F., Oxley, D., Santos, F., Clarke, J., Mansfield, W., et al. (2014). Resetting transcription factor control circuitry toward ground-state pluripotency in human. Cell 158, 1254–1269.

Taniguchi, H., He, M., Wu, P., Kim, S., Paik, R., Sugino, K., Kvitsiani, D., Fu, Y., Lu, J., Lin, Y., et al. (2011). A resource of Cre driver lines for genetic targeting of GABAergic neurons in cerebral cortex. Neuron 71, 995–1013.

Tiberi, L., Bonnefont, J., van den Ameele, J., Le Bon, S.D., Herpoel, A., Bilheu, A., Baron, B.W., and Vanderhaeghen, P. (2014). A BCL6/BCOR/SIRT1 complex triggers neurogenesis and suppresses medulloblastoma by repressing Sonic Hedgehog signaling. Cancer Cell 26, 797–812.

Vanner, R.J., Remke, M., Gallo, M., Selvadurai, H.J., Coutinho, F., Lee, L., Kushida, M., Head, R., Morrissy, S., Zhu, X., et al. (2014). Quiescent sox2(+) cells drive hierarchical growth and relapse in sonic hedgehog subgroup medulloblastoma. Cancer Cell 26, 33–47.

Visvader, J.E. (2011). Cells of origin in cancer. Nature 469, 314–322.

Vong, K.I., Leung, C.K.Y., Behringer, R.R., and Kwan, K.M. (2015). Sox9 is critical for suppression of neurogenesis but not initiation of gliogenesis in the cerebellum. Mol. Brain 8, 25.

Wassarman, K.M., Lewandoski, M., Campbell, K., Joyner, A.L., Rubenstein, J.L., Martinez, S., and Martin, G.R. (1997). Specification of the anterior hindbrain and establishment of a normal mid/hindbrain organizer is dependent on Gbx2 gene function. Development 124, 2923–2934.

Whyte, W.A., Orlando, D.A., Hnisz, D., Abraham, B.J., Lin, C.Y., Kagey, M.H., Rahl, P.B., Lee, T.I., and Young, R.A. (2013). Master transcription factors and mediator establish super-enhancers at key cell identity genes. Cell 153, 307–319.

Wu, C.C., Hou, S., Orr, B.A., Kuo, B.R., Youn, Y.H., Ong, T., Roth, F., Eberhart, C.G., Robinson, G.W., Solecki, D.J., et al. (2017). mTORC1-Mediated Inhibition of 4EBP1 Is Essential for Hedgehog Signaling-Driven Translation and Medulloblastoma. Dev. Cell *43*, 673–688.e5.

Yan, K., Rousseau, J., Littlejohn, R.O., Kiss, C., Lehman, A., Rosenfeld, J.A., Stumpel, C.T.R., Stegmann, A.P.A., Robak, L., Scaglia, F., et al.; DDD Study; CAUSES Study (2017). Mutations in the Chromatin Regulator Gene BRPF1 Cause Syndromic Intellectual Disability and Deficient Histone Acetylation. Am. J. Hum. Genet. *100*, 91–104.

Yang, Z.J., Ellis, T., Markant, S.L., Read, T.A., Kessler, J.D., Bourboulas, M., Schüller, U., Machold, R., Fishell, G., Rowitch, D.H., et al. (2008). Medulloblastoma can be initiated by deletion of Patched in lineage-restricted progenitors or stem cells. Cancer Cell *14*, 135–145.

You, L., Chen, L., Penney, J., Miao, D., and Yang, X.J. (2014). Expression atlas of the multivalent epigenetic regulator Brpf1 and its requirement for survival of mouse embryos. Epigenetics *9*, 860–872.

Yu, X., Ye, Z., Houston, C.M., Zecharia, A.Y., Ma, Y., Zhang, Z., Uygun, D.S., Parker, S., Vyssotski, A.L., Yustos, R., et al. (2015). Wakefulness Is Governed by GABA and Histamine Cotransmission. Neuron *87*, 164–178.

STAR★METHODS

KEY RESOURCES TABLE

REAGENT or RESOURCE	SOURCE	IDENTIFIER
Antibodies		
Anti-NeuN (1:2000)	Millipore	Cat# ABN78, RRID:AB_10807945
Anti-PCNA (1:2000)	Millipore	Cat# MAB424, RRID:AB_95106
Anti-Sox9 (1:2000)	Millipore	Cat# AB5535, RRID:AB_2239761
Anti-Sox2 (1:500)	Abcam	Cat# ab97959, RRID:AB_2341193
Anti-posphoH3 (1:500)	Abcam	Cat# ab97959, RRID:AB_2341193
Anti-Green Fluorescent Protein (1:200)	Thermo Fisher Scientific	Cat# A-11122, RRID:AB_221569
Anti-Doublecortin (1:500)	Millipore	Cat# AB2253, RRID:AB_1586992
Anti-Brpf1 (1:500)	Thermo Fisher Scientific	Cat# PA5-27783, RRID:AB_2545259
Anti-DYKDDDDK Tag (1:500)	Thermo Fisher Scientific	Cat# PA1-984B, RRID:AB_347227
Anti-Neuro D (A-10) (1:100)	Santa Cruz Biotechnology	Cat# sc-46684, RRID:AB_671759
Anti-Phospho-S6 Ribosomal Protein Ser235/236 (1:100)	Cell Signaling Technology	Cat# 2211, RRID:AB_331679
Anti-Phospho-Akt Ser473 (1:100).	Cell Signaling Technology	Cat# 4058, RRID:AB_331168
Alexa Fluor 488 goat anti-mouse (1:500)	Thermo Fisher Scientific	Cat# A28175, RRID:AB_2536161
Alexa Fluor 546 goat anti-rabbit (1:500)	Thermo Fisher Scientific	Cat# A-11010, RRID:AB_2534077
Alexa Fluor 647 goat anti-rabbit (1:500)	SouthernBiotech	Cat# 4030-31, RRID:AB_2795939
Alexa Fluor 488 goat anti-rabbit (1:500)	Thermo Fisher Scientific	Cat# A-11008, RRID:AB_143165
Alexa Fluor 488 goat anti-rat (1:500)	Thermo Fisher Scientific	Cat# A-11006, RRID:AB_2534074
Mouse IgG-heavy and light chain Biotinylated (1:250)	Bethyl	Cat# A90-116B, RRID:AB_309457
Anti-Synaptophysin - Clone 27G12	Leica Biosystems	Cat# NCL-L-SYNAP-299, RRID:AB_564017
Anti-Glial Fibrillary Acidic Protein (GFAP) - Clone GA5	Leica Biosystems	Cat# NCL-GFAP-GA5, RRID:AB_563739
Mouse Anti-Catenin, beta - Clone 14/Beta-Catenin	BD Transduction Laboratories	Cat# 610154, RRID:AB_397555
Anti-YAP1 (63.7)	Santa Cruz Biotechnology	Cat# sc-101199, RRID:AB_1131430
Anti-GAB1	Abcam	Cat# ab59362, RRID:AB_941700
Bacterial and Virus Strains		
10-beta Competent *E. coli* (High Efficiency)	NEB	Cat# C3019H
One Shot Stbl3 Chemically Competent *E. coli*	Invitrogen	Cat# C737303
Biological Samples		
Human adult SHH MB (nodular/desmoplastic) brain section from a 44-year-old female patient	Dr. Felice Giangaspero (University Sapienza of Rome)	N/A
Human adult SHH MB (nodular/desmoplastic) brain section from a 40-year-old male patient	Dr. Felice Giangaspero (University Sapienza of Rome)	N/A
Chemicals, Peptides, and Recombinant Proteins		
Poly-D-lysine	Sigma-Aldrich	Cat# P0899-50MG
Neurobasal medium	Thermo Fisher Scientific	Cat# 21103-049
Fetal Bovine Serum	Thermo Fisher Scientific	Cat# 10270106
D-(+)-Glucose	Sigma-Aldrich	Cat# G5767
Penicillin-Streptomycin (10,000 U/mL)	Thermo Fisher Scientific	Cat# 15140122
L-glutamine	GIBCO 100x	Cat# 25030081
Paraformaldehyde	Acros Organics	Cat#AC169650010
DMEM/F12	Thermo Fisher Scientific	Cat# 31330038
N-2 Supplement (100X)	Thermo Fisher Scientific	Cat# 17502048
B-27 Supplement (50X), serum free	Thermo Fisher Scientific	Cat# 17504044
EGF Recombinant Human Protein	Thermo Fisher Scientific	Cat# PHG0313

(Continued on next page)

REAGENT or RESOURCE	SOURCE	IDENTIFIER
FGF2-Basic Recombinant Human Protein	Thermo Fisher Scientific	Cat# PHG0264
8-Bromo-cAMP	Santa cruz	Cat# Sc-201564a
4-Hydroxytamoxifen	Sigma-Aldrich	Cat# H7904
Tamoxifen, 98% (50 mg/Kg)	Alfa Aesar	Cat# J63509
NucleoBond® Xtra Midi kits	Macherey-Nagel	Cat 740410.50
NucleoSpin® Gel and PCR Clean-up	Macherey-Nagel	Cat 740609.250
NucleoSpin® Plasmid (NoLid)	Macherey-Nagel	Cat 740499.250
T4 DNA ligase (5 U/μL)	Thermo Fisher Scientific	Cat# EL0011
T4 DNA ligase Buffer (10X)	Thermo Fisher Scientific	Cat# B69
in vivo-jetPEI transfection reagent	Polyplus-transfection	Cat# 201-50G
Sucrose	Biosigma	Cat# S5016
bovine serum albumin (BSA)	SEQENS IVD / H2B	Cat# 1000-70
Triton X-100	Sigma-Aldrich	Cat# T8787
Normal Goat Serum	Sigma-Aldrich	Cat# S26
Hoechst	Abcam	Cat# 33258
Vectastain Elite ABC Kit Standard	Vector Labs	Cat# PK-6100
DAB Peroxidase Substrate Kit	Vector Labs	Cat# SK-4100
Hematoxylin	Abcam	Cat# ab220365
TRIzol Reagent	Invitrogen	Cat# 15596018
iScript cDNA synthesis kit	Biorad	Cat# 1708891
Power SYBR Green PCR Master Mix	Thermo Fisher Scientific	Cat# 4367659
OptiPrep Density Gradient Medium (60% Iodixanol)	Sigma-Aldrich	Cat# D1556
Tween-20	Sigma-Aldrich	Cat# P9416
IGEPAL® CA-630	Sigma-Aldrich	Cat# I3021
Digitonin	Promega	Cat# G9441
2x TD reaction buffer from Nextera kit	Illumina	Cat# FC-121-1030
Nextera Tn5 Transposase	Illumina	Cat# FC-121-1030
MinElute PCR Purification Kit	QIAGEN	Cat# 28004
Next High-Fidelity 2 × PCR Master Mix	NEB	Cat# M0541L
Critical Commercial Assays		
Click-iT EdU imaging kit	Invitrogen	Cat# C10632
Deposited Data		
Raw and analyzed data (ATAC-seq)	This paper	GEO: GSE127733
Experimental Models: Cell Lines		
Primary *ex-vivo* cerebellar cell culture from P7 mice	This paper	N/A
Human AF22 neuroepithelial-like stem cells	Falk et al., 2012	N/A
Experimental Models: Organisms/Strains		
M. musculus: Rosa26-LSL-SmoM2-EYFP	The Jackson Laboratory	Cat# JAX:005130, RRID:IMSR_JAX:005130
M. Musculus: Rosa26-LSL-tdTomato	The Jackson Laboratory	Cat# JAX:007908, RRID:IMSR_JAX:007908
M. musculus: Ptch1 flox/flox	The Jackson Laboratory	Cat# JAX:012457, RRID:IMSR_JAX:012457
M. musculus: Math1-creER	The Jackson Laboratory	Cat# JAX:007684, RRID:IMSR_JAX:007684
M. musculus: Sox9 flox/flox	The Jackson Laboratory	Cat# JAX:013106, RRID:IMSR_JAX:013106
M. musculus: Math1-GFP	The Jackson Laboratory	Cat# JAX:013593, RRID:IMSR_JAX:013593
M. musculus: Etv1-creER	The Jackson Laboratory	Cat# JAX:013048, RRID:IMSR_JAX:013048
M. musculus: Foxn1 nude mice	The Jackson Laboratory	Cat# JAX:002019, RRID:IMSR_JAX:002019
M. musculus: Gabra6-cre	Dr. William Wisden (Imperial College London)	N/A

Continued

REAGENT or RESOURCE	SOURCE	IDENTIFIER
Oligonucleotides		
PCR primers and shRNA target sequences are in Table S2	N/A	N/A
Recombinant DNA		
pNeuroD1-IRES-GFP	Guerrier et al., 2009	RRID:Addgene_61403
pNeuroD1-cre-IRES-GFP	This paper	N/A
pAAV-hsyn-flex-dsRed-shvgat	Yu et al., 2015	RRID:Addgene_67845
pAAV-hSynI-cre	This paper	N/A
pPB CAG rtTA-IN	Takashima et al., 2014	RRID:Addgene_60612
pRCF-Brpf1	Dr. Jacques Côté (Laval University Cancer Research Center)	N/A
pPB-CAG-3xFlag-BRPF1-IRES-GFP	This paper	N/A
pPB-CAG-3xFlag-BRPF1-TR-IRES-GFP	This paper	N/A
pDZ264	Larson et al., 2011	RRID:Addgene_35193
pPB-CAG-LSL-MCS-IRES-GFP	This paper	N/A
pPB-CAG-LSL-tdTomato	This paper	N/A
pPB-CAG-LSL-BRPF1 TR-IRES-GFP	This paper	N/A
SmoM2 (W535L)-pcw107-V5	Martz et al., 2014	RRID:Addgene_64628
pPB-CAG-LSL-MCS-IRES-Venus	This paper	N/A
pPB-LSL-SmoM2-IRES-Venus	This paper	N/A
pR275 lenti-NeuroD1prom-CreERT2-WPRE	Dr. Franck Polleux (Columbia University)	N/A
pPB-hSynI-MCS-IRES-Venus	This paper	N/A
pPB-hSynI-creER-IRES-Venus	This paper	N/A
pCMVHahyPBase	Wellcome Sanger Institute, Cambridge UK	N/A
pCAG-GLI1	Tiberi et al., 2014	N/A
pSilencer2.1-CAG-Venus (pSCV2)	Dr. Franck Polleux (Columbia University)	N/A
pSCV2-sh1Gli1	This paper	N/A
pSCV2-sh1Gli2	This paper	N/A
pPB-CAG-Venus	This paper	N/A
pPB-CAG-MCS-IRES-GFP	This paper	N/A
Software and Algorithms		
ImageJ	NIH	https://imagej.nih.gov/ij/
Prism 6	GraphPad Software	https://www.graphpad.com/
Adobe Illustrator	Adobe	https://www.adobe.com/it/products/illustrator.html
Adobe Photoshop	Adobe	https://www.adobe.com/it/products/photoshop.html
FastQC	Brabaham Bioinformatics	https://www.bioinformatics.babraham.ac.uk/projects/fastqc/
Trimmomatic	Bolger et al., 2014	N/A
Bowtie2	Langmead and Salzberg, 2012	N/A
SAMtools	Li et al., 2009	N/A
BEDtools version 2.24.0	Quinlan and Hall, 2010	https://bedtools.readthedocs.io/en/latest/
bedGraphToBigWig program	ENCODE	https://www.encodeproject.org/software/bedgraphtobigwig/
UCSC Genome Browser	N/A	http://genome.ucsc.edu/
HOMER software	Heinz et al., 2010	N/A

Continued

REAGENT or RESOURCE	SOURCE	IDENTIFIER
TM4 MeV v4.9 software	MeV	http://mev.tm4.org/
BoxPlotR	N/A	http://shiny.chemgrid.org/boxplotr/
ngsplot 2.47	Shen et al., 2014	N/A
Enrichr	Chen et al., 2013; Kuleshov et al., 2016	N/A
GREAT	McLean et al., 2010	N/A
Gene set enrichment analysis (GSEA)	Subramanian et al., 2005	N/A
Rank Ordering Of Super-Enhancers (ROSE) tool	Whyte et al., 2013; Lovén et al., 2013	N/A
AffyQC module tool	Eijssen et al., 2013	N/A
affy package	Gautier et al., 2004	N/A
BrainArray custom CDF (mouse4302mmengcdf version 22)	Dai et al., 2005	N/A
rma normalization method	Irizarry et al., 2003	N/A
org.Mm.eg.db	Bioconductor	https://bioconductor.org/packages/release/data/annotation/html/org.Mm.eg.db.html
limma package	Ritchie et al., 2015	N/A
Database for Annotation, Visualization and Integrated Discovery (DAVID) Bioinformatics Resources v6.8	Huang et al., 2009	N/A
fgsea package (GSEA)	Subramanian et al., 2005; Sergushichev, 2016	N/A
KEGG Pathways dataset (mouse profile, accessed in January 2018)	N/A	https://www.genome.jp/kegg/
Gene Set Knowledgebase (GSKB)	Bioconductor	http://ge-lab.org/gskb
COMBAT normalization (inSilicoMerging package)	COMBAT	N/A
Gene Expression Omnibus (GEO)	NCBI	https://www.ncbi.nlm.nih.gov/geo/
Custom CDF (HuGene11stv1_Hs_ENTREZID, ver 22)	BrainArray	http://brainarray.mbni.med.umich.edu/Brainarray/Database/CustomCDF/CDF_download.asp
org.Hs.eg.db	Bioconductor	N/A
Ensembl database (accessed in January 2018)	N/A	http://www.ensembl.org//useast.ensembl.org/index.html?redirectsrc=//www.ensembl.org%2Findex.html
mouse4302.db	Bioconductor	N/A
hugene11sttranscriptcluster.db	Bioconductor	N/A
HOM_MouseHumanSequence.rpt	N/A	http://www.informatics.jax.org/
library(oligo)	Bioconductor	N/A
library(pd.mouse430.2)	Bioconductor	N/A
library(mouse4302.db)	Bioconductor	N/A
library(genefilter)	Bioconductor	N/A
library(pd.hugene.1.1.st.v1)	Bioconductor	N/A
library(hugene11sttranscriptcluster.db)	Bioconductor	N/A
library(sva)	Bioconductor	N/A
library(data.table)	CRAN	N/A
library(factoextra)	CRAN	N/A
library(pheatmap)	CRAN	N/A

LEAD CONTACT AND MATERIALS AVAILABILITY

Further information and requests for resources and reagents should be directed to and will be fulfilled by the Lead Contact, Luca Tiberi (luca.tiberi@unitn.it). Plasmids generated in this study are available upon request with Material Transfer Agreements

EXPERIMENTAL MODEL AND SUBJECT DETAILS

Mice

Rosa26-LSL-SmoM2 (#005130), *Rosa26-LSL-tdTomato* (#007908), *Ptch1*^{flox/flox} (#012457), *Math1-creER* (#007684), *Sox9*^{flox/flox} (#013106), *Math1-GFP* (#013593), *Etv1-creER* (#013048), nude mice (#002019) were purchased from The Jackson Laboratory. Males and females *Gabra6-cre;LSL-SmoM2* mice were analyzed at E16.5, P7, P14, P21, P28, 3 months, > 5 months. Males and females *Gabra6-cre;LSL-tdTomato* mice were analyzed at P0, P4, P7, P10, P14, P21. Males and females *Gabra6-cre;Ptch1*^{flox/+} mice were analyzed at 3 months and > 5 months whereas males and females *Gabra6-cre;Ptch1*^{flox/flox} mice were analyzed at P14, 3 months and > 5 months. Males and females *Gabra6-cre;LSL-SmoM2;Sox9*^{flox/flox} mice were analyzed at 4 weeks and 3 months. Males and females *Gabra6-cre;LSL-tdTomato;Math1-GFP* mice were analyzed at P0 and P7. Males and females *Math1creER;LSL-SmoM2* mice were injected with tamoxifen at P5 or P21 and then analyzed at 1 months, 3 months and > 5 months. Males and females *Math1-creER;Ptch1*^{flox/+} mice were injected with tamoxifen at P5 and analyzed at 4 months. Males and females *Etv1-creER;LSL-SmoM2* mice were transfected with pPB-BRPF1 TR at P90 and then injected with tamoxifen. Those mice where analyzed at 138 days post injection. Males and females *LSL-SmoM2* mice were analyzed at P14, P28, 3 months and > 5 months. Males and females *LSL-SmoM2* mice were transfected with pNeuroD1-cre, pNeuroD1-cre + BRPF1 TR or pNeuroD1-cre + BRPF1 WT, phSynI-cre or phSynI-cre + BRPF1 TR and analyzed at 40, 60 and 100 days post injection. We did not detect any sex dependet differences in all mice analyzed. We thank Prof. William Wisden for providing us with *Gabra6-cre* mice. Mice were housed in a certified Animal Facility in accordance with European Guidelines. Mice were monitored daily for neurological symptoms of brain tumors: weight loss, hydrocephalus, kyphosis, altered gait, lethargy; and euthanized immediately when recommended by veterinary and biological services staff members. The experiments were approved by the Italian Ministry of Health as conforming to the relevant regulatory standards.

Human Adult SHH Medulloblastoma Samples

Human adult medulloblastoma brain sections from a 44-year-old female patient and a 40-year-old male patient have been provided by prof. Giangaspero from Department of Radiologic, Oncologic and Anatomo Pathological Sciences, University Sapienza of Rome, Rome, Italy and IRCCS Neuromed, Pozzilli, Isernia, Italy.

Cell Lines and Primary Cell Cultures
Primary Ex Vivo *Cerebellar Cell Cultures*

Cerebella were dissected from P7 *LSL-SmoM2* mice (males and females) and cells were dissociated by pipetting in dissociation medium (81,8 mM Na2SO4, 30 mM K2SO4, 5,8 mM MgCl2, 0,25 mM CaCl2, 1 mM HEPES pH 7,4, 20 mM Glucose, 0,2 mM NaOH). Cells were nucleofected with 10 μg of total DNA in 100 μl of nucleofection buffer (5mM KCl, 15mM MgCl2, 10 mM Glucose, 120 mM K2HPO4/KH2PO4, pH7.2), using the A-033 program and a Nucleofector 2b Device (Amaxa). For the nucleofection ten different combinations of plasmids were used.

Combination 1: pPB CAG-IRES-GFP, pPB CAG-Venus, pPBase;
Combination 2: pPB CAG-BRPF1 WT-IRES-GFP, pPB CAG-Venus, pPBase;
Combination 3: pPB CAG-BRPF1 TR-IRES-GFP, pPB CAG-Venus, pPBase;
Combination 4: phSynI-cre, pPB CAG-IRES-GFP, pPB CAG-Venus, pPBase;
Combination 5: phSynI-cre, pPB CAG-BRPF1 WT-IRES-GFP, pPB CAG-Venus, pPBase;
Combination 6: phSynI-cre, pPB CAG-BRPF1 TR-IRES-GFP, pPB CAG-Venus, pPBase;
Combination 7: phSynI-cre, pCAG-GLI1, pPB CAG-IRES-GFP, pPB CAG-Venus, pPBase;
Combination 8: phSynI-cre, pPB CAG-BRPF1 WT-IRES-GFP, pPB CAG-Venus, pCAG-GLI1, pPBase;
Combination 9: phSynI-cre, pPB CAG-IRES-GFP, pPB CAG-Venus, psh1-Gli1, psh1-Gli2, pPBase;
Combination 10: phSynI-cre, pPB CAG-BRPF1 TR-IRES-GFP, pPB CAG-Venus, psh1-Gli1, psh1-Gli2, pPBase.

Nucleofected cells were plated in poly-D-lysine coated 24-well plates (each cerebellum was used to fill 4 wells) and grown in Neurobasal medium supplemented with: 20% FBS, 3 mM KCl, 2,1 mg/ml glucose, penicillin/streptomycin and 2mM L-glutamine. Medium was partially changed every 3 days. Cells were fixed after 7 days of growth using PFA 4%.

AF22 Cell Cultures

Human iPSC-derived neuroepithelial-like stem cells AF22 at passage 30, were cultured in a 1:1 ratio mixture of Neurobasal and DMEM/F12 media supplemented with N2 (1:100), B27 (1 μl/ml), 10 ng/ml EGF and 10 ng/ml FGF2. 2x10^6 AF22 cells were nucleofected with 20 μg plasmid DNA in 200 μl nucleofection buffer using the T-020 program and a Nucleofector 2b device (Amaxa). AF22 cells were differentiated into neurons as previously described (Falk et al., 2012). Briefly, neurons were induced culturing the cells for three weeks in a 1:1 ratio mixture of Neurobasal and DMEM/F12 media supplemented with N2 (1:100), B27 (1:50) and 300 ng/ml cAMP. After 19 days of differentiation, 500 ng/ml 4-Hydroxytamoxifen was added to the differentiation media. Two days later neurons were collected for downstream analyses. Four nucleofection plasmid combination were tested.

Combination 1: pPB-hSynI-creER, pPB-CAG-LSL-tdTomato, pPBase;
Combination 2: pPB-hSynI-creER, pPB-CAG-LSL-tdTomato, pPB-LSL-SmoM2, pPBase;
Combination 3: pPB-hSynI-creER, pPB-CAG-LSL-tdTomato, pPB-LSL-BRPF1 TR, pPBase;
Combination 4: pPB-hSynI-creER, pPB-CAG-LSL-tdTomato, pPB-LSL-SmoM2, pPB-LSL-BRPF1 TR, pPBase.

METHOD DETAILS

Plasmids

The coding sequence of Cre recombinase was cloned into pNeuroD1-IRES-GFP creating pNeuroD1-cre-IRES-GFP. pNeuroD1-IRES-GFP is a gift from Franck Polleux (Guerrier et al., 2009) (Addgene plasmid # 61403). The coding sequence of cre recombinase was cloned into pAAV-hsyn-flex-dsRed-shvgat (Yu et al., 2015) (Addgene#67845), forming pAAV-hSynI-cre (phSynI-cre). The coding sequence of human BRPF1 was amplified by PCR from a plasmid of Dr. Jacques Côté (Laval University Cancer Research Center, Canada) and cloned into pPB CAG rtTA-IN (Takashima et al., 2014) (Addgene #60612), forming pPB-CAG-3xFlag-BRPF1-IRES-GFP (pPB-BRPF1 WT). Truncated human BRPF1 was amplified by PCR from WT 3xFlag-BRPF1 (1-574aa) and cloned into pPB-CAG rtTA-IN (Takashima et al., 2014) (Addgene #60612) forming pPB-CAG-3xFlag-BRPF1-TR-IRES-GFP (pPB-BRPF1 TR). The coding sequence of tdTomato was amplified by PCR from pDZ264 (Larson et al., 2011) (Addgene#35193) and cloned into pPB-CAG-LSL-MCS-IRES-GFP, forming pPB-CAG-LSL-tdTomato. Truncated human BRPF1 was amplified by PCR from pPB-CAG-3xFlag-Brpf1-TR-IRES-GFP and cloned into pPB-CAG-LSL-MCS-IRES-GFP, forming pPB-CAG-LSL-BRPF1 TR-IRES-GFP (pPB-LSL-BRPF1 TR). The coding sequence of human SmoM2 was amplified by PCR from SmoM2 (W535L)-pcw107-V5 (Martz et al., 2014) (Addgene#64628) and cloned into pPB-CAG-LSL-MCS-IRES-Venus, forming pPB-LSL-SmoM2-IRES-Venus (pPB-LSL-SmoM2). The coding sequence of creER^{T2} was cloned from pR275 lenti-NeuroD1prom-CreERT2-WPRE (gift from Franck Polleux) and cloned into pPB-hSynI-MCS-IRES-Venus, forming pPB-hSynI-creER-IRES-Venus (pPB-hSynI-creER). The plasmid encoding a hyperactive form of the piggyBac transposase, pCMVHahyPBase (PBase) was provided from the Wellcome Sanger Institute, Cambridge UK. The plasmid encoding the overexpression of GLI1 transcription factor (pCAG-GLI1) was provided by Tiberi et al. (2014). Double-stranded oligonucleotides coding for mouse Gli1 shRNA (target sequence, 5′- TCGGAGTTCAGTCAAATTA −3′) (Tiberi et al., 2014), mouse Gli2 shRNA (target sequence, 5′- AATGATGCCAACCAGAACAAG −3′) (Tiberi et al., 2014) were cloned downstream of the U6 promoter into the pSilencer2.1-CAG-Venus (pSCV2) (gift from Franck Polleux) according to the pSilencer instructions from Ambion, forming pSCV2-sh1Gli1 and pSCV2-sh1Gli2. Venus was amplified from pSCV2, to generate pPB-CAG-Venus plasmid (pPB-Venus). The backbone pPB-CAG-MCS-IRES-GFP (pPB-GFP) was used as readout of nucleofection efficiency in *ex vivo* cerebellar assay. All plasmid used for *in vivo* transfection, *ex vivo* nucleofection and AF22 cell culture; pNeuroD1-cre-IRES-GFP (pNeuroD1-cre), pAAV-hSynI-cre (phSynI-cre), pPB-CAG-3xFlag-Brpf1-IRES-GFP (pPB-BRPF1 WT), pPB-CAG-3xFlag-Brpf1-TR-IRES-GFP (pPB-BRPF1 TR), pPB-CAG-LSL-BRPF1-TR-IRES-GFP (pPB-LSL-BRPF1 TR), pPB-LSL-SmoM2-IRES-Venus (pPB-LSL-SmoM2), pPB-hSynI-creER-IRES-Venus (pPB-hSynI-creER), pPB-CAG-LSL-tdTomato, pPB-CAG-IRES-GFP (pPB-GFP), pPB-CAG-Venus (pPB-Venus), pCAG-GLI1, pSCV2-sh1Gli1 (psh1-Gli1), pSCV2-sh1GLI2 (psh2-Gli2), pCMV-HahyPBase (PBase) are purified using the NucleoBond® Xtra Midi kits (Macherey-Nagel).

In Vivo Transfection of Granule Neurons

A mix of plasmid DNA (0,5 μg/μl) and *in vivo*-jetPEI transfection reagent (Polyplus-transfection) was prepared according to the manufacturer's instructions. pPBase and piggyBac donor plasmids were mixed at a 1:4 ratio. P21-24 and 2, 3-month-old *LSL-SmoM2* mice (males and females) were anaesthetised with 2% isoflurane and medially injected at −1.6 mm rostral to lambda, 0 mm midline, and 1 mm ventral to the skull surface, with 10 μL of DNA transfection reagent mix using a Syringe with a 30-gauge needle.

Transplantation of Tumor Cells in Nude Mice

Tumor of 4-month-old *Gabra6-cre;LSL-SmoM2* mouse was single cell dissociated in trypsin and resuspended in Neurobasal medium at a concentration of 3,2x10^{-4} cells/μl. For transplantation, 4-month- old nude mice (males and females) were anaesthetised with 2% isoflurane and medially injected at −1.6 mm rostral to lambda, 0 mm midline, and 1 mm ventral to the skull surface, with 10 μL of freshly isolated tumor cells using a 26 s-gauge Hamilton syringe. The cells were injected slowly, and the incision was sutured with one or two drops of medical glue. Animals were monitored for 50 days post-transplantation; brains were fixed by perfusion with 4% paraformaldehyde and then appropriate cryoprotected in 30% sucrose (wt/vol, Merck).

Histopathological Evaluation

Three *Gabra6-cre;LSL-SmoM2* tumors were diagnosed by neuropathologists Francesca Gianno and Felice Giangaspero. In addition to standard hematoxylin and eosin staining, immunostaining was done on formalin-fixed paraffin-embedded tumors after dewaxing and rehydrating slides. Antigen retrieval was performed by incubating slices in citrate based pH 6.0 epitope retrieval solution. Primary antibodies were incubated overnight at 4°C and secondary antibodies for 1 hour at room temperature in Antibody solution. ABC solution was used 2 hours at room temperature (Vectastain Elite ABC Kit Standard PK-6100). The sections were incubated with the

substrate at room temperature until suitable staining was observed (DAB Peroxidase Substrate Kit, SK-4100). Nuclei were counter-stained with Hematoxylin (Abcam, ab220365).

Immunofluorescence

E16.5, P0, P4, P7, P10, P14, P21, P28, 3, 4, 7-month-old mice (males and females) were perfused with 4% paraformaldehyde and then brains were cryoprotected in 30% sucrose (wt/vol, Merck). Immunofluorescence stainings were performed on slides, 20/30-μm-thick cryosections. Blocking and Antibody solutions consisted of PBS supplemented with 3% goat serum, 0.3% Triton X-100 (Sigma). Primary antibodies were incubated overnight at 4°C and secondary for 1 h at 15–25°C. Nuclei were stained with bisbenzimide (Hoechst#33258, Sigma). Sections and coverslips were mounted with Permanent Mounting Medium (PMT030).

EdU Staining

P19 *Gabra6-cre;LSL-SmoM2* and *Gabra6-cre;LSL-tdTomato* mice (males and females) were i.p. injected with 50 mg/kg EdU and sacrificed at P21. EdU staining was conducted on brain slices, using Click-iT EdU imaging kit (Invitrogen, Carlsbad, CA), according to the manufacturer's protocol. This protocol was adapted for histological staining of brain tissue as follows. Slides containing mounted frozen brain sections were fixed with 4% paraformaldehyde in phosphate buffer saline (PBS) for 15 min. Fixation step is required to maintain previous staining since EdU labeling has to be performed later. Slides were washed with 3% bovine serum albumin (BSA) in PBS and then permeabilized with 0.5% Triton X-100 in PBS for 20 min. The sections were again washed with 3% BSA in PBS and then incubated with a Click-iT reaction cocktail containing PBS 1X, 4 mM CuSO4, Alexa Fluor® 488 Azide, and reaction buffer additive for 30 min, while protected from light. The sections were washed once more with 3% BSA in PBS and the incubated with Hoechst (#33258) for DNA staining.

Imaging

Images were acquired with a Zeiss Axio Imager M2 (Axiocam MRc, Axiocam MRm), and Zeiss Axio Observer Z1 equipped with Colibri 1, ApoTome 1 and Cell Observer modules. Confocal imaging was performed with either Leica TCS Sp5 or NIKON Eclipse TI2 Spinning Disk confocal Imager optical. Images were processed using ImageJ software. Figures were prepared using Adobe Photoshop (Adobe).

Cell Quantification

For quantification of Sox9/Sox2/PCNA positive cells in 4-week-old *Gabra6-cre;LSL-SmoM2* mice, we used at least three sections of each brain (three brains for each marker), quantified cells: 101 Sox9$^+$/Hoechst$^+$ cells within 2700 Hoechst positive cells, 119 Sox2$^+$/Hoechst$^+$ cells within 2700 Hoechst positive cells, 2672 PCNA$^+$/Hoechst$^+$ cells within 2700 Hoechst positive cells. For quantification of Edu and NeuN double positive cells, we used at least three sections in three different brains, quantified cells: 79 Edu$^+$/NeuN$^+$ cells within 900 Edu positive cells in *Gabra6-cre;LSL-SmoM2* mice, 0 Edu$^+$/NeuN$^+$ cells within 477 Edu positive cells in *Gabra6-cre;LSL-tdTomato* mice. For quantification of Edu and tdTomato double positive cells, we used at least three sections in three different brains of *Gabra6-cre;LSL-tdTomato*, quantified cells: 0 Edu$^+$/tdTomato$^+$ cells within 368 Edu positive cells. For quantification of tdTomato and PCNA double positive cells we have used at least six sections of each brain (three brains for each time point), we quantified: P4 = 927 tomato positive cells, P7 = 9145 tomato positive cells, P10 = 42940 tomato positive cells, P14 = 106090 tomato positive cells. For quantification of tdTomato and pH3 double positive cells we have used at least six sections of each brain (three brains for each time point), we quantified: P4 = 4786 ph3 positive cells, P7 = 842 ph3 positive cells, P10 = 1676 ph3 positive cells, P14 = 350 ph3 positive cells. For quantification of tdTomato and Sox2 double positive cells we have used at least six sections of each brain (three brains for each time point), we quantified: P10 = 8905 sox2 positive cells, P14 = 8422 sox2 positive cells. For quantification of tdTomato and Sox9 double positive cells we have used at least six sections of each brain (three brains for each time point), we quantified: P10 = 7953 sox9 positive cells, P14 = 8061 sox9 positive cells. To identify the tomato positive cells *Rosa26-CAG-LSL-tdTomato* mice without cre have been used to detect background levels. For quantification of tdTomato and GFP double positive cells in *Gabra6-cre;Math1-GFP;LSL-tdTomato* mice, we used at least three sections of each brain (three brains for each time point), quantified cells: P0 = 0 GFP$^+$/tdTomato$^+$ cells within 41 tdTomato positive cells, P7 = 0 GFP$^+$/tdTomato$^+$ cells within 1805 tdTomato positive cells. For quantification of Sox9/Sox2/PCNA and GFP double positive cells in P21 *Rosa26-CAG-LSL-SmoM2* mice transfected with pNeuroD1-cre-IRES-GFP at least three sections of each brain have been used (three brains for each marker), quantified cells: GFP$^+$/Sox9$^+$ = 0 cells, GFP$^+$/Sox9$^-$ = 1105 cells, GFP$^+$/Sox2$^+$ = 0 cells, GFP$^+$/Sox2$^-$ = 978 cells, GFP$^+$/PCNA$^+$ = 0 cells, GFP$^+$/PCNA$^-$ = 1182 cells. For quantification of Sox9/Sox2/PCNA/pH3 and tdTomato double positive cells in 2-month-old *Rosa26-CAG-LSL-SmoM2* mice transfected with phSynI-cre and pPB-CAG-LSL-tdTomato at least three sections of each brain have been used (three brains for each marker), quantified cells: tdTomato$^+$/Sox9$^+$ = 0 cells, tdTomato$^+$/Sox9$^-$ = 2361 cells, tdTomato$^+$/Sox2$^+$ = 0 cells, tdTomato$^+$/Sox2$^-$ = 819 cells, tdTomato$^+$/PCNA$^+$ = 0 cells, tdTomato$^+$/PCNA$^-$ = 1139 cells, tdTomato$^+$/pH3$^+$ = 0 cells, tdTomato$^+$/pH3$^-$ = 2005 cells. For quantification of Sox9/Sox2/PCNA/pH3 and tdTomato double positive cells in 3-month-old *Etv1cre-ER;LSL-SmoM2* mice transfected with pPB-CAG-LSL-tdTomato at least three sections of each brain have been used (three brains for each marker), quantified cells: tdTomato$^+$/Sox9$^+$ = 0 cells, tdTomato$^+$/Sox9$^-$ = 390 cells, tdTomato$^+$/Sox2$^+$ = 0 cells,

tdTomato$^+$/Sox2$^-$ = 532 cells, tdTomato$^+$/PCNA$^+$ = 0 cells, tdTomato$^+$/PCNA$^-$ = 410 cells, tdTomato$^+$/pH3$^+$ = 0 cells, tdTomato$^+$/pH3$^-$ = 570 cells. For the quantification of the nucleofected *ex vivo* cerebellar cells, we quantified at least 300 cells GFP+NeuN+ cells for each condition from three biological repeats. The background levels of GFP/YFP have been detected in cerebellar cells nucleofected without plasmids.

RNA Isolation and Real-Time PCR Analysis
Total RNA from samples were isolated with TRIzol Reagent (Invitrogen) and reverse transcribed using iScript cDNA synthesis kit (Biorad) according to the manufacturer's instructions. Quantitative PCR was performed using Power SYBR Green PCR Master Mix (Applied Biosystems).

Survival Analysis
Survival analysis was performed calculating the lifespan in days of every *Rosa26-LSL-SmoM2*, *Gabra6-cre; Rosa26-LSL-SmoM2* and *Rosa26-LSL-SmoM2* mouse transfected with each specific combination of plasmids. Kaplan-Meier survival curves (Figures 4D and 5F) do not take in consideration *LSL-SmoM2* mice transfected with pNeuroD1-cre+BRPF1-TR (Figure 4C) and phSynI-cre+BRPF1-TR which were sacrificed at a fixed experimental endpoint. Mice died due to undetermined causes during the study were censored in the analysis.

ATAC-Seq
ATAC-Seq Samples Preparation
We performed ATAC-seq on frozen cerebella from P14 *Gabra6-cre;LSL-SmoM2* and control *Gabra6-cre* mice and on hSynI-creER+LSL-tdTomato, hSynI-creER+LSL-BRPF1 TR, hSynI-creER+LSL-SmoM2 and hSynI-creER+LSL-SmoM2+LSL-BRPF1 TR nucleofected AF22 neuroephitilial-like stem cells, as previously described (Corces et al., 2017). Briefly, we first dounced frozen cerebella in 2 mL cold homogenization buffer (0.017 mM PMSF, 0.17 mM β-mercaptoethanol, 320 mM sucrose, 0.1 mM EDTA, 0.1% NP40, 5 mM CaCl2, 3 mM Mg(Ac)2, 10 mM Tris pH 7.8) and pelleted at 100 RCF for 1 min. We next isolated nuclei by transferring 400 ul of supernatant in a plastic tube and sequentially added 400 ul of 50% Iodixanol solution (homogenization buffer and 50% Iodixanol solution), 600 ul of 29% Iodixanol (homogenization buffer, 160 mM and 29% Iodixanol solution) and 600 ul of 35% Iodixanol solution (homogenization buffer, 160 mM and 35% Iodixanol solution) to the bottom of the tube, avoiding mixture of layers. At this point cell lines were also processed in order to isolate their nuclei. We centrifuged for 20 min at 3,000 RCF and we discarded upper layers of the gradient in order to collect 200 ul from the nuclei band. We counted nuclei and transferred 50.000 into a tube with 1 mL of ATAC-Resuspension Buffer (RSB) + 0.1% Tween-20 (10 mM Tris-HCl pH 7.4, 10 mM NaCl, 3 mM MgCl2, 0.1% Tween-20). We pelleted nuclei by centrifuging for 10 minutes at 500 RCF and resuspended in 50 ul cold ATAC-RSB containing 0.1% NP40, 0.1% Tween-20, and 0.01% Digitonin,. We lysed for 3 minutes on ice and washed with 1 mL of cold ATAC-RSB + 0.1% Tween-20. We then transposed the samples by resuspending in 50 ul of transposition mix (25 ul 2x TD buffer, 100nM transposase, 16.5 ul PBS, 0.5 ul 1% digitonin, 0.5 ul 10% Tween-20, 5 ul H2O) and incubated at 37°C for 30 minutes. We purified the transposed DNA using the QIAGEN MinElute PCR Purification Kit (cat. # 28004) and eluted in 10 μL elution buffer. Next we amplified the transposed DNA fragments in the PCR mix (10 μL transposed DNA, 10 μL nuclease-free H2O, 2.5 μL 25 μM PCR Primer 1, 2.5 μL 25 μM Barcoded PCR Primer 2 and 25 μL NEB Next High-Fidelity 2 × PCR Master Mix cat. # M0541L). The final ATAC-seq libraries were purified using the QIAGEN MinElute PCR Purification Kit, quantified at the Qubit Fluorometer (Invitrogen, cat. #Q33226) and quality controlled with the High Sensitivity DNA Assay at the 2100 Bioanalyzer (Agilent, cat. # G2939BA). Four and three independent biological replicates, sequenced as independent libraries, were performed for *Gabra6-cre;LSL-SmoM2* and control *Gabra6-cre*, respectively. Two independent biological replicates, sequenced as independent libraries, were performed for hSynI-creER+LSL-tdTomato, hSynI-creER+LSL-BRPF1 TR, hSynI-creER+LSL-SmoM2 and hSynI-creER+LSL-SmoM2+LSL-BRPF1 TR cell lines. All libraries were sequenced as single reads of 50 bp with the Illumina HiSeq2500.

ATAC-Seq Data Processing
Sequenced reads from all independent sequenced libraries were quality assessed by using fastQC (https://www.bioinformatics.babraham.ac.uk/projects/fastqc/) and trimmed with Trimmomatic (Bolger et al., 2014). Reads from biological replicates were merged for all analysis, unless differentially stated in figure legends. Total reads were aligned to either the mouse genome NCBI37/mm9 or the human genome GRCh37/hg19 using Bowtie2 (Langmead and Salzberg, 2012), using the parameters '–very-sensitive -k 1', thus discarding ambiguous reads mapping at multiple sites. Duplicated reads and reads mapping on mitochondrial DNA were discarded for further analysis with SAMtools (Li et al., 2009). Normalized BigWig tracks of ATAC-seq signals were generated with BEDtools 2.24.0 (https://bedtools.readthedocs.io/en/latest/) (Quinlan and Hall, 2010) and the bedGraphToBigWig program (https://www.encodeproject.org/software/bedgraphtobigwig/) and visualized on the UCSC Genome Browser (http://genome.ucsc.edu/). The HOMER software (Heinz et al., 2010) was further used to analyze ATAC-seq data. The command 'findPeaks' was used for peak calling with these parameters '-size 150 -minDist 1000'; the command 'get-DifferentialPeaks' was used to find peaks with differential ATAC-seq signals between two conditions ('-F 2 -P 0.001'); the command 'findMotifsGenome.pl' was used for motifs enrichment analysis; the command 'annotatePeaks.pl' was used to annotate peaks to related genes and genomic regions and to count the

number of normalized reads on specific regions. Tag counts were then used to produce heatmaps with TM4 MeV v4.9 software (http://mev.tm4.org/) and boxplots with with BoxPlotR (http://shiny.chemgrid.org/boxplotr/). Average tag density plot of the normalized (RPM) ATAC-seq signals were generated with the ngsplot 2.47 (Shen et al., 2014) command ngs.plot.r and plotted with GraphPad Prism (GraphPad Software, San Diego, California, USA, https://www.graphpad.com). Annotated genes were checked for biological processes and pathways enrichment using both Enrichr (Chen et al., 2013; Kuleshov et al., 2016) and GREAT(McLean et al., 2010). Gene set enrichment analysis was performed with GSEA (Subramanian et al., 2005) on publicly available gene sets. Super-enhancers were called with the Rank Ordering Of Super-Enhancers (ROSE) tool (Lovén et al., 2013; Whyte et al., 2013), using the ATAC-seq signal and with default parameters.

Microarray Analysis
Differential Gene Expression Analysis
As a first step, we checked the quality of the raw data file (CEL file) using the AffyQC module tool (Eijssen et al., 2013) observing that the quality indicator values were within the recommended thresholds. Then we follow the quantification procedures using a standard workflow: raw data files were processed with affy package (Gautier et al., 2004) using BrainArray custom CDF(Dai et al., 2005) (mouse4302mmengcdf version 22) and normalized/summarized using rma method(Irizarry et al., 2003). The additional gene annotation was retrieved using org.Mm.eg.db package (https://bioconductor.org/packages/release/data/annotation/html/org.Mm.eg.db.html.). To obtain the differential gene list, we used the principles of linear models and empirical bayes methods as implemented in the limma package (Ritchie et al., 2015). In this way we obtained a list of 1183 differential expressed genes (absolute log fold change greater than 1.5 and multiple-testing adjusted p values < 0.05 (Benjamini and Hochberg, 1995). The functional annotation was performed using two approaches: a) the upregulated genes or downregulated genes (Huang et al., 2009) were analyzed separately through the Database for Annotation, Visualization and Integrated Discovery (DAVID) Bioinformatics Resources v6.8 using the stringent parameter set equal to "high" and the background parameter set to match the actual microarray platform. b) Gene set enrichment analysis was performed using the version implemented in fgsea package (Sergushichev, 2016; Subramanian et al., 2005) performing 10000 permutations and using as database the combination of the KEGG Pathways dataset (mouse profile, accessed in January 2018) and the Gene Set Knowledgebase (GSKB), a comprehensive knowledgebase for pathway analysis in mouse (for detail see http://ge-lab.org/gskb).

Gene Expression Comparison
Mouse comparison. We download from Gene Expression Omnibus the raw data from different datasets (GEO: GSE11859, GSE24628, GSE33199) comprehending several types of Medulloblastoma mouse models as well normal cerebellum tissues. The low level analysis was performed as described above. To remove the possible batch bias and compare these samples to our data, we performed COMBAT normalization as implemented in inSilicoMerging package (Johnson et al., 2007). Then we performed Classical Multidimensional Scaling of all merged datasets, plotting the results of the two principal coordinates.

Human comparison. We download from Gene Expression Omnibus the raw data of the GEO: GSE85217 dataset. The low level analysis was performed as described above with the differences of the used custom CDF (HuGene11stv1_Hs_ENTREZID, ver 22) and the annotation package (org.Hs.eg.db). Then we used the human-mouse orthologs mapping information from the Ensembl database (accessed in January 2018) to re-annotate the mouse dataset into human identifiers. Also in this case, we used the COMBAT normalization method to reduce the differences between platforms and organisms. Then we calculated the median values of the Sonic Hedgehog Pathway genes using the human gene list from KEGG database.

Similarity of Mouse and Human Adult SHH MB
Our pNeuroD1-cre+BRPF1 TR, phSynI-cre+BRPF1 TR and *Gabra6-cre;LSL-SmoM2* mice data and *Math1-cre;LSL-SmoM2* mice data (GEO: GSE11859) were combined with human adult and infant SHH MB data (GEO: GSE85217). As previously described, data was normalized using rma method and COMBAT was used to remove potential batch bias. Annotation for mouse data was obtained using mouse4302.db package while annotation for human data was obtained using hugene11sttranscriptcluster.db package. Human-mouse orthologs mapping was performed using HOM_MouseHumanSequence.rpt table available from www.informatics.jax.org. Hierarchical clustering using differential expressed genes from Al-Halabi et al. (2011), with observed absolute log2 fold change greater than 2 was performed using Pearson's correlation coefficient as distance measure. Clustering analysis was performed on samples.

QUANTIFICATION AND STATISTICAL ANALYSIS

Statistical Analysis
Quantitative Real-Time-PCR Analysis
Data are presented as mean + s.e.m. of three biologically independent P14 cerebella (Figure S3A) or differentiated AF22 cells (Figure S6H). Two-tailed Student's t test was used for calculating significance values.
Ex Vivo Cerebellar Cell Cultures
Data are presented as mean + s.e.m. of three biologically independent *ex vivo* experiments. Two-tailed Student's t test was used for calculating significance values. PiggyBac n = 1733 cells, BRPF1 WT n = 1841 cells, BRPF1 TR n = 1637 cells, hSynI-cre n = 1185

cells, hSynI-cre+BRPF1 WT = 1321 cells, hSynI-cre+BRPF1 TR = 837 cells, hSynI-cre+BRPF1 WT+GLI1 n = 4238 cells, hSynI-cre+GLI1 n = 2156 cells, hSynI-cre+shGli1+shGli2 n = 3796, hSynI-cre+BRPF1 TR+shGli1+shGLi2 n = 3505 (Figure S5J).

Survival Statistical Analysis

Data were displayed using the Kaplan-Meier format and statistical significance of the results was tested using the Log-rank (Mantel-Cox) test. *Gabra6-cre;LSL-SmoM2* n = 23 mice, *LSL-SmoM2* n = 11 mice (Figure 1C); pNeuroD1-cre + BRPF1 TR n = 17 mice, pNeuroD1-cre + BRPF1 WT n = 19 mice (Figure 4D); phSynI-cre + BRPF1 TR n = 12 mice, phSynI-cre n = 22 mice (Figure 5F).

DATA AND CODE AVAILABILITY

The data discussed in this publication have been deposited in NCBI's Gene Expression Omnibus (GEO). The accession number for the ATAC-seq data reported in this paper is GEO: GSE127733.